Red Air Drone

Final Report

AE3200: Design Synthesis Exercise

Group 25 – (2021/2022)

Yamac Birol	5017300	Ozan Kiresi	5026563
Wouter Boullart	5042216	Lowie De Malsche	5011280
Mikola Byelov	5054532	Tim Middendorp	5009871
Dani Hotters	4769732	Matej Moravcik	5010926
Max van Hugten	4998510	Jasper Vallinga	4806735

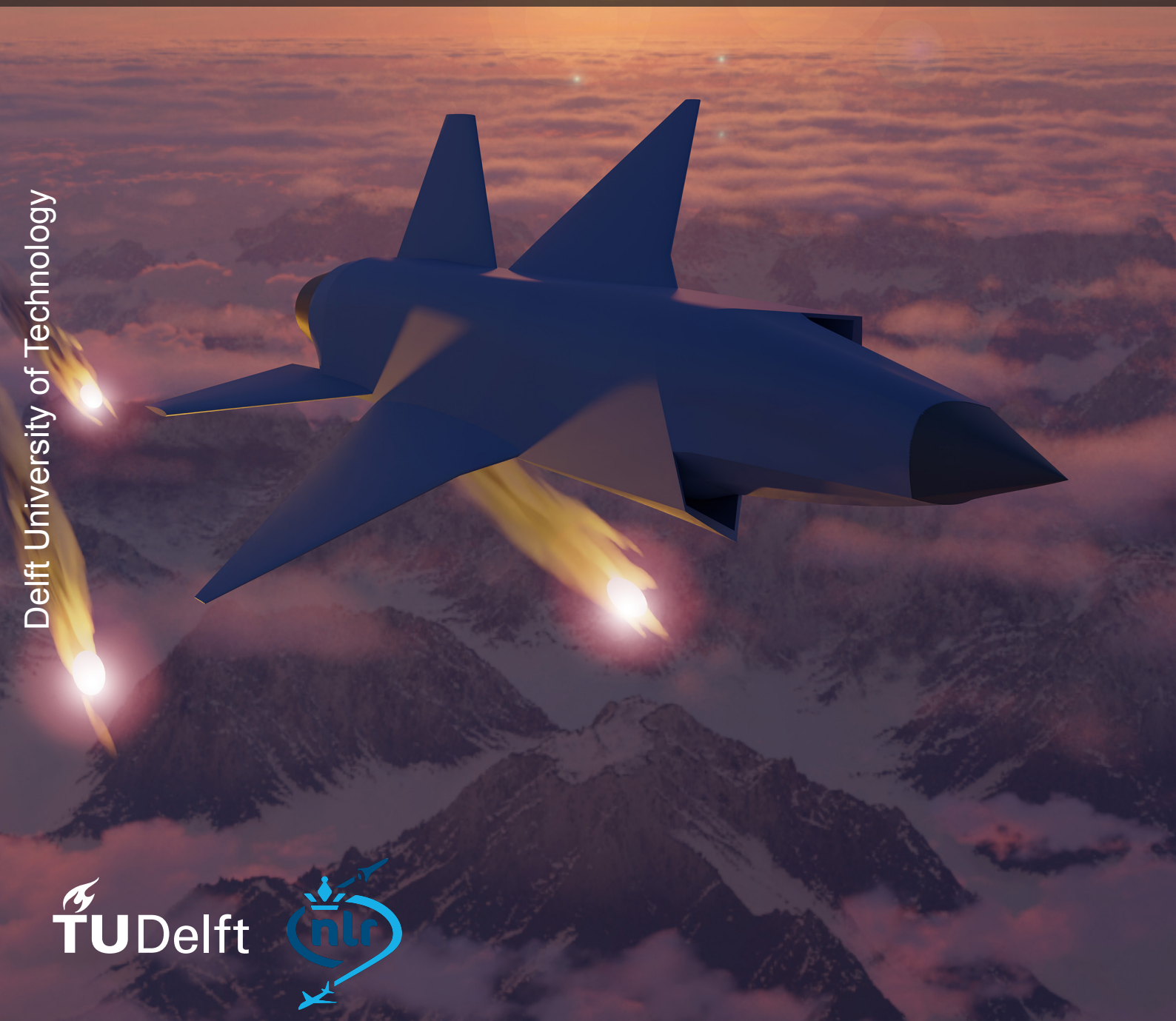

Delft University of Technology

TU Delft

nlr

This page is intentionally left blank.

Red Air Drone
Final Report

by

Group 25 – (2021/2022)

Yamac Birol	**5017300**	**Ozan Kiresi**	**5026563**
Wouter Boullart	**5042216**	**Lowie De Malsche**	**5011280**
Mikola Byelov	**5054532**	**Tim Middendorp**	**5009871**
Dani Hotters	**4769732**	**Matej Moravcik**	**5010926**
Max van Hugten	**4998510**	**Jasper Vallinga**	**4806735**

to complete the AE3200: Design Synthesis Exercise course of the bachelor Aerospace Engineering at the Delft University of Technology. To be defended publicly on Thursday June 23, 2022.

Project duration:	April, 2022 – June, 2022	
Course:	AE3200: Design Synthesis Exercise	
Tutor:	Dr. Ir. Alexander in 't veld	
Teaching Assistant:	Eilidh Radcliff	
Institution:	Delft University of Technology	
Place:	Faculty of Aerospace Engineering, Delft	
Supporting Staff:	Ir. Paul Roling	TU Delft, AE-C&O
	Gitte van Helden	TU Delft, AE-SSE
	Ir. Jacco Dominicus	NLR
	Ir. Harmen Bronkhorst	NLR
	Ir. Tom Pruijsers	NLR
	Ir. Dennis van Oorspronk	NLR
	Ir. Joep Wezel	NLR

Cover Image:	Final render of the red air drone detailed in this report deploying flares
Style:	TU Delft Report Style (AE)

TU Delft nlr

Preface

We are a group of ten students majoring in Aerospace Engineering at the Delft University of Technology. In our final quarter of the third year, for the AE3200 Design Synthesis course, commissioned by NLR, we are designing an adversary drone concept to be used in red air missions.

We target this report to readers, who are interested in the design process of a red air adversary drone. We refer those interested in the configuration and design to chapter 4. Those more interested in the final are referred to chapter 9. The people who are interested in the performance are referred to chapter 10. Furthermore, those interested in the market analysis are referred to chapter 13. For specifics, refer to the table of contents.

We would like to thank our tutor, Dr. Ir. *Alexander in 't Veld*, our coaches, Ir. *Paul Roling* and *Gitte van Helden*, and all DSE teaching assistants, for their advice, care, and guidance; furthermore, we would like to give a special thanks to Ir. *Jacco Dominicus*, Ir. *Tom Pruijsers*, and the other supporting staff from NLR. We would also like to express our gratitude to the professors at the Delft University of Technology for their knowledge and support during the DSE.

DSE Group 25 - (2021/2022)
Delft, June 2022

Abstract

Training in realistic conditions is crucial for fighter pilots. During this training, a red air team is used to represent adversary threats. Currently, the red air team is made up of friendly aircraft that mimic the tactics of the expected adversaries. However, this method has its limitations, such as that these friendly aircraft do not correctly mimic the performance and detectable emissions of the real adversary aircraft. Furthermore, using real combat aircraft has other downsides. They require active fighters and pilots that require expensive training, and using real aircraft means that these expensive combat aircraft need to spend a lot of their service life filling the role of red air instead of flying real missions. As red air flying hours are not considered to be useful training for the pilots flying them, there is no need for using combat-ready aircraft that can carry real armament, nor for a pilot in the cockpit.

Using real combat aircraft has other extensive costs attached to it and is unsustainable looking at its real intended purpose. Just to have a real combat aircraft in the red air fleet requires acquisition of the aircraft, taking it away from active service that it was designed for. It needs a (ground)crew to operate it. It also needs lots of maintenance, requiring mechanics, engineers, tools, hardware, and much more. All of this and the combat aircraft is not used for its designed capabilities in flag missions when it is part of the red team. Therefore, there is a desire for a UAV that can match the performance of the real adversaries, is less expensive to operate, and is more sustainable than the current alternatives to fill the role of red air.

The outcome of the design exercise shown in figure 1. The result is an UAV that can fly at speeds over Mach 1.6, has a maximum normal load factor of 6 g, can sustain a 4 g turn, is low observable, and it is much smaller than currently used aircraft. Because of its size, the UAV is also significantly more sustainable, and cheaper to operate, than the current alternatives. The small size and optimized design also predict that it will have small radar cross-section, therefore, augmentation can be used for the drone to mimic the observability of real adversaries. This ensures that when blue air pilots are training, their instruments show a realistic image of a real adversary.

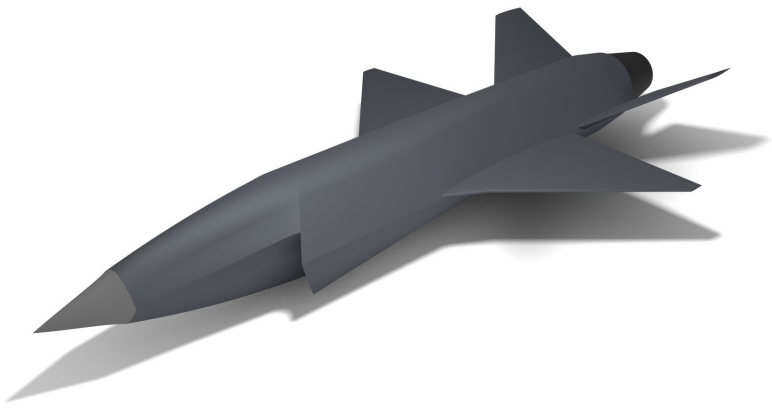

Figure 1: *Render of the red air drone.*

It is therefore concluded that the final design is a promising concept for conducting red air missions. However, the design provided in this report is not a detail design. Further development of the UAV is needed to get to an operational aircraft. Recommendations for this future development are given in the report.

Contents

List of Tables

List of Figures

Nomenclature

Abbreviations

avg.	average
c.g.	centre of gravity
e.g.	exempli gratia (for example)
eq.	equivalent
est.	estimate
etc.	et cetera
i.e.	id est (that is)
max	maximum
min	minimum

Acronyms

AC	Aerodynamic centre
ADAIR	Adversary Air
ADF	Automatic Direction Finding
ADR	Automatic Dead Reckoning
AFT	After
AoA	Angle of Attack
APU	Auxiliary Power Unit
AR	Aspect Ratio
BIST	Built-in Self Test
BIT	Built-in Test
BLOS	Beyond Line Of Sight
BVR	Beyond Visual Range
CAD	Computer Aided Design
CAINS	Carrier Aircraft Inertial Navigation System
CC	Combustion Chamber
CER	Cost Estimating Relationship
CFD	Computational Fluid Dynamics
CG	Centre of Gravity
CMS	Countermeasures
CPFH	Cost Per Flying Hour
CV	Carrier Vehicle
DID	Deliverable Item Description
DME	Distance Measuring Equipment
DoD	Department of Defense
DOT	Design Option Tree
DSE	Design Synthesis Exercise
ECM	Electronic countermeasures
EGI	Embedded GPS/INS
EGT	Exhaust Gas Temperature
EO	Electro-Optical
EW	Electronic Warfare
FBS	Functional Breakdown Structure
FCS	Flight Control System
FEM	Finite Element Method
FFD	Functional Flow Diagram
FOD	Foreign Object Damage
FRC	Flight Recording System
FWD	Forward
GCS	Ground Control Station
GPS	Global Positioning System
GPU	Ground Power Unit
HARS	Heading and Attitude Reference System
HLD	Heavy Lift Device
HLD	High Lift Devices
HPT	High Pressure Turbine
IFA	Inflight Alignment / Aided INS
IFF	Identification, Friend or Foe
IFR	Instrumental Flight Rules
ILS	Instrument Landing System
IMU	Inertial Measurement Unit
INS	Inertial Navigation System
IR	Infrared
ISA	International Standard Atmosphere
L/D	Lift over Drag ratio
LDG	Landing
LEX	Leading Edge Extension
LHV	Lower Heating Value
LNG	Landing Gear
LPT	Low Pressure Turbine
MAC	Mean Aerodynamic Chord
MIDS	Multifunctional Information Distribution System
MLG	Main Landing Gear
MNS	Mission Need Statement
MOD	Modifications
MTOW	Maximum Take-Off Weight
NATO	North Atlantic Treaty Organization
NGAT	Next-Generational Aerial Target
NSW	Normal Shock Wave
OEW	Operating Empty Weight
OSW	Oblique Shock Wave
PDU	Power Distribution Unit
POS	Project Objective Statement
PPS	Post Production Support
PS	Power System
PSL	Primary Satellite Link
RAD	Red Air Drone
RAM	Ram Air Turbine
RAMS	Reliability, Availability, Maintainability and Safety

RCS	Radar Cross-Section
ROC	Rate Of Climb
RR	Reimbursible Rate
RRAT	Remove, Reduce, Accept, or Transfer
S/L	Sea Level
S/T	Static
SAS	Stability Augmentation System
SATCOM	Satellite Communication
SHF	Super High Frequency
SWOT	Strength, Weakness, Opportunity, and Threat
T/O	Take-off
TA	Teaching Assistant
TACAN	Tactical Air Navigation
TCAS	Traffic Collision Avoidance System
TERCOM	Terrain Contour Matching
TERNAV	Terrain Navigation
TRL	Technology Readiness Level
TSFC	Thrust Specific Fuel Consumption
UAV	Unmanned Aerial Vehicle
UHF	Ultra High Frequency
USAF	United States Air Force
USMC	United States Marine Corps
USN	United States Navy
V&V	Verification & Validation
VFR	Visual Flight Rules
VHF	Very High Frequency
VOR	Very high frequency Omni-directional Range

Greek Symbols

β	Shock wave angle	deg
δ	Control surface deflection	deg
ϵ	Downwash angle	deg
ϵ	Frontal coverage angle	deg
η	Efficiency	-
γ	Climb angle	deg
γ	Heat capacity ratio	-
λ	Taper ratio	-
$\Lambda_{0.25h}$	Horizontal tail quarter chord sweep	deg
λ_h	Horizontal tail taper ratio	-
Λ_{LE}	Main wing leading edge sweep angle	rad
Π	Pressure ratio	-
ρ	Density	kg/m^3
σ	Structural Stress	N/m^2
τ	Aileron effectiveness	-
θ	Ramp angle	deg

Latin Symbols

$\dot{m}$	Mass flow	kg/s
A	Channel area	m^2
B	Boom area	m^2
b	Wing span	m
c	Chord length	m
C_D	Wing drag coefficient	-
C_d	Airfoil drag coefficient	-
c_p	Specific heat capacity	J/kg/K
C_{t}	Volume coefficient of the tail	-
C_L	Wing lift coefficient	-
C_l	Airfoil lift coefficient	-
D	Drag	N
E	Elastic modulus	N/m^2
e	Oswald efficiency factor	-
L	Lift	N
l_{t}	Distance from the quarter chord of the wing to the quarter chord of the tail	
M	Mach number	-
n	Load factor	-
P	Power	Nm/s
p	Pressure	N/m^2
p	Roll rate	deg/s
q	Dynamics pressure	N/m^2
R	Gas constant of air	J/kg/K
S	Wing surface area	m^2
S_{t}	Tail surface area	m^2
T	Temperature	k
T	Thrust	N
t	Thickness	m
V	Velocity	m/s
W	Weight	kg

Executive Overview

For the training of pilots realistic conditions are crucial for training effectiveness. Currently, when it comes to training from airborne threats like missiles or adversary aircraft, a red air team is used. This red air team is filled by friendly aircraft; however, there are limitations to using these aircraft. These aircraft do not correctly mimic the capabilities of real adversaries. Furthermore, using fighter aircraft in the red air team is expensive, and the pilots performing the red air mission will not learn anything new. Therefore, there is a desire for a drone that can match the performance of the real adversaries to fill the role of red air.This report entails the need and design of a Red Air Drone (RAD) for performing these training missions. Furthermore, it elaborates the operational concept and estimated costs of using this drone.

Concept Selection

The concept which formed the basis for the final design stage was chosen by the trade-off, mainly because of its good transonic and supersonic performance and good storage possibilities in the fuselage. The concept is a very good choice in terms of aerodynamic performance, both in terms of (sub)transonic and supersonic and structural performance, where it scored second-highest. This is mainly due to use of delta wing, which offers good transonic performance, as a result of high leading-edge sweep. Delta wing design is also proved concept for supersonic flight. Another change in the configuration is the fuselage shape, as it again offers better low observability performance and easier incorporation of the Y-duct to the body.

Sustainability

Military Red Air missions are often performed using modern fighters like F-16, or advanced jet trainers. These aircraft are, however, designed to perform different missions than the Red Air mission. Therefore, these platforms are, in a way, over-designed for these missions. The platforms used by air forces and private contractors were also not designed specifically for the Red Air mission. Consequently, current platforms are too big, too heavy, and thus not the most efficient solution to provide Red Air for blue air training.

Looking at the operational sustainability of the RAD compared to the current platforms, considerable differences are present. The main difference being that the RAD is much smaller than current alternatives as it is designed specifically for this task, which means consumes much less fuel. Regarding environmental sustainability, the RAD will produce less noise emissions than the current platforms, also mainly because of its smaller engine. It will also differentiate itself by having fewer parts and less material.

The RAD is undoubtedly more sustainable than the current platforms used for the red air mission. However, efforts were made to ensure that the sustainability of the RAD is optimised during the design. The wing box and fuselage structure have been designed with recyclable materials such as aluminium in mind. Economic sustainability is pursued by analysing and minimising the costs while adding more value to the product.

Looking at the future of the RAD, all three sustainability pillars, social, economic, and environmental, can be further optimised. The most important added benefit with respect to social sustainability is that the reach of it can be extended. Not only fighter pilots can benefit, but all parties involved with providing red air for blue air training will see benefit through the RAD. Secondly, the logistic, operations and production can be optimised. Hereby improving the economic and environmental sustainability.

The design of a military supersonic stealth UAV can raise some ethical concerns about how it will be used and if it will be used for its intended purpose. The RAD is used for blue air training by emulating red air and thus train pilots for combat. This training has been shown to increase the chances of survival of the pilots and it can thus be argued that it would be unethical not to provide it. Furthermore, Red Air exercises are already flown today and will continue to do so in the future. Overall, the RAD does not provide new military capabilities and only provides a Red Air platform in a more sustainable and cost-effective manner compared to current fighters filling the role.

Configuration

The configuration of the RAD can be divided into the external and internal configuration. The external configuration shown in figure 2a includes several main aspects: a compound delta wing, a fuselage housing a buried afterburning turbojet with a shape optimized through area ruling, a V-tail combining both horizontal and vertical tail and a variable exhaust nozzle at the back. The wing has been positioned relatively aft to retain a good balance between longitudinal stability and controllability due to the centre of gravity being relatively aft (due to the heavy engine and afterburner) as well.

The internal configuration shows all the mission systems, variable systems and key systems (e.g., the engine). They have been positioned in a way that is required for their correct functioning, considering the centre of gravity location and providing easy accessibility. Finally with all the required systems and elements of the RAD in, a final MTOM (maximum take-off mass) of 2126.2 kg has been found.

Aerodynamics

The aerodynamic characteristics, along with the weight and propulsion characteristics, determine the performance of the RAD and are the defining factor of its mission capabilities. The lift and drag performance of the RAD will determine its flight envelope, cruising efficiency, the range and many more factors that rely on the aerodynamic performance. The goal is to have the best drag at the most important flight conditions, which for the RAD is, cruising at Mach 0.9 and dashing to Mach 0.95 and 1.6 or even Mach 2.

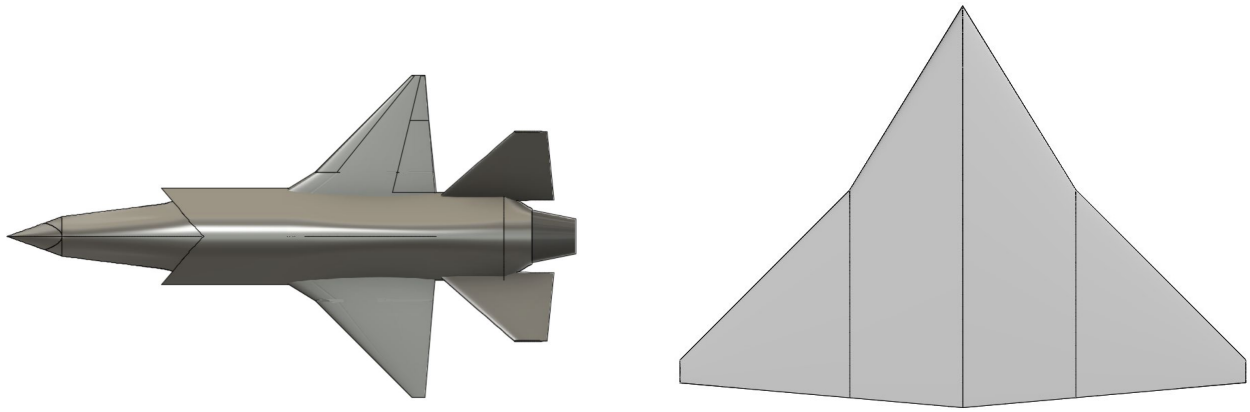

(a) *The external configuration of the RAD.* **(b)** *The wing of the RAD shown from the top view.*

Figure 2: *The RAD external configuration and wing structure.*

As the RAD will be cruising at Mach 0.9 for most of its flight profile, its aerodynamic performance is optimised for this. The supercritical NASA SC(2)-0404 airfoil was chosen for its great transonic performance. It is a thin airfoil, which is good for supersonic performance as well. The wing has the same airfoil throughout, and the planform is shown in figure 2b. The wing is a cropped compound delta wing and the dimensions of the wing are given in table 1.

Table 1: *The wing dimensions of the RAD.*

Area [m^2]	C_r [m]	AR [-]	C_t [m]	λ [-]	b [m]	MAC [m]
4.53	2.6	3	0.15	0.057	3.66	1.26

The wing has a large sweep and small aspect ratio to optimise the transonic and supersonic performance. Figure 3 shows the performance of the RAD compared to the fighters it is tries to emulate.

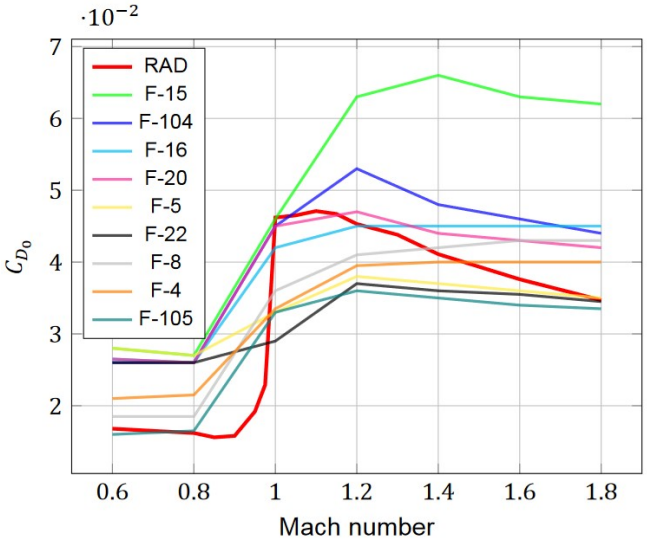

Figure 3: *The C_{D_0} of the RAD and fighter aircraft with increasing Mach number.*

The figure shows that the RAD has a good low transonic drag performance where it will cruise and good high supersonic drag performance where it will dash.

Propulsion and Power

The propulsion and power system of the aircraft propels the aircraft to desired speed and altitudes and provides enough power to the aircraft systems. The requirements for this system arise from both stakeholder requirements and other systems. Thus, it is essential to know several aircraft system parameters before starting to design the propulsion and power system.

The propulsion system provides the necessary thrust to the aircraft. For the design of the propulsion system, first the engine is selected. The engine selection was based on the thrust required during the flight envelope. This thrust required comes from the preliminary drag estimations following the weight estimations. With the required thrust estimations, thrust ranges for engine selection is determined. Within this range several engines and their specifications are compared by looking at not only the thrust but the specific fuel consumption, inlet and maximum diameters, length and bypass ratio. Each one of these criteria affect the design of the whole aircraft and when changed, sum up to significant value changes in parameters such as the weight, drag and lift. As the engine grew in size and weight, it was observed that the drag and weight increased substantially. Thus, it was critical to select the smallest engine possible while adhering to the thrust and power requirements. The drag values for the supersonic speeds were found to be greater than the subsonic speeds. Thus, supersonic speeds required more thrust to reach than subsonic speeds.

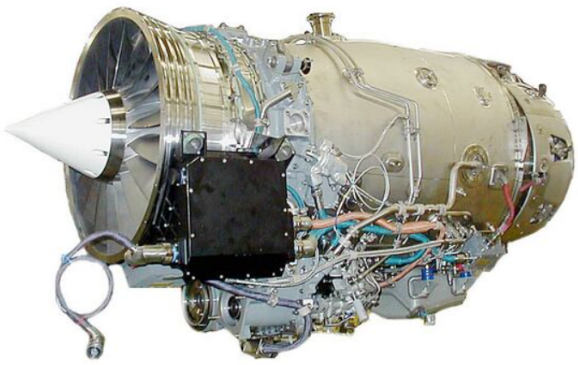

Figure 4: *A picture of the F3 engine.*

It was decided that due to the sheer difference of thrust required during subsonic and supersonic speeds, the difference in times spent in these speed regimes and the added drag with increasing engine size and mass, selecting a smaller engine and using an afterburner just for supersonic speeds was a better option than selecting a big engine providing enough thrust for supersonic speeds and throttling back during subsonic speeds. Hence, engines with desired thrust ranges for subsonic speeds were considered, and their afterburner performance was calculated. Also, the altitude and Mach number effects to the static sea level thrust for each engine were consid-

ered in this analysis. After conducting the analysis, IHI Corporation's F3 engine was selected with an afterburner option for further analysis. The F3 engine with an afterburner option exits conceptually and is called the XF3-400. The engine will provide a maximum dry thrust of 16.4 kN and a wet thrust of 29.5 kN at static sea level condition. This engine has a mass of 340 kg which is less than the first estimation. Finally, the engine will have a length of 2.7 m including the added afterburner. The engine can be seen in figure 4 [1].

After the engine is selected, the intake and exhaust are designed considering the conditions during the supersonic dash manoeuvre, as this condition is determined to be the driving case for the design. The goal of the intake is to decelerate the incoming flow while keeping the total pressure constant. The intake is designed such that the oblique shock waves are external and do not proceed inside. However, after further investigation, it was determined that an external compression cowl would have observability issues due to lower cowl length. As the cowl length decreases, the engine becomes visible from the outside. Hence, the cowl length was increased such that this view was prevented. The cowl and the bump inside the intake created the necessary shock waves to decelerate the flow to subsonic speeds. This part of the intake is called the supersonic diffuser. After that, the flow encounters the subsonic diffuser, which further decelerates the subsonic flow.

Subsonic diffuser achieves this by increasing the cross-sectional area. The flow then reaches the engine fan. The F3 engine is modelled using thermodynamic cycle analysis using several assumptions. These assumptions are broad because the supersonic performance of the engine is different from the subsonic performance. From the custom propulsion system model, it was possible to get the thrust ratios for desired Mach numbers and altitudes. On top of this, at supersonic speeds the use of the afterburner required the exhaust nozzle to be variable geometry due to high velocities of the flow after the afterburner. The exhaust nozzle throat and exit areas are calculated using the model for considering the optimal expansion case. Furthermore, a generic gas turbine engine consisting of valves, pressure pumps and heat exchanges is modified to complete the RAD's propulsion system which also includes an afterburner fuel system. Finally, the power system components; alternator, rectifier and battery are sized with respect to the power requirements.

Empennage and Control Surfaces

The RAD will use a canted fin configuration as empennage, this combines both the horizontal and vertical stabiliser in one design. These canted fins provide stability. Control is achieved using two ruddervators on the canted fins. This configuration has been chosen to reduce weight compared to full moving fins; however, if more control is desired it is recommended to change the design to fully moving fins. The fins are angled at approximately 30°, since the horizontal stability was the most demanding. The canted fins have the same sweep angles on the leading and trailing edges as the wing for low observability reasons.

Furthermore, the RAD makes use of leading-edge flaps and trailing edge plain flaps to achieve a higher lift at take-off and landing. Ailerons on the outer parts of the wing are there separately from the HLDs whose layout can be seen on the right wing in figure 2a.

Centre of Gravity

The centre of gravity was calculated, this resulted in a c.g. of 3.67 m (max FWD) and 4.00 m (max AFT). The centre of gravity distribution can be seen in figure 5.

[1] Source: https://customer-janes-com.tudelft.idm.oclc.org/Janes/Display/JAE_0107-JAE_ (retrieved on 15 June 2022)

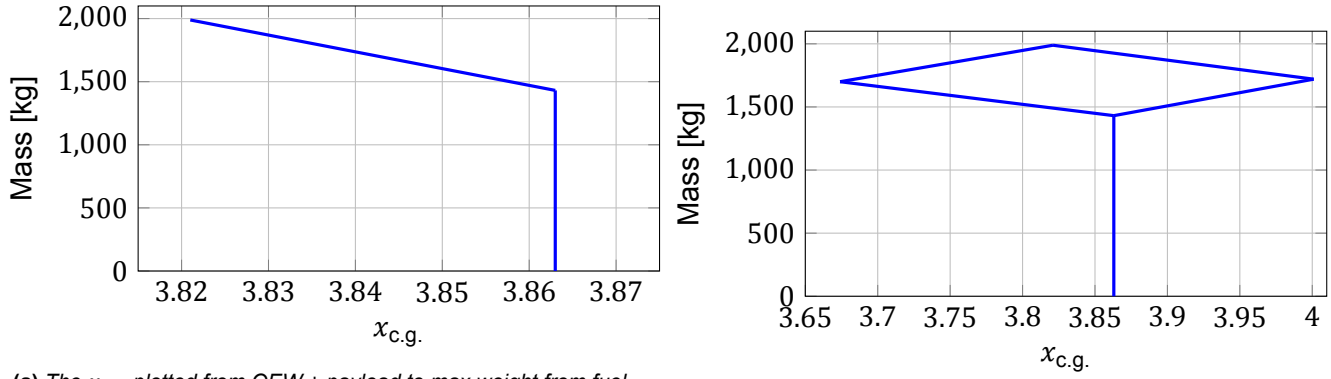

(a) *The $x_{c.g.}$ plotted from OEW + payload to max weight from fuel, this assumes the fuel is removed from the two fuel tanks with the same percentage during flight.*

(b) *The extremes of the $x_{c.g.}$ plotted for the max AFT and max FWD case that is possible.*

Figure 5: *The $x_{c.g.}$ plotted during the flight and the extreme values possible when the fuel is not distributed correctly over the two fuel tanks. The straight line is the OEW.*

Landing Gear

Various configurations are possible for the landing gear. A trade-off was done between the tricycle, bicycle and tail wheel types. The bicycle type was quickly discarded because of the negative effects of the needed outrigger gears. Eventually, a tricycle landing gear configuration based on storage requirements and controllability after touchdown. Due to the low weight of the RAD, a conventional wheel layout is used. No arresting hook needs to be present on the RAD as this was a given requirement.

To size the tires, the maximum static load for each wheel was determined. The nose tire has a diameter of 280 mm and a width of 100 mm. The main wheels have a diameter of 340 mm and are 120 mm wide. With these tires, the aircraft will be able to operate from airports with paved runways and taxiways. Based on a turnover requirement of 63 degrees, a scrape angle of 15 degrees, and a nose loading between 8% and 15% the layout was constructed.

The nose gear folds forward when stored. The main landing gear folds forwards as well. However, it is turned slightly to store the wheels into the fuselage. Figure 6 gives a visual representation of the landing gear locations.

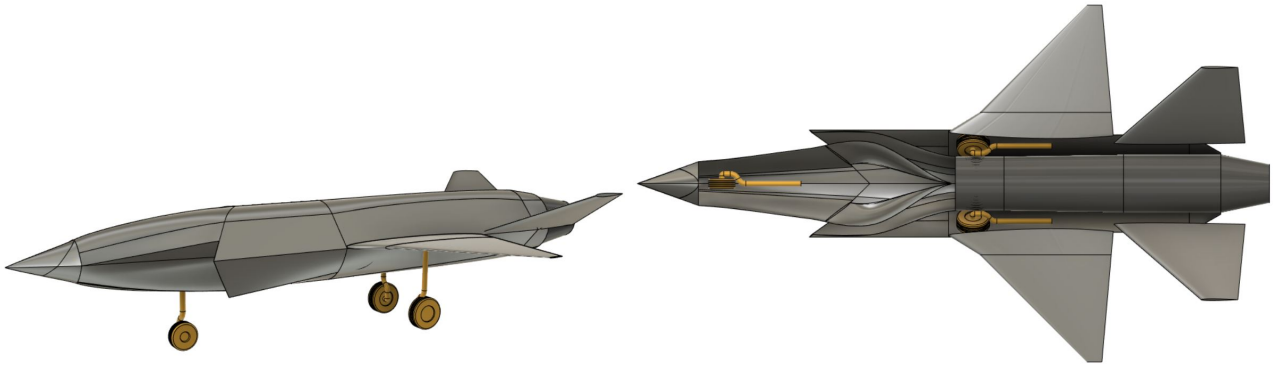

(a) *Extended*

(b) *Stored*

Figure 6: *Landing gear location.*

Structures

The ultimate purpose of aircraft structures is to transfer loads throughout the aircraft. These loads originate from a multitude of sources. The most obvious loads are the lift, drag, and thrust forces. The lift force mainly originates from the wing. However, a non-negligible amount of lift is generated in the body, and depending on the balance of the aircraft, the empennage. The drag acts on the entire wetted area of the aircraft. The thrust is generated

by the engine and is introduced to the structure in the fuselage. Another load case that should not be overlooked is the landing. During landing, most of the vertical speed is absorbed by the landing gear in a very short period.

In order for the aircraft to withstand these different loads, the structure should be designed to transfer each of them. Due to time constraints, only the wingbox could be designed. For this design, the internal shear forces, moments and shear flows were considered. A configuration was made that satisfies the Tresca failure criterion, which predicts failure for combined normal and shear stresses. The layout of this configuration can be seen in figure 7. This configuration is only the initial sizing. Further iterations on this design must be made to optimise the wingbox design and reduce the weight.

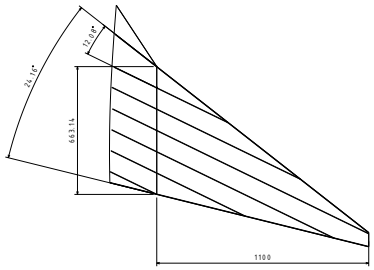

Figure 7: *Internal layout of the wingbox.*

The two wingboxes connect with structural elements that go around the engine. These structural elements also provide a hard point for the landing gear to attach to. From these structural elements, structural elements transfer the load throughout the rest of the aircraft. The empennage structure is built very similarly to the wingbox structure. The loads of the empennage are introduced to the fuselage as well and transferred to the rest of the aircraft through structural elements in the fuselage.

Final Design

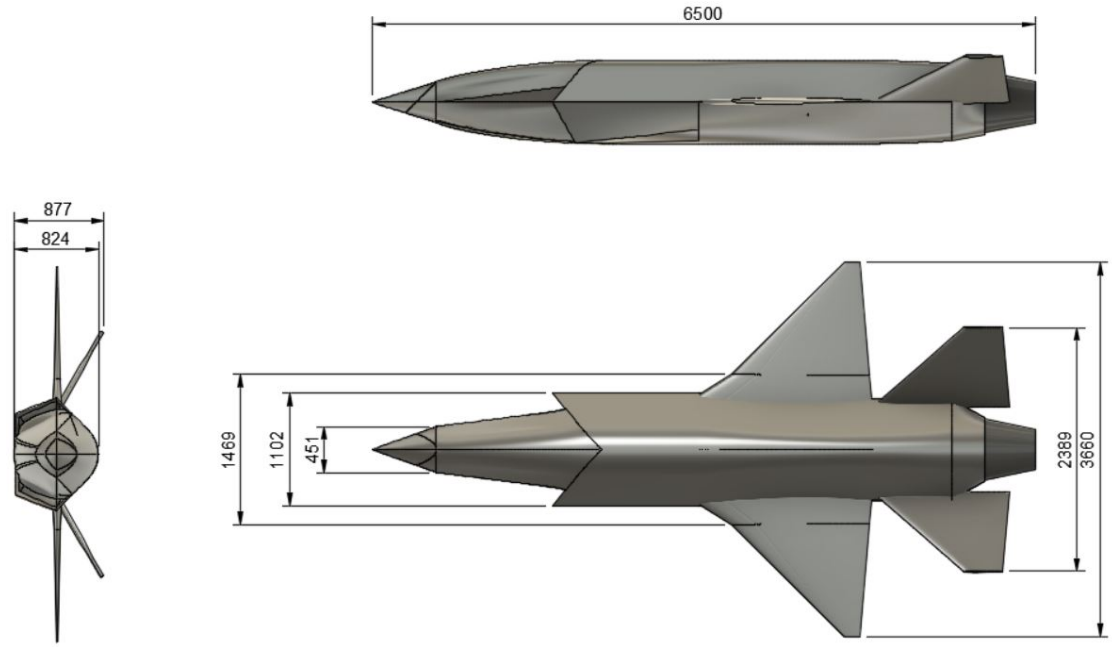

Figure 8: *Dimensions of the RAD body*

Low Observability

The low observability requirements create a driving force behind the design of the UAV as in every aspect of the design, low observability must be considered to reduce the radar cross-section to a sufficiently low value such that the RAD can emulate the stealth capabilities of other aircraft by augmenting the radar cross-section and/or infrared signature.

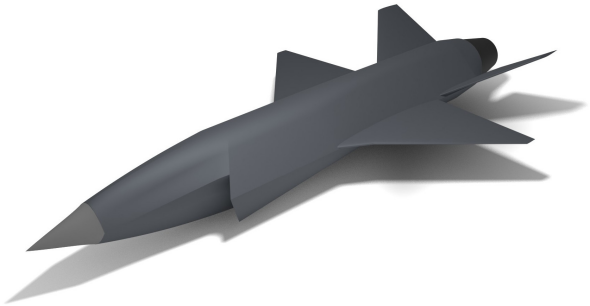

Figure 9: *The RAD from an isometric perspective*

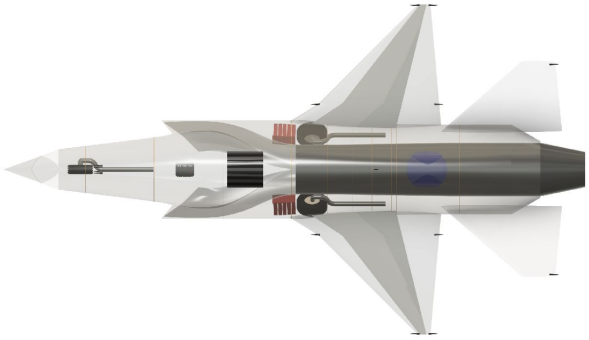

Figure 10: *The RAD with a transparent body*

When taking a look at the design as seen in figure 9 it looks rather special and the trade-offs between aerodynamics and low observability can be clearly seen due to the sharp edges and non-conventional fuselage design. This helps the low observability by reducing the number of directions that radar energy is redirected to. The edges are also grouped together as much as possible to reduce the amount of angles radar energy would be deflected towards. The nose and fuselage are a trade-off between low observability and aerodynamics, it takes advantage of non-constant radii curvature to spread out the radar energy more whilst still being smooth for aerodynamics.

The intake is quite special as it tries to be low observable, aerodynamic, well performing and use the least amount of space as possible. For these reasons the intake incorporates a concave V-shape design as this allows the intake duct to slightly bend outwards before going back to the engine face, hiding the engine from view and further lowering the radar cross-section as seen in figure 10. Lastly, the body and intake duct will be coated with a radar absorbent material to absorb as much radar energy as possible to further reduce the radar cross-section. With the RAM applied, the radar cross section is below the required value of 0.01 m^2 therefore reaching our requirements.

The infrared observability is also of importance, especially for future uses, but was more difficult to reduce. A V-Tail tail was employed for this reason and covers the engine from certain angles.

Performance

After a detailed design of different elements of the RAD it can be found that the RAD meets most of the performance requirements. Looking at 11 it can be seen that for the newly obtained T/W_{TO} and W/S the requirements cruise, manoeuvre, take-off, land and dash are still satisfied.

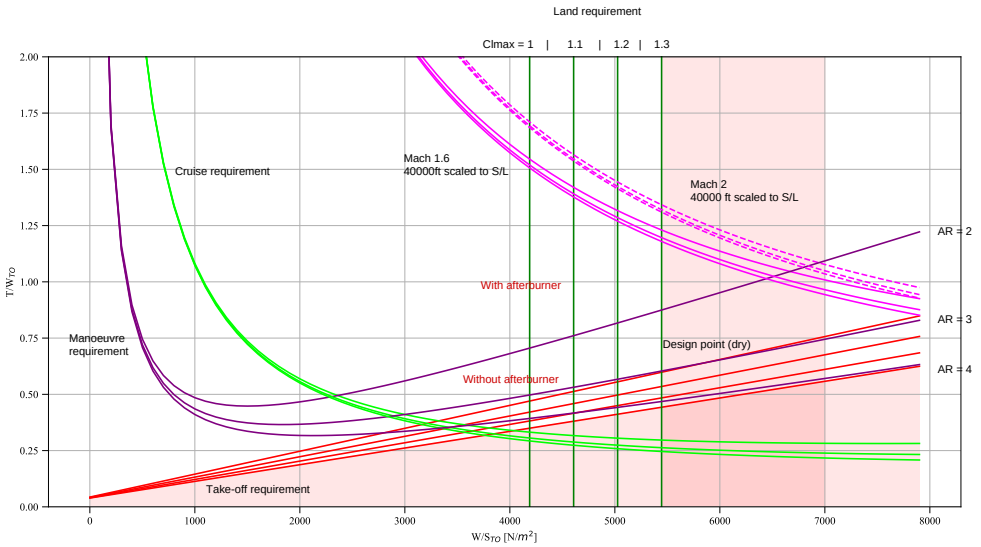

Figure 11: *The design space with the chosen design point in the conceptual design and the resulting preliminary design points.*

Looking into more detail of the mission profile it can be found that a ground distance of 1,623 ft is required, excluding the ground run distance for the airborne part of the take-off(but it will never exceed 4,000 feet). Furthermore for the climb to altitude a average Rate of Climb (ROC) of 125.6 m/s is found. For the dash manoeuvres figure 12 shows the available thrust and the drag for different Mach numbers. It can be seen that with a wet configuration (with afterburner) Mach 2 can be reached theoretically (practically it would take too much time to accelerate to it). Furthermore, figure 13 depicts the available thrust and drag for the cruise Mach number versus the altitude. It can be seen that at all altitudes the thrust is enough to overcome the drag.

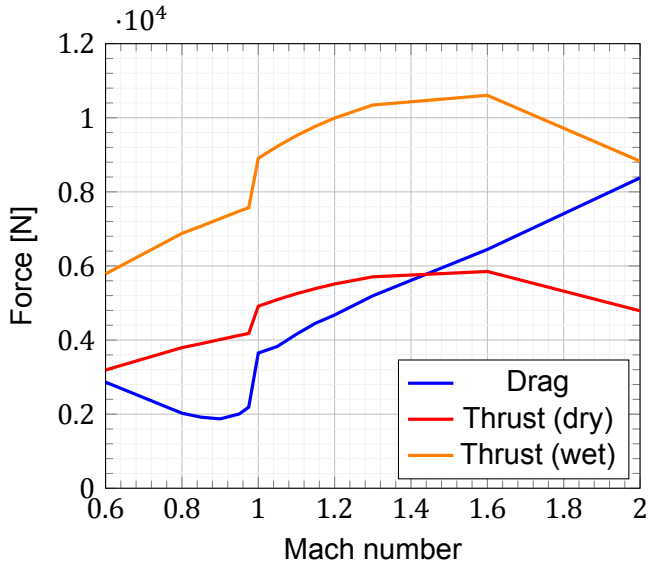

Figure 12: *Thrust and Drag versus Mach number at 40,000 ft.*

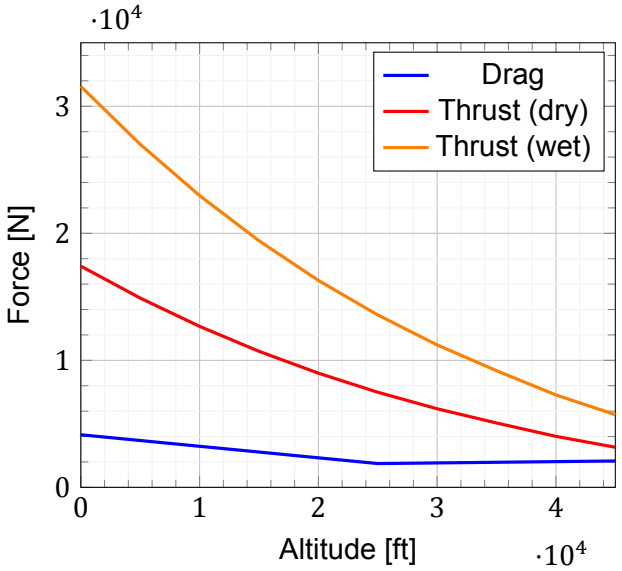

Figure 13: *Thrust and Drag versus altitude at Mach 0.9.*

For the landing a distance of 1,734 m was found, thereby adhering to the requirement of a landing distance smaller than 1,829 m. Lastly for the reference mission profile a required fuel mass of 518 kg was found and if the RAD would use all its fuel for loiter, it would have an endurance of 3.21 hours.

Operations and Logistics

Primary System

The operations of the RAD can be divided into two systems. First, the primary system. The primary system consists of the elements that are directly involved in flying the aircraft. Therefore, the primary system contains the RAD, the Ground Control Station (GCS) and the communications system linking the two throughout the flight. No new GCS model needs to be designed, as the RAD is compatible with GCS systems currently in use for military UAVs. This is because the RAD uses the same communication link types as currently operational UAVs.

Support System

The second system is the support system. This contains all the support and logistics that happens in the background. The support system can then be divided into eight sections: Refurbishments, Maintenance, Transport, Facilities, Training, Technical Publications, Spares and Tools. These elements all need to be planned for to keep the aircraft flying in both the short and long term.

Reliability, Availability, Maintainability and Safety Characteristics

Reliability is an important aspect in assessing the efficiency of operations. The most impactful components on the reliability of the RAD are the engine and the mission systems. This also affects its availability, as downtime due to an unreliable component reduces the RADs ability to operate efficiently. Availability is also reduced by the minimum interval between flights, which is needed to perform critical checks and to refuel the aircraft. The maintainability of the aircraft is excellent. Due to its relatively small size, components are easily accessible. Furthermore, due to the nature of their operation, many mission systems are placed near the system. As these are defined as unreliable components, this placement allows maintenance time and downtime to be minimised.

Lastly, the safety of operating the RAD is considered in the design with several factors. All safety-critical func-

tions are designed with a fail-safe or redundant architecture. Moreover, even if this fails, the RAD can carry a parachute system which allows it to slow down and land.

Future Development

The project design and development logic consider the planning after the design phase is finished. The post development logic consists of five stages. These include stage 1 which entails the verification and validation of the prototype design. Followed up by stage 2 that requires the design to be certified. Stage 3 considers the production process. Stage 4 is when the product is in use and performing its red air mission. Finally, stage 5 details the end-of-life strategy. Optionally, during the final stage the drone can be used for actual target practice resulting in a ceremonial end-of-life.

Return on Investment

There is a big gap in the market for the RAD to operate in. No current alternative can mimic the signature and performance of enemy aircraft at the same time. That is where the RAD comes in.

First, development costs were estimated using a design software program. This was determined to be 223 Million USD, which is below the target of a request made by the US Air Force[2], while the RAD outperforms the requirements set in this request.
Production costs were then estimated using an empirical method to estimate airframe production cost, using an assumed production volume of 200 units. Following that, engine costs were predicted using an empirical method for military jet engines.

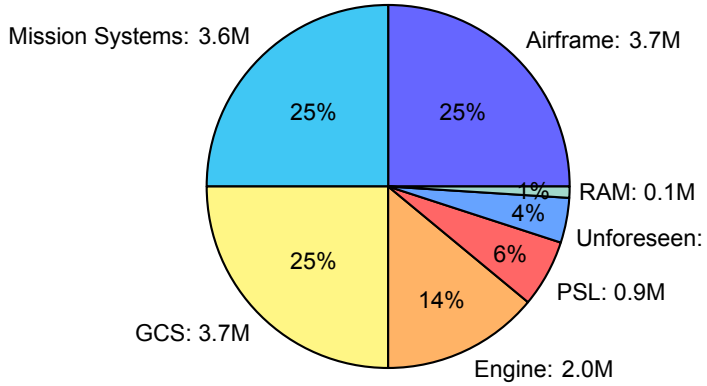

Figure 14: *Composition of full system costs.*

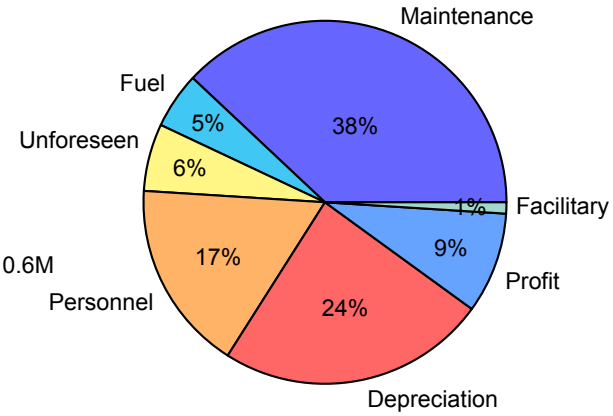

Figure 15: *Composition of commercial charge type CPFH.*

Then, the costs of acquiring a Ground Control Station and Primary Satellite Link were found. Using a target cost price, the budget left for mission systems could be determined. Due to their classified nature, no price estimate could be made for these. Lastly, unforeseen costs and the costs for Radar Absorbent Material were included. This resulted in a total system cost distribution as seen in figure 14. Assuming a profit margin of 5%, an acquisition cost of 15.3 million USD is reached.

Furthermore, the RAD offers lower operational costs than any current alternative. The operational cost is built up of various factors. Foremost, maintenance costs dominate the operational cost. When considering all levels of maintenance, maintenance costs 3000 USD per flight hour. Following that, the fuel price is considered. However, this is not significant in the total picture. Then, unforeseen costs are included to cover unpredictable or varying costs like transport costs. Following that, personnel costs are included, which includes costs for all personnel needed for an hour of operation. The next factor is depreciation, which aims to recover the acquisition cost of the system within 8000 flight hours. Then, a faciliatory charge and profit margin bring the total operational cost to 7,897 USD per hour.

[2]Source: https://imlive.s3.amazonaws.com/Federal%20Government/ID629538839000663258696052186073181753l5/Next_Gen_Aerial_Target_RFI.pdf (retrieved on 7 June 2022)

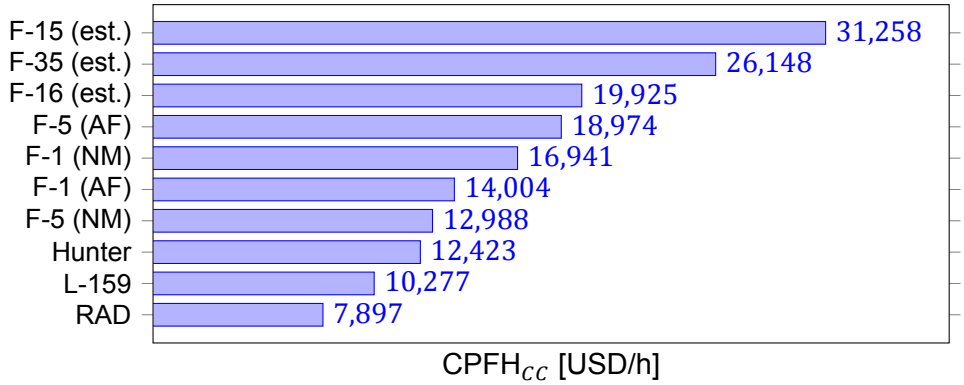

Figure 16: *Comparison with commercial CPFH.*

The breakdown of this number can be found in figure 15. However, this is only the price for a commercial company offering Red Air services. This number lowers significantly for other types of Cost per Flight Hour. In the end, the RAD is cheaper than any alternative in any Cost per Flight Hour type.

Eventually, the RAD offers a significant improvement in costs and charges over any alternative. The cost comparison to commercial alternatives can be found in figure 16. Overall, the RAD is expected to provide a breakthrough in the market. It offers capabilities matching or exceeding any alternative, all while being cheaper to operate.

1 Introduction

The red flag exercises were introduced in 1975 after the disappointing performance of USAF fighter pilots in air-to-air combat during the Vietnam War. After their introduction, the exchange ratios have improved significantly, increasing the survival rate of the pilots [1]. Since then, the Red Flag exercises have been extended to all NATO countries. The main purpose of the red air aircraft is to take on the role of an aggressor for the purpose of providing realistic training aid for blue air - the friendly aircraft. To achieve this, the red air preferably must be able to mimic the performance and detectable emissions of adversaries. Up until now, the red air aircraft have been friendly fighter jets or advanced jet trainers. However, by developing a UAV specifically for the purpose of training, there is space to improve the shortcomings of the aircraft now in use for this role. The aircraft currently used during red air include the F-16, and since recently also the F-35. These aforementioned aircraft are high-priced, require complex training of their pilots, and do not correctly mimic the performance and emission of the genuine adversary aircraft. The shortage of capable red air pilots is so evident that the USAF is outsourcing the key part of the training to commercial companies; however, these contracts are described as ”overpriced and underwhelming”[1].

The red air drone aims to solve these problems. It is more economical, more sustainable, can match the performance of the real adversaries and can augment its detectable emissions. UAV pilots also do not require survival training and extensive medical checks as fighter pilots do. Furthermore, with increased levels of automation, one drone pilot will be capable of operating more than one drone, alleviating the pressure on staff needed for a red air aircraft. The purpose of this report is to assess the feasibility, design challenges and competitiveness of such a system and that it meets the requirements that ensure the UAV will improve the training exercise quality, while being more economical and sustainable. The red air drone shall be able to fly under IFR and VFR, have a maximum speed higher than Mach 1.6, cruise at Mach 0.9, have a service ceiling of higher than 45,000 ft, and a frontal radar cross-section of less than 0.01 m^2. Furthermore, the UAV shall have systems that emulate the radar and infra-red emissions of other fighter aircraft.

The report is structured as follows. The concept selection process is outlined in chapter 2. Next, the sustainable design methodology is described in chapter 3. Afterwards, the overall design, consisting of the external design, the internal layout, and the mission systems of the drone are introduced in chapter 4. After the design has been introduced, the chapter 5 dives into aerodynamic performance of the red air drone. Next, the propulsion subsystem is discussed in chapter 6. Afterwards, the controllability and stability of the aircraft is addressed in chapter 7, where empennage, control surfaces, and the landing gear are designed. The next chapter, chapter 8 offers a discussion on materials to be used, and on the structures of the RAD. Chapter 9 discusses detectable emissions of the red air drone, offers final sizing, and discusses system interfaces and communications. The drone performance is discussed in chapter 10. Chapter 11 outlines operations and logistic concept of the red air drone. In chapter 12 the developmental risks are analysed and the manufacturing, assembly and integration plan, including the future project development, are elaborated on. The economics of the design are presented in chapter 13. Whether all the requirements are met is discussed with help of a compliance matrix in chapter 14. Finally, conclusions and recommendations are given in chapter 15.

[1]Source: https://www.businessinsider.nl/air-force-pilots-shortage-leading-to-red-team-adversary-outsourcing-2017-8?international=true&r=US (retrieved on 14 June 2022)

2
Concept Selection Process

This chapter outlines functions that the red air drone has to fulfil in section 2.1. This is done using functional flow diagram and functional breakdown structure. An overview of all tasks needed to design a drone can be found in the Gantt chart in figure 2.6. Next, in the project description section 2.2, the mission and project objective statements are given. These represent the backbone of the red air drone project. Afterwards, the stakeholder requirements are outlined in section 2.3. These requirements were translated into four different concepts that entered the trade-off in the Midterm report [2]. The overview of the selection process is summarized in section 2.4. Lastly, the result of the trade-off is presented in section 2.4.1. The selected concept is then developed further throughout the report and is converted into the final red air drone design.

2.1. Concept Function

The functional flow diagram (FFD), figure 2.4 and functional breakdown structure (FBS), figure 2.5 are used to show the coherent order of functions the red air system must perform. In this report, the functional flow goes three levels deep, whereas the functional breakdown goes one level deeper.

Figure 2.1 presents top level functions, on which, both functional flow and functional breakdown diagrams expand.

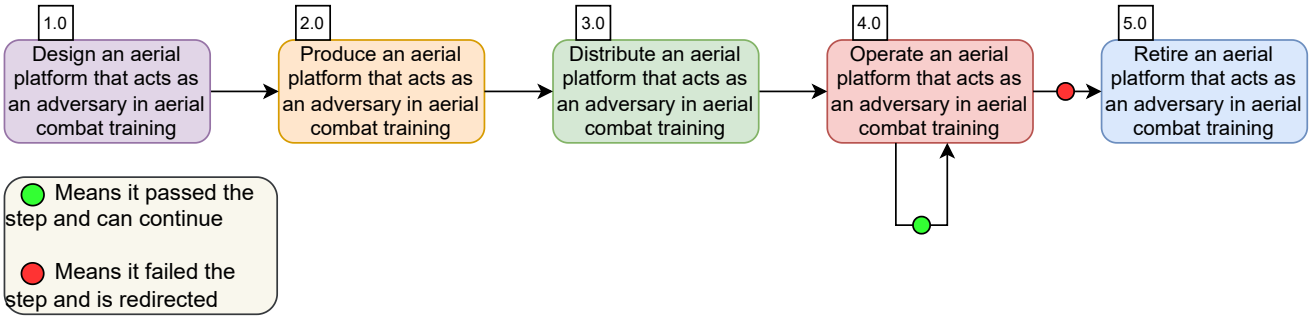

Figure 2.1: *Top level function of the functional flow and functional breakdown diagrams.*

Firstly, the aerial system has to be designed, then produced, distributed, operated and once it reaches end-of-the-life phase it has to be retired.

2.2. Project Description

The mission statement and project objective statement outline the goals of the red air drone and of this project. The further project developments are built with these statements in mind.

Mission Statement

Provide an aerial system that acts as an adversary in aerial combat training.

Project Objective Statement

Win the OS symposium by designing a UAV that can be used as an effective and realistic adversarial training aid, emulating missile, and fast jet threats, including radar signatures, electronic and infrared countermeasures, which is more cost-effective and sustainable than current alternatives.

2.3. Stakeholder Requirements

The red air drone must improve the training quality of the Red Flag exercises, while being more economical, and sustainable. To achieve all these ambitions, a set of stakeholder requirements was formulated.

Table 2.1: *List of stakeholder requirements for the red air Drone.*

Identifier	Type	Requirement
RAD-TE-PER-01-01	Driving	The maximum speed of the RAD shall be at least Mach 1.60 above 30,000 feet.
RAD-TE-PER-01-02	Driving	The RAD shall have a typical cruise speed of Mach 0.90 from S/L to ceiling.
RAD-TE-PER-01-03	Driving	The RAD shall have a minimum endurance of 1.5 hours between T/O and LDG.
RAD-TE-PER-01-04		The RAD shall have a minimum flight ceiling of 45,000 feet.
RAD-TE-PER-01-05	Driving	The RAD shall be able to perform a dash move increasing its Mach number by at least 0.7 while staying in the nominal flight envelope.
AD-TE-PER-02-01		The RAD shall have a payload capacity of at least 78 kilograms.
RAD-TE-PER-02-02		The RAD shall be operational for temperatures between ISA -30°C to ISA +30°C.
RAD-TE-PER-02-03		The RAD shall be able to take off from a paved runway with maximum length of 6,000 feet at altitudes from S/L to 4,000 feet MSL.
RAD-TE-PER-03-01	Driving	The RAD shall be able to sustain loads higher than 4g for an altitude of 25,000 feet & at Mach number of 0.90.
RAD-TE-PER-04-01-A	Driving	The RAD structure shall withstand load factors lower than -1.
RAD-TE-PER-04-01-B		The RAD structure shall withstand load factors higher than 6.
RAD-TE-LO-01-01		The geometry of the RAD shall be designed such that it has an RCS less than 0.1 m^2.
RAD-TE-LO-01-03		The RAD shall carry RCS enhancing systems onboard.
RAD-TE-LO-02	Driving	The RAD shall have IR detection confusion features and IR signature enhancing systems.
RAD-TE-LO-02-01		The RAD shall carry chaff/flare dispensers onboard.
RAD-TE-LO-02-02		The RAD shall carry IR emitters onboard.
RAD-TE-SYS-01	Driving	The RAD shall have an internal volume of at least 14 litres available for the payload and onboard systems.
RAD-TE-SYS-02-01		The RAD shall provide a minimum continuous electrical power of 5 kW.
RAD-TE-SYS-02-02		The RAD shall be able to provide a minimum peak electrical power of 10 kW.

2.4. Trade-off and Selection Process

The trade-off is part of the midterm report [2] and the most important parts of it are outlined in this section. The winner of the trade-off is further developed throughout this report. The four concepts entering the trade-off are visualized in figure 2.2.

Lamina

The first concept is named Lamina, it is shown in figure 2.2a. It has a cigar shaped fuselage with a swept back wing and taper configuration, horizontal stabilisers, and a canted tail. The D-shaped dorsal air inlet is positioned on top of the fuselage at the front with the air ducts going through the body towards a single engine housed inside the body, and the exhaust at the back. The configuration of Lamina is conventional in the sense that it has an empennage with both a horizontal stabiliser and vertical stabiliser (canted fins).

Genesis

The second configuration, Genesis, can be seen in figure 2.2b. Genesis has a long, slender body with a delta wing planform. The Y-duct intakes are mounted on the sides extending into the body where the engine is housed, with the exhaust in the back. Instead of a conventional empennage, Genesis uses two canted fins together with the ruddervator for control and stability. The fuselage allows for sufficient volume for systems and fuel.

Sabrinus

The third configuration, Sabrinus, can be seen in figure 2.2c. This configuration is a flying wing body with a Pelikan tail and no horizontal stabilizers. A dorsal intake is used extending into the body where the engine is

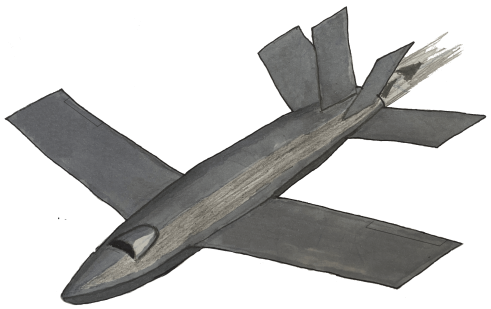

(a) *Configuration 1: Lamina.*

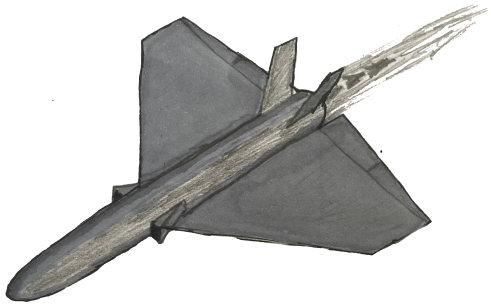

(b) *Configuration 2: Genesis.*

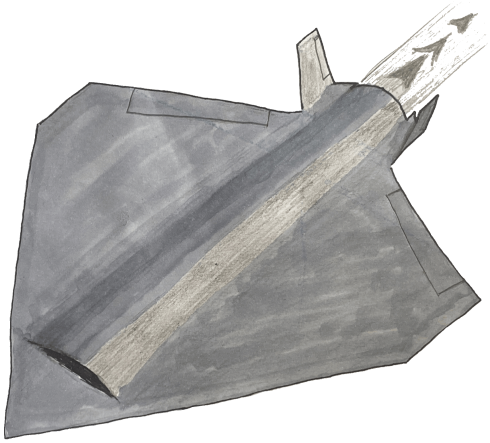

(c) *Configuration 3: Sabrinus.*

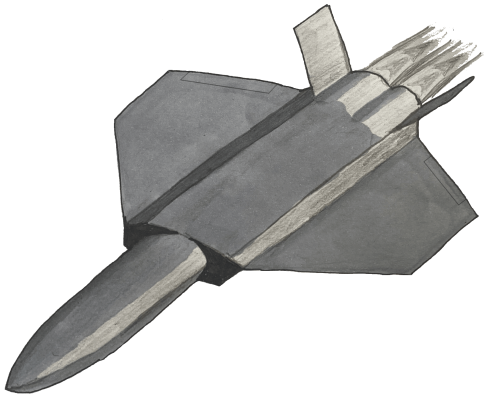

(d) *Configuration 4: Veloci.*

Figure 2.2: *Configurations entering the final system trade-off.*

located and the exhaust on the back. The body has consistent angles and is low profile. The use of a Pelikan tail is unique about this configuration. Additionally, next to the Pelikan tail, ruddervators are used for control and stability. The unique thing about Sabrinus is that the body shape is superb for low observability.

Veloci

The fourth configuration, shown in figure 2.2d is called Veloci, it incorporates a long thin conical fuselage with a trapezoidal wing on the back: centre mounted wing with large tip chord relative to its root chord. Furthermore, it has moving canted fins which will be used for the pitch and yaw control. Lastly, Veloci has two air intakes on its sides reaching into the aircraft where the two engines are housed.

2.4.1. Trade-off Results

For system trade-off, four main categories were identified: planform design, control surfaces & empennage design, acceptability, and Development & manufacturability. Each of these categories have sub-criteria, for example the planform design category incorporates L/D at transonic and supersonic speeds, structural performance and volume, and the complexity of high lift devices. The final score for each category can be seen in table 2.2, where the 'Genesis' concept won and therefore, it is developed further in this report.

Table 2.2: *Final trade-off table including all categories.*

Final concept trade-off					
Aspect / Concept	Planform design	Empennage	Acceptability	Develop. & Manuf.	**Final score**
Lamina	2.2	4.0	3.2	4.0	3.1
Genesis	3.6	3.3	3.4	3.3	3.5
Sabrinus	4.1	3.2	2.5	1.8	3.3
Veloci	3.1	4.0	3.5	3.2	3.4

Genesis was a very good choice in terms of aerodynamic performance, both in terms of (sub)transonic and supersonic and structural performance, where it scored second-highest. This is mainly due to use of delta wing, which offers good transonic performance, as a result of high leading-edge sweep. Delta wing design is also proved concept for supersonic flight. When it comes to empennage, the V-tail originally proposed for the concept was changed to Pelikan tail proposed in Sabrinus concept, as it offers better IR low observability, thanks to partially shielding the engine nozzle, with very little drawbacks when compared to the V-tail. Another change in the configuration is the fuselage shape, which was taken from the Veloci concept, as it again offers better low observability performance and easier incorporation of the Y-duct to the body.

The sensitivity study was performed to confirm that the trade-off results are valid even when trade-off criteria weights are varied. All the sub-criteria used in the trade-off were varied by 50%. Some combination of variation produced a different winner, which is expected with this big variation, however the worst-case scenario for Genesis was a second place, confirming that it indeed is a desirable choice. Therefore, this concept has the best chance to fulfil all the requirements after the detailed design phase.

2.5. Project diagrams

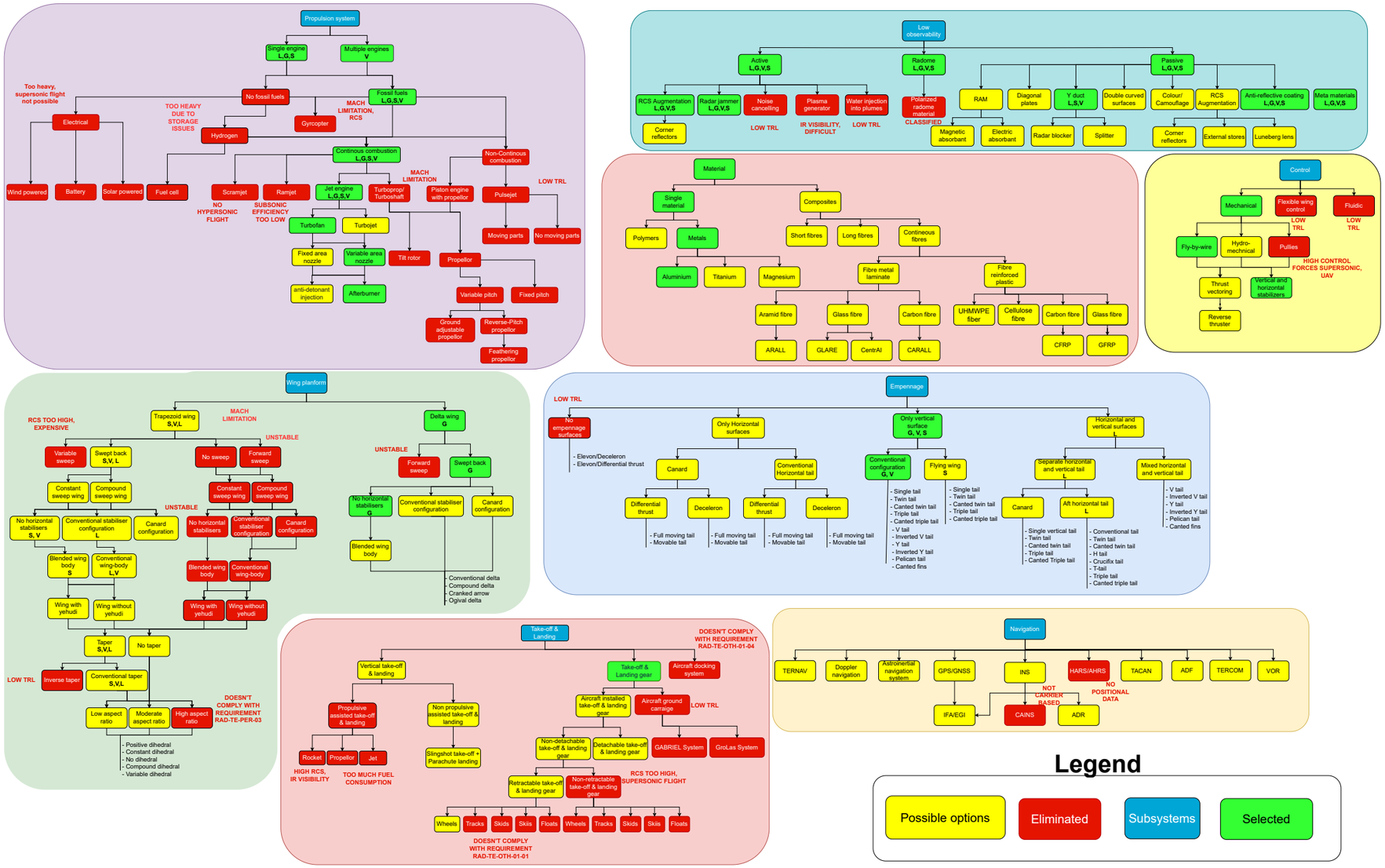

Figure 2.3: *Design option tree of the RAD.*

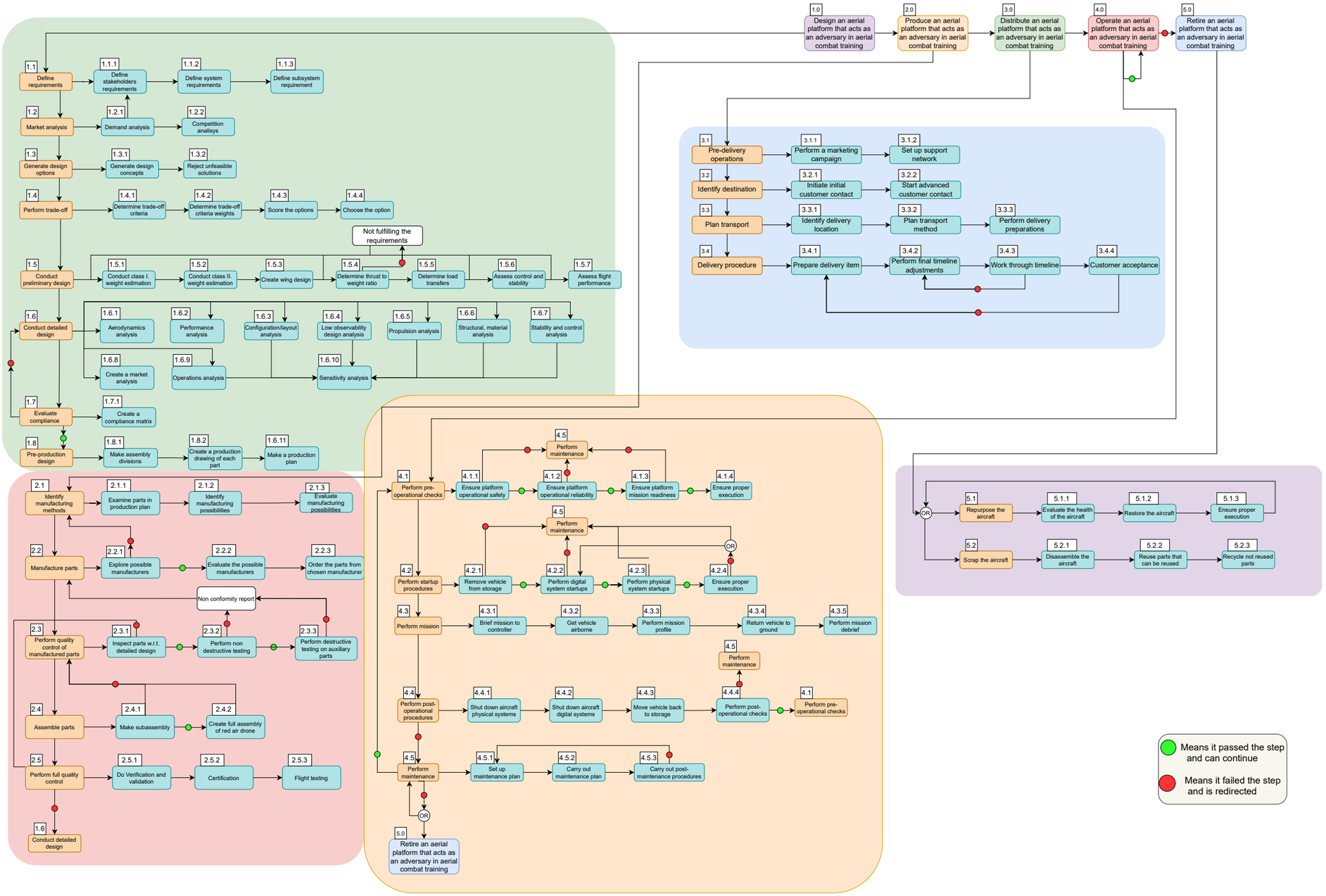

Figure 2.4: *Functional flow diagram for the RAD.*

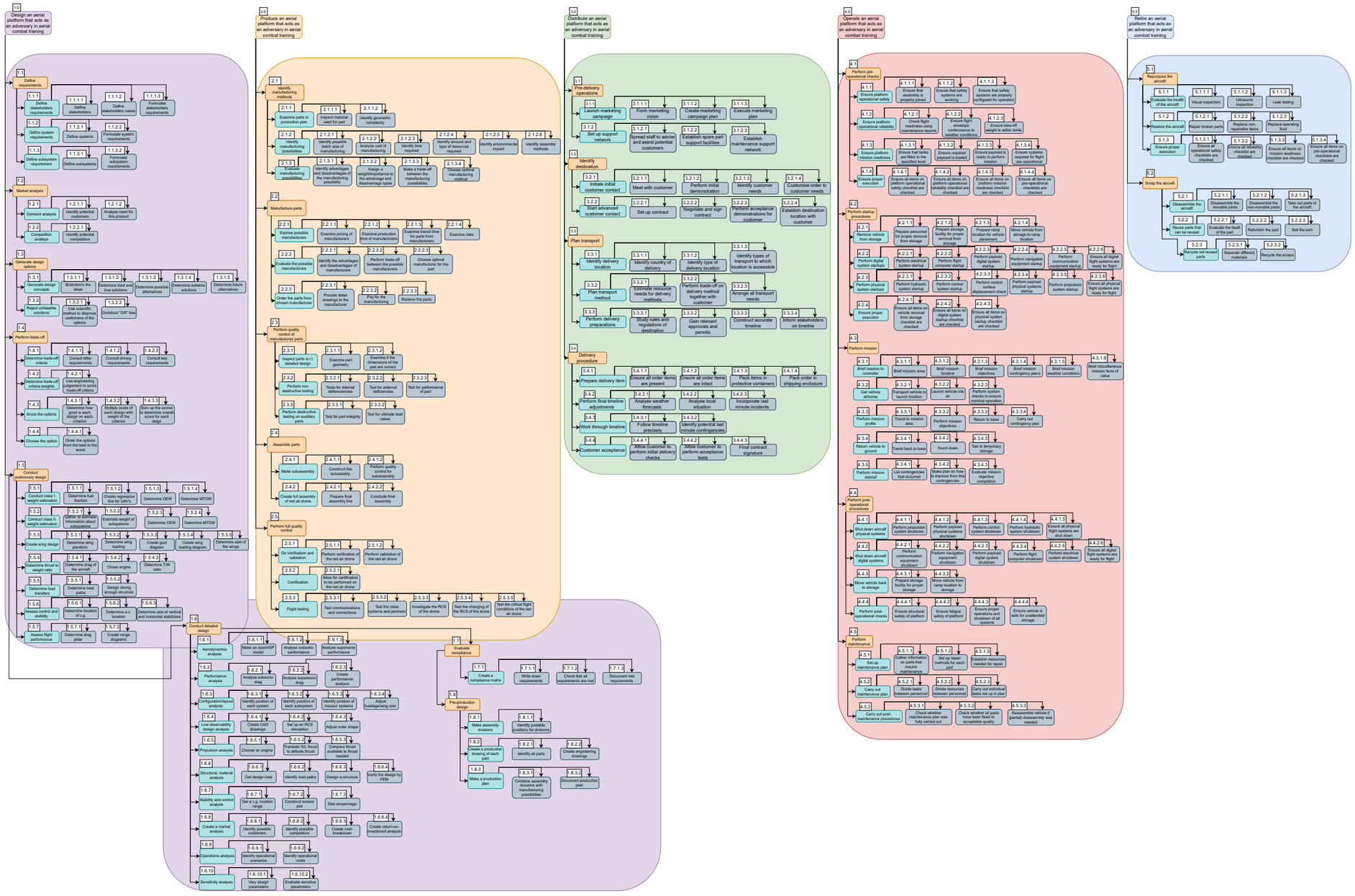

Figure 2.5: *Functional breakdown structure for the RAD.*

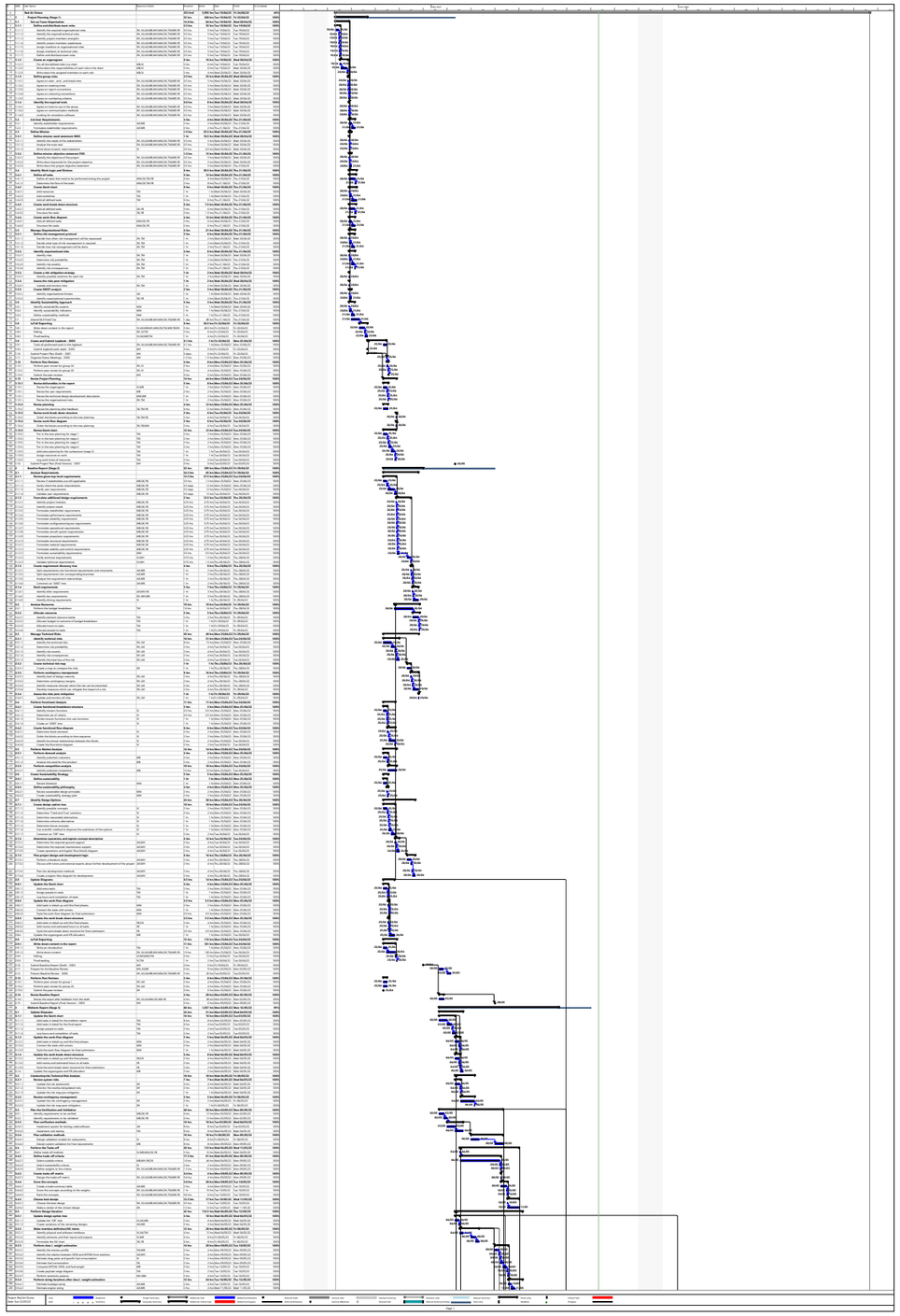

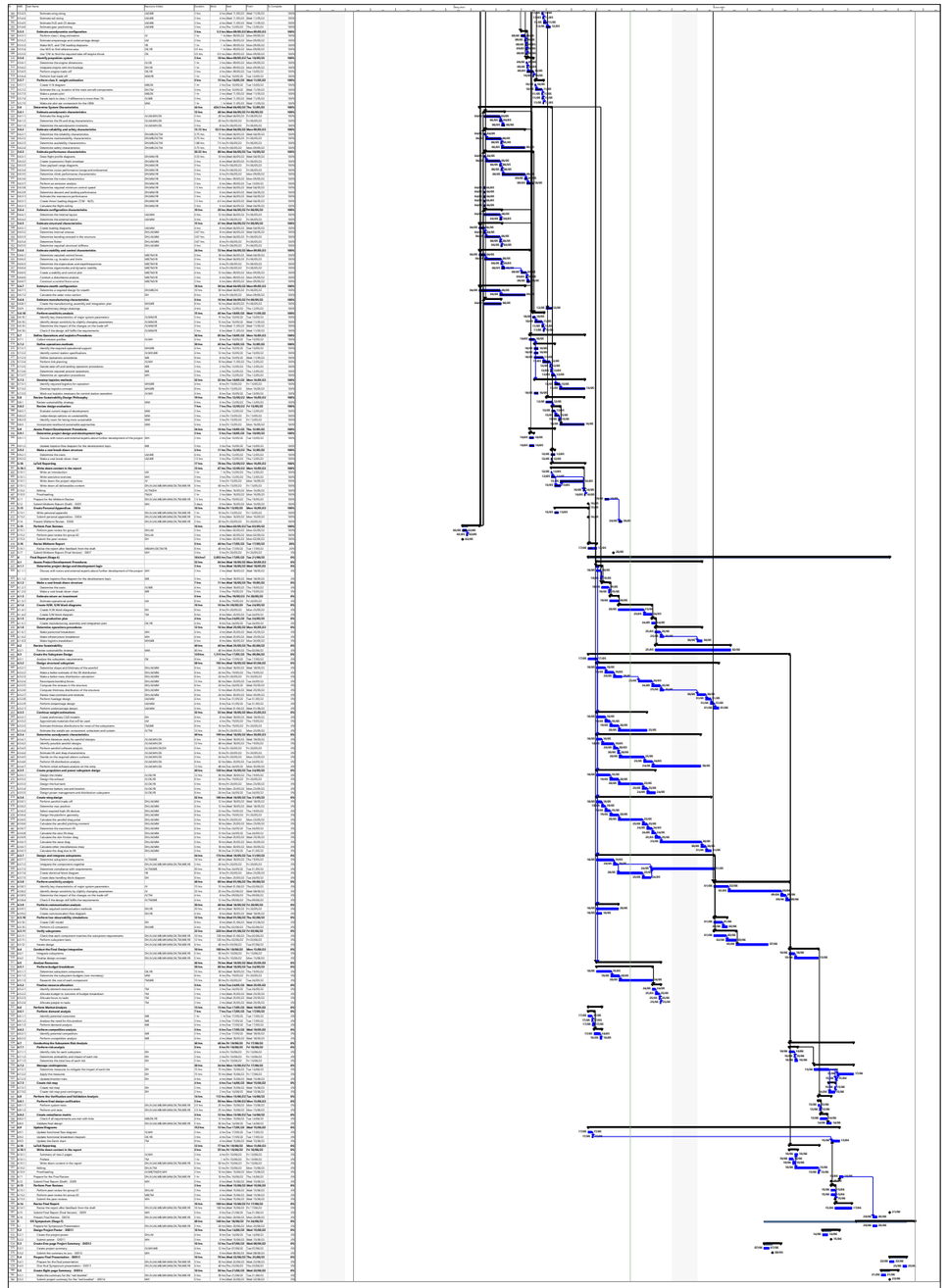

Figure 2.6: *The project Gantt chart displaying all the performed tasks during the project.*

3
Sustainable Design Methodology

The sustainability aspect is central to the RAD, as it represents a market opportunity for a platform capable of fulfilling the role of a red air aircraft while being more sustainable than current alternatives. The sustainability of the project is broken up into several aspects. Section 3.1 outlines the environmental and social sustainability aspects of the RAD, compared to the current alternatives. How environmental and economical sustainability is considered throughout the design is summarised in section 3.2. Section 3.3 describes he future outlook of the of the RAD with respect to social, economic and environmental sustainability. Finally, section 3.4 discusses the ethical considerations of this project and the RAD. This chapter is based on the sustainability chapters in the Baseline [3, pp. 44–45] and Midterm [2, pp. 46–48] reports.

Table 3.1: *The sustainability requirements of the RAD.*

ID	Description
RAD-CO-SUS-01	The RAD shall comply with the environmental sustainability requirements.
RAD-CO-SUS-01-01	The noise emissions of the RAD shall be lower than 109dB felt at 1000 ft.
RAD-CO-SUS-01-02	The RAD shall use less fuel than the F-16.
RAD-CO-SUS-01-03	The RAD shall be at least 80% recyclable.
RAD-CO-SUS-02	The RAD and its associated ground systems shall be maintained with sustainability philosophy.
RAD-CO-SUS-02-01	The periodic maintenance time of RAD shall not exceed the periodic maintenance time of the F-16..
RAD-CO-SUS-02-02	The periodic maintenance of RAD shall be performed with already available tools.
RAD-CO-SUS-02-03	The maintenance of the ground control station shall be completed within ”TBD” hours.

3.1. General Environmental Considerations

Military red air missions are often performed using modern fighters such as the F-16. These aircraft were, however, designed to perform much more demanding operations than the red air mission. Therefore, these platforms are, in a way, overdesigned for red air. Also less capable platforms like the L-159 and Hawk T2 that are used by private contractors such as Draken[1] were not designed for the specific red air mission.

These aircraft were designed to carry payloads that are not needed for the red air mission, resulting in bigger, heavier jets that inherently use more fuel to perform the same mission as the RAD. Furthermore, as the RAD is a UAV, the weight of a pilot and the required systems for an onboard pilot are not required, further reducing the weight comparatively. The bigger engines needed for the aforementioned oversized jets also produce higher noise levels than the smaller engine of the RAD.

Looking at the operational sustainability of the RAD compared to the current platforms, considerable differences are present. The main difference being that multiple RADs can be moved by air transport simultaneously. This is less polluting than having to fly the aircraft to their desired location. Furthermore, the pilot flying the RAD and the Ground Control Station do not have to be transported with the drone. The drone can be operated from a fixed location, reducing emissions. Regarding production and maintenance, the RAD differentiates itself from the current aircraft by having less parts and less material. On top of that, the RAD uses much less fuel to fly its mission profile. It it is assumed that every jet depletes its fuel tank completely when flying a red air mission. The

[1] Source: https://theaviationist.com/2022/04/12/draken-will-provide-red-air-to-raf/ (retrieved on 22 May 2022)

resulting fuel use compared to competitors can then be found in figure 3.1[2] [3] [4] [5] [6] [7] [8] [9].

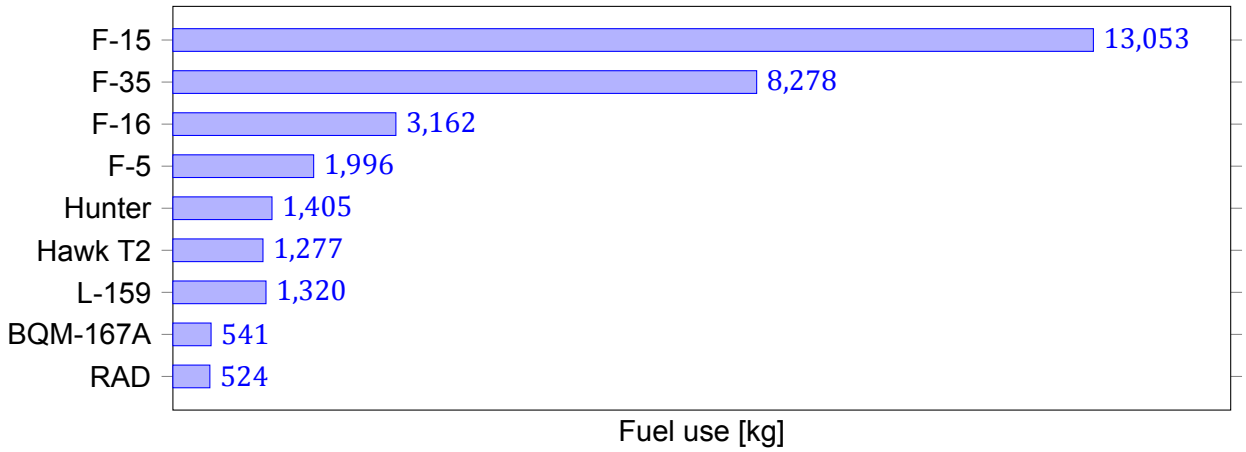

Figure 3.1: *Red air alternatives fuel use.*

Clearly, the RAD is much more fuel efficient than its competitors. Even if its competitors use half of their fuel capacity to complete the mission profile, the RAD is still more efficient. Furthermore, the BQM-167A, Hawker Hunter, Hawk T2 and L-159 cannot exceed Mach 1 (in level flight), so they are unable to fly the prescribed mission profile.

This further confirms that the RAD is inherently more sustainable than any alternative, as it is designed for this exact mission profile. It exceeds even a target drone that was designed to have lower capabilities than the RAD. Over 10,000 red air flight hours, the RAD can save between 85,000 and 62,645,000 kg of fuel over existing alternatives. That is equivalent to the fuel usage of up to 895 flights from London to New York using a Boeing 747-400[10]. Furthermore, this saves up to $1.98 \cdot 10^8$ kg of CO_2 emissions over 10,000 flight hours[11].

On top of that, the sustainability of the RAD is not just in its fuel consumption. It also produces much less noise than many alternatives, which must use afterburners in order to take off. This produces a lot of noise near populated areas, which should be avoided. The RAD can take off without the use of an afterburner, which is both fuel and noise efficient. This makes sure that the RAD reaches one of its objectives: Causing less noise pollution than current alternatives. Socially, the RAD is more sustainable by providing better training opportunities to fighter pilots, and thereby protecting the community.

3.2. Design Considerations

To ensure environmental sustainability, the design of the RAD will feature as much sustainable materials as feasible. The wing box and fuselage structure will be designed with recyclable material such as aluminium in mind. For the RAD, the use of composites will be kept to a limit and will only be used where it is essential. Efforts

[2] Source: https://customer-janes-com.tudelft.idm.oclc.org/Janes/Display/JAU_1617-JAU_#Specifications (retrieved on 18 June 2022)
[3] Source: https://customer-janes-com.tudelft.idm.oclc.org/Janes/Display/JAWA1183-JAWA#Specifications (retrieved on 18 June 2022)
[4] Source: https://customer-janes-com.tudelft.idm.oclc.org/Janes/Display/JAWA1347-JAWA#Specifications (retrieved on 18 June 2022)
[5] Source: https://en.wikipedia.org/wiki/Northrop_F-5 (retrieved on 16 June 2022)
[6] Source: https://assets.publishing.service.gov.uk/media/5423018f40f0b61346000b95/dft_avsafety_pdf_028723.pdf (retrieved on 16 June 2022)
[7] Source: https://customer-janes-com.tudelft.idm.oclc.org/Janes/Display/JAWA1048-JAWA#Specifications (retrieved on 16 June 2022)
[8] Source: https://customer-janes-com.tudelft.idm.oclc.org/Janes/Display/JAWA0186-JAWA#Specifications (retrieved on 16 June 2022)
[9] Source: https://customer-janes-com.tudelft.idm.oclc.org/Janes/Display/JUAV9494-JUAV#Specifications (retrieved on 16 June 2022)
[10] Source: https://www.flightdeckfriend.com/ask-a-pilot/how-much-fuel-does-a-jumbo-jet-burn (retrieved on 19 June 2022)
[11] Source: https://www.eesi.org/papers/view/fact-sheet-the-growth-in-greenhouse-gas-emissions-from-commercial-aviation (retrieved on 16 June 2022)

are made to choose an engine that is as efficient as possible without sacrificing the performance of the RAD. As discussed in the Baseline report [3], sustainability drivers can be identified for each stage of life of the RAD.

Economic sustainability is pursued by analysing and minimising the costs in the cost breakdown and adding more value to the product. This is analysed in the market analysis.

3.3. Outlook to the Future

All three pillars of sustainability, social, economic, and environmental, can be further optimised. The main benefit of the RAD with respect to social sustainability is that it optimises training for fighter pilots. However, the use of the RAD will changes the way in which red air for blue air training is conducted. Making it cheaper and more sustainable. When done well, not only will the fighter pilots' benefit, but eventually all parties involved with providing red air for blue air training will see some kind of benefit through the use of the RAD.

Secondly, the logistics, operations, and production processes can be optimised with respect to the aforementioned sustainability drivers. Hereby improving the economic and environmental sustainability. During the further design phases the noise characteristics of the RAD can be analysed and optimised. Flight profiles for cruise can also be optimised, as not the full red air mission is spent in a combat environment.

3.4. Ethics

The development of a military supersonic stealth UAV can raise some ethical concerns about how it will be used for its intended purpose. As the RAD can go supersonic and has stealth technology incorporated in its design, it can be seen a threat or weapon if used for non-training purposes. However, the RAD has no weapons bays to carry weapons and it has only 3 attachment point which are all far too small and not strong enough to carry weapons. Furthermore, the RAD is so small and light that current weaponry is about half the size of the RAD, meaning it would not be able to carry any, let alone take off with it.

The bottom line is that the RAD does not introduce anything new into the military capabilities. There are red air missions providing training for blue air today and it will continue to be provided in the future. The current fighters used for the red air mission are very much capable of being used for offensive and defensive missions and the RAD is only capable of simulating this in terms of RCS and performance. Furthermore, red air training is performed to increase the chances of survival of pilots, which one could argue would be unethical not to provide. Overall, the RAD does not provide new capabilities and only provides red air for blue air training in a more sustainable and cost-effective manner compared to current fighters filling the role.

4 Configuration

With a clear idea of the required elements and subsystems to be on the RAD concept [4], it is possible to obtain a general layout of the RAD. First, the requirements are listed in table 4.1, then the external layout is treated in section 4.1, generally describing where some of the bigger RAD systems are located and why. The systems that are required for the RAD to operate its mission are described in section 4.2. Following, the internal layout is shown in section 4.3 which describes where the internal (sub)systems are positioned. Using the known RAD systems and elements the masses of them are given in subsection 4.3.5, together with the total RAD mass. The communication equipment is outlined in section 4.4. Next, the budget breakdown is discussed in section 4.5. Finally, the resource allocation is presented in section 4.6.

Table 4.1: *Requirements for the configuration of the RAD.*

ID	Description
RAD-TE-SYS-01	The RAD shall have an internal volume of at least 14 L available for the payload and onboard systems.
RAD-TE-SYS-02	The RAD shall be able to provide power to all necessary equipment onboard for safe operation.
RAD-TE-SYS-03	The RAD shall have the necessary systems to complete its mission.
RAGP-TE-SYS-04-02	The RAD shall have necessary equipment on ground for IFR operations.

4.1. External Layout

For the external layout, the wing and propulsion group are of key importance. The final external layout of the aircraft can be seen in chapter 9, where the final design is displayed.

4.1.1. Wing Group

The wing group consists of two elements:

- Wing, with all its according mobile surfaces
- Empennage

The wing has been chosen to be a cropped compound delta wing (more details about the wing are found in chapter 5) with the leading edge located at 2.52 m from the front of the fuselage (nose) as can be seen in figure 4.1. The main reason for selecting this planform was the additional L/D that it offers compared to the normal delta wing. The wing has been positioned relatively aft to retain a good balance between longitudinal stability and controllability due to the centre of gravity being relatively aft as well. The supercritical NASA SC(2)-0404 airfoil was chosen for its great transonic performance; the wing has the same airfoil throughout. Leading edge flaps are present on the RAD, as well as trailing edge plain flaps. This is to achieve a higher lift at take-off. Ailerons on the outer parts of the wing are separated from the HLDs. All of these moving wing surfaces are shown in figure 4.5.

The empennage (described in chapter 7) has been chosen to consist of canted fins mainly for low observability reasons. The canted fins have been positioned as aft as possible to increase the moment arm from the centre of gravity to the aerodynamic centre of the empennage.

4.1.2. Propulsion Group

The propulsion group designs the inlets and nozzles, the inlets can be seen from the front in figure 4.4. The inlets have been designed in a way that is optimised for the flight conditions that occur when flying Mach 1.6 at 40,000 ft altitude. A side inlet configuration was chosen to gain space for the internal systems without facing performance

reduction at high AoA. Side inlets are also well integrated into the fuselage, minimising their impact on the RCS. Further features of the intake design are that it is diverterless, has a Y-duct, and has D-shaped intakes. Due to the presence of an afterburner, a variable nozzle was needed to accommodate higher jet velocities. By having a variable geometry, the exhaust velocity can be maximised by changing the exit pressure. To achieve supersonic exit velocities, a convergent divergent nozzle was designed.

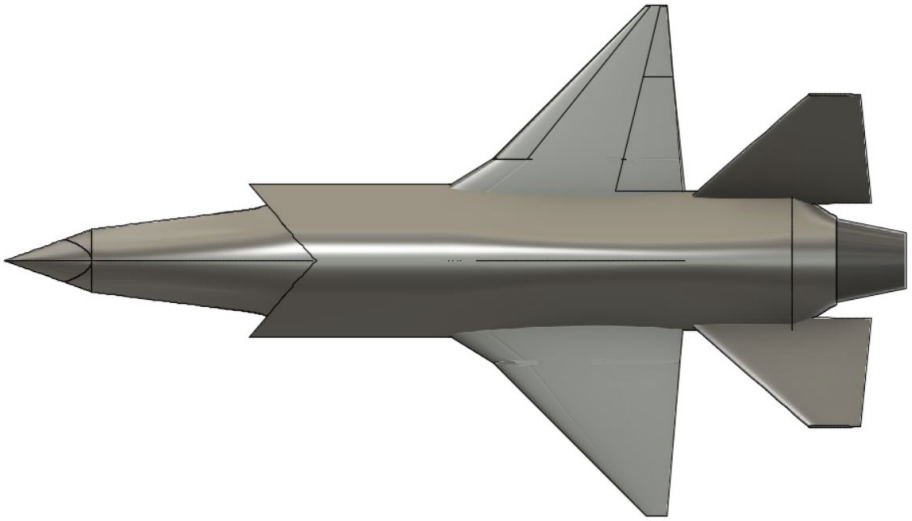

Figure 4.1: *External top view of the RAD.*

4.1.3. Fuselage Group

The fuselage group considers the nose and fuselage shape as seen from the outside. The nose and fuselage are a trade-off between low observability and aerodynamics, it takes advantage of non-constant radii curvature to spread out the radar energy more whilst still being smooth for aerodynamics. A faceted design has not been chosen for the nose because of its poor aerodynamic performance. The nose length is determined by the Mach cone. It shifts the Mach cone forward, allowing the wing planform to be further optimised. The fuselage shape is generally governed by area ruling and RCS requirements. It also provides easy incorporation of the Y-duct into the body.

4.2. Mission Systems

The drone is required to carry mission systems (mission payload) that can be changed on base depending on the mission profile. This system payload profile is decided on by the project guide [4]. First, the requirements are listed in table 4.2, following this, subsection 4.2.1 describes the mission systems. Finally, subsection 4.2.2 lists all systems and estimates the mass and volume characteristics.

Table 4.2: *Requirements for the mission systems.*

ID	Description
RAD-TE-PER-02-01	The RAD shall have a payload capacity of at least 78 kg.
RAD-TE-SYS-03	The RAD shall have the necessary systems to complete its mission.
RAD-TE-SYS-03-01	The RAD shall carry the necessary equipment for manipulating observability.
RAD-TE-SYS-03-01-A	The RAD shall carry radar cross-section enhancement systems.
RAD-TE-SYS-03-01-A1	The RAD shall have two forward facing and two rear facing antennae for the active radar cross section transmitter.
RAD-TE-SYS-03-01-A2	The RAD shall have two forward and two rearward antennae for passive radar cross section reflector.
RAD-TE-SYS-03-01-B	The RAD shall have an infrared signature enhancer at the rear of the aircraft.
RAD-TE-SYS-03-01-C	The RAD shall carry a radar emulator and a radar jammer.
RAD-TE-SYS-03-01-D	The RAD shall have two antennae in the front and two antennae in the rear for both the radar jammer and radar emulator.
RAD-TE-SYS-03-01-E	The RAD shall carry a radar warning receiver.

ID	Description
RAD-TE-SYS-03-02	The RAD shall have equipment for conducting military communications.
RAD-TE-SYS-03-02-A	The RAD shall carry an IFF system.
RAD-TE-SYS-03-02-B	The RAD shall be able to conduct Link 16 communications.
RAD-TE-SYS-03-03	The RAD shall have the necessary equipment for VFR operations.

4.2.1. Mission System Description

The drone is required to carry several systems to perform its mission. These systems are described in the project reader [4]. It was decided to call these mission systems, or bluntly mission payload. Officially, most of the systems discussed in this chapter should not be considered payload, but as they are not included in the class I. and class II. weight estimations, their weights have been included as payload mass in those calculations.

The required systems require a total continuous power of 5 kW, as well as a total peak power of 10 kW according to the reader [4]. This power consumption does not include the optional desired systems nor take additional electrical power for future add-on systems into account.

4.2.2. Drone Mission Systems

All mission systems can be seen below in table 4.3. The minimum required payload is estimated to have a mass of 78 kg and a volume of 78 L. To make the product more desirable several optional systems have been considered as well resulting in an estimated total mass of 131 kg and a volume of 104 L. To make the product even more desirable it would be favourable to have additional payload capacity, as well as additional electrical power for future add-on systems. This extra capacity has been established by adding extra weight and rounding off the values giving a mass of 150 kg and a volume of 125 L.

Table 4.3: *Mass and volume characteristics of mission systems for the RAD as stated by the project reader [4].*

Component	Mass [kg]	Volume [L]	Note
Minimum Required Mission Systems			
Active RCS enhancement systems	2.5	1	Requires power, space inside the fuselage, two forward facing antennas, and two facing rearward.
Passive RCS enhancement systems	2	1 (est.)	Requires reserved space for two passive RCS reflectors on the forward, and two on the rear part of the platform; distributed on top, and bottom.
Infrared signature enhancer	4	5	Requires space at the rear of the aircraft.
Radar emulator	0.5 + 3*	1	*Requires space for the antennas; two in front, and two in the rear.
Radar jammer	1	1	Shared antennas with radar emulator.
Radar warning receiver	10	2	-
IFF system	0.5	1	-
MIDS terminal	3	3	For Link 16 communications.
VFR and IFR operations system	9 [5] (avg.)	8 (est.)	Consists of ILS, VOR, DME, GPS, IMU, transponder, VHF/UHF radios, lights, TCAS, etc. [6], [7].
Icing conditions equipment	3 (avg.)	3 (est.)	Placed in the wing and canted fins. Mass is dependent on wing and fin sizing [8]. Requires 0.5 kW (est.) of power.
Autopilot	1	1	Garmin GFC™600 Digital Autopilot.
Camera system	2.5 (est.)	2 (est.)	Estimate by team, depends on how many cameras are required and the image quality.
Two AN-ALE 47 chaff/flare dispensers	2×17	2×24	This is the only payload that must be reloaded after mission. Specifications were found online[1], mass used is loaded[2].
Flight recording system	2 (est.)	1 (est.)	Estimate by team, no specifics were found online.

[1]Source: https://www.wbparts.com/rfq/5865-01-334-8349.html (retrieved on 16 May 2022)
[2]Source: https://de.wikipedia.org/wiki/AN/ALE-47 (retrieved on 24 May 2022)

Component	Mass [kg]	Volume [L]	Note
Total Minimum	**78** (est.)	**78** (est.)	Requires 6 kW of continues power and 11 kW of total peak power.
Optional Desired Systems			
Parachute recovery system	35 (est.)	15 (est.)	Weight and placement depend on how acceptable damage is to the drone. Estimate is made with a mass of 2,000 kg, a landing speed of 10 m/s, and a C_D of 1.5. It is also assumed the total recovery system weight is twice the weight of the parachute [9].
BLOS communication	5 (est.)	3 (est.)	Estimate by team, this system requires extra power, two options are considered: communications by relays or electronically steerable antennas for satcom [10].
EO/IR camera system	5 (est.)	3	Weight depends on gimbal and image quality. E.g. Octopus Epsilon 180[3].
Spherical optical sensor system	8 (est.)	5	Weight depends on sensor quality. E.g. SkEye Waps™[4].
Total Desired	**131** (est.)	**104** (est.)	Total desired payload characteristics. Requires 1 kW of additional power.
Total + Extra Capacity (Desired)	**150**	**125**	To make the product more desirable, it is convenient to have extra payload capacity for future operations. As well as a surplus of power, if possible 15 kW of peak power.

In table 4.3 the VFR and IFR systems have a mass of 9 kg [5], as these are all the avionic system required in a UAV. These systems have been decided on for the further detailed design of the drone. The systems include the ILS: Garmin GRA™5500; the VOR, DME, & GPS: Garmin SL40; the IMU sensors: Garmin G3X™System Sensor Kits (high-performance); the transponder: Garmin GTX™45R; the radio: Garmin GTR 20; the TCAS: Garmin GTS™855 TCAS/ACAS I; and finally, the autopilot: Garmin GFC™600 Digital Autopilot. The total costs of these systems combined is roughly 55,000 $ USD (FY2022). The estimated power consumption for these systems combined including the lights[5] are estimated to be 0.5 kW [11].

The autopilot is the core component of the UAV avionics system. These systems together are composed of computing and sensing subsystems. These include the on-board computer; IMU (acceleration and magnetic sensors); a Global Positioning System (GPS) receiver; battery monitoring and power distribution board; and an on-board camera [12].

The heated de-icing equipment is estimated to have a mass of 3 kg, and have a volume of 3 L, using 0.5 kW of power according to estimations by relating the wingspan of the *Northrop Grumman RQ-4 Global* to the wingspan of the RAD [8], this system should exceed CS-25 ice protection requirements [13], [14].

4.3. Internal Layout

For the internal layout all the groups are important, as each can and has to house (sub)systems in them.

[3]Source: https://octopus.uavfactory.com/uav-payloads-equipment/epsilon-180 (retrieved on 24 May 2022)
[4]Source: https://www.elbitsystems-uk.com/what-we-do/air-space/c4isr/eo-intelligent-systems (retrieved on 24 May 2022)
[5]Source: https://aeroleds.com/products/sunbeacon-ii-beacon-light/ (retrieved on 24 May 2022)

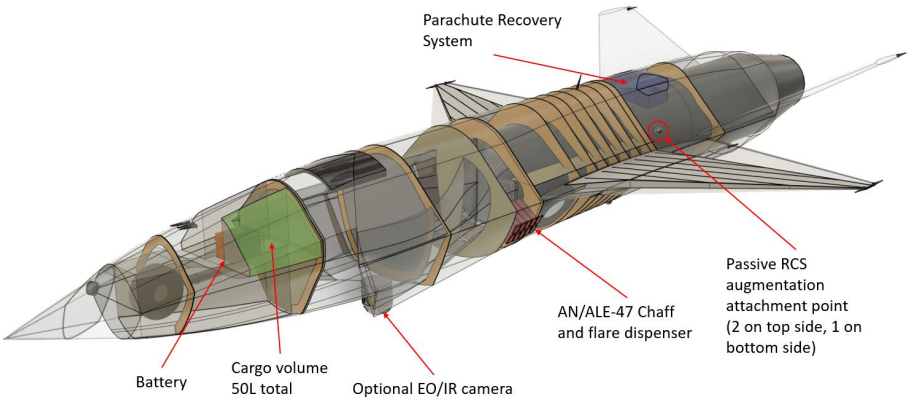

Figure 4.2: *Internal side view of the RAD.*

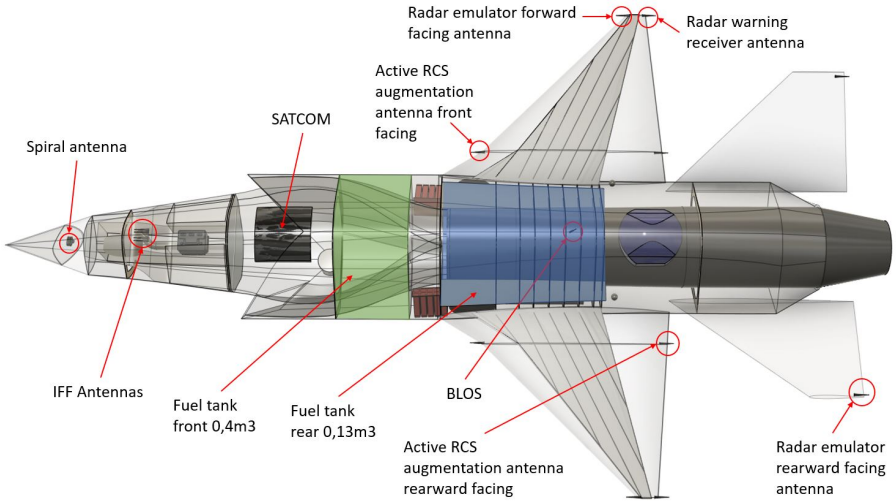

Figure 4.3: *Internal top view of the RAD.*

Figure 4.4: *Front view of the RAD with the optional EO/IR camera attached.*

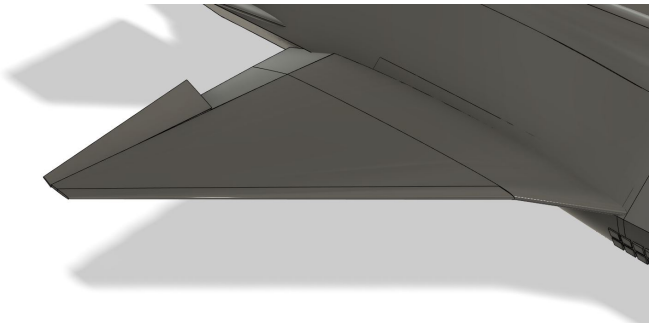

Figure 4.5: *View of the wing with the HLDs deflected.*

4.3.1. Propulsion Group

Arguably the heaviest of the groups, internally it contains the following elements:

- Engine
- Afterburner
- Air induction systems
- Intake
- Engine starter
- Feed/fuel systems
- Power/electrical systems

As the RAD is more or less designed around the engine, because the engine is the main component to obtain the high speeds set out by the requirements, and the engine plus the afterburner are the largest components of the RAD, most of the positioning (of all groups) is done around the engine. The engine and the afterburner are placed up till the end of the fuselage along the longitudinal axis. As can be seen in figure 4.2 and 4.3 the engine & afterburner take up a very considerable part of the fuselage.

The air induction systems are assumed to be positioned in the front of the engine with two intakes positioned on the outside at the sides of the RAD extending into the fuselage, where they join into one big nozzle and enter the engine. All the remaining elements of the propulsion group have been positioned around the engine. This is not shown in 4.2 and 4.3 as this requires a more in depth analysis of proper connection lines not done at this stage of the design.

4.3.2. Fuselage Group

As seen in figure 4.2 and 4.3 depict a lot of separate systems: which will be described in this document as mission systems, the systems required to perform the mission. The following elements are included in the current internal layout of the RAD:

- Landing gear
- Fuselage structure
- Mission systems

The location of the stored landing gear can be found in 7.7b. The fuselage structure shown in 4.3 is still a small part of the required structure, but it does provide an insight in what one can expect size and location wise for some of the main load carrying structures. Lastly the mission systems have been positioned around the fuselage on the required locations as described in 4.2.

4.3.3. Wing Group

Like the fuselage group also the wing group internally already contains some key systems, mostly the wing structure. Again, some mission systems are housed in the wings, due to the requirement of them being there (like the radar emulator and the radar warning receiver). Some additional mission systems have been positioned there due the available free space and the high probability of low interference with other systems if they are placed in the wings. Lastly, as can be seen in figure 4.3, the inner dark grey part of the wing is the wing box with the correct spars positioned.

4.3.4. Variable Group

Finally, a key group which contains all the elements whose mass can change throughout the flight consider:

- Fuel
- Chaff/Flares

In figure 4.2 and 4.3 the fuel tanks are indicated with green and blue boxes. Their location, as well as size is still subject to change in case additional fuel space would be required. The chaff/flares dispensers are located on the bottom middle of the fuselage.

4.3.5. Full System Mass

With all the required systems and elements described, their masses are shown in table 4.4. The MTOM(maximum take-off mass) and OEM(operating empty mass) in this table will be used for all calculations throughout the report.

Table 4.4: *The main element masses of the RAD divided in their appropriate groups.*

Element	Mass [kg]	Element	Mass [kg]
Individual groups			
Wing group:		**Propulsion group:**	
Wing structure	69.1	Engine	340.0
Empennage structure(Class II)	31.5	Afterburner	161.0
		Air induction systems (intakes etc.)	267.1
		Power/electrical system	121.7
Fuselage group:		**Variable group**	
Landing gear	96.0	AN-ALE 47 (2x)	34.0
Fuselage structure	248.2	Fuel(body)	444.0
Mission systems(including flight control systems)	210.1	Fuel(wing)	80.0
Paint	23.4		
Total masses			
MTOM:	2126.2	**OEM:**	1568.2

4.4. Communications

The RAD carries a Satellite Communication (SATCOM) system and an SHF communication system. SATCOM is used to achieve true Beyond Line of Sight (BLOS) communication, while SHF is used when the RAD is flying close to the GCS (within line of sight and 150 NM of the sender) or a relay station. SHF is preferred when low-latency control is needed, as communication through this method has lower delays. Current Ground Control Stations (GCS) already use SATCOM and SHF to control UAVs[6], which makes compatibility with existing UAV control systems better.

Whereas the *MQ-9* uses a conventional dish antenna for its satellite communications, space limitations and RCS minimisation mean that a Phased Array antenna is better suited for the RAD. This antenna can be placed on top of the drone, flush with the skin[7], while not taking up much thickness[8]. This means that the SATCOM antenna has no impact on the RCS of the aircraft.

Antennas for SHF communication do have to be mounted on the bottom part of the aircraft, as communication with ground stations is needed. In order to minimise the RCS, and because it is a secondary communication system, a very compact antenna can be used, such as the one made by JEM Engineering[9]. The antenna can be placed in the radome, at an angle to not deflect any incoming radar waves straight back to the sender.

If it is found that this placement produces too much of an impact on RCS, the compact antenna could be placed on the landing gear. Low-latency control is mostly only needed around airports, which often has the landing gear retracted anyway. The only change would be that the RAD retracts its landing gear later, when SATCOM control is allowable. However, this is obviously not optimal, so placement in the radome is preferred.

4.5. Budget Breakdown

Technical resources drive the cost of a product, and these resources have the tendency to grow during the development of the design. Therefore, a maximum value for the resources, including a reserve or contingency, were established in the previous report [2]. This budget is carefully managed during the execution of the design

[6]Source: https://customer-janes-com.tudelft.idm.oclc.org/Janes/Display/JUAV9266-JUAV (retrieved on 10 June 2022)
[7]Source: https://jemengineering.com/wp-content/uploads/2021/05/HSA-2438C-Datasheet-Rev6.pdf (retrieved on 10 June 2022)
[8]Source: https://jemengineering.com/wp-content/uploads/2021/05/JEM-238MFC-Datasheet-Rev5.pdf (retrieved on 10 June 2022)
[9]Source: https://jemengineering.com/wp-content/uploads/2021/05/HSA-218-Datasheet-Rev7.pdf (retrieved on 10 June 2022)

process. A first version of the budget breakdown was presented in the baseline report [3], a final updated version will now be discussed. Firstly, in subsection 4.5.1 a relevant set of reference aircraft is set up. Secondly, subsection 4.5.2 sets up the different parameters for which a budget will be made. Following this, the actual budget breakdown is done in subsection 4.5.3.

4.5.1. Reference Aircraft

To gather meaningful data, a set of similar aircraft needs to be gathered. The similarity can be in mission or in performance requirements. The set of reference data is based on the following reference aircraft:

ŞimŞek drone[10]: The ŞimŞek drone is a Turkish target drone produced by Turkish Aerospace. It is used for both surface-to-air and air-to-air training. It carries payloads to help it simulate air targets.

Do-DT45[11]: The Do-DT45 is a drone developed by Airbus Defence & Space. It is mainly used to simulate air-launched threats to aerial, ground, or sea-based platforms. On top of this, there is a family of target drones from Airbus. From this family, the Do-DT45 shows the closest performance and mission profile to that of the RAD.

BQM-177A[12]: The BQM-177A is an aerial target made by Kratos Defense and Security Solutions. It is a reusable simulator of various aerial threats. Its mission payload is more advanced than that of the ŞimŞek, as the BQM-177A active radar augmentation measures and ECM.

BQM-167A[13]: The BQM-167A is like the BQM-177A, but larger. Its maximum launch weight is higher than that of the BQM-177A, while fighter higher and with a higher range. The payloads of the two drones are similar.

Banshee[14]: The Banshee is a family of target drones made by QinetiQ Targets Systems. The most similar variant to the RAD is the Banshee Twin Jet, which has a comparable size and performance to the other drones in the family, but a higher top speed.

F-5E Tiger II[15]: The F-5 Tiger II belongs to the other end of the spectrum. It is a fighter aircraft developed by Northrop Grumman. Its performance far exceeds the performance of any drone mentioned above. Its top speed is remarkably close to that of the RAD.

Other relevant aircraft are the *XQ-58A* (also called *XQ-222*) and the *MQ-28A*, which show closer design goals and performance than the current reference aircraft. However, as these are novel designs, data available for these aircraft is limited to the point where they provide little use to this budget breakdown. Therefore, all relevant reference aircraft have been gathered. They are visualised in figure 4.6. In order to get an idea of their performance and size, some data has been visualised in table 4.5.

[10] Source: https://customer-janes-com.tudelft.idm.oclc.org/Janes/Display/juava551-juav (retrieved on 8 May 2022)
[11] Source: https://customer-janes-com.tudelft.idm.oclc.org/Janes/Display/JUAV9372-JUAV (retrieved on 8 May 2022)
[12] Source: https://customer-janes-com.tudelft.idm.oclc.org/Janes/Display/JUAVA553-JUAV (retrieved on 8 May 2022)
[13] Source: https://customer-janes-com.tudelft.idm.oclc.org/Janes/Display/juav9494-juav (retrieved on 8 May 2022)
[14] Source: https://customer-janes-com.tudelft.idm.oclc.org/Janes/Display/JUAV0167-JUAV (retrieved on 8 May 2022)
[15] Source: https://customer-janes-com.tudelft.idm.oclc.org/Janes/Display/JAU_1652-JAU_ (retrieved on 8 May 2022)

(a) *ŞimŞek* [12] **(b)** *Do-DT 45* [13] **(c)** *BQM-177A* [14]

(d) *BQM-167A* [15] **(e)** *Banshee (Jet 80 Variant)* [16] **(f)** *F-5E Tiger II* [17]

Figure 4.6: *Reference aircraft used for the budget breakdown.*

Table 4.5: *Reference aircraft specifications used for the budget breakdown.*

	Simsek[10]	**Do-DT45**[11]	**BQM-177A**[12]	**BQM-167A**[13]	**Banshee**[14]	**F-5**[15]
MTOW [kg]	75	75	635	930	N/A	11,214
Payload [kg]	10	8	122	N/A	N/A	N/A
Range [km]	90	100	N/A	740	100	2,481
Endurance [min]	45	53	60	180	53	N/A
Thrust [kN]	0.4	0.44	4.5	4.45	1.08	32/44.5
Max speed	400 kts	427 kts	M 0.95	615 kts	390 kts	M 1.64
Length [m]	2.3	2.15	5.18	6.15	2.95	14.45
Span [m]	1.5	1.8	2.13	3.18	2.49	8.13

As none of the aforementioned aircraft come close to the performance goals of the RAD, a somewhat unorthodox budgeting method is used. Instead of using reference data and including a contingency factor, a minimum and maximum range is taken. A fudge factor multiplied with the budgets of existing drones is not possible, as there are no reference aircraft which have both a subsonic and supersonic version [15]. This would make any fudge factor a pure guess.

As such, the existing target drones are used as minimum budget estimations, as their performance in most categories is much lower than that of the RAD. On the other hand, the F-5 far exceeds the performance of the RAD in most categories. Therefore, the F-5 will be used to estimate the maximum budget needed.

4.5.2. Budget Parameters

Now that data is obtained, a budget for each parameter was created. These budgets can be found in table 4.6. The highest value from the first five reference aircraft is taken as a minimum, thus excluding the F-5. As all these first five underperform compared to the requirements for the RAD, it can be concluded that their budgets for technical parameters will be lower than the design values of the RAD. As it turns out, the BQM-177A and BQM-167A have the highest values for each budget parameter. The maximum is then defined each time by the F-5. Note that the maximum thrust with afterburner of the RAD will likely be closer to the maximum dry thrust of the F-5, as on-board systems, and payload of the RAD weighs far less. However, it is not possible to produce a fudge factor purely based on payload or onboard systems weight, so the maximum is not considered for this, as this has been budgeted already in section 4.2.

This still leaves quite large margins for technical parameters. However, as no aircraft exists that has similar performance to the RAD, this is the only budget where one can confidently conclude that the design values for the RAD are within it. For example, if one would also consider a subsonic trainer aircraft, there would be a large uncertainty in the budget. This is caused by the inability to assess the impact of a single design parameter on a budget component. For example, the RAD's top speed is far higher, while its payload capacity is much lower. It is then not possible to see which factor is dominant, so if the budget for the RAD should be higher or lower than this reference value. This would be possible if reference aircraft would exist where only one design parameter is different, but unfortunately, these do not exist.

Table 4.6: *Established design budgets that should be considered for future iterations of the design.*

Budget Type	Min. Budget		Max. Budget
OEW [kg]	235	–	4,410
Max. Fuel Weight [kg]	350	–	1,996
MTOW [kg]	930	–	6,728
Thrust [kN]	4.5	–	44.5

4.5.3. Contingency Management

The contingency margins are only assigned to independent design variables to prevent placing margins on parameters that already have margins. Two distinct types of margins are defined. Firstly, the requirement margin, which accounts for the evolving design requirements. These provide reserves that could allow for the future evolution of the product [16]. The other being the margin accounting for model uncertainty. A margin is assigned if it is believed that the estimate of a particular performance value is optimistic, which could emerge due to the models not being sufficiently accurate [16].

For requirement contingency margin, the independent parameters considered are the maximum speed and the radar cross-section. Setting the margin to 10% would allow the project to be more future proof. This leads to maximum speed of M = 1.76 at 40,000 ft and frontal, geometric radar cross-section of 0.09 m^2.

For system contingency margin, three distinctive design stages are distinguished, and contingency margins are specified for each parameter for each design stage. The stages are the initial sizing stage, the preliminary design stage, and the detailed design stage. The margins decrease from the initial sizing stage towards the detailed design stage. Independent parameters that are assigned contingency margins are OEW, transonic drag, maximum wet thrust, electrical power, on-board computer capacity and control data link.

The initial sizing stage consists of initial class I. and class II. weight and drag estimations, and early estimates in other fields. Therefore, these models will have the highest contingency margin, as they are least accurate. Next stages go into more detail, therefore more precise information is known about the drone and because of that also the contingency margin decreases. An overview of contingency margins for considered design parameters and for identified design stages can be found in table 4.7.

Table 4.7: *Contingency margins for different design stages.*

Parameter	Design goal	Maximum value	Initial sizing stage margin	Preliminary stage margin	Detailed design stage margin
OEW	2,216	4,410 kg	20%	15%	5%
Transonic drag	3 kN (@ 40,000 ft)	10 kN (@ 40,000 ft)	25%	20%	10%
Maximum wet thrust	29.5 kN (S/L)	44.5 kN (S/L)	20%	15%	10%
Maximum electrical power	12 kW (peak)	20 kW (peak)	20%	10%	5%

4.6. Resource Allocation

Since the resources for the design of this project are limited, they must be allocated competently. In terms of money, there is no money. However, €100,- worth of paper for printing was available [4], which has been used

customarily in displaying the design to other groups. Therefore, the only resources were the project members doing the DSE.

4.6.1. List of Resources

All resources that can be used during this project are listed below:

- €100 printer credit
- Ten student engineers
- Internet
- Free online tools (student licences)
- Laptops sufficient for doing the project
- Facilities at TU Delft (not always)
- Mentors
- Teaching Assistants
- Assistance from NLR

4.6.2. Allocation of Resources to Tasks

The ten students committed to this project were distributed along all the tasks. This was done by using the Gantt chart and work break-down structure. All tasks have been determined and are displayed in the Gantt chart which can be seen in figure 2.6. Project members themselves also have functions as listed in the organogram from the project plan [17]. The person that oversaw the Gantt chart had an overview of all tasks and assigned people to tasks according to their department. The chairman gave out tasks to project members if they were finished with their task and required to work on something else.

4.6.3. Allocation of Time For Tasks

It was estimated how much work each task was going to require. As members together will work quicker, big tasks are tasked to multiple members at once. Every member can spend 8 hours of work per working day. In the end, more than just these 8-hour workdays were needed to finish all tasks. An estimated 60 hours per person were needed outside of sessions to finish all tasks in time. Given the enthusiasm the team members had for this project, motivation for this was not a problem. However, it is recommended that the allowed time to complete all tasks is increased by one-week next year, as six workdays out of the ten weeks were not spent working because they were national holidays. This extra week would reduce work outside of official hours to 20 hours per person, which is more acceptable. The team would gladly have done more engineering work, but time constraints outside of their control restricted them severely in this.

5 Aerodynamic Performance Estimation

The aerodynamic performance is critical to the operation of the RAD. It will dictate the speed and altitude the RAD can reach and how its overall flight envelope will look like. The aerodynamic performance must be such that the requirements for the flight envelope can be met in the chapters for propulsion (chapter 6) and performance (chapter 10).

5.1. Airfoil

Airfoil selection is a key design choice in the design. The shape of an airfoil has a major impact on the drag and lift of the wing and therefore the overall performance of the aircraft. The choice of airfoil heavily depends on the mission profile of the aircraft and its performance requirements.
The RAD must be able to cruise efficiently at Mach 0.9 and dash at speeds of Mach 0.95 and Mach 1.6. This means it will predominantly operate in the transonic region, while dashing twice for a short period to supersonic speeds of Mach 1.6. Therefore, a supercritical airfoil was chosen to optimize the transonic performance and delay the Mach drag-divergence M_{dd} number [18, pp. 342–346]. The NASA SC(2)-0406 airfoil was initially chosen as airfoil due to its high Mach drag divergence number, relatively high drag bucket width and comparatively large enclosed area. The values can be observed in table 5.1 below.

Table 5.1: *General characteristics of trade-off airfoils*[1].

Airfoil	$C_{l_{\max}}$	$\frac{t}{c}$ [%]	$L/D_{\max}$	Drag bucket width	M_{DD}	Enclosed Area
NASA SC(2)-0404	0.8	4	34	0.25	0.87	2.72
NASA SC(2)-0406	0.85	6	35	0.35	0.85	4.08

The high enclosed area allowed for more fuel to be stored in the wing and decreased the weight of the wing due to lighter structures required. However, this is accompanied by a higher thickness to chord ratio, t/c. This is very significant for the supersonic performance as supersonic wave drag rises with $(t/c)^2$ [19, p. 30a]. As wave drag makes up a large part of the overall drag in the supersonic regime, this culminated in the RAD having a large supersonic drag. The drag was so significant, that the RAD could not easily reach the required supersonic speed of Mach 1.6 if at all. Furthermore, with the consideration that several systems such as landing gear doors still had to be added, the drag would slightly increase the more detail is added. Thus, this narrow margin was deemed unacceptable and the airfoil was changed to the NASA SC(2)-0404. This is the same airfoil as NASA SC(2)-0406 but with a 2% decrease in t/c. This does incur some penalties, such as a lower $C_{l_{\max}}$, which can be seen in table 5.1. However, this is more in line with the trend seen in figure 5.1, where aircraft that can fly at Mach 1.6 usually have airfoils with a t/c ratio between 3 and 5 percent.

Several considerations do have to be mentioned in relation to this choice of airfoil, which have also been outlined in [2]. Firstly, the structural performance and fuel volume of the wing is drastically changed with such a thin airfoil. The fuel volume in the wing will be smaller and the wing will be heavier overall due to additional required structures for the thin wing. Another consideration comes from the unknown performance of the supercritical airfoil in the supersonic regime. Almost all supersonic aircraft shown in figure 5.1 use a 6-series airfoil or similar but not a supercritical one. An example is given for a F-16 wind tunnel test using a supercritical section, which found that,

[1] All numbers sourced from: http://airfoiltools.com/ (retrieved on 13 May 2022)

while getting a 5% mission increase, it had a 70% decrease in supersonic acceleration. This was deemed unacceptable when combined with the development risk of an innovative technology (innovative technology being supercritical airfoils). However, it is noted that future combat aircraft will have the benefit from further research and development [19, p. 35].

As mentioned in the Mid-term report [2], there have been aircraft with supercritical airfoils that can perform supersonic flight, such as the X-29, which had a maximum speed of Mach 1.6. However, one of the designers of the X-29 mentions that one of the big problems was the high supersonic drag, although it is not mentioned if that was mainly due to the airfoil [1]. Finally, a NASA wind tunnel investigation of the application of supercritical airfoil to a variable sweep fighter aircraft was on variable-sweep [21] compared NASA supercritical airfoils with NACA 6-series airfoils. It notes a benefit of cruise Mach number capability of about 0.10 with supercritical compared to conventional NACA 64A-series airfoils [21, p. 17]. Furthermore, the drag polars appear to be very similar when comparing the NACA 64A-series and the supercritical at Mach 1.6 [21, p. 217]. It must be noted however that these airfoils had a $t/c \approx 0.11$ and the sweep was very high at the Mach 1.6 conditions [21, pp. 5–6].

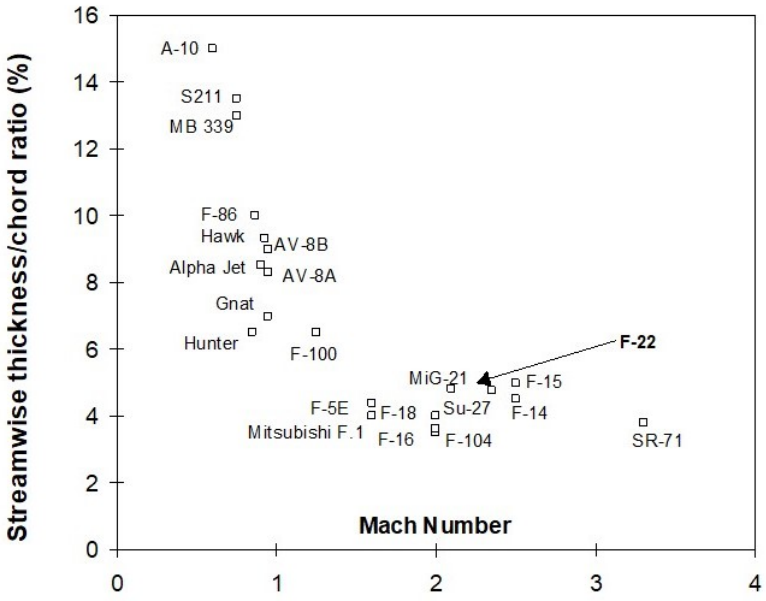

Figure 5.1: *Relation between Mach number and $\frac{t}{c}$ ratio [20, Lec. 2].*

In conclusion, the NASA SC(2)-0404 airfoil was chosen in favour of the NASA SC(2)-0406 airfoil in order to decrease the supersonic wave drag by decreasing the t/c. With the aforementioned considerations, a risk is presented in choosing a supercritical airfoil. Mainly, the high supersonic drag [19, p. 35] and the respective limited data on supersonic aircraft with supercritical airfoils is a definite risk when considering the requirement of dashing at Mach 1.6. However, as the RAD will predominantly operate in the in high transonic region, the NASA SC(2)-0404 airfoil is chosen. This has significant upsides with the higher Mach drag divergence number and is thinner than the NASA SC(2)-0406 airfoil to better accommodate the wave drag.

5.2. Wing Planform

The wing planform was derived from the design point, provided from the weight estimations done in the Midterm [2]. The design point is shown in table 5.2, where the AR is given as a minimum.

Table 5.2: *The design point for the RAD after iterating.*

S [m^2]	W/S [N/m^2]	T/W [-]	MTOW [kg]	AR [-]
4.53	4605	0.513	2126	3

The RAD must be able to cruise at Mach 0.9 and dash at speeds of Mach 0.95 and Mach 1.6. This means that the planform will feature a large sweep and a low aspect ratio, which help with minimising wave drag over the wing at transonic and supersonic speed. Furthermore, at high speeds the drag-due-to-lift becomes relatively less important and therefore a lower aspect ratio is useful as this saves weight [19].

To understand how much sweep, taper ratio and what AR is optimal for the planform, the Raymer book of "Aircraft Design, A Conceptual Approach" [22] was consulted. Usually, for subsonic aircraft the Λ_{LE} is found using the

[1] Source: http://www.dept.aoe.vt.edu/~mason/Mason_f/AnX-29StoryV3.pdf (retrieved on 23 May 2022)

critical Mach number of the aircraft. However, for supersonic aircraft, the Mach cone is the most significant as this leads to significant losses in lift and increased drag [22, p. 79]. From figure 5.3 it can be seen that the RAD, at Mach 1.6, requires approximately $\Lambda_{LE} = 51.3°$ to stay outside the Mach cone, which also follows the historic trend. As mentioned in the Mid-term report [2], the large amount of sweep is problematic as it leads to an increased pitch-up risk when combined with a small AR. However, the nose of the RAD shifts the Mach cone forward as shown in figure 5.2. This allows the sweep to be decreased and still be outside the Mach cone. The minimum nose length relation for a specific Mach angle μ is shown in equation (5.1).

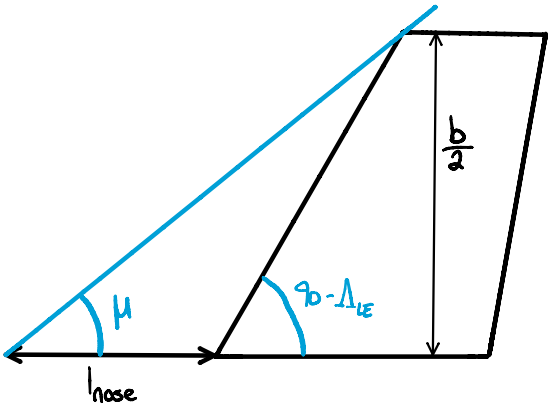

Figure 5.2: *The forward shift of the Mach cone due to the nose.*

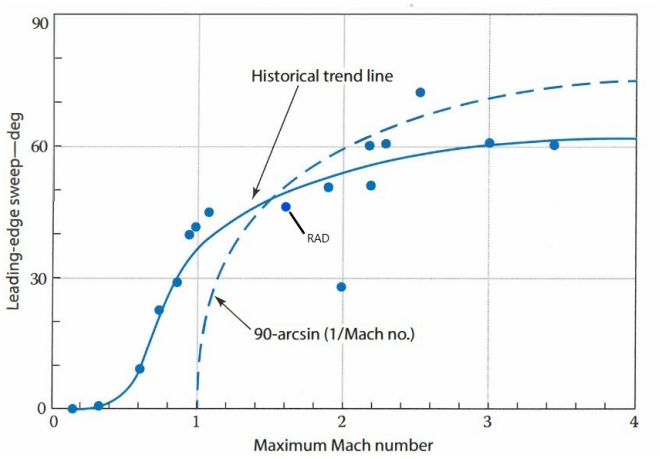

Figure 5.3: *The historic trend of the wing sweep with RAD indicated [22, p. 79].*

$$l_{\text{nose}} = b \cdot \left(\frac{1}{2\tan(\mu)} - \frac{1}{2\tan(90 - \Lambda_{\text{LE}})} \right) \tag{5.1}$$

As the RAD operates in the transonic regime for most of its flight profile, a large sweep is useful for delaying the onset of supersonic flow over the wing. However, large sweep also leads to a smaller AR due to pitch-up risk. A lower aspect ratio is undesirable as the amount of wing affected by the wing tip vortices is greater. Thus, a balance had to be found between the AR and the Λ_{LE}, while considering the AR lower limit from the design point.

The taper ratio λ must be increased as the sweep increases to account for the loading of the wing tips to keep the desired elliptical lift distribution over the wing. For heavily swept wings the λ usually between 0.2-0.3. 0.2 is a lower limit due to tip stall, except for delta wings which can have a taper ratio below 0.2 [19, p. 85]. From figure 5.4, the F-16 and F-5, which are similar in performance as the RAD, are at the lower limit of the taper ratio and would ideally be lower. As a delta wing was the design choice for the RAD [2], due to the great transonic and supersonic performance of delta wings [19, pp. 52–61], the taper ratio is not limited and thus can be as low as the Mirage and Mig-21.
With the aforementioned considerations for the sweep, AR and taper ratio, in combination with the design point, the wing planform was designed. The design chosen is a cropped compound delta, which can be observed in figure 5.5. The main dimensions of the wing are outlined in table 5.3.

Table 5.3: *The wing dimensions of the RAD.*

Area [m^2]	C_r [m]	AR [-]	C_t [m]	λ [-]	b [m]	MAC [m]
4.53	2.6	3	0.15	0.057	3.66	1.26

The wing is split into two distinct sections, where section 1 is the inner part of the wing and the 2 the outer part. Most of section 1 will be inside the fuselage and thus will be functioning as wing strakes, which provides the benefit of vortex lift [19, pp. 88–89]. The wing planform section dimensions are outlined in table 5.4 below.

5.3. Lift Performance

The calculation of the overall lift performance of the aircraft is very manageable for the subsonic regime. However, when traversing to transonic and supersonic regimes it becomes exceedingly difficult to estimate. That

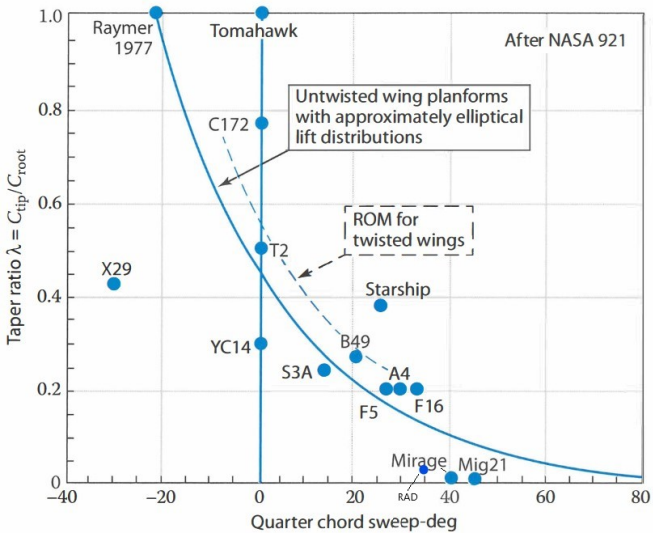

Figure 5.4: *Effect of sweep on taper ratio [22, p. 84].*

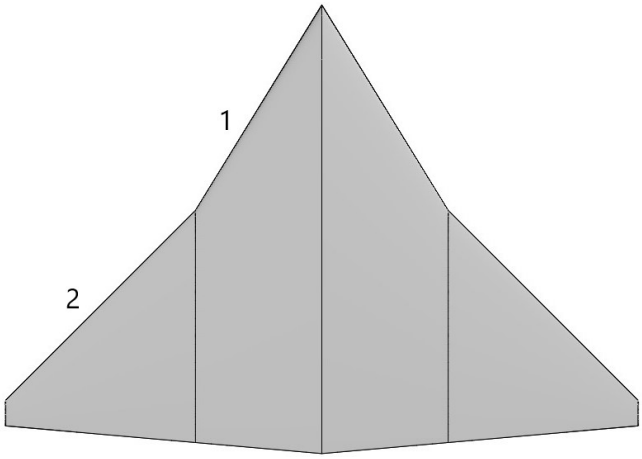

Figure 5.5: *The wing of the RAD shown from the top view.*

Table 5.4: *The dimensions of the wing sections of the RAD.*

Section	Area [m^2]	C_r [m]	AR [-]	C_t [m]	λ [-]	b [m]	Λ_{LE} [deg]	Λ_{TE} [deg]
1.	1.44	2.6	0.37	1.34	0.52	0.73	58°	5°
2.	0.82	1.34	1.47	0.15	0.11	1.1	45°	5°

being said, as the RAD cruises at Mach 0.9, it is able to produce a lot of lift with relatively small C_L. Therefore, the lifting performance of the RAD is mainly focused on low-speed conditions, namely on take-off and landing, as these require high lift at slower speed. The lift curve and $C_{L_{max}}$ are thus important for these conditions. The $C_{L_{max}}$ is so important in fact, that it will usually determine the wing area, which has a great influence on cruise drag. This strongly influences the aircraft take-off weight and therefore influences the sizing of the aircraft, hence it being an input for the iteration of the weight. However, estimation of the $C_{L_{\text{max}}}$ is very unreliable calculation to the point where wind-tunnel test cannot predict maximum lift with great accuracy [22, p. 404].

Table 5.5: *The most important parameters from the lift curve in clean configuration.*

$C_{L_{\text{max}}}$	C_{L_α} [CL/deg]	$\alpha_{Lift=0}$ [deg]	$C_{L_{\alpha=0}}$
0.87	0.06	-1.5	0.09

The RAD was modelled in the XFLR5 software [23] in order to attain an estimate of the lift performance. Figure 5.6 below shows the lift curve for the RAD at Mach 0.2, where the significant values from the graph are shown in the table 5.5.

It is important to note some considerations about the results found. Usually the $C_{l_{\text{max}}}$ of airfoil is lower than $C_{L_{\text{max}}}$ of the wing. However, if the wing is swept and has a very sharp leading edge, it can actually have a higher $C_{L_{\text{max}}}$ than the airfoil. This is the case for the RAD, where the $C_{L_{\text{max}}} = 0.87$, while the $C_{l_{\text{max}}} = 0.8$. The higher $C_{L_{\text{max}}}$ is due to the vortex lift over the wing, which is due to the sharp leading edge and high wing sweep [19, pp. 88–91]. However, it is unclear how well the software estimates the vortex lift and if it can account for the vortex lift of the wing strakes. Additionally, as aforementioned, the true value of $C_{L_{\text{max}}}$ is already very difficult to accurately determine. Therefore, the value of $C_{L_{\text{max}}}$ can only be observed as an estimate.

In addition, at the stall point, the XFLR5 software works better with thick airfoils with large leading-edge radii. However, the RAD wings have neither of these, which made the exact stall point and $C_{L_{\text{max}}}$ harder to estimate accurately. The leading-edge vortices, due to the sharp leading edge, provide very complicated lift profile for high angels of attack, which the software had some trouble with converging for the stall region. That being said, the XFLR5 software did converge for a number of stall points and corrected for the points for which it did not. Furthermore, it provided airfoil results and the wing results that do match nicely to the expected increase

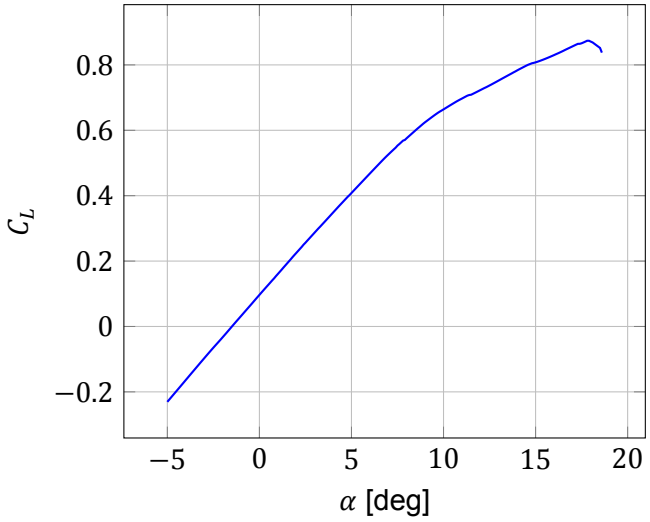

Figure 5.6: *The clean configuration lift curve of the RAD at Mach 0.2 and* Re = 7,130,000.

in C_L performance due to the sharp leading edge and high sweep. The convergence for angels of attack before stall were consistent and converged properly for the wing. Also, the results provided by XFLR5 were consistent with the lift curve validated with the DATCOM method [24], up to stall angels, and can thus be seen as a good estimate. The $C_{L_{\text{max}}}$ is, as mentioned before, still very difficult to estimate and to properly validate, even a flight test is required to get a true value [22, p. 404].

5.4. Drag Peformance

The drag performance is critical to the design and performance of the RAD. The drag is composed of the zero lift drag C_{D_0} and the lift-induced drag C_{D_i}. The zero lift is important for both subsonic and supersonic conditions and comprises of the parasite and wave drag. The wave drag becomes predominant at supersonic speed and is therefore critical in determining whether the RAD can fly at supersonic speed [19, pp. 18–20]. In figure 5.7 the drag breakdown for typical supersonic fighters is displayed, where the high wave drag contribution in the supersonic regime is emphasized.

$$C_D = C_{D_0} + C_{D_i} \tag{5.2}$$

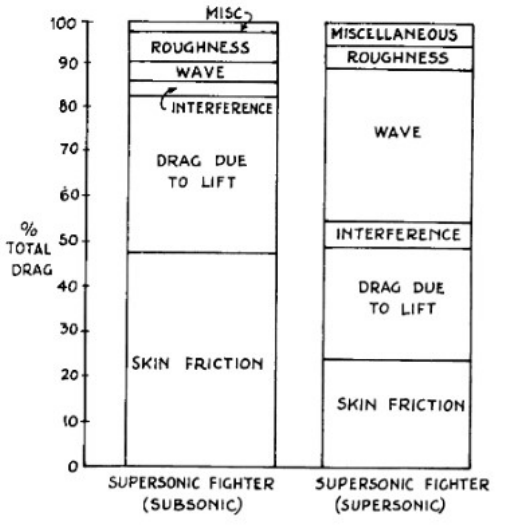

Figure 5.7: *The drag breakdown for a typical supersonic fighter.*

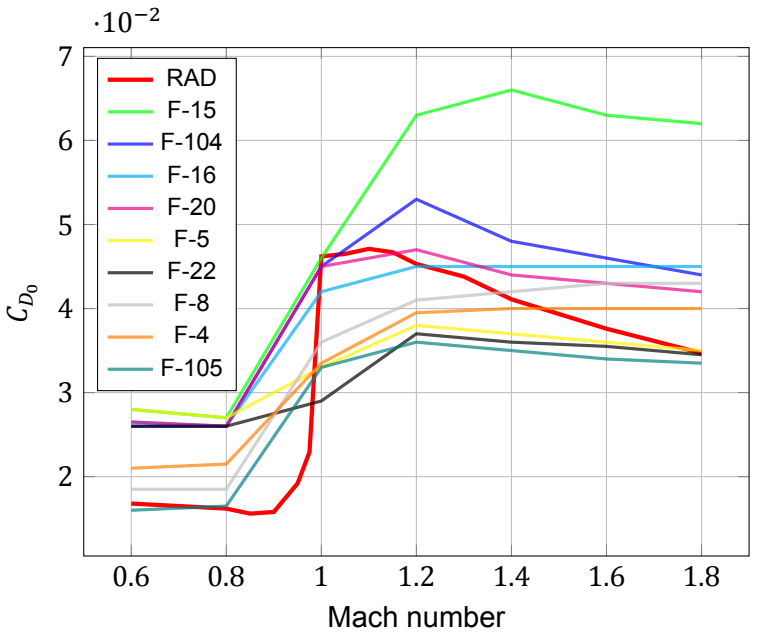

Figure 5.8: *The* C_{D_0} *of the RAD and fighter aircraft with increasing Mach number.*

To estimate the parasite and wave drag in order to get the C_{D_0}, NASA's OpenVSP software [25] was used. The software was setup to use the Hoerner method for the wing components and Hoerner streamline-body method to calculate the zero lift drag component [26]. The wave drag uses a method described in [27]. The RAD was modelled in the OpenVSP software and was analysed using the aforementioned methods. With this the C_{D_0} of the RAD was investigated, which gives the first indication of the drag performance when compared with the aircraft it's supposed to emulate. In figure 5.8 the C_{D_0} change with Mach number is shown for the RAD and a number of fighter aircraft.

In figure 5.8 it shows that the OpenVSP analysis places the RAD in the same area as the fighters it is trying to emulate when it comes to drag performance. However, the smaller fighters such as the F-5E, which are more similar in size to the RAD than the larger jets, have a better drag performance. While the subsonic C_{D_0} performance is better than most fighters, the increase in wave drag is greater when compared to the other aircraft in figure 5.8. This means that the subsonic and low transonic performance of the RAD is considerably better than its high transonic and supersonic performance.

The supersonic performance is mainly attributed to the wave drag, which in turn is heavily influenced by area ruling [19, pp. 153–159]. The OpenVSP software makes use of the area rule as a measure of the wave drag for the RAD model. The software makes cuts along the model to investigate the area and how it changes along the length [27]. This is where some consideration must be made for RAD, and the wave drag calculation method. From figure 5.8 it is clear that the high transonic drag performance, Mach 1-1.2, is worse than the supersonic drag performance, from Mach 1.2 onward. This difference in performance can be seen in the wave drag performance of the RAD in figure 5.9 and figure 5.10, which show the area ruling for Mach 1 and Mach 1.6 respectively.

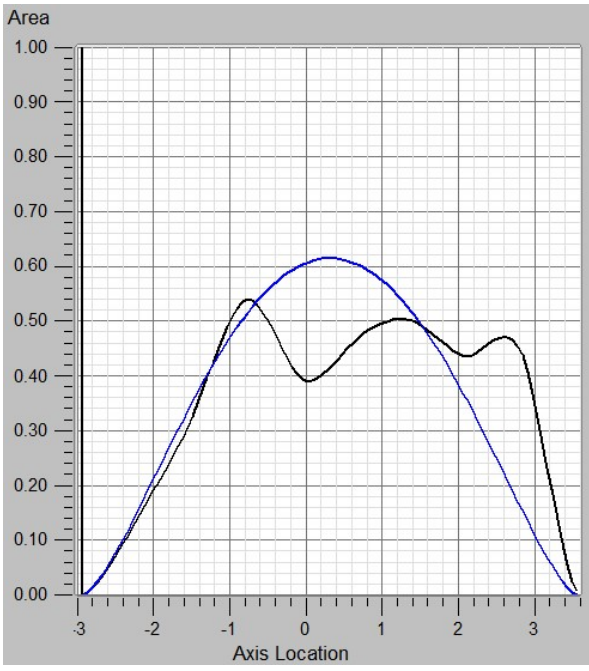

Figure 5.9: *The area ruling of the RAD at Mach 1 with Sears-Haack Body as ideal area ruling.*

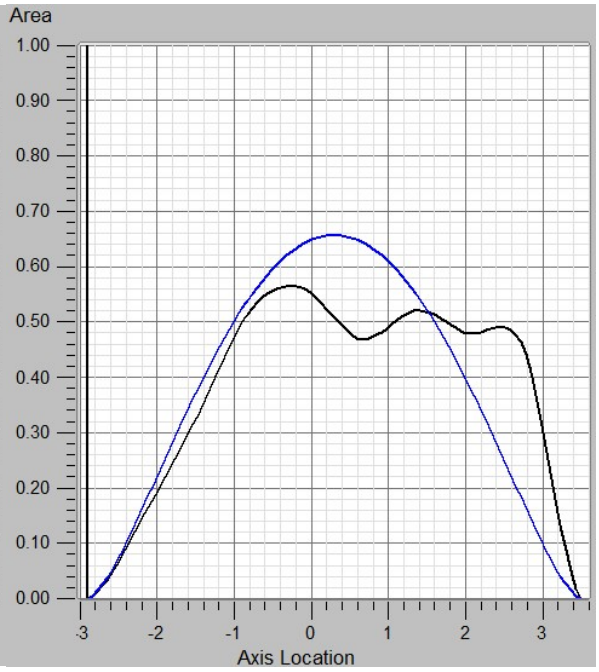

Figure 5.10: *The area ruling of the RAD at Mach 1.6 with Sears-Haack Body as ideal area ruling.*

The figures show that the area ruling for the RAD at Mach 1.6 more closely follows the ideal distribution shown by the Sears-Haack Body line. The Sears-Haack Body follows the ideal line for the relation of length and volume for the wave drag [27]. In both figures it can be observed that the nose of the RAD nicely follows the curve, however there is a dip between the end of the nose/intake and the wing. The second bump is due to the wing, which is cushioned by making the fuselage thinner at the wing. The final bump is due to the tail, which are placed far back for stability. These cause an increase in wave drag and this is more pronounced in the Mach 1 case, hence the increased wave drag at high transonic speeds and lower wave drag at supersonic speed. In order to decrease the wave drag and thus improve the overall drag performance of the RAD, it is recommended to apply more aggressive area ruling. This means making the cross-sectional area curves, seen in figures 5.9 and 5.10,

more closely follow the Sears-Haack Body curve, especially for Mach 1.

There are some considerations, however. The OpenVSP software investigates how far the line for the RAD is from the ideal curve and provides a wave drag estimate on that basis. However, the number of cuts made have a significant impact on the estimation and there is no ideal number of cuts [27]. This means that, when changing the number of cuts applied on the RAD, the wave drag estimate can change somewhat or even drastically when a large change in cuts is done. Additionally, the model in OpenVSP did not have all the systems incorporated and did not totally match the more exact CAD model of the RAD, which may change the overall accuracy of the estimation. There were attempts made to use the CAD model, however, the mesh integration was very unreliable and bad and gave very unrealistic values. Furthermore, in OpenVSP it is hard to accurately incorporate intake and exhaust areas, which is important as these do not contribute to wave drag [27]. This means that the overall wave drag estimation may be somewhat higher than the actual wave drag that the RAD will experience. In addition, the number of cuts was chosen such that the outcome was slightly more conservative to account for possible inaccuracies.

Thus, the wave drag profile of the RAD can only be seen as an estimate, although it is believed that the estimate is reasonably accurate at this stage as the variation of the values was not too great. The OpenVSP software did provide consistent result for the model made in OpenVSP and responded correctly to changes in area ruling. The overall wave drag may be slightly overestimated, but the overall values are well within reason, as seen in figure 5.8 and OpenVSP software was consistent with its estimations for the model. The recommendation is to model the RAD with all the systems incorporated and a more precise design to allow for more accurate wave drag values to be found. This will decrease the sensitivity of the number of cuts and provide more accurate values. This will help with applying area ruling more accurately, with which the RAD drag performance can increase greatly.

5.5. Lift to Drag Ratio

The overall efficiency of the RAD is measured by its L/D performance and is important for the dashing and cruising conditions. The lift of the RAD was simply calculating using the lift equation, assuming it only produced the lift for level flight, and the drag estimation was explained in the previous section. For all L/D analyses, the worst-case scenario was assumed, which means a $+30^{\circ}$ temperature delta was added to the standard atmosphere and the RAD was always assumed to be at maximum weight. With this, the L/D performance of the RAD was analysed for all important flight conditions. For the supersonic dash to Mach 1.6, figure 5.11 shows how the L/D changes with Mach number as the RAD accelerates from subsonic to supersonic at an altitude of 40,000 ft.

Figure 5.11 shows that the L/D performance of the RAD ideal at Mach 0.9 in the low transonic region. The shape of the graph makes sense as the C_L required to fly at 12192 meters altitude at speeds lower than Mach 0.8 would create a lot of lift induced drag, hence a low L/D. At transonic speeds, before the Mach drag divergence, the C_L required is small due to the speed and as such the L/D is particularly good. As the RAD enters the high transonic region, the L/D decreases again due to the addition of wave drag. In supersonic the lift only changes to a small extent while the drag increases at to a larger extent.

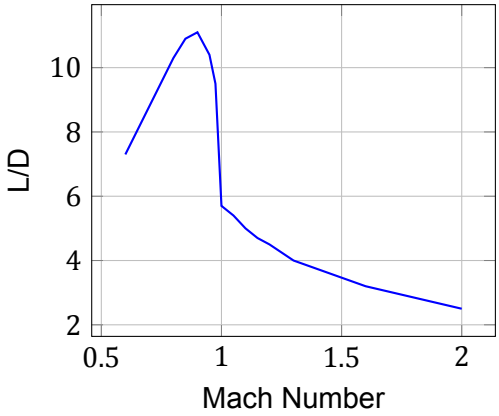

Figure 5.11: *The L/D of the RAD at 40,000 ft altitude.*

The other important flight conditions of the RAD are listed in table 5.6. Once again, the worst-case scenario is assumed with maximum weight and the $+30^{\circ}$ temperature delta.

The RAD cruises with a L/D of 10.4 which is the highest of the other flight conditions the RAD must be able to operate at. This is a good indication that the aim of designing the rad for cruise condition has succeeded. However, the values can be improved a great deal, especially for the supersonic performance, where the RAD performs particularly poorly due to the great amounts of wave drag. To conclude, the L/D is good for cruise conditions and most of the subsonic conditions but not great for the supersonic conditions. The recommendation is to improve L/D greatly for supersonic speeds by making better models for the wave drag and more focus on area ruling to decrease the wave drag.

Table 5.6: *The L/D performance of the RAD at different flight conditions.*

Flight condition	Altitude [ft]	Mach	Drag [kN]	L/D
Sea level cruise	0	0.9	3.7	5.0
Cruise	25000	0.9	2.0	10.4
High altitude cruise	45000	0.9	2.1	10.1
Low altitude supersonic dash	30000	1.6	6.0	2.2
Subsonic dash	40000	0.95	2.0	10.1
Supersonic dash	40000	1.6	6.1	3.2
Fast supersonic dash	40000	2	8.0	2.5

.

6

Propulsion and Power System Design

Propulsion system accounts for intake, engine, nozzle and fuel system which are essential for all types of propulsive aircraft. Especially for highly manoeuvrable supersonic aircraft a detailed intake design is necessary, which has been done for RAD in section 6.1. The engine has also been selected and analysed to meet the performance requirements in 6.2. To complete the propulsion system, nozzle and fuel system is designed which are documented in section 6.3 and 6.6, respectively. Finally, the power system components and layout is reported in section 6.7.1.

6.1. Intake Design

Intake is an essential part of the aircraft propulsion system. Especially for high manoeuvrable supersonic jets. Intakes need to be designed such that it provides a correct mass flow with an acceptable velocity for the engine without adding too much torsion, drag and structural weight. Furthermore, the intake should not increase the radar cross section of the aircraft drastically in order to comply with the low observably requirements.

For this project the intake is designed for Mach 1.6 at 40,000 ft altitude. The intake parameters such as intake size, type and location are therefore specifically selected for the given design point. In the following subsections the intake parameter and selection methodology are explained. The driving intake design criteria for the RAD includes maximum pressure recovery, minimum torsion, minimum RCS. The design parameters for the intake are the intake shape, location and type. They must be optimized for the intake design criteria.

6.1.1. Intake Shape

In most general terms, the intakes can be classified as either circular (or partly circular) or two-dimensional (polygon). Circular intakes are structurally advantageous resulting in a low duct weight and also minimize the wetted area per unit of flow area [19, p. 117]. However, for supersonic speeds circular intakes require installation of cone-shaped spikes in front of the inlets which adds weight and increases the required inlet size and increases the RCS. On the other hand, two-dimensional inlets do not require a cone spike but instead they require an internal ramp system for shock waves appearing at supersonic speeds. Ramps are effective for shock waves, however due to the shock interactions at the walls of the inlet, designing such a system for optimum performance is complex [19, p. 118]. Instead, a variable ramp system can be used to adjust the flow for different flight conditions. It comes with a weight penalty due to actuators, however. The intake shape can also be half-round or D-shaped which fits along the fuselage side. Both the cone-spike and ramps can be inserted for supersonic speeds. Since D-shaped intakes give a larger design space for the internal design, it will be used in RAD.

6.1.2. Intake Location

The intake can be placed at different locations of the aircraft depending on the mission and requirements. The most simple and basic placement of the inlet integrated into the nose (nose intake). The air entering the inlet will be directed to the engine with minimum torsion as the nose intake coincides with the engine fan. The downside of the nose intake is that it creates a large RCS, and it reduces the available space at the nose for housing the mission & flight systems. The second location for the intake is the top (dorsal intake) which is the best for the FOD criteria. However, at high AoA the aircraft blocks the intake, and the engine does not get enough mass flow and performance decreases. The other possible location for the inlet is the bottom of the fuselage (ventral intake), which performs the best at high AoA since the aircraft fore-body acts as an efficient flow straightener maintaining high pressure recovery and low distortion. The disadvantages of placing the intake at the bottom arise in terms of FOD and RCS as the inlet being closer to the ground. The inlet can also be placed at the sides of the fuselage (side-mounted intake) to gain space for the radar and other equipment without facing performance

reduction at high AoA. The downsides of side-mounted inlet are the performance reduction at high sideslip and fuselage boundary layer. As the aircraft sideslips, one of the inlets are blocked by the fuselage while the other one is exposed to the flow, which causes one side of the inlet to be more effective than the other. Lastly, the intake can be placed towards the leading edge of the wing root (wing-root leading edge intake) to gain space in the fuselage. However, for this type of installation, intake cross section needs to be changed rapidly which introduces high flow friction and thus reducing performance. Furthermore, the wetted area of the wing decreases at the root causing lift reduction and structural complexity [19, pp. 123–127].

By considering the design criteria and mission requirements, the fuselage mounted side intakes are selected for the RAD propulsion system. As the low RCS is a driving requirement nose and ventral intakes are eliminated. As the wing of the RAD is relatively thin, the wing-rooted inlets are eliminated due to structural limitations and size engine size. Furthermore, as dorsal intakes have low performance at high manoeuvres, it is not a feasible option for highly manoeuvrable RAD. Therefore, the side-mounted intake is selected for RAD by assuming a low sideslipping flight.

Since the RAD has one engine, the side-mounted intakes need to converge just before the entrance of the engine fan which is possible with a Y-shaped duct. Unlike, the S-duct in ventral and dorsal intakes, in Y-duct there is a pressure loss at the convergence point, which can be analysed via CFD simulation and wind tunnel test at the final design phase. For preliminary/detailed design phase, the analysis is performed assuming the internal characteristics of a typical S-duct.

6.1.3. Intake Type

At supersonic speeds an intense shock wave forms just ahead of the intake lips, decelerating the flow speed. If the deceleration process is done via single a normal shock wave, the stagnation pressure by means of pressure recovery reduces enormously. Using multiple weaker shocks, the pressure loss can be reduced. In order to create weaker shocks in the intake there has to be an inclined surface against the flow, which are created either with cone-spikes or compression ramps. These weaker shocks can be created before the entrance of the inlet (external compression), inside the inlet (internal compression) or both (mixed compression). Internal and mixed compression is more desirable for speeds larger than Mach 2.5 as the pressure recovery of external compression decreases drastically at higher Mach numbers.
For the flow speeds smaller than Mach 2, the difference in pressure recovery for the different compression types is small. Furthermore, internal and mixed compression introduces shock reflections and interactions inside the inlet, which brings uncertainty to the flow. Therefore, simpler and a more reliable external compression intake is used in the RAD since the speed requirement for the RAD is below Mach 2. The external compression is possible with a ramp-wedge system which is composed of one or multiple wedges just before the intake. Ideally, an isotropic curved ramp gives the best pressure recovery creating infinitely many weak shock waves however, it also creates cowl-lip drag and shock/boundary layer interactions. Because of the relatively low supersonic performance requirements of the RAD, a ramp with constant gradient is selected for the intake [19, pp. 128–133].

Furthermore, a diverterless intake design is selected to lower the RCS of the aircraft. A diverter (splitter) plate may be an option to remove the undesired boundary layer forming on the fuselage, however this option is eliminated since it increases RCS more than it increases engine performance and it increases boundary layer bleed drag.

6.1.4. Supersonic Diffuser

Supersonic inlets have two parts; the supersonic diffuser is the part where the supersonic airflow compresses the flow to subsonic speeds by using a shock wave system. The subsonic diffuser is the part where the flow compresses isentropically in a fully subsonic regime. The supersonic diffuser of the RAD is designed such that it contains an external compression ramp which first forms an oblique shock wave and then a normal shock wave at the peak of the ramp. A simulation that can calculate the state variables after two shock waves is made. For the oblique shock wave the simulation first require θ and β as geometrical inputs, plus atmospheric state variables and the flight speed in terms of Mach number. The simulation uses equations (6.1), (6.2), (6.3), (6.4), and (6.5), taken from NASA [1]. For all the equations given in this subsection, subscript '1' refers to air flowing upstream (before the oblique shock wave) and subscript '2' refers to air flowing downstream (after the oblique shock wave

[1]Source: https://www.grc.nasa.gov/www/k-12/airplane/oblique.html (retrieved on 14 June 2022)

of the oblique shock wave. The subscript 't' refers to the stagnation (total) state variables and γ (specific heat ratio of the air) is a dimensionless constant with a value of 1.4.

$$\tan\theta = 2\cot\beta\frac{M_1^2\sin^2(\beta)-1}{M_1^2(\gamma+\cos 2\beta)+2} \quad (6.1) \qquad M_1^2\sin^2(\theta-\beta) = \frac{M_1^2\sin^2(\theta)+5}{7M_1^2\sin^2(\theta)-1} \quad (6.2)$$

$$\frac{T_2}{T_1} = \frac{(7M_1^2\sin^2(\theta)-1)(M_1^2\sin^2(\theta)+5)}{36M_1^2\sin^2(\theta)} \quad (6.3) \qquad \frac{p_2}{p_1} = \frac{7M_1^2\sin^2(\theta)-1}{6} \quad (6.4)$$

$$\frac{p_{t_2}}{p_{t_1}} = \left[\frac{6M_1^2\sin^2(\theta)}{M_1^2\sin^2(\theta)+5}\right]^{\frac{7}{2}}\left[\frac{6}{7M_1^2\sin^2(\theta)-1}\right]^{\frac{5}{2}} \quad (6.5)$$

After passing the OSW, the Mach number decreases but the flow still stays as supersonic and as the duct converges, the flow compresses more forming a normal shock wave at the throat. The air passes through the NSW and becomes subsonic. The simulation then calculates the state variables after the NSW using the previously outputted state variables and normal shock wave equations (6.6), (6.7), (6.8), (6.9), and (6.10) [2].

$$M_2^2 = \frac{(\gamma-1)M_1^2+2}{2\gamma M_1^2-(\gamma-1)} \quad (6.6) \qquad \frac{p_2}{p_1} = \frac{2\gamma M_1^2-(\gamma-1)}{\gamma+1} \quad (6.7)$$

$$\frac{p_{t_2}}{p_{t_1}} = \left[\frac{(\gamma+1)M_1^2}{(\gamma-1)M_1^2+2}\right]^{\frac{\gamma}{\gamma-1}}\left[\frac{(\gamma+1)}{2\gamma M_1^2-(\gamma-1)}\right]^{\frac{1}{\gamma-1}} \quad (6.8)$$

$$\frac{\rho_2}{\rho_1} = \frac{(\gamma+1)M_1^2}{(\gamma-1)M_1^2+2} \quad (6.9) \qquad \frac{T_2}{T_1} = \frac{[2\gamma M_1^2-(\gamma-1)][(\gamma-1)M_1^2+2]}{(\gamma+1)^2M_1^2} \quad (6.10)$$

6.1.5. Subsonic Diffuser

As the flow becomes subsonic after it passes the normal shock wave at the throat of the intake, the airflow is guided to the engine fan via a subsonic diffuser. In the subsonic diffuser, the flow is assumed to be isentropic, meaning the friction and heat transfer is neglected. Using the isentropic relations shown in euqations (6.13), (6.11), and (6.12) [3], the state variables at the entrance of the engine fan are calculated. The subscript '*' is used for the throat, and the subscript 'e' is used for the end of the diffuser. Since Y-duct configuration have two symmetric entries, the throat area used in the simulation refers to the total throat area. Geometrical (actual) throat area is assumed to be the half of the total throat. Thus, the pressure loss at the convergence of the two ducts are neglected for that matter. As the pre-compressed flow leaves the subsonic diffuser, it enters the engine fan, where the potential energy in the form of pressure is inverted into kinetic energy to propel the aircraft.

$$\frac{p_e}{p_{e_t}} = \left(1+\frac{\gamma-1}{2}M_e^2\right)^{-\frac{\gamma}{\gamma-1}} \quad (6.11) \qquad \frac{T_e}{T_{e_t}} = \left(1+\frac{\gamma-1}{2}M_e^2\right)^{-1} \quad (6.12)$$

6.1.6. Intake Size

A geometrical simulation outputting the supersonic diffuser length, subsonic diffuser length, interior cowl length and their relative distances to the centre line is made. It uses the throat area of the diffuser, the fan area of the engine and four angles: θ (ramp angle), β (OSW angle), ϵ (frontal coverage angle) and μ (focus angle) as inputs. By iterating the input variables, a suitable size for the inlet is found which is demonstrated in table 6.1. Figure 6.1 and 6.1 show the top and the front view of the inlet geometry with the defined parameter.

[2]Source: https://www.grc.nasa.gov/www/k-12/airplane/normal.html (retrieved on 14 June 2022)
[3]Source: https://www.grc.nasa.gov/www/k-12/airplane/isentrop.html (retrieved on 14 June 2022)

$$\frac{A}{A^*} = \left(\frac{\gamma+1}{2}\right)^{-\frac{\gamma+1}{2(\gamma-1)}} \frac{\left(1+\frac{\gamma-1}{2}M_e^2\right)^{\frac{\gamma+1}{2(\gamma-1)}}}{M_e} \tag{6.13}$$

Parameter	Value
Supersonic diffuser	27 cm
Subsonic diffuser	62 cm
cowl	21 cm
Outer radius	40 cm
Inner radius	36 cm
μ	8.9°
θ	13°
β	58°
ϵ	140°

Table 6.1: *Final Intake parameters.*

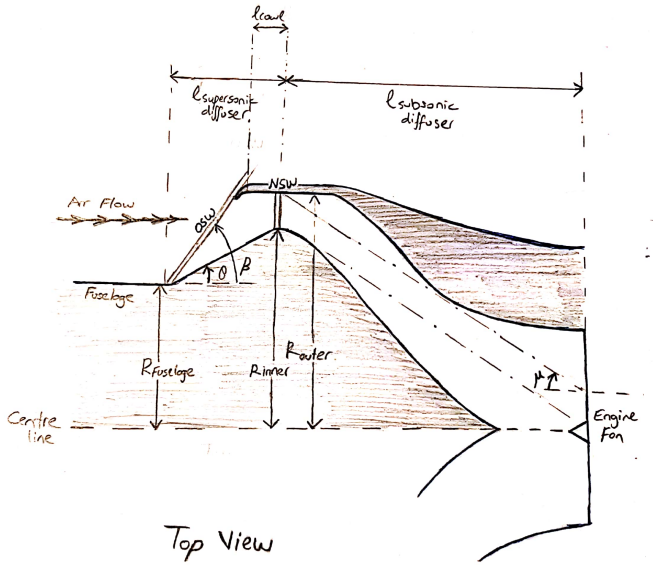

Figure 6.1: *Inlet geometry from the top view.*

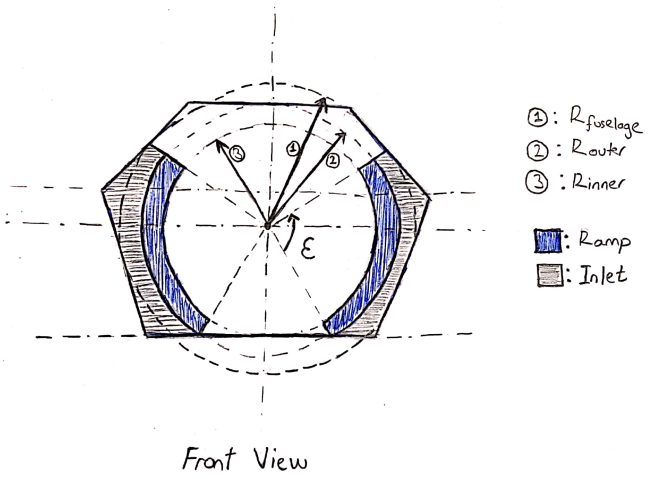

Figure 6.2: *Inlet geometry from the front view.*

6.1.7. Recommendations

The cowl lip shape is also an important intake geometry parameter and needs to be designed such that the pressure recovery compensates and ideally exceeds the performance loss due to drag. In low subsonic flight regimes, a blunt cowl lip is preferred as it avoids the boundary layer separations, however at supersonic regimes blunted lip creates cowl shock and boundary layer separation due to spillage. In contrast, at subsonic speeds, a sharp cowl lip causes flow separation at high AoA which may cause distortion in the engine. Since RAD must fly both in subsonic and supersonic regime, the cowl lip bluntness is not optimally designed due to lack of resources. In the further design phase, a better design can be made using more complex analysis and advanced tools. Alternatively, using a variable radius inlet, optimum performance at all flight conditions can be achieved with weight and cost penalties. Furthermore, the previously iterated cowl length is increased to lower the observability of the engine. Because of this modification, the OSW forming on the supersonic diffuser ramps is reflected into the inlet, which essentially result in internal compression. Effects caused by internal compression can be analysed in depth at further design stage, resulting in a compromise between low observably and performance.

6.2. Engine Selection

After the flow has passed from the intake, it comes to the engine. For the engine selection, the engines in the midterm report were considered [2]. Considering the thrust ranges needed to comply with the requirements, several engines were discarded. Furthermore, a Japanese engine was added to the list due to its availability and thrust range. These engines and their specifications can be seen in table 6.2. From the drag estimations

from chapter 5, each engine in table 6.2 is able to provide enough thrust for subsonic flight conditions while being available for purchase. On top of this, all the indicated engines have desirable proportions and specific fuel consumptions. However, a more detailed size analysis is conducted before selecting the engine.

Table 6.2: *The engine options for the RAD [28].*

Manufacturer	Model	Thrust (dry) [kN]	SFC (g/kNs)	m [kg]	d_{inlet} [m]	Length [m]
Rolls Royce	F405 Adour	29	20.9	603	0.56	1.95
Williams	FJ44-4	16	13.02	295	0.64	1.74
General Electric	J85	12.7	27.00	181.4	0.46	1.1
IHI Corporation	F3	16.4	19.38	340	0.56	2

All the engines are analysed and their advantages and disadvantages has been laid out:

F405 Adour: Out of all the engines in the table, Rolls Royce's F405 Adour is the one that gives the highest thrust. This engine was left in the selection procedure in case a higher thrust than expected would have been necessary for high Mach number, high altitude flight conditions after several iterations. Following from its high thrust range, its mass is also the highest out of the indicated engines having double the mass of the engine with second highest mass. Thus, this engine should not be selected if more thrust is absolutely necessary as this much mass increase will cause drastic effects on the drag. On the other hand, F405 Adour has low specific fuel consumption compared to its competitors. This leads to more thrust with higher fuel efficiency. Another important parameter is the maximum diameter. The maximum diameter determines the shape and size of the fuselage. This in turn directly affects the drag of the aircraft. A shorter maximum diameter is preferable for this reason. The inlet diameter of the engine is also an essential consideration. The inlet diameter is directly coupled to the subsonic diffuser inside the intake as it corresponds to the exit area of the subsonic diffuser. This diameter is one of the parameters needed for calculating the velocity entering the engine itself which in turn is a significant parameter for estimating the thrust available. However, it is not possible to determine whether an inlet diameter for the engine has good proportions due to its dependency on the intake design. In the case of F405 Adour which has a relatively small inlet diameter, considering a fixed intake throat area, the velocity of the flow entering the engine fan is relatively high. A high speed is not preferable as it limits the maximum amount of velocity increase possible for the engine decreasing maximum thrust.

FJ44-4: The Williams International's FJ44-4 has a medium thrust compared to other engines in table 6.2. However, it is seen that with just 16 kN of thrust it is not possible to reach supersonic speeds in high altitudes, as discussed in chapter 5. Thus, this engine could be selected with an afterburner. This afterburner would increase the thrust, however, would increase the mass, specific fuel consumption and length. Also, an afterburner would increase the complexity of the exit nozzle as it would have to be a variable geometry nozzle to try decrease or increase the static pressure to match the outside pressure for maximum thrust efficiency. Furthermore, FJ44-4 has a low mass, half the mass estimated in the midterm report [2]. Hence, considering the snowball effect on the aircraft mass, this will decrease the drag increasing the acceleration of the aircraft to desired speeds. Also, FJ44-4 has a relatively big inlet and maximum diameters. This translates into a lower velocity entering engine fan but a longer fuselage diameter and higher total drag. This is due to the engines relatively high bypass ratio of 5:1. The thrust of the bypass would become negligible compared to the thrust provided by the added afterburner and hence would become inefficient due to the added drag from its size. Finally, FJ44-4 has medium to short length which is desirable as it decreases the length of the fuselage making the aircraft more stable in the directional axis.

J85-GE-13: General Electric's J85 has the lowest thrust out of the indicated engines. However, also has the lowest mass. It could be that the significantly decreased mass of the total aircraft decreases the thrust required so much that the thrust available from the J85 is enough to push the aircraft to desired speeds. However, it has a high specific fuel consumption which means more fuel may be needed. J85 also has the shortest length of all indicated engines which is desirable for stability reasons.

F3: IHI Corporation's F3 has medium thrust compared to the engines in table 6.2. In terms of specifications, it is comparable to the FJ44-4. However, as a difference, F3 has a low bypass ratio of 0.9 lowering the inlet diameter

and indirectly the maximum diameter. The low inlet diameter means a relatively high velocity is entering the engine fan, although the maximum diameter is low and hence the fuselage diameter and with it the drag estimations go down meaning that the increased velocity in the engine can be compensated with a smaller fuselage diameter in terms of required thrust. Also, the mass and specific fuel consumption of the F3 are on the lower side which is desirable. Nonetheless, like the FJ44-4, an afterburner needs to be implemented with the engine for achieving the supersonic dash manoeuvres. The F3 has a conceptual variant XF3-400 which is a supersonic capability demonstrator with an afterburner. Thus, it is known that the F3 is capable of housing an afterburner. The XF3-400 is capable of a wet thrust of 29.5 kN at sea level while increasing the total mass of the engine to 501 kg and the specific fuel consumption while using the afterburner to 60.9 kg/kN/s. Furthermore, the already high length will reach a length of 2.73 m. This means a longer and a more unstable fuselage which has an effect on the empennage sizing.

Now that the advantages and disadvantages of each engine have been discussed, an analysis can be conducted using the drag estimations.of the aircraft which gives the thrust required at two key requirement fight conditions. These conditions include the cruise which is Mach 0.9 at 25,000 ft and the supersonic dash manoeuvre with a Mach of 1.6 at 40,000 ft. Two design points are considered due to the possible use of an afterburner for the supersonic dash changing the engine configuration drastically. However, the thrust values for the engines only give the static sea level conditions and hence are not accurate at the on-design conditions. So, a model is needed to observe the variations of thrust with altitude and Mach number. For the purpose of the engine selection this was done using a plot for a generic military turbofan [29]. This graph can be seen in figure 6.9. The thrust variation is given as a ratio of the thrust at various altitudes and Mach numbers versus the thrust at static sea level conditions. The thrust at a specific condition can be found by multiplying this ratio with the thrust at static sea level condition. However, this plot only gave limited altitudes, one being above the ceiling of the RAD. Thus, a regression analysis was performed on the plot. For each Mach number, 3 altitudes and corresponding thrust ratios are taken to plot these points. A parabolic curve can be fitted through these points to get a rough estimate of thrust variation with altitude at a certain Mach number. With this method it was possible to get the thrust of each engine at the design point conditions with or without an afterburner.

The thrust ratio at the cruise condition is 0.47 and at the supersonic dash manoeuvre is 0.41. In chapter 5 the drag at these design points can be seen. For the cruise condition the drag is estimated to be 2000 N, for supersonic dash manoeuvre drag is estimated to be 7,000 N and the start of the dash manoeuvre which is at Mach 0.9 and 25,000 ft with a 4g manoeuvre produces a drag of 10,000 N.

The F405 Adour has a thrust of 29 kN at static sea level condition which proves to be enough for all the design conditions. However, during cruise, which is the most time spent during the flight, F405 Adour provides excessive amount of thrust which proves unnecessary considering the added mass of the engine itself.

The FJ44-4 has a thrust of 16 kN at static sea level condition which proves enough for subsonic conditions however, during the dash manoeuvres the dry thrust is not enough and hence, requires an afterburner. With an afterburner the FJ44-4 is estimated to produce enough thrust for all the flight conditions. Nevertheless, the high bypass ratio of the engine deems to be an unnecessary source of drag after the addition of an afterburner.

The J85 provides enough thrust for the subsonic phases of the flight conditions. However, during the transition to the supersonic speeds it also requires an afterburner. However, even with the afterburner the acceleration in the dash manoeuvres will be low and hence, slow. Also, the J85 already has a high specific fuel consumption and with the added afterburner the fuel consumption will be too much decreasing efficiency drastically. Finally, J85's small inlet diameter could prove unfeasible with the intake design during supersonic speeds.

The F3 has a thrust of 16.4 kN at static sea level condition and its performance is comparable to the FJ44-4. It

will also require an afterburner, however as the XF3-400 concept exists the specifications are known. It is known that with afterburner the wet thrust will be 29 kN which is enough for the supersonic phase. Also has low bypass ratio and a relatively good specific fuel consumption.

Comparing all the indicated engines together, F405 Adour and J85 are directly eliminated as they show the upper and lower boundary conditions respectively. FJ44-4 and F3 have comparable specifications, however F3 has a low bypass ratio which is desirable when using an afterburner and hence, F3 with an afterburner (XF3-400) is selected for the iterations. The F3 can be seen in figure 6.3 [4].

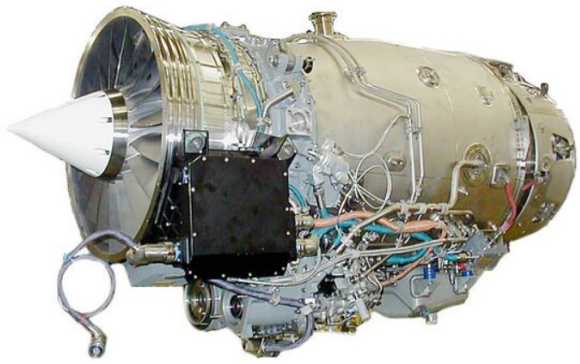

Figure 6.3: *A picture of the F3 engine.*

6.3. Nozzle Design

The flow will be accelerated to high speeds and temperatures inside the F3 engine and afterburner to reach the nozzle. As the F3 engine has an afterburner, the exhaust pipe must be bigger to accommodate higher jet velocities and hence, the nozzle geometry has to be variable to increase or decrease the static pressure to match the ambient pressure. The static pressure has to match the ambient pressure as this is the most optimal case considering the thrust equation (6.14). This is due to the exhaust velocity being maximum when exit pressure matches ambient pressure and the mass flow having a much higher value than the exit area.

$$F_N = \dot{m} * (V_e - V_0) + A_e * (P_e - P_0) \tag{6.14}$$

There is also a very essential relation between the throat area, exit area and the exit Mach number. The ratio of the exit area to the throat area of the nozzle determines the exit Mach number. Thus, it is possible to manipulate the flow by changing the throat and exit areas. A drawing of the afterburner and nozzle can be seen in figure 6.4. The bypass air has several usage in the nozzle. First of all, some of the bypass air mixes with fuel and the hot exhaust from the turbine to decrease the temperature a little so that the temperature difference after the afterburner can be maximised. The other part of the bypass air enters the little channels around the exhaust pipe to cool the temperatures of the walls of the pipe. After the afterburner the temperatures increase up to 1700 - 1800 K and the cooling flows are necessary to help keep the structural integrity of the pipe walls. Finally, when the bypass flow comes to the exit it is mixed with the exhaust flow to help get the pressure close to the ambient pressure. This is possible as the bypass flow has been relatively untouched (just increased pressure from the fan) and decreases the temperature to help match the ambient conditions as well as decreasing infrared signature [19]. However, this process is optimal when the pressure of the exhaust is overexpanded and will decrease the thrust when the flow is at optimal properties.

The flow after the afterburner has a subsonic speed. To achieve supersonic exit velocities, a convergent divergent nozzle is designed. If the flow has completed its expansion to the ambient pressure at the throat, the exit

[4]Source: https://customer-janes-com.tudelft.idm.oclc.org/Janes/Display/JAE_0107-JAE_ (retrieved on 15 June 2022)
[4]Source: https://engineering.purdue.edu/~propulsi/propulsion/index.html (retrieved on 15 June 2022)

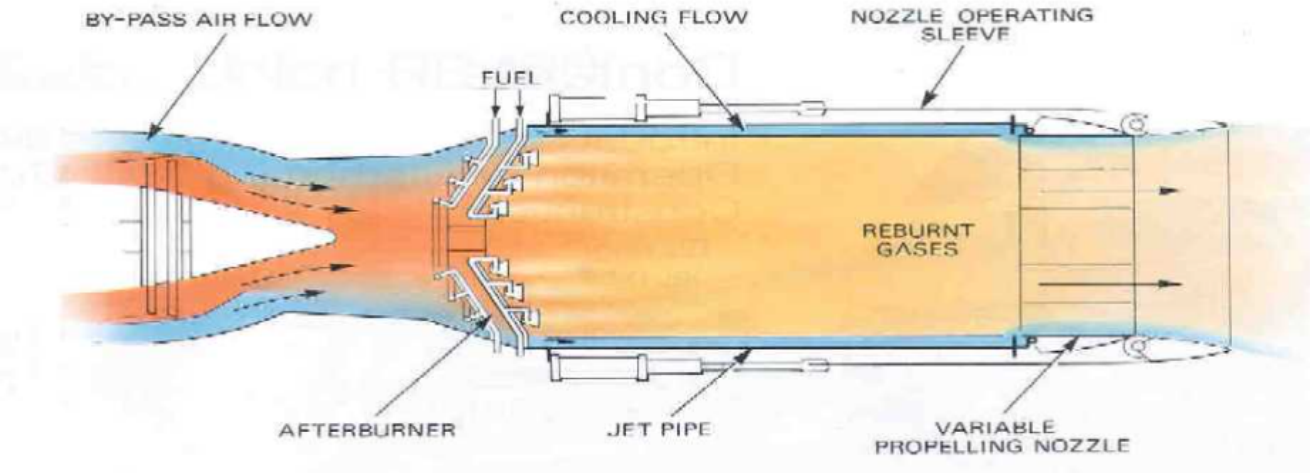

Figure 6.4: *Drawing of a generic nozzle with an afterburner*[4]

area will be the same as the throat area to prevent any changes to the flow as it is at its optimal in terms of thrust. Usually this is not the case during supersonic speeds as the exhaust velocities required for the supersonic speeds are very high and require a convergent divergent nozzle to achieve accelerate the flow to speeds necessary to create sufficient thrust during supersonic conditions. Also, for the RAD supersonic speeds will be achieved via the afterburner and hence, the flow after the afterburner will have very high temperatures and pressures which will need to match the ambient. Considering the total pressure as the sum of dynamic and the static pressure, as the velocity increases the static pressure assuming the total pressure stays constant throughout the nozzle. This assumption can be made as we assume the flow completely expands to the ambient pressure at the exit and there are no shock waves forming inside the nozzle, making the processes inside the nozzle isentropic. This means that the total pressure will mostly stay constant. Thus, a variable geometry nozzle is also essential for altering the flow properties to match the ambient and achieve the optimal condition. For subsonic flight conditions, usually just a convergent duct is enough to achieve the necessary thrust. Thus, it is more probable to get the throat area same as the exit area, as the flow is already expanded to ambient at the throat.

The details on the actuators manipulating the throat area and exit area will not be discussed in this report. It is assumed that the flight computer and the actuators can provide with the computed throat and exit areas. Another important consideration is the maximum exit area to throat area ratio. As this ratio increases, the exit area increases as well. However, the increased exit area creates drag and if it is not limited would increase thrust required more than thrust available. Hence, a limit must be set. This limit is set at 1.7 as it is usually taken as the norm [19]. This will be the area ratio at maximum afterburner thrust.

6.4. Propulsion System Model

Now that all the components of the propulsion system have been established, a dedicated model can be made to get a thrust estimation at any point during the flight. This model is done by following the flow from the inlet entrance to the nozzle exit and model its behaviour throughout.

6.4.1. Model Assumptions

For the model, several assumptions are made to simplify the process. Later on, several assumptions will be explored to validate the results. These assumptions include:

- The gas is considered an ideal gas throughout the propulsion system.
- International Standard Atmosphere conditions were used for calculating atmospheric conditions.
- Inside the engine every process is adiabatic and except for the combustion chamber is also isentropic.
- The specific heat of the air and the specific heat of the gas after combustion are constant. Also the ratio of the specific heats are constant before and after the combustion chamber. $c_{p_a} = 1005$ J/(kg * K), $c_{p_g} = 1150$ J/(kg * K), $\gamma_a = 1.4$, $\gamma_g = 1.33$ where subscript a refers to air before combustion and subscript g refers to gas after the combustion the air-fuel mixture.
- The mass flow is constant until the combustion chamber which includes only air, the mass flow is also

constant after the combustion chamber until the afterburner which is the mixture of air and fuel and finally the mass flow is constant until the nozzle exit which is the mixture of air from the engine, bypass air, fuel and afterburner fuel.

- The efficiencies and pressure ratios are assumed as in table 6.3. These were determined using trial and error such that the engine model matched the static sea level thrust of the F3 engine. Only the pressure ratio of the compressor and the fan are used from the engine data [5].
- The fan is connected to the low pressure turbine while the fan is connected to the high pressure turbine as F3 is a twin-spool engine.
- Due to the complex flow relations in the intake, the supersonic diffuser and subsonic diffuser is assumed to decelerate the flow to a constant Mach value however, different velocities because of temperature differences.

Property	Value	Unit
η_{fan}	0.90	-
$\eta_{compressor}$	0.86	-
η_{cc}	0.97	-
η_{FT}	0.90	-
η_{CT}	0.90	-
$\eta_{mechanical}$	0.97	-
η_{nozzle}	0.90	-
$\eta_{afterburner}$	0.90	-
LHV	$42.8{\cdot}10^{-6}$	J/kg
T04	1535	K
T07	1950	K
P_{fan}	2.7	-
$P_{compressor}$	14	-
P_{cc}	0.96	-
$P_{afterburner}$	0.97	-

Table 6.3: *The constants assumed for the propulsion system model.*

Throughout the model, a reference inlet diameter (A_i) of 0.14 m^2 is used. This value was calculated using this iterating this engine model with a separate low observability and aerodynamics analysis at each iteration to find the optimal inlet area. The model is divided into two: the subsonic phase and the supersonic phase, which includes the afterburner.

For the subsonic and supersonic phase several equations were used: For compressible flows, equations (6.12) and (6.11) give the relation between the total properties with respect to velocity, Mach and static properties. These relations are used when switching from total properties or vice versa is required, which are the case for intake and exhaust calculations. During the intake the static properties of the flows are translated into total properties for the engine analysis and during the exhaust nozzle the total properties are switched back to static properties for the further analysis of the flow with respect to the ambient properties.

The mass flow is always calculated at the entrance of the intake and, as mentioned before, assumed constant until fuel is added. At the intake the mass flow is calculated using equation (6.15). The intake area is fixed, and the density depend on the atmospheric conditions. Equation (6.16) is used to compute the necessary amount of fuel to increase the temperature of the fuel to the combustion chamber temperature.

$$\dot{m} = \rho * V * A_i \tag{6.15}$$

$$\dot{m}_f = \frac{\dot{m}_{hot} * c_{p_g} * (T_{0,4} - T_{0,3})}{LHV * \eta_{cc}} \tag{6.16}$$

For the nozzle flows, it is essential to know the Mach number relation with the area ratio. This happens in the exhaust nozzle, where a sonic throat is created using variable geometry and the proper exit area is calculated using the necessary Mach number needed at the exit for optimal thrust. For this, equation (6.17) is used, and the supersonic solution is taken in this case. If this exit area is too big, specifically greater than 1.7 times the throat area, then 1.7 is used as the ratio and the corresponding Mach number is calculated which then leads to the static pressure at the exit which creates a pressure differential between the ambient pressure. For the subsonic inlet equation (6.17) is used and the subsonic solution is taken as for the intake the divergent part acts as a subsonic diffuser and has its throat area equal to the exit are of the supersonic diffuser throat area. For supersonic conditions, the supersonic diffuser is assumed to decelerate the flow to below Mach 1.
For calculating temperature and pressure changes across the compressor and turbine, equation (6.18) and equation (6.19) are used, respectively. The pressure ratio of the compressor is taken from the engine manufacturer and is kept as a constant throughout the iterations.

[5] Source: https://customer-janes-com.tudelft.idm.oclc.org/Janes/Display/JAE_0107-JAE_ (retrieved on 15 June 2022)

$$(\frac{A_e}{A_t})^2 = \frac{1}{M^2} * [\frac{2}{\gamma+1} * (1 + \frac{\gamma-1}{2} * M^2)]^{\frac{\gamma+1}{\gamma-1}} \quad (6.17) \qquad T_{0,1} = T_{0,0} * [\frac{1}{\eta_{\text{compressor}}} * (\Pi_{\text{compressor}}^{\frac{\gamma-1}{\gamma}} - 1)] \quad (6.18)$$

For the nozzle calculations, also the throat area needs to be calculated. This is done by the means of equation (6.20) assuming the flow is sonic at the throat. This is equation is used in the exhaust nozzle calculations to get the throat area for further calculations of the exit area.

$$P_{0,1} = P_{0,0} * [1 - \frac{1}{\eta_{turbine}} * (1 - (\frac{T_{0,1}}{T_{0,0}})^{\frac{\gamma}{\gamma-1}})] \quad (6.19) \qquad A_t = \frac{\dot{m} * R * T_t}{\rho_t * V_t} \quad (6.20)$$

The temperature change in the turbine is a very significant parameter to understand the efficiency of the engine. As the fan is connected to the low-pressure turbine and the compressor to the high pressure turbine, two different calculations have to be performed. The temperature difference is dependent on the work done by the compressor or the fan and the efficiency of the mechanical efficiency of the shaft. Equation (6.21) shows one of the possible calculations necessary to find the temperature change through the turbine. This temperature difference will be directly connected to the thrust available from the engine as maximum temperature increase is desired, the lower the temperature decrease in the turbine the better for the thrust. Also, the turbines drive the fan and compressor and hence, the temperature change across the turbines should not be too small as well. The temperature change should be optimised for maximum efficiency.

$$T_{0,4} - T_{0,45} = \frac{\dot{m}_{air} * c_{p_a} * (T_{025} - T_{02})}{\eta_{mech} * (\dot{m}_{hot} + \dot{m}_{fuel}) * c_{p_g}} \quad (6.21) \qquad \Pi_{critical} = \frac{1}{(1 - \frac{1}{\eta_{nozzle}} * \frac{\gamma_g - 1}{\gamma_g + 1})^{\frac{\gamma_g}{\gamma_g - 1}}} \quad (6.22)$$

The critical pressure ratio is the ratio used to determine whether the core is chocked or unchoked. This determines the exit area as well as the thrust. The nozzle is unchoked when the flow is fully expanded at the throat. Usually this is not the case, as the actual pressure ratio is generally greater than the critical pressure ratio. However, the exit area is variable and, hence, can be manipulated to achieve the critical pressure ratio. If this is possible without increasing the exit to throat area ratio beyond 1.7, then it is possible to get complete expansion. Nevertheless, during high Mach number high altitude flight conditions, this is usually not possible, and a pressure differential is created. Equation (6.22) is used to compute this critical pressure ratio.

Now that the equations for the model are known, the logical flow of the model can be elaborated. The model first checks whether the incoming flow to the intake is supersonic or not. This is essential as firstly, the supersonic diffuser in the intake creates shock waves according to the incoming Mach number to slow the flow down to subsonic speeds leaving the intake throat. This is due to the assumption that the subsonic diffuser can decelerate the flow down to a certain Mach number. Secondly, when the supersonic phase of the flight is initiated, the afterburner is also turned on. The use of an afterburner drastically changes the flow properties after the turbine. The dynamic pressure and the total temperature increase immensely. This results in the flow being accelerated to high exit velocities.

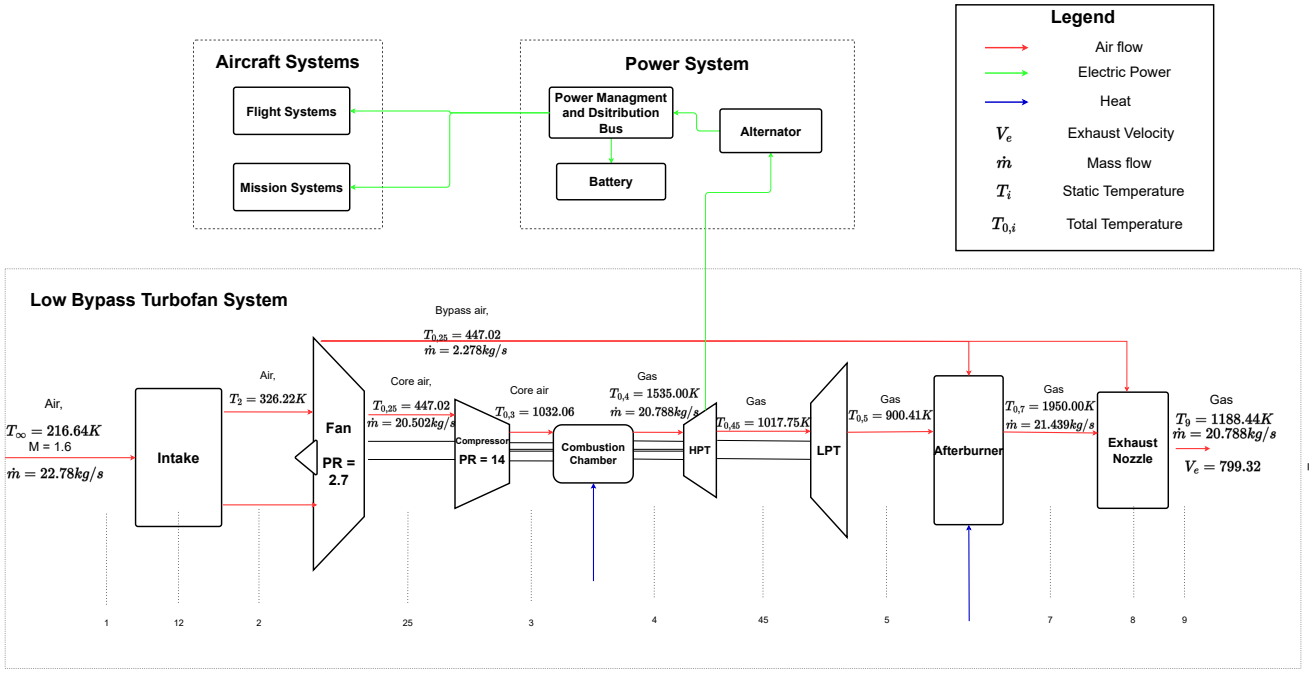

Figure 6.5: *The layout of the propulsion system for Mach 1.6 at 40000 feet.*

In the propulsion system layout in figure 6.5 the connections between different stations are shown.

- **Station 1:** This station indicates the entrance of the intake. More specifically, this station is the entrance of the supersonic diffuser. The working of the supersonic diffuser is outlined in subsection 6.1.4. At this station, the flow properties are equal to the atmospheric conditions and ambient conditions are transformed into total properties by adding the effect of the velocity
- **Station 12:** This station indicates the exit of the supersonic diffuser and the start of the subsonic diffuser. This station is considered to be the throat of the intake and the flow coming to this station is assumed to be subsonic even when the aircraft has supersonic speeds due to the shock interactions at the supersonic diffuser. The area ratio of the throat with the engine inlet diameter determines the Mach number entering the engine fan, while the isentropic relations determine the velocity. Isentropic relations are used when there are no shock waves forming in the intake. At this station, the static pressure is increased significantly due to the shock waves.
- **Station 2:** This station indicates the exit of the intake and the entrance of the engine fan. At this point, the subsonic diffuser has decelerated the flow while increasing both static temperature and pressure. The goal of the intake was to decelerate the flow without changing the total properties. However, this is not the case in reality, and hence the total properties drift slightly from the station 1 values. At the fan, the air is compressed slightly at a ratio of 2.7
- **Station 25:** This station indicates the fan exit and the entrance of the compressor. The compressed air from the fan enters the compressor to get even more compressed at a ratio of 14. After the compressor, the flow has very high temperature and pressure.
- **Station 3:** This station indicates the exit of the compressor and the entrance of the combustion chamber. The preferable flow properties here are high total pressure and low temperature. As the combustion chamber increases the temperature, a high temperature difference gives more energy to the flow. High pressure and temperature are needed for work output to the turbines. Here, it is assumed that fuel is added such that the combustion temperature stays constant throughout the flight.
- **Station 4:** This station indicates the exit of the combustion chamber and the entrance of the high pressure turbine. The high-pressure turbine is connected to the compressor by a shaft. High temperatures are needed as the turbines will collect some temperature to use it as work to drive the compressor and have enough temperature at the exhaust nozzle to create sufficient thrust. At the combustion chamber the fuel is added using equation (6.16).
- **Station 45:** This station indicates the exit of the high pressure turbine (HPT) and the entrance of the low pressure turbine (LPT). The temperature is decreased significantly and will decrease even more in the low-pressure turbine, which will use the work to drive the fan.

- **Station 5:** This station indicates the exit of the LPT and the entrance of the afterburner. The afterburner is used only in supersonic dash manoeuvre. For the conditions shown in figure 6.5 the afterburner is on. Some bypass air here mixes with the exhaust from the turbine and afterburner fuel to increase the flow temperature to high temperatures.
- **Station 7:** This station indicates the exit of the afterburner and the entrance of the exhaust nozzle. At this point the temperature of the flow is at its maximum. The cool flow at the walls of the exhaust pipe decreases the temperature slightly. This is neglected for this study. Also the mass fuel of the afterburner is calculated here using equation (6.16). It should be noted that the usage of afterburner increases the specific fuel consumption significantly and hence uses more fuel than the regular combustion.
- **Station 8 and 9:** These stations indicate the entrance and the exit of the exhaust nozzle respectively. At these stations, the goal is to maximize the exhaust velocity. This happens when the ambient pressure matches the exit pressure. Here, first the Mach number that satisfies this condition is checked. After that, using this Mach number, the exit to throat area ratio is calculated using equation (6.17). If this area is greater than 1.7 the Mach number corresponding to this area ratio is computed and then thrust is computed using equation (6.14) where ambient pressure doesn't match the exit pressure creating a pressure gradient. At low Mach numbers and altitudes, it is possible to achieve an area ratio of 1 where the flow is completely expanded at the throat of the nozzle. The figure 6.7 show the variations of the area ratios with changing Mach number and altitudes. All the plots show that during high subsonic speeds the area ratio sees a dip. Assuming constant altitude, as the Mach number increases the mass flow increases with it creating thrust more efficiently. After around 0.9 the area ratio increases drastically as the afterburner is turned on. A decrease after reaching the maximum area ratio indicates that the Mach number at that altitude is not possible to achieve. It can also be observed that as the altitude and Mach number increases the exit area wants to increase more to get to higher Mach values however, due to high drag penalties this growth is limited. Table 6.4 shows the nozzle areas during the design point flight conditions.

Condition	A_e [m^2]	A_t [m^2]
Mach 0.9 at 25000 feet	0.144	0.095
Mach 0.95 at 40000 feet	0.149	0.087
Mach 1.6 at 40000 feet	0.222	0.130

Table 6.4: *The throat and exit area of the nozzle at design points.*

The model calculates the thrust ratio of the engine at specific flight conditions and the static sea level condition. As it was not feasible to model the F3 engine without knowing the actual parameters inside the engine, this ratio was calculated to model the engine performance with altitude and Mach number variations. After the ratios are calculated, the static sea level dry and wet thrust of the F3 engine was multiplied with the respective condition thrust ratio to find the thrust of the engine at any point. To compute the thrust, the outlined model was used with equation (6.14).

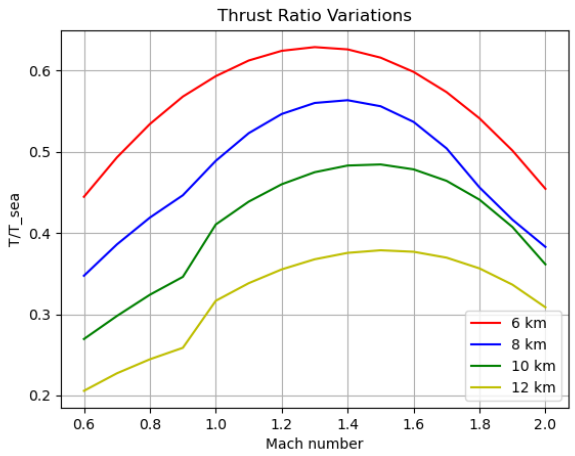

Figure 6.6: *The variation of the thrust ratio due to Mach number and altitude changes.*

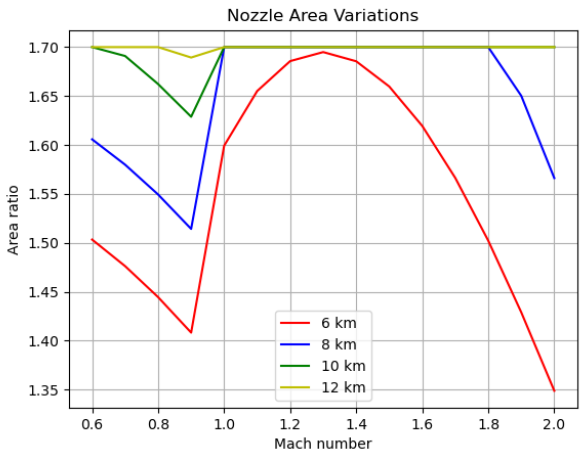

Figure 6.7: *The variation of the area ratios in the exhaust nozzle due to Mach number and altitude changes.*

The figure 6.6 shows the ratio of the thrust at specific conditions and the static sea level versus the Mach number and altitude. This way it is possible to calculate the thrust available at any point in the flight envelope. From the plot it can be seen that the thrust increases to a maximum and then starts to decrease. This trend is caused by the exhaust nozzle design. The nozzle area ratio was optimised for the supersonic dash manoeuvre condition. This point can be seen at the maximum point in the graph representing the 12 km curve. The decrease after the maximum indicates that the optimal area ratio is increasing however, the area ratio was limited to 1.7 due to aerodynamic concerns. Thus, after the optimal condition at a specified altitude, as the exit area cannot increase anymore the optimal thrust is not provided and decreases.
Finally, looking at the reference mission, the thrust values for necessary flight conditions can be computed using the custom model.These values can be seen in table 6.5.

Flight condition	Altitude [m]	Mach	Thrust dry [kN]	Thrust wet [kN]
Sea level cruise	0.00	0.9	15.3	31.7
Cruise	7620	0.90	7.7	16.1
High altitude cruise	13716	0.90	3.2	6.6
Low altitude supersonic dash	13716	1.60	8.7	18.1
Subsonic dash	12192	0.95	4.4	9.1
Supersonic dash	12192	1.60	6.7	14.0
Fast supersonic dash	12192	2.00	5.9	8.8

Table 6.5: *Thrust performance of the propulsion system at different flight conditions*

6.4.2. Recommendations

Propulsion system model has broad assumptions. These assumptions include the assumptions made generally in the early stages of design and assumptions due to the complex flow relations for supersonic speeds. For supersonic speeds it is recommended to conduct a CFD analysis to calculate the flow properties at respective stations inside intake and exhaust nozzle as they mostly have the broad assumptions. It is also recommended that the specifications of the F3 engine should be collected better by contacting IHI Corporation for the using in the model of the propulsion system. This way it would be possible to determine accurate thrust ranges for various altitudes and Mach numbers and, design the exhaust nozzle and intake more accurately. This would also have a snowball effect on the whole aircraft mass and size, as these parameters will decrease with a more optimal propulsion system design.

6.5. Verification and Validation

The propulsion system model has been created using several assumptions which were mentioned earlier in this section. These assumptions may drift the results away from the reality and hence, the validity of the assumptions must be checked. For these reasons, a validation analysis of the model should be performed. However, before checking whether the model is giving accurate results, the model should be checked whether it gives the desired outputs. This requires a verification analysis of the model.

For the verification of the propulsion system, the Gasturb 14 engine simulation software was used. The Gasturb is a software that models the engine based on the data provided which is also capable of optimizing several engine parameters including but not limited to the net thrust and SFC. Gasturb is being used by professionals, researchers and students as it has variety of modes.

Property	Model value	Gasturb 14 value	Difference [%]
T_2 [K]	326.22	327.67	-0.44
$T_{0,25}$ [K]	447.02	453.00	-1.33
$T_{0,3}$ [K]	1032.06	994.61	3.70
$T_{0,45}$ [K]	1017.75	1063.06	-4.36
$T_{0,5}$ [K]	900.41	934.77	-3.74
$P_{0,2}$ [K]	73392	78321	-6.50
$P_{0,25}$ [K]	198160	211468	-6.50
$P_{0,3}$ [K]	2774253	2871734	-3.45
$P_{0,45}$ [K]	402152	487488	-19.18
$P_{0,5}$ [K]	231449	273142	-16.5

Table 6.6: *Custom model and Gasturb model station values for Mach 1.6 at 12000 m*

The table 6.6 shows the comparison of the custom model station temperature and pressure values and values computed using Gasturb 14 software. In the Gastrub 14 software there are already available engine data. The closest engine data in the software to the F3 engine with an afterburner is a generic twin spool turbojet with an afterburner. The selection of the turbojet engine already introduces some errors to the calculations however, these errors are estimated to be low as the most prominent difference between the engines are the bypass ratio and the bypass air used in the custom model is used for auxiliary operations such as cooling, entering the afterburner without having a direct effect on the thrust calculations. On the other hand, The thrust ranges for the both engines introduce significant errors as the Gasturb model engine has a higher thrust range than the F3 engine with an afterburner. Nevertheless, looking at table 6.6 the pressure values for stations 45 and 5 are off by an almost 20 %. This is due to the fact that the RAD having a custom designed intake which lowers the total pressure entering the engine fan significantly even though the static pressure is increased, the Mach number is decreased significantly lowering the total pressure. The ideal intake would decrease the Mach number entering the engine inlet without changing the total pressure, however in reality this is not possible and is computed accordingly. Also, the thrust of the Gasturb 14 model turbojet is more than the thrust available from the F3 engine with afterburner. This would require more pressure and temperature after the turbine meaning the lower values point towards a lower thrust value which is the case in this analysis.

The propulsion system is validated going back to the main reason this model was created which was to provide thrust ratios for different Mach numbers and altitudes. This was first done using figure 6.9 which was interpolated to get thrust ratio estimations. As the model has very broad assumptions, due to the design phase of the aircraft, and it is not possible to acquire the F3 engine data, validation was done using the figure 6.6 a plot which clearly lays-out the thrust variation with Mach number and altitude.

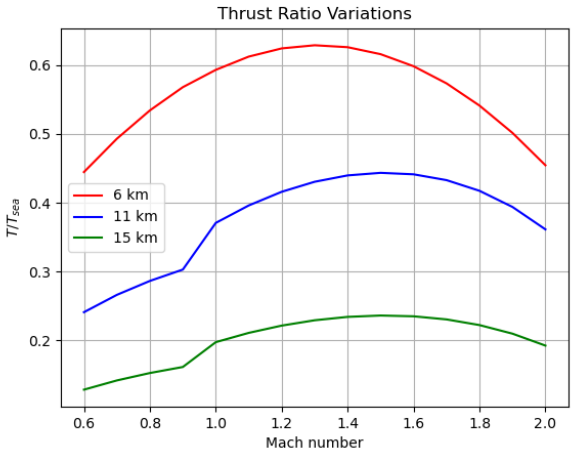

Figure 6.8: *Model calculation of the thrust variation at the same altitude and Mach number as used to plot the generic military low bypass turbofan engine thrust variation.*

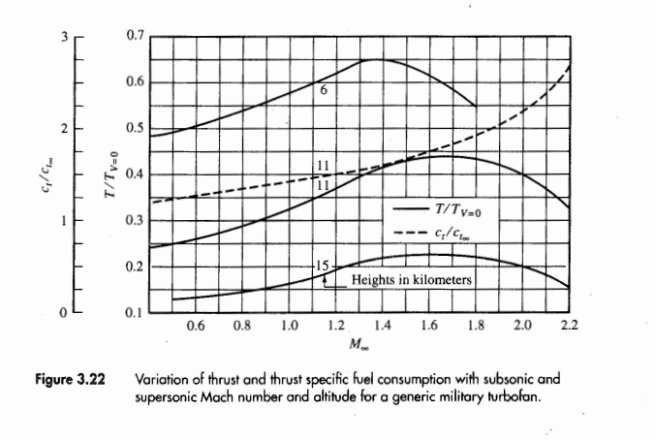

Figure 6.9: *Thrust variation with altitude and Mach number [29].*

Looking at figure 6.8 it is possible to see the same trend as the figure 6.6 when the altitudes are kept constant. As mentioned in section 6.4, when the altitude decreases to a certain point, the area ratio necessary for optimal thrust gets a lower value. When this value is lower than 1.7, the complete expansion is possible achieving optimal thrust. This pattern can be also observed here at an altitude of 6 km as the plot produced by the custom model shows that the engine is able to sustain higher thrust ratios longer at 6 km than the figure 6.6. Furthermore, the values at the local maxima and minima of each plot have similar values at similar Mach numbers. This concludes that the custom model can produce accurate thrust ratios with varying altitudes and Mach numbers.

6.6. Fuel System

Aircraft fuel system is responsible for storage, distribution and management of the fuel regardless of the operating conditions. The fuel needs to be delivered to the engine with correct pressure, temperature and flow rate. To achieve this, fuel system components such as valves, pumps and heat exchangers are arranged properly with the way it is arranged in a classic gas turbine engine. As there is an afterburner in RADs propulsion system, few adjustments are made in the fuel system layout to meet the afterburner fuel need.

To manage the aircraft stability and control, a centre of gravity pump is used which manages the fuel distribution in the tanks. The pump is controlled via the flight computer, and it sends the fuel from the front fuel tanks to the after tanks to shift the centre of gravity backwards and vice versa. As the fuel management within the fuel tanks is mainly related with control and stability, chapter 7, this section focuses on the fuel management after the fuel tanks.

The fuel system layout is seen in figure 6.10. and it shows how the fuel is sent from the tanks to the combustıon chamber station by station. First of all, the stored fuel in the tanks is fed to the fuel system by a booster pump. An engine shut-off valve stops the fuel flow in case of an engine failure to prevent a catastrophic hazard. In normal operating conditions, the shut-off valve is open, and it passes the fuel to the low-pressure pump via a low pressure valve. After passing the low-pressure pump, the fuel goes to the air-fuel heat exchanger, where the cold fuel is heated up with the warm air. If the fuel is already warm enough, it passes to the next station via bypass valve 'a'. The warm fuel then enters the fuel filter, where the dust or particles smaller than a micron is filtered out from the system. The bypass valve 'b' is used to transfer the fuel to the next station if the filter fails. Afterwards, the fuel is sent to high pressure pump and fuel control unit. The bypass valve 'c' is used to transfer the fuel directly to the high-pressure pump if there are multiple component failures (heat exchanger and filter). It ensures that the engine is fed even though the fuel is not ideally threaded, which is not a prior concern as the aircraft must make an emergency landing in such a case. The primary fuel control unit is a complex equipment which is responsible to send correct fuel flow to the engine. It uses the air pressure, temperature, engine rpm and other state inputs and throttle position as the control input, and it outputs the fuel such that the air/fuel flow ratio is fixed inside the combustion chamber. The fuel coming out from the primary control unit enters the fuel flow transmitter which indicates the burn rate (fuel consumption) to the ground station where the RAD is controlled. Then, the fuel goes to the oil-fuel heat exchanger where it is heated up more by the oil, which makes it easier for fuel to atomize in the fuel nozzles. The bypass valve 'd' is used to bypass the fuel if the exchanger fails. As the fuel warms up, the oil cools down, which is sent to the other engine parts that requires cooling. The fuel passing through the heat exchanger enters the secondary fuel control unit, which distributes the fuel going to the main combustion chamber and to the afterburner. The fuel going to the main combustion chamber is divided into two fuel nozzles via a flow diverter & dump valve. Finally, the primary and the secondary fuel nozzles spray the fuel with different pressure levels into the combustion chamber to increase chemical efficiency in the chamber. Also, the afterburner nozzle sprays the fuel to the afterburner chamber to increase thrust and the performance of the engine.

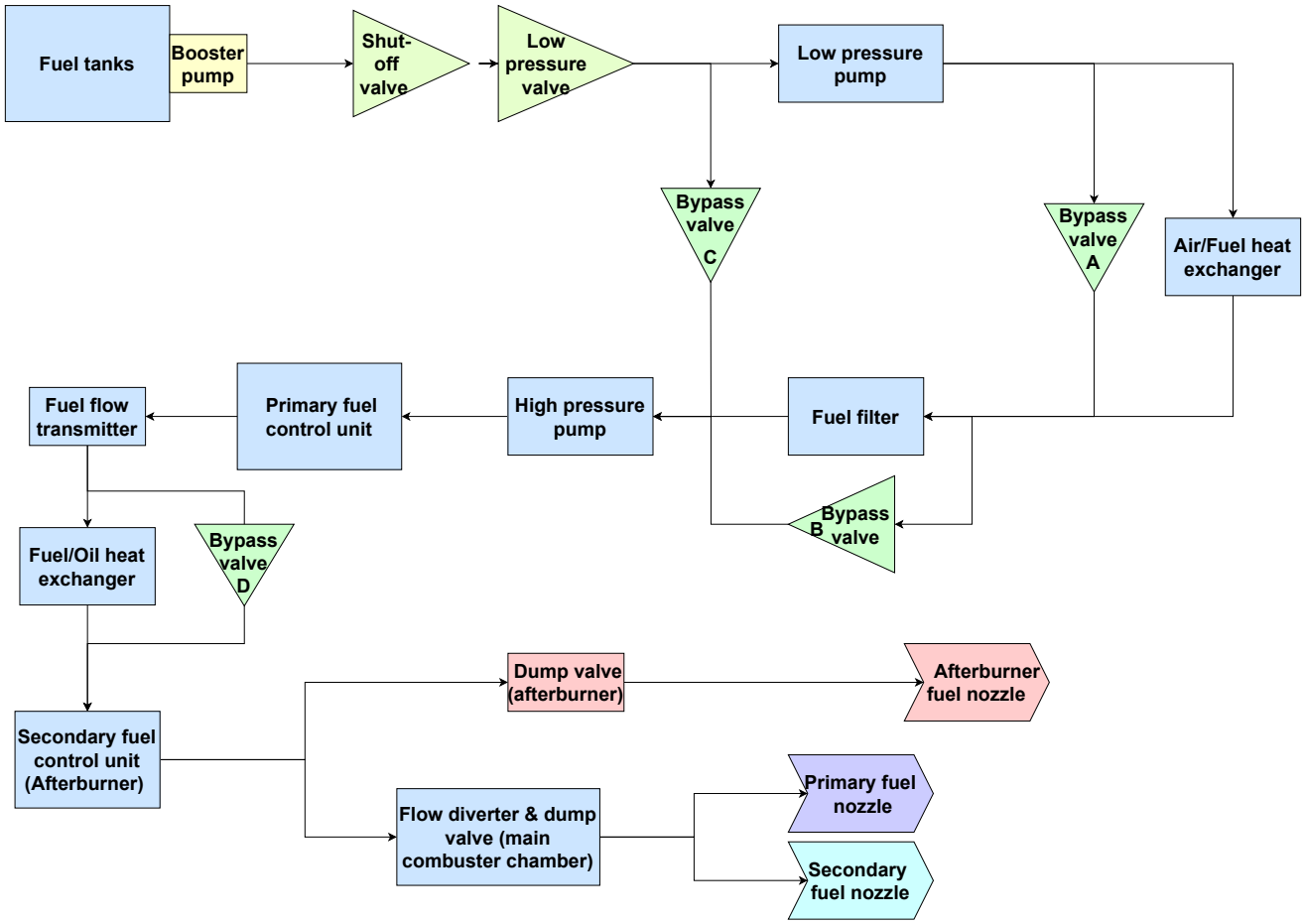

Figure 6.10: *The fuel system layout*

6.7. Power System

Aircraft power system is responsible for generation, transmission, distribution and storage of electrical energy [30]. Power system components needs be to be designed and sized such that the flight and mission system can work continuously throughout the whole mission duration.

6.7.1. Power System Design

RAD-TE-SYS-02-01 and RAD-TE-SYS-02-02 requirement states that the power need of the mission systems of RAD is 5kW at nominal conditions with a peak power need of 10kW. In addition to mission systems, there are flight systems such as navigation and GPS which are essential not just for RAD mission but for all aerospace missions. By adding the power need of flight systems to the power budget with an acceptable safety margin, the total power need of RAD can be estimated as 6 kW at nominal conditions with 12kW peak power.

To meet the power requirement, there needs to be an internal energy source on board of the aircraft. Since kinetic energy produced by the engine is larger than the required electrical energy (0.5 - 1 [31]), powering the systems via the engine is the most efficient and logical drive system for RAD. Other drive system options such as auxiliary power unit (APU) and Ram Air Turbine (RAT) are heavy and large for unmanned supersonic trainers, and they are used in multi engine transport or commercial aircraft. Furthermore, the engine is started via a ground power unit using a huffer cart since there is not an APU on-board to start the engine.

Using a generator/alternator small portion of the kinetic energy produced by the engine is converted to electrical energy to power the systems. Multi-phase AC generators are widely used in recent aeronautical applications as they are smaller and cheaper than the alternatives thus in RAD a three-phase alternator is used [31]. RF4-10 three-phase permanent magnet alternator is selected for RAD because of its high reliability and performance. It can produce 8 kW power with 1500 coil rpm, and 9.6 kW with 1800 coil rpm which is higher than the nominal power requirement. When the peak power is needed the secondary energy source, the battery, provides the remaining power need of the RAD.

A transformer-rectifier unit (TRU) is needed to convert the high voltage AC current produced by the alternator to a low voltage DC current for the primary electric power management & distribution bus. TR1010 TRU produced by Electrocube is selected for this purpose, which can convert the high voltage (400 V) AC output produced by the alternator to a low voltage (24 V - 28 V) high current electricity. The power coming from TRU to the power distribution buses (primary & secondary) needs to be distributed to all the mission and flight systems. The primary power distribution is achieved with two primary power distribution units (PPDU) produced by 'Ametek Aerospace & Defence' and 'Brancora Industries'. The secondary power distribution is achieved with a SPUD manufactured by 'Ametek', which is activated during an emergency or PPDU failure.

For emergency situations such as an engine failure, a rechargeable (secondary) battery is used to power the flight and mission systems. In such a situation, high power consuming mission systems are turned-off and the battery prioritise to power the flight systems, with an estimated power need of 5kW. The emergency duration is assumed to be the 25% of the minimum endurance of RAD which is equal to 23 minutes. With these assumptions and a small safety margin, the minimum required energy stored in the battery is estimated as 2 kWh. Using the battery power and energy requirement the battery can be sized. As lithium-ion batteries higher power and energy density compared to the other rechargeable battery types such as nickel-cadmium or nickel-metal-hydride, they are used in RAD for weight and space saving [31]. The volumetric energy, gravimeter power & energy density of mid-range lithium-ion batteries are 450 Wh/L, 500 W/kg and 150 Wh/kg, respectively [31]. Using these specific values, the required battery size and mass is calculated as 14 kg and 4.5 L.

The ground power unit is responsible for starting the engine and charging the battery fully before take-off. It is assumed that the customer of RAD is equipped with such a unit to give the pre-flight power support to RAD.

6.7.2. Electrical Block Diagram

Electrical block diagram is provided to show the electrical flow in between components of the power system. It also gives an overview for readers to visualize the power system.

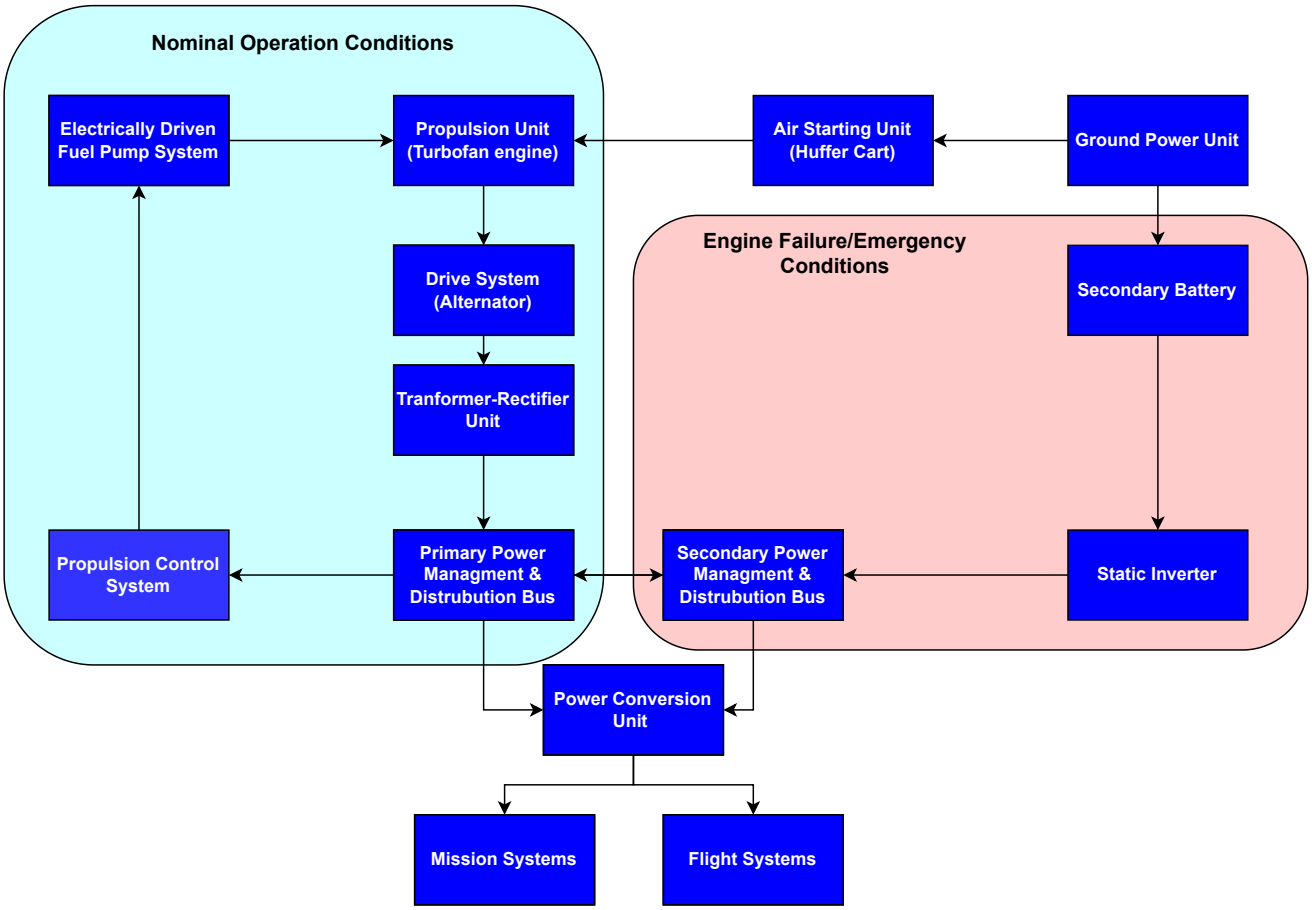

Figure 6.11: *Electrical Block Diagram*

6.7.3. Power System Sizing

The power system components are required to fit in the fuselage of RAD. The components are therefore selected such that they are small and light as possible and they deliver required electrical power to the systems. Table 6.7 shows the selected PS components and their sizing.

Table 6.7: *Power system components used on the RAD.*

PS Element	Model	Manufacturer	Mass[kg]	Size[cm * cm * cm]	Volume[L]
Alternator	RF4-10	RFL	39	23.6 * 18.9 * 18.9	6.6
Rectifier	TR1010	Electrocube	12	15.9 * 21.1 * 32	10.7
Primary PDU	-	Ametek	8.3	-	11.2
Primary PDU	EASA CS-LURS	Brancaro	2.2	20 * 15.5 * 9.5	2.9
Secondary PDU	-	Ametek	6.2	30.9 * 28.6 * 10.2	9
Li-ion Battery	-	-	14	-	4.5

6.8. Conclusions

After a thorough analysis of each engine at hand, the F3 was selected for the iterations due to its low weight and size as well as its afterburner compatibility. F3 engine has a static sea level thrust of 16.4 kN with a specific fuel consumption of 19.8 g/kN/s. However, it was decided that during supersonic speeds this thrust was not enough and hence, an afterburner was used. With this afterburner the static sea level thrust was increased to 29.5 kN while the specific fuel consumption at this condition increased to 60.9. However, the maximum thrust, 31.7 kN, occurs at Mach 0.9 at sea level. Coming back to the intake, the goal was to decelerate the incoming flow while keeping the total pressure constant. This was achieved by first, a supersonic diffuser including an external expansion configuration and second, a subsonic diffuser including an S-duct shape for low observability. Nevertheless, the total pressure was not constant and decreased with increasing Mach number.
Also, the exhaust nozzle was designed for optimal supersonic performance. Exhaust nozzle throat and exit areas were determined for different flight conditions. Maximum exhaust nozzle throat and exit areas were 0.130 m^2 and 0.222 m^2, respectively with a Mach number of 1.6 at 40,000 ft.

The engine was also used to provide power to the aircraft systems. An alternator is connected to the high-pressure turbine of the engine. For the alternator, RF4-10 from RFL was selected. on top of this, in times of emergency, a Li-ion battery was selected to kick in after an outage.

7 Empennage, Control Surfaces, and Landing Gear Design

In this chapter, the elements which give the RAD control and stability is discussed. As control and stability is an important aspect for aeroplanes, this is steered by the empennage for this drone. As without proper control surface sizing the drone might crash resulting in mission failure. Firstly, section 7.1 oversees the empennage design. Secondly, the horizontal stabiliser is discussed in section 7.2. Thirdly, in section 7.3 the vertical stabiliser is considered, it should be noted that a canted fin configuration is used and that these sections treat only the vertical and horizontal component of the canted fins to later assemble these into the real canted fins. Fourthly, the centre of gravity is calculated in section 7.4. Furthermore, the movable wing surfaces are detailed in section 7.5, and the control surface designs are considered in section 7.6. Finally, the landing gear design is elaborated in section 7.7.

Several requirements were taken into consideration for designing the empennage, mobile wing surfaces, and landing gear. These are listed below in table 7.1.

Table 7.1: *Requirements for the empennage and landing gear.*

ID	Description
RAD-TE-PER-02-04	The RAD shall be able to operate in T/O and LDG for the set-out wind limits.
RAD-TE-PER-02-04-A	The RAD shall be able to operate in T/O and LDG for a 25 kt maximum cross-wind component.
RAD-TE-PER-02-04-B	The RAD shall be able to operate in T/O and LDG for a continuous wind gusting of 35 kt.
RAD-TE-PER-02-04-C	The RAD shall be able to operate in T/O and LDG for a maximum wind gusting of 42 kt.
RAD-TE-LDG-01	The turnover angle shall not be more than 63°.
RAD-TE-LDG-02	The scrape angle shall not be lower than 15° [32].
RAD-TE-LDG-03	The nose gear shall be loaded with at least 8% percent of the aircraft weight with the c.g. in the most aft position.
RAD-TE-OTH-01-01	The RAD shall be able to taxi on a paved taxiway.
RAD-TE-OTH-01-02	No arresting equipment shall be needed to operate the RAD.

7.1. Empennage Design

In conventional aircraft configurations, separate vertical and horizontal stabilisers form an empennage positioned at the tail of the aircraft. However, other arrangements of an empennage, such as the V-tail configuration, feature stabilisers which contribute to a combination of longitudinal and directional stabilization and control. Since a V-shaped tail is better for low observability during the trade-off, it has been chosen to use this configuration [2]. This resulted in the use of two canted fins that provide both longitudinal and directional control, also known as a V-tail configuration.

Thus, both pitch and yaw control are obtained by using this canted fin configuration. The advantages for this empennage are as follows: the tail is lighter in design due to the reduced number of parts and components. Additionally, it has almost the same wetted surface but less aerodynamic drag, because of the smaller interference between empennage and fuselage. There is a reduced risk of debris impact while on the ground, since it is positioned higher and angled. Finally, less engine exhaust and wing downwash impingement are experienced

[33] on the empennage.
The disadvantages are as follows: the system is more complex to decouple the lateral and longitudinal control. Furthermore, the system has higher torsion loads on the fuselage compared to a conventional tail to generate the same lateral or vertical force. Finally, the systems has adverse yaw-roll coupling when correcting for sideslip angles [33].

7.1.1. Preliminary Sizing

First, preliminary sizing of the horizontal tail and vertical tail are considered, as there is little data on v-tail sizing. The surface of the horizontal and vertical tail will be combined by an angle to give the required stability and control. The sizing of the vertical and horizontal tail is an iterative process that, during the preliminary stages of design, is largely empirical. Therefore, the sizes are compared to existing aircraft as a basis for the design. The primary function of the stabilisers is to provide stability, thus comparing this to existing designs should give a good rule of thumb.

The method used for this sizing is by using tail volume coefficients taken from literature data of fighter aircraft, which is a common procedure in this preliminary phase. The volume ratios are non-dimensional, which relate the size of the wing and length of the aircraft to the required tail area. The calculation for this sizing method can be found below in equations (7.1) and (7.2).

$$C_{\mathrm{HT}} = \frac{S_{\mathrm{HT}} l_{\mathrm{HT}}}{S_{\mathrm{w}} c_{\mathrm{MAC}}} \tag{7.1}$$

$$C_{\mathrm{VT}} = \frac{S_{\mathrm{VT}} l_{\mathrm{VT}}}{S_{\mathrm{w}} b} \tag{7.2}$$

Where C_{XT} is the volume coefficient; S_{XT} is the surface of the tail; l_{XT} is the distance from the quarter chord of the wing to the quarter chord of the tail.

Since most of the values from this equation are changed during the design process, the calculated surface and angle was iterated automatically. The resulting required angle can be calculated by $\arctan\left(\frac{S_{\mathrm{VT}}}{S_{\mathrm{HT}}}\right)$.

From literature data, the following horizontal tail volume coefficients were found: 0.307 [34]; 0.20-0.75 [35]; 0.4 [36]; 0.362 [37]. As well as the following vertical tail volume coefficients: 0.064 [34]; 0.041-0.130 [35]; 0.070 [36]; 0.077 [37].

The values of 0.362 for the horizontal tail volume, and a volume of 0.077 for the vertical tail volume are used for the sizing of the tail as these were from Roskam [37] and generally centred in between what was found in the literature. It should be noted however that these values are for fighters, which need more agility; furthermore, they have a quickly changing c.g. range after disposing their payload. Thus, the calculated surface area by this method is likely overestimated. Finally, a tail surface of 1.2 m^2 is estimated based on these methods with an angle of 32° from the horizontal perspective.

The canted fins are using a symmetrical airfoil, NACA 0004, as the net force will change direction during the flight depending on which direction the ruddervators are deflected. The airfoil had supersonic speeds in mind, resulting in the relatively low thickness to chord ratio. A symmetrical airfoil should always be used for the horizontal and vertical stabiliser, thus the canted fins use it as well, as the net force will change direction during the flight depending on which direction the elevator or rudder is deflected, and in this case the ruddervator [38].

The aspect ratio of the horizontal tail should be less than that of the wing [39], since a lower aspect ratio wing stalls at higher angles of attack. This allows the control authority to still be available after the wing has stalled. A typical aspect ratio for a vertical tail is in the range of 1.3 to 2.0. Therefore, an aspect ratio between these values was aimed. The aspect ratio was decided by automatic iterations, because the sweep of the fins is kept like the sweep of the wings.

7.1.2. Supersonic Stability

During supersonic flight, the vertical tail becomes less effective with increasing Mach number [39]. The stability of the craft is reduced because the lift, or side force, produced by the tail reduces with speed for each degree of

sideslip angle. This results from the very different pressure distribution, because of shock waves and expansion waves. However, the plane can be controlled by computers maintaining the stability, if it is still controllable. One additional consideration to improve stability is to pump the fuel around to adjust the c.g. location such that it enhances stability, this does add extra weight to the design, nonetheless.

7.2. Horizontal Stabiliser

The horizontal stabiliser provides longitudinal stability. Calculations for a horizontal stabiliser are used for establishing a final canted fin design. The longitudinal stability provided by the horizontal stabiliser can be calculated by using equation (7.3).

$$\bar{x}_{\text{c.g.}} = \bar{x}_{\text{AC}} + \frac{C_{L_{\alpha_{\text{h}}}}}{C_{L_{\alpha_{\text{A-h}}}}}\left(1 - \frac{d\epsilon}{d\alpha}\right)\frac{S_{\text{h}} l_{\text{h}}}{S\bar{c}}\left(\frac{V_{\text{h}}}{V}\right)^2 \tag{7.3}$$

$$C_{L_{\alpha_h}} = \frac{2\pi(\text{AR})_{\text{h}}}{2 + \sqrt{4 + \left(\frac{(AR)_{\text{h}}\beta}{\eta}\right)^2\left(1 + \frac{\tan\left(\Lambda_{\frac{1}{2}c_{\text{h}}}\right)^2}{\beta^2}\right)}} \tag{7.4}$$

where $\bar{x}_{\text{c.g.}}$ is the position of centre of gravity measured from the start of the mean aerodynamic chord; $\bar{x}_{\text{AC}}$ is the position of the aerodynamic centre measured from the start of the MAC; $\eta = 0.95$; this equation can also calculate $C_{L_{\alpha_w}}$. $C_{L_{\alpha_{\text{h}}}}$ can be calculated using equation (7.4) [24]. $C_{L_{\alpha_{\text{A-h}}}}$ can be calculated using equation (7.5). $\frac{d\epsilon}{d\alpha}$ is calculated using equation (7.6) [40]; however, it is assumed the fin encounters little downwash effects due to the angle, therefore $\frac{d\epsilon}{d\alpha} = 0$ is used as filling in equation (7.6) assumes a flat stabiliser and results in a value of 0.814. $\left(\frac{V_{\text{h}}}{V}\right)^2 = 1$ is assumed in this case.

$$C_{L_{\alpha_{\text{A-h}}}} = C_{L_{\alpha_{\text{w}}}}\left(1 + 2.15\frac{b_{\text{f}}}{b}\right)\frac{S_{\text{e}}}{S_{\text{w}}} + \frac{\pi}{2}\frac{b_{\text{f}^2}}{S_{\text{w}}} \tag{7.5}$$

$$\frac{d\epsilon}{d\alpha} = \frac{K_{\epsilon_\Lambda}}{K_{\epsilon_{\Lambda=0}}}\left(\frac{r}{r^2+m_{\text{tv}}^2}\frac{0.4876}{\sqrt{r^2+0.6319+m_{\text{tv}}^2}} + \left[1 + \left(\frac{r^2}{r^2+0.7915+5.0734m_{\text{tv}}^2}\right)^{0.3113}\right]\left\{1 - \sqrt{\frac{m_{\text{tv}}^2}{1+m_{\text{tv}}^2}}\right\}\right)\frac{C_{L_{\alpha_{\text{w}}}}}{\pi(\text{AR}_{\text{w}})} \tag{7.6}$$

where K_{ϵ_Λ} can be calculated by using equation (7.7); and $K_{\epsilon_{\Lambda=0}}$ can be calculated with equation (7.8).

$$K_{\epsilon_\Lambda} = \frac{0.1124 + 0.1265\Lambda_{\frac{1}{4}c} + 0.1766\Lambda_{\frac{1}{4}c}^2}{r^2} + \frac{0.1024}{r} + 2 \tag{7.7}$$

$$K_{\epsilon_{\Lambda=0}} = \frac{0.1124}{r^2} + \frac{0.1024}{r} + 2 \tag{7.8}$$

where $r = L_{\text{h}}/(b/2)$ and $m_{\text{tv}} = \tan(\alpha_0)L_{\text{h}}/(b/2)$; with L_{h} being the length from quarter chord wing to quarter chord fin.

$$\bar{x}_{\text{AC}} = \left(\frac{x_{AC}}{\bar{c}}\right)_{\text{wf}} = \left(\frac{x_{AC}}{\bar{c}}\right)_{\text{w}} - \frac{1.8}{C_{L_{\alpha_{\text{A-h}}}}}\frac{b_{\text{f}}h_{\text{f}}l_{\text{fn}}}{S_{\text{w}}\bar{c}} + \frac{0.273}{1+\lambda}\frac{b_{\text{f}}c_g(b-b_{\text{f}})}{\bar{c}^2(b+2.15b_{\text{f}})}\tan\left(\Lambda_{\frac{1}{4}c_{\text{w}}}\right) \tag{7.9}$$

The horizontal stabiliser also provides longitudinal controllability. The controllability can be calculated by using equation (7.10). In this case, a fixed tail configuration is used. The reason for using a fix tail opposed to full moving is because we do not require to be highly maneuverable.

$$\bar{x}_{\text{c.g.}} = \bar{x}_{\text{AC}} + \frac{C_{m_{\text{AC}}}}{C_{L_{\text{A-h}}}}\frac{C_{L_{\text{h}}}}{C_{L_{\text{A-h}}}}\frac{S_{\text{h}}l_{\text{h}}}{S\bar{c}}\left(\frac{V_{\text{h}}}{V}\right)^2 \tag{7.10}$$

where $\bar{x}_{\text{AC}}$ can be calculated using equation (7.9). $C_{L_{\text{h}}}$ can be calculated with equation (7.14). $C_{m_{\text{AC}}}$ is calculated using equation (7.11) [33].

$$C_{m_{\text{AC}}} = C_{m_{\text{AC}_{\text{w}}}} + \Delta_{\text{flaps}}C_{m_{\text{AC}}} + \Delta_{\text{fuselage}}C_{m_{\text{AC}}} \tag{7.11}$$

$$C_{m_{\text{AC}_{\text{w}}}} \approx C_{m_{0_{\text{airfoil}}}}\left(\frac{(AR)_{\text{w}}\cos(\Lambda)^2}{(AR)_{\text{w}} + 2\cos(\Lambda)}\right) \tag{7.12}$$

$$\Delta_{\text{fuselage}} C_{m_{\text{AC}}} = -1.8\left(1 - \frac{2.5 b_{\text{f}}}{l_{\text{f}}}\right) \frac{\pi b_{\text{f}} h_{\text{f}} l_{\text{f}}}{4 S \bar{c}} \frac{C_{L_0}}{C_{L_{\alpha_{\text{A-h}}}}} \quad (7.13)$$

$$C_{L_{\text{h}}} = \begin{cases} -1 & \text{Full moving tail} \\ -0.8 & \text{Adjustable tail} \\ -0.35(AR)_{\text{h}}^{\frac{1}{3}} & \text{Fixed tail} \end{cases} \quad (7.14)$$

All these equations together result in a scissor plot, where it can be determined what stability and controllability the horizontal stabiliser provides. An example of a scissor plot is shown in figure 7.1 where all regions are explained. The resulting scissor plot for the horizontal tail part of the V-tail is depicted in figure 7.2. The horizontal tail surface is calculated from $S_{\text{canted fins}} = \arctan\left(\frac{S_{\text{VT}}}{S_{\text{HT}}}\right)$. The most forward location of the c.g. is $\bar{x}_{\text{c.g.}}$ = 0.17, while the most aft part is $\bar{x}_{\text{c.g.}}$ = 0.43. This means that the drone is controllable and in most of the cases stable, only with an uneven fuel distribution the drone is instable, but section 7.4 explains that this is unlikely to happen.

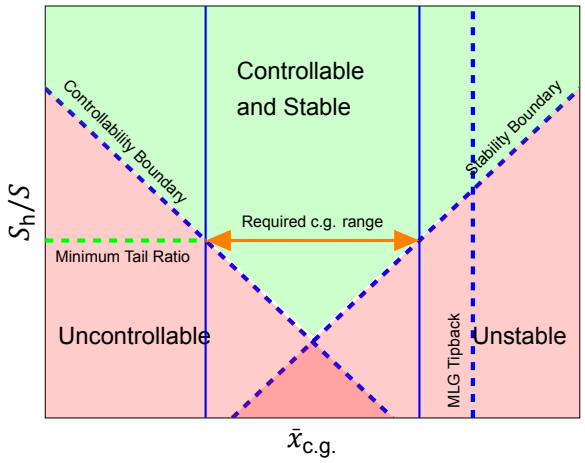

Figure 7.1: *An example of a scissor plot, displaying all regions of interest.*

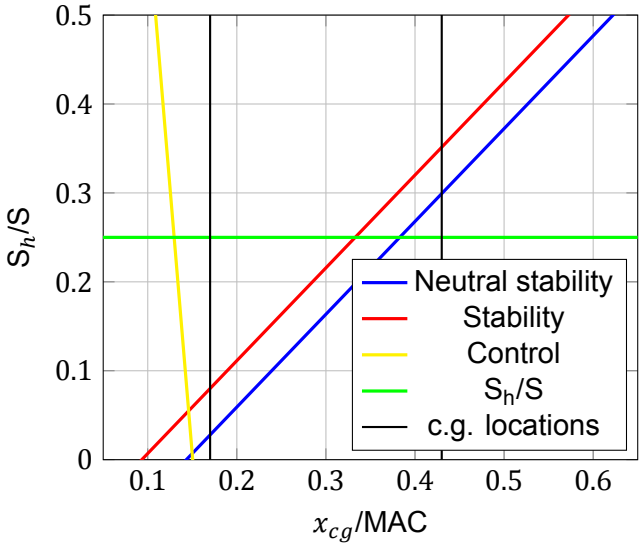

Figure 7.2: *Scissor plot, displaying the stability and controllability of the chosen V-tail configuration. The most forward location of the c.g. is $\bar{x}_{c.g.}$ = 0.17, while the most aft part is $\bar{x}_{c.g.}$ = 0.43. This scissors plot is only valid for the subsonic region.*

7.3. Vertical Stabiliser

For sizing the vertical stabiliser, the method from Torenbeek [41] for sizing for lateral stability was used. It can be seen from equation (7.15) (derived from the equation which comes from taking the sum of moments around the z-axis of the aircraft and then non-dimensionalising it) that the vertical tail size is dependent on the yawing moment coefficients due to different aspects of the aircraft. Estimating each of these coefficients can potentially be done using the DATCOM methods [24] for subsonic, transonic and supersonic speeds to see what size would be required for each speed regime. This approach was, however, not followed, as the equations in the DATCOM to estimate these coefficients require a lot of additional input parameters not yet known in this stage of the design. Therefore, a more crude approach was take, proposed in Torenbeek [41]: find $C_{n_{\beta_{\text{A-v}}}}$ and from that determine $\frac{S_{\text{v}} l_{\text{v}}}{Sb}$ by reading it off from equation (7.15) (which gives the tail surface ratio for different $C_{n_{\beta_{\text{A-v}}}}$ based on aircraft with fuselage mounted engines).

$$\frac{S_{\text{v}} l_{\text{v}}}{Sb} = \frac{C_{n_\beta} - (C_{n_{\beta_f}} + C_{n_{\beta_p}} + \Delta_i C_{n_\beta})}{C_{Y_{v_\alpha}} (V_{\text{v}}/V)^2} = \frac{C_{n_\beta} - C_{n_{\beta_{\text{A-v}}}}}{C_{Y_{v_\alpha}} (V_{\text{v}}/V)^2} \quad (7.15)$$

As applying this method using the equations proposed by Torenbeek [41] did not yield a reasonable $C_{n_{\beta_{\text{A-v}}}}$, it was decided to use the DATCOM method to estimate this coefficient and then use the graph 7.3 from Torenbeek to find the proposed tail surface. Equation (7.16) is the DATCOM equation for the yawing moment coefficient of the wing body without the tail and is a function of geometry, as well as the Reynolds's number. It is applicable for all speeds.

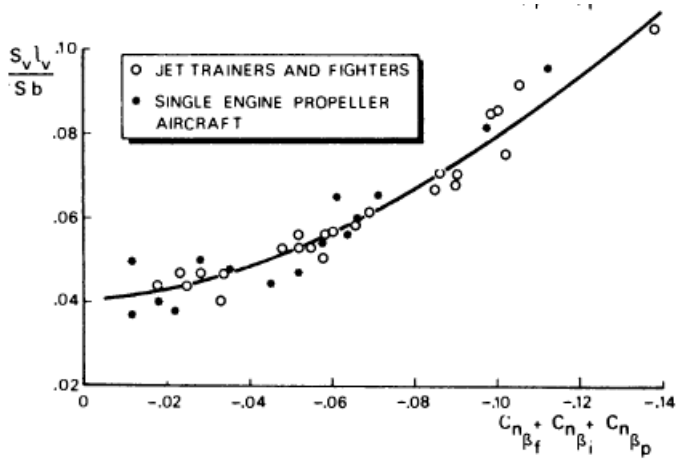

Figure 7.3: *Figure depicting required vertical tail size for aircraft with fuselage housed engines [41].*

$$C_{n_{\beta_{A\text{-}v}}} = -K_N K_{R_l} \frac{S_{bs}}{S_w} \frac{l_b}{b_w} \tag{7.16}$$

Using the described above steps, it was found that the vertical stabiliser should have a surface area of 0.391 m for directional stability. This shows that the horizontal stabiliser is more requiring in size than the vertical stabiliser. Therefore, in the sizing this has been considered.

7.4. Centre of Gravity

The centre of gravity must be calculated for determining the stability and controllability of the drone. Furthermore, this is important to know for the placement of the landing gear. Calculating the centre of gravity was an iterative process, as the c.g. shifted with every change in the design. The equation for calculating the c.g. is shown in equation (7.17).

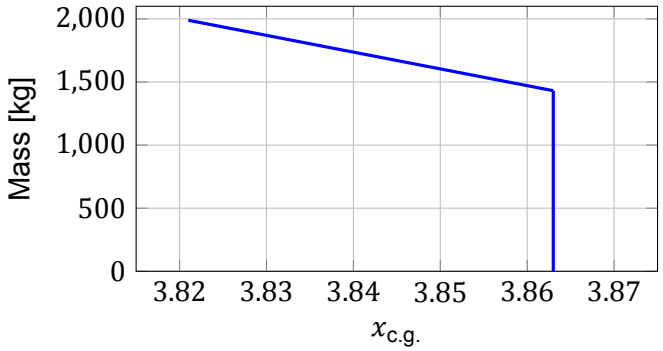

(a) *The $x_{c.g.}$ plotted from OEW + payload to max weight from fuel, this assumes the fuel is removed from the two fuel tanks with the same percentage during flight.*

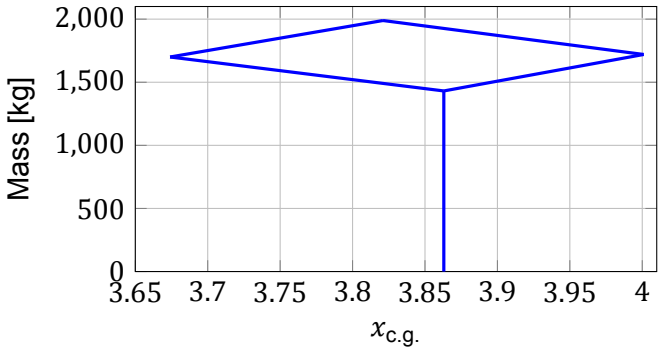

(b) *The extremes of the $x_{c.g.}$ plotted for the max AFT and max FWD case that is possible.*

Figure 7.4: *The $x_{c.g.}$ plotted during the flight and the extreme values possible when the fuel is not distributed correctly over the two fuel tanks. The straight line is the OEW.*

$$x_{\text{c.g.}} = \frac{\sum_i x_{\text{c.g.}_i} \cdot W_i}{\sum_i W_i} \tag{7.17}$$

Finally, this resulted in a c.g. of 3.67 m (max FWD) and 4.00 m (max AFT), which can be seen depicted in figure 7.4b. The centre of gravity distribution for fuel can be seen in figure 7.4a.

7.5. Movable Wing Surfaces

The design of the movable wing surfaces is discussed together here, as the approach taken to the size and position of each is coupled. First, the ailerons are sized to meet rolling requirements [42]. Based on the required aileron size, it is possible to see how the flaps can be sized and positioned.

7.5.1. Ailerons

The method for sizing the ailerons is taken from Gudmundsson [43, Ch. 8]. It is based on getting the correct steady-state roll rate p, the transient motion is not designed for here. The method was incorporated into code which requires some geometrical parameters of the wing and ailerons, airfoil characteristics and aileron effectiveness (τ). The main idea how the method is applied is by playing around with input variables of the code to find a steady roll rate, which matches the one from requirements. The steady aircraft roll rate is given by equation (7.18). However, before starting the steps, several parameters must be determined.

As first step it was assumed that the ailerons used have a maximum deflection angle of 20° both up and down, this is a middle value from the typical deflection angles in Gudmundsson [43, Ch. 8]. Furthermore, due to the high chances of the control system stretching in flight, reducing the maximum deflection of the ailerons in flight compared to the deflections on the ground, it was assumed that during flight the ailerons can only deflect for 50% of their maximum ground deflection(this is an intermediate value between 25% and 75% as suggested in [43, Ch. 8]). This assumed relatively bad performance in flight was chosen to have additional redundancy.

Secondly, it is important to determine the speed at which equation (7.18) is evaluated. As speed is directly proportional to the roll rate, the lowest speed of the mission profile is used (stall speed V_s), as it gives the lowest roll rate.

Next up the roll requirement must be selected, for the RAD it was assumed that it is of Class IV.A for roll requirements. Class IV.A is for high manoeuvrable aircraft such as fighters.

Lastly, it is important to choose the aileron geometry. The aileron span (start and end point of the ailerons along the wing) and the aileron to lifting surface chord ratio. For the ratio, it is assumed that the ailerons use all the volume behind the rear spar of the wing (along the selected aileron span, at least). This span, however, will be varied to get the required steady-state roll rate. The method follows the following steps:

1. Find the roll damping coefficient C_{l_p} using equation (7.19).
2. Find the Aileron Authority derivative $C_{l_{\delta_a}}$ using equation (7.20). Estimate τ with figure 7.5 using the control surface to lifting surface chord ratio as input. For b_1 select some location along the wing. For b_2 select the tip of the wing.
3. Solve equation (7.18). See if the obtained p matches the p from the requirement for Class IVA aircraft.
4. If the roll rate matches the one as inquired by the requirement: the ailerons are sized. Else select a different b_1 and repeat the steps until the requirement is met.

$$p = -\frac{C_{l_{\delta_a}}}{C_{l_p}}\delta_a\left(\frac{2V}{b}\right) \tag{7.18}$$

$$C_{l_p} = -\frac{4(c_{l_\alpha} + c_{d_0})}{S_{ref}b^2}\int_0^{b/2} y^2 c(y)dy \tag{7.19}$$

$$C_{l_{\delta_a}} = \frac{2c_{l_\alpha}\tau}{S_{ref}b}\int_{b_1}^{b_2} c(y)dy \tag{7.20}$$

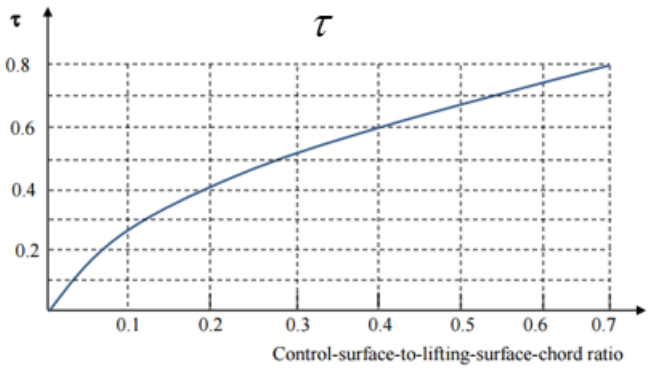

Figure 7.5: *Aileron effectiveness constant as function of lifting surfaces to chord ratio [42].*

Performing these design steps with the code developed by the team, one obtains ailerons with a size given in table 7.2.

7.5.2. High Lift Devices

Now that the layout of the ailerons is known, it is possible to position the high lift devices(HLD's) in the remaining space. For the high lift devices, both leading edge flaps and plain trailing edge flaps have been used. Sizing has been done using equation (7.21) [42].
There are several design choices and distinctions which are used to size the HLD's. The wing itself can be divided into two parts which can be used to position the movable wing surfaces on (area where the fuselage is located on is unusable): the inner higher sweep part and the outer smaller sweep part, subscripts will be used to make a distinction for several parameters for these two. Furthermore, it is decided that the trailing edge devices are positioned along the full span of the outer smaller sweep part of the wing. Lastly, as was described a bit in the intro, table 7.2 displays that the trailing edge flaps will be positioned based on the required span length the ailerons require.

Using the fact that the leading edge flaps are positioned along the full span of the outer wing part, equation (7.21) was used to find the $\Delta C_{L_{max}}$ for the leading edge flaps(result shown in table 7.2). Where $\Delta C_{l_{max}}$ is 0.3 [42] for normal leading edge flaps.

Due to the ailerons and the fuselage being present, not the full span was available for the trailing edge flaps. Therefore, the S_{wf} was calculated, which was still available for the trailing edge flaps. Furthermore, plain flaps were used, which have a $C_{l_{max}}$ of 0.9 [42]. Filling this together with some geometric parameters into equation (7.21) gives the results shown in table 7.2 for the $\Delta C_{L_{max}}$ from the trailing edge flaps. Table 7.2 also shows the $C_{L_{max}}$ that is achievable using the HLD's.

$$\Delta C_{L_{\text{max}}} = 0.9 \Delta C_{l_{\text{max}}} \frac{S_{\text{wf}}}{S} \cos\left(\Lambda_{\text{hinge-line}}\right) \tag{7.21}$$

Table 7.2: *Movable wing surface data.*

Outputs:	Value	Unit	Outputs:	Value	Unit
Ailerons:			**LE flaps**		
C_{l_p}	-0.6484	[-]	$\Delta C_{L_{\text{max-LE}}}$	0.072	[-]
$C_{l_{\delta_a}}$	0.0849	[-]	$b1 - b2$	$0.73232 - 1.83$	[m]
p	1.218	rad/s	**TE flaps**		
$b1 - b2$	$1.49 - 1.83$	m	$\Delta C_{L_{max-TE}}$	0.372	[-]
p_{req}	1.208	rad/s	$b1 - b2$	$0.5 - 1.83$	[m]
			General		
			$C_{L_{max}}$	1.3139	[-]

7.6. Control Surface Design

The canted fins can provide both longitudinal and directional control by using either a full moving fin or using ruddervators. It has been decided to use ruddervators, because a full moving fin will give too much controllability which is unnecessary and thus adds unnecessary extra weight/complexity. This resulted in a fixed tail configuration.

7.6.1. Ruddervator Sizing Recommendation

The ruddervators have not been sized in this stage of the design, however it will be in a fixed tail configuration and for now it has been chosen to use a ruddervator size of 30% of the tail area, as this was found to be in line with literature data [37]. It is recommended for the future design of the drone that the ruddervator design is carefully considered, as for now too little data was available for the sizing [44], [45].

7.7. Landing Gear Design

In this section, the landing gear configuration is chosen, sized and positioned based on the landing and take-off requirements, weight estimations, and centre of mass estimations.

7.7.1. Configuration

Various configurations are possible for the landing gear. The configuration is chosen based on two decisions [32, p. 10]. The first choice related to a fixed or retractable landing gear. For the RAD a retractable landing gear is chosen because of the high drag that is paired with a fixed landing gear. A retractable landing gear has minimal aerodynamic drag, high weight, and high complexity [32, p. 11]. The second decision to be made is about the type of landing gear. The types considered for the RAD are tricycle, bicycle, and tail gear. Other types like air cushions or tracks were already omitted during the early design stages.

Bicycle type landing gears need outrigger gears that are stored in the wings during flight. Due to the design of the wing this was deemed not possible and therefore, the bicycle type was omitted. A comparison between the tricycle and tail gear types was done, which showed the tricycle gear as the better option. The mean reasons were that the storage of the landing gear in the tail gear type was not optimal with respect to the design of the RAD, and the better controllability after touchdown for the tricycle type [32, p. 11].

Due to the low weight of the RAD, a conventional wheel layout is used. This means that only 1 nose wheel and 2 (1 for each strut) main wheels are needed [46, p. 28]. As prescribed by RAD-TE-OTH-01-02 [3], no arresting hook needs to be present on the RAD.

7.7.2. Sizing and Location

To size the tires, the maximum static load for each wheel was determined. Then the tires were sized, using the method from [47], and comparing the results to other UAVs with similar weights like the X-47 Pegasus. The nose tire has a diameter of 280 mm and a width of 100 mm. The main wheels have a diameter of 340 mm and are 120 mm wide. With this tire choice, the aircraft will be able to taxi on a paved taxiway, as prescribed by RAD-TE-OTH-01-01 [3]. For this stage of the design, it is assumed that these tire sizes will be able to carry the dynamic loads related to landing and take-off.

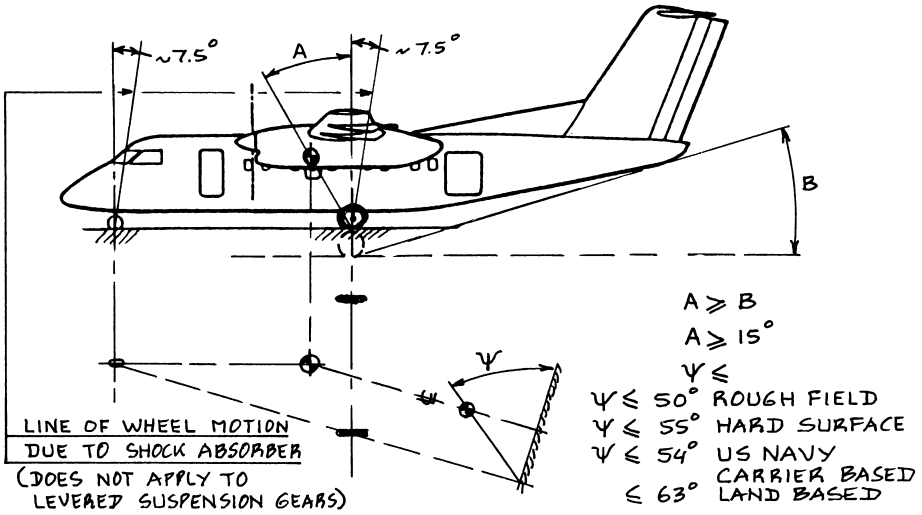

Figure 7.6: *Tricycle landing gear position requirements [32, p. 76]*

Several requirements are in place that determine the location of the main wheels and nose wheels. These are based on figure 7.6 Firstly, the turnover angle of the landing gear configuration shall not be more than 63 degrees for land-based aircraft [48, p. 37]. Also, the scrape angle shall not be lower than 15 degrees with the main gear struts fully compressed [32, p. 76]. Finally, the nose wheel shall be placed such that it will carry a minimum of 8% and a maximum of 15% of the aircraft weight [48, p. 28]. As a result of a combination of these requirements and the available space in the fuselage, the final layout described in table 7.3 is chosen. Note that the coordinates are described from the nose of the aircraft and the fuselage centreline.

Table 7.3: *Landing gear location from taking the nose as reference point.*

x - main wheels	4.265 mm
x - nose wheel	2.588 mm
y - main wheels	531 mm
z - main wheels	950 mm
z - nose wheel	980 mm

The nose gear folds forward when stored. A benefit of this is that, in case of a hydraulic failure, the nose gear can be extended by using gravity and placing it in the wind stream. The main landing gear folds forward as well. However, it is turned slightly to be able to store the wheels into the fuselage. Figure 7.7 gives a visual representation of the landing gear locations.

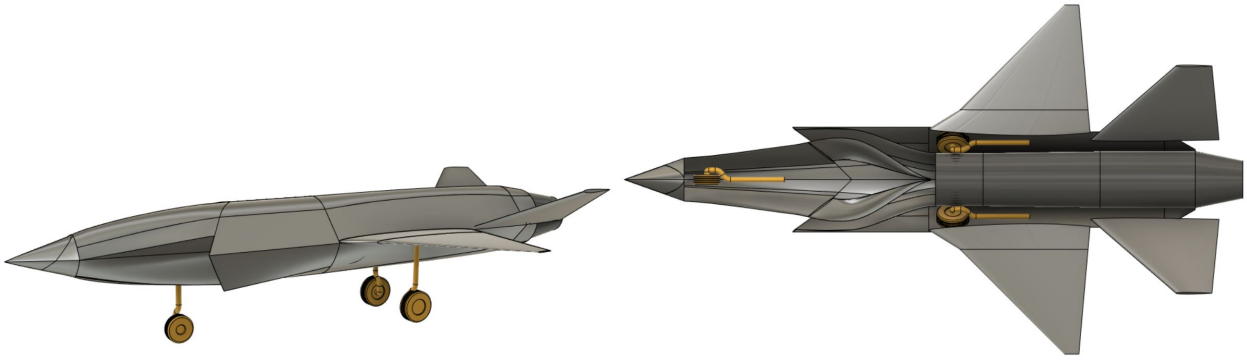

(a) *Extended* **(b)** *Stored*

Figure 7.7: *Landing gear location*

7.8. Conclusion and recommendations

It is recommended to calculate the control and stability in the supersonic case as well. This has been neglected for now, as the DATCOM methods [24] for supersonic stability required a lot of parameters, which were considered too detailed for this stage of the design. The sizing of the canted fins should thus be checked more carefully for a final design of the drone before it can enter production.

For estimating the vertical tail size, only the lateral stability aspect was considered. This is a general applicable equation to any aircraft, as each aircraft must possess stick-fixed and stick-free directional stability in normal operational conditions. Finding the required vertical tail size for crosswind landings using methods from [41] was not possible due to the absence of some control derivatives, which are also too complex at this point of the design to use the DATCOM method to find them. To get a better idea of the exact vertical tail size and to meet the crosswind requirements, it is recommended to do the crosswind landing sizing.

To improve the aileron design, it is recommended to find the new function c(y), as the c(y) function used is the one for the wing of the previous iteration. Furthermore, structures must be taken into account for ailerons, so they cannot extend up until the end of the wingspan and go up until the rear spar chord wise. Also with the approach taken the ailerons are designed separate from the HLDs, it is however better and easier to use flaperons.

For the next stages of design, it is recommended to investigate the tire choice. For example, the rim dimensions, dynamic loading, deformations, and tire profile. For this preliminary sizing, only the aircraft weight and landing speed were considered. Furthermore, the current tire choice must be validated regarding the landing speeds because assumptions were made with respect to the load bearing capabilities of the chosen tire sizes.

8 Structures of the UAV

In this chapter, material selection, structural design of the wing, the fuselage and the empennage is described. The driving requirements in the structural design and material selection can be seen in 8.1. Section 8.1 describes the different types of materials that can be used in the RAD, and in what scenario they should be used. Next, section 8.2 describes the process that was used to design the structures in the wing. Finally, sections 8.3, and 8.4 give recommendations on the design of the empennage and fuselage structures respectively.

The considered loads in the structures use an ultimate load factor, n_{lim} of 6, and with a safety factor of 1.5, the ultimate load factor n_{ult} becomes 9.

Table 8.1: *Requirements for the material selection and the structure of UAV to be considered.*

ID	Description
RAD-TE-PER-04	The RAD shall withstand loads/accelerations as specified by the stake- holders.
RAD-TE-PER-04-01	The RAD structure shall be able to withstand load factors during operation.
RAD-TE-PER-04-01-A	The RAD structure shall withstand load factors lower than -1.
RAD-TE-PER-04-01-B	The RAD structure shall withstand load factors higher than 6.

8.1. Material selection

This section analyses the different material categories that are considered for the RAD. The analysis is only made for metals and composites, as the other design options were eliminated in the previous design stage due to them not being feasible for the design. Important aspects of each material are assessed, and important advantages and disadvantages are listed.

8.1.1. Metals

For the metals' category, 3 metals are considered: aluminium, titanium, and steel. There are some characteristics that all these materials have in common. First, most metals are ductile. This gives them a natural damage resistance, as the metal will deform before it breaks. Secondly, the metals considered here, can all be recycled easily. furthermore, metals can be welded, and can be machined much easier than composites, making them far easier to use in manufacturing. Lastly, metals are reflective to radar waves. This effect can be both desirable and undesirable, depending on the design of the aircraft.

When comparing the different metals, four important criteria are considered, density, Young's modulus, yield strength, and fracture toughness. From these criteria, three additional indexes are derived. These are the tension index, the bending index, and the plate bending index. These indexes are measures of the stiffness of the material with respect to the density. The higher these indexes score, the lighter the structure made from the material can be for a given stiffness. The stiffness indexes are calculated using equations (8.1), (8.2), and (8.3) [49]. Fracture toughness is the resistance of a material to propagate an existing crack [50]. While this criterion has no direct impact on the structural performance, it plays an important role in the damage tolerance of the material. Furthermore, it is a determining factor in how often the aircraft will need to be inspected. Therefore, while having no direct impact on performance, it is still an important aspect of the design.

$$\text{Tension index} = \frac{E}{\rho} \quad (8.1) \qquad \text{Bending index} = \frac{E^{1/2}}{\rho} \quad (8.2) \qquad \text{Plate bending index} = \frac{E^{1/3}}{\rho} \quad (8.3)$$

The criteria and indexes found are reported in table 8.2. And will be used in the rest of the metals trade-off discussion.

Table 8.2: *Material properties of the considered metals [51, pp. 1176–1180].*

Material	Density	Young's modulus	Yield strength	Fracture toughness	Tension index	Bending index	Plate bending index
Unit	$[kg \cdot m^{-3}]$	[GPa]	[MPa]	$[MPa \cdot m^{\frac{1}{2}}]$	$[MPa \cdot m^3 \cdot kg^{-1}]$	$[MPa^{\frac{1}{2}} \cdot m^3 \cdot kg^{-1}]$	$[MPa^{\frac{1}{3}} \cdot m^3 \cdot kg^{-1}]$
Aluminium	2,500-2,900	68-82	30-500	22-35	23.44-32.8	0.09-0.115	0.014-0.017
Titanium	4,400-4,800	90-120	250-1,200	14-120	18.75-27.3	0.063-0.079	0.0093-0.0112
Steel	7,600-8,100	190-210	170-1,000	62-150	23.5-27.6	0.054-0.06	0.0071-0.0078

Aluminium

Aluminium has the lowest density of all the metals considered. On its own, density is not an important measure. However, as can be seen in figure 8.1, there is a linear relation between the density of the metals that are considered in this trade-off, and the Young's modulus of the metals. Therefore, aluminium has the largest stiffness indexes. The biggest downsides of aluminium are the yield strength and the fracture toughness. With the lowest yield strength, aluminium will need the largest volume of the materials to resist the same load. The fracture toughness is the lowest as well-meaning, the airframe will need to be inspected more often compared to other metals.

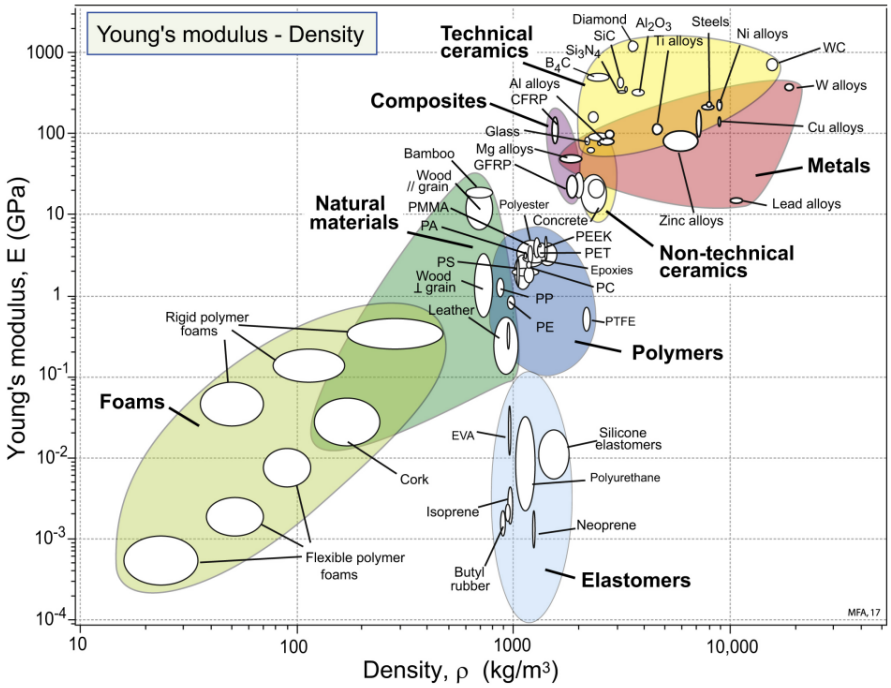

Figure 8.1: *Young's modulus-density chart [51, Fig. 4.8]*

Titanium

Titanium has by far the highest yield strength with respect to its density. Furthermore, it has a higher fracture toughness and heat resistance than aluminium, and higher stiffness indexes than steel. This makes titanium an excellent material for an airframe. Cost, however, is what makes titanium not feasible for most designs. The price per kg of titanium is four times higher than that of stainless steel, which is in itself up to ten times more expensive than other steels, and ten times higher for aluminium. Furthermore, titanium parts are more difficult to manufacture than aluminium parts, further increasing the cost.

Steel
Steel has the lowest stiffness indexes of all the metals considered. Furthermore, it has the lowest yield strength compared to the density of the material. This makes it generally too heavy to be considered for aircraft. Next to this aspect, steel parts are more difficult to manufacture, and more expensive than aluminium parts, further driving up the cost. The redeeming factors of steel are the high fracture toughness and heat tolerance. Therefore, the only components for which steel should be considered are components that are limited in size, need high heat tolerance, or need a high fracture toughness.

8.1.2. Composites
Composites are typically made of fibres that are combined in a resin. These fibres can be short fibres, long fibres, or continuous fibres. In this analysis, only continuous fibres will be considered. The build-up of these composites has large implications on the performance of the material. As the bulk of the strength comes from the fibres, composites have low performance in the direction that is transverse to the fibres and a high performance in the longitudinal direction. This anisotropic behaviour can be mitigated by layering these fibres at different angles. Using this method, quasi-isotropic behaviour of the material can be reached. While the quasi-isotropic composites can reach performances that are higher than those of metals, composites are brittle, meaning higher design margins are often needed.

Composites have clear advantages over metals. They can be specifically designed for the load that they will have to resist, making them far lighter than metals in an anisotropic situation. Furthermore, using modern techniques, composites can even be considerably lighter in quasi-isotropic tension cases. Even though, composites have high performance, they have downsides. Composites are brittle, making them more sensitive to failure than ductile materials that deform before braking. Furthermore, composites have a low heat resistance, making them infeasible in and around heat sources.

In this section, composites are generalised. This is done because the strength and properties are highly dependent on the makeup of the composite. However, an important difference between carbon fibre and glass fibre should be noted. Glass fibre is transparent to radar waves while carbon fibre is reflective. This means that glass fibre would be a perfect material for the radome. However, when glass fibre is used for other parts of the aircraft, radar waves could reflect on the internal structure of the aircraft, possibly increasing the radar cross-section. Because carbon fibre reflects radar waves, it is unsuited for the radome, but better suited for other parts of the aircraft.

8.1.3. Trade-off Criteria
When choosing a material for the different parts of the aircraft, one should mostly consider the total mass that the structure will have. Having a lower mass will have a snowball effect on all other parts of the aircraft, making the wings smaller for the same wing loading, needing less thrust for the engine, overall improving the performance of the aircraft. However, the cost of the construction and operation of the aircraft should be considered as well. For example, building the entire aircraft of titanium could increase the performance. However, titanium is several times more expensive than other alternatives, as discussed in subsection 8.1.1. Similarly, the cost of operation should be considered. If a component is highly sensitive to fatigue, a heavier component that requires less maintenance could be considered as a means of operational cost reduction.

The ultimate goal of this DSE is to develop a system that is not only more sustainable, but also less expensive to operate, while fulfilling the top-level requirements. In the end, it is up to the designer to come up with a final design that balances these criteria to achieve an optimal design.

8.2. Wing Structure
The purpose of the structure in the wing is to support the shape of the airfoil, and to provide a load path between the skin that produces the aerodynamic loads based on the pressure distribution over it and the rest of the aircraft.

Due to the time constraints of the DSE, the group could only come up with a first layout of the wingbox structure. The methods used to get to this design are outlined in this subsections 8.2.1 to 8.2.4. The verification and validation of this layout is discussed in subsection 8.2.5. Information on the aeroelastic structural instability, and

an analysis of the frequency response of the wing, are subsequently given in 8.2.6. Finally, recommendations on the further development of the wing structure is given in subsection 8.2.7.

8.2.1. Design Loads and Loading Diagrams

The wingbox is the primary loading structure within the wing that must withstand the lift forces, drag forces, and wing weight. The drag force is assumed to be significantly lower than the lift force, such it does not require any special analysis. Assuming that the lift produced is equal to the weight of the aircraft and taking into account the design load factor of six and a safety factor of 1.5, resulting in an ultimate load factor of 9, the wingbox has to transfer $n_{\text{ult}} \cdot \text{MTOW} = 9 \cdot 20856.06$ N = 187704.54 N of lift force. Using the lift distribution provided for subsonic conditions by OpenVSP that can be seen in figure 8.2, internal forces and moments can be calculated. For the subsonic regime, the aerodynamic centre of a wing section is assumed to be at the quarter chord point. This assumption is valid as the airfoil chosen is very thin, therefore thin airfoil theory is applicable. In the supersonic regime, the aerodynamic centre moves to half-chord. The subsonic regime was identified as being more critical as the lift force creates bigger torsion due to bigger moment arm to the centre of gravity of the wingbox, which was assumed to be at the centroid of the wingbox.

The lift distribution is shown for the whole wing span, however only the part from y > 0.5 m is the exposed wing and the part for y < 0.5 m is the fuselage. The lift distribution leads to internal shear force, and moment distribution. In combination with airfoil moment around the aerodynamic centre, it also contributes to the torsion distribution about the centroid of the wingbox.

8.2.2. Structural Simplification

In order to quickly analyse and iterate wingbox shape, a structural idealization is made, in which skin and spars are considered to have zero thickness and all the area is concentrated in booms. Boom area is defined using equation (8.4) where t_D is thickness between ith and jth boom, b is the distance between them and σ_j and σ_i is the normal stress ratio between adjacent booms. This normal stress ratio can also be obtained by taking the ratio of the booms' distances from the neutral axis. In this analysis it is assumed that the wing shape is symmetrical, therefore wingbox is also symmetrical. While the whole airfoil is not symmetric, between 20% and 70% of the chord, the shape is almost symmetrical. Therefore, this assumption was found to be reasonable for the first configuration. These percentages are also the chord locations of front and back spar they were chosen based on the height of the airfoil at that location, and on the required space for leading and trailing edge high lift devices. Furthermore, the wingbox is simplified to two trapezoids that lay inside the wingbox. This is also a conservative simplification, as the moment of inertia resulting from this will be smaller than the real value.

$$B_i = \frac{t_D \cdot b}{6} \cdot \left(2 + \frac{\sigma_j}{\sigma_i}\right) \tag{8.4}$$

8.2.3. Stresses in the Structure

In the wingbox a combination of compression stresses due to bending and shear stresses due to torsion are present. To accurately predict failure criteria for a combination of these, Tresca failure criterion is used. It specifies that a material point yields when the maximum shear stress at that point reaches the maximum shear stress in a uniaxial tension specimen at yield [1]. In our case, the maximum shear stress allowable is a half of the yield stress.

8.2.4. Determining the Configuration

The material chosen for the wingbox is aluminium 6061-T6. Aluminium was chosen because the high plate bending index makes it a perfect material to make a wingbox. Furthermore, the low material cost and high manufacturability ensure that the production cost of the wingbox stays as low as possible. The type of aluminium chosen, 6061-T6 was chosen because of the high fracture toughness and high corrosion resistance. These characteristics reduce the maintenance costs.

The methods for the structural simplifications and the stress calculations as specified in subsections 8.2.2, and 8.2.3 were automated using python. Using this python code, iterations were made to find the required skin thick-

[1] Source: https://www.sciencedirect.com/topics/engineering/tresca-criterion (retrieved on 10 June 2022)

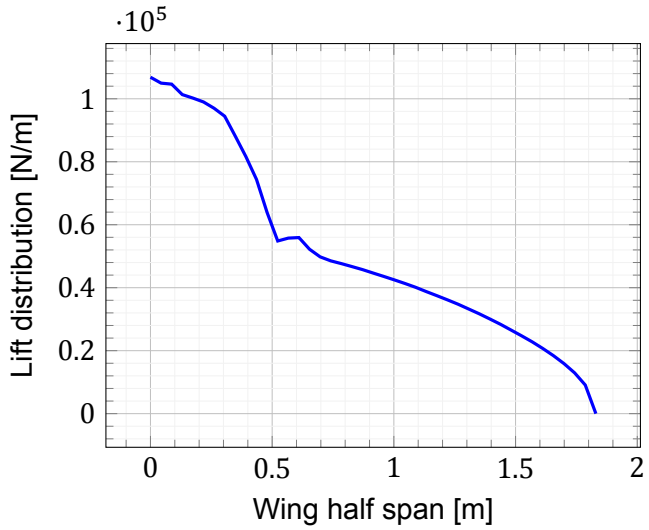

Figure 8.2: *Lift distribution at Mach 0.3, scaled for ultimate load factor.*

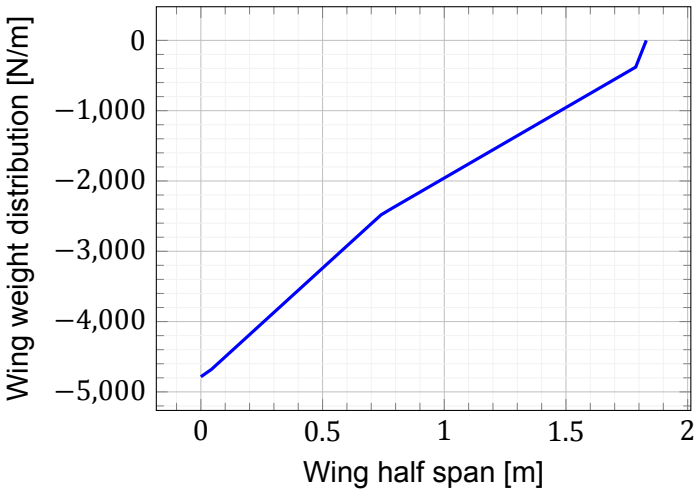

Figure 8.3: *Wing weight distribution at 9g normal load factor.*

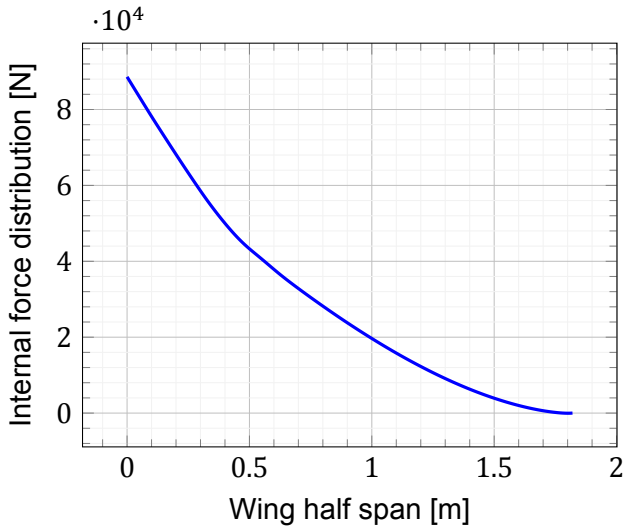

Figure 8.4: *Internal shear force in the wing due to lift.*

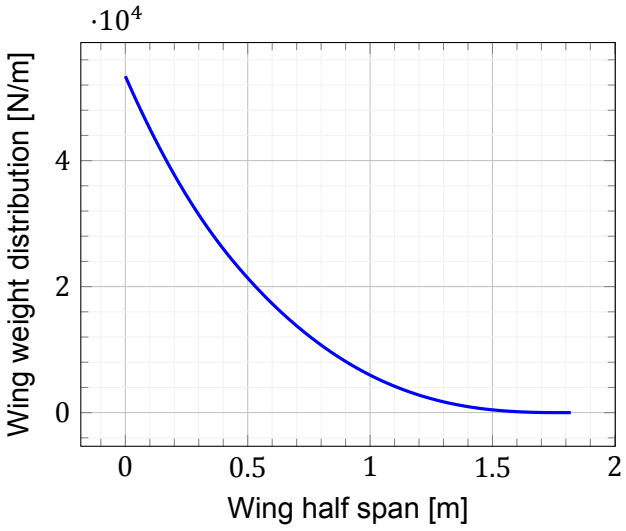

Figure 8.5: *Internal bending moment due to lift and airfoil moment around aerodynamic centre.*

ness for different spar configurations. After this analysis was done, the stringer size and pitch was determined using the methods described in chapter 9 of the book Aircraft Structures for Engineering Students [52]. Due to the small size of the wing, the stringer size was found to be very similar to the spar size. Therefore, the spar configuration was chosen to be determined by the stringer pitch. The result of this analysis can be seen in figure 8.6. Five spars were chosen to be equally spaced across the distance between the front spar and the rear spar at the kink of the wing, located 1.1 m from the tip of the wing. Then, A final spar was added from the rear spar to the root of the wing starting at the kink, to provide buckling stability in the section closer to the root of the wing. These six middle spars are parallel to each other at the angle of the bisection of the front and rear spar. This configuration causes some spars to end at the front or rear spar as they progress through the wing. This way, there is a natural end to the spars, reducing the number of spars closer to the tip of the wing. Furthermore, the spars don't abruptly end, reducing stress concentrations.

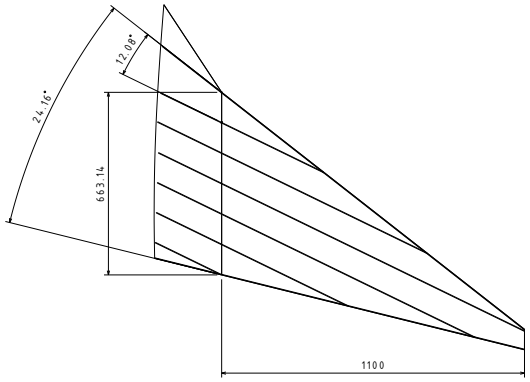

Figure 8.6: *Wingbox layout.*

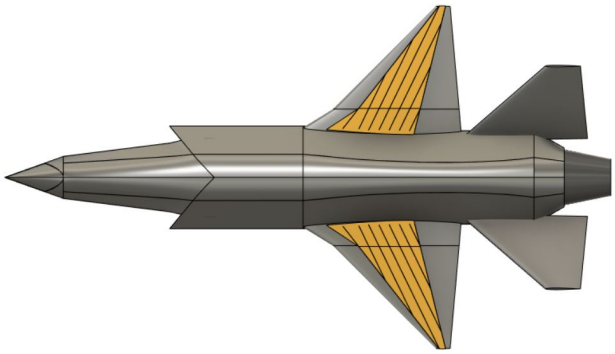

Figure 8.7: *Location of the wingbox with reference to the aircraft.*

The skin thickness found in the analysis was 3 mm. Because the spars experience similar loads to the skin at the point where they attach to the skin, the spars were chosen to be the same thickness as the skin. Calculations were made for shear buckling for shear buckling stability of the spars. However, due to the small size of the wing, it was found that no stiffening elements are needed to prevent shear buckling in this configuration. The total combined weight of both wingboxes in this configuration is 46 kg, and the total fuel capacity is 80 kg A summary of the configuration is given in table 8.3.

Table 8.3: *Overview of the wingbox configuration*

Part name	Length [m]	Thickness [mm]	Material
Lower skin	1.55	3	Al-6061T6
Upper skin	1.55	3	Al-6061T6
Leading edge spar	1.65	3	Al-6061T6
Spar #2	0.65	3	Al-6061T6
Spar #3	1.07	3	Al-6061T6
Spar #4	1.47	3	Al-6061T6
Spar #5	1.21	3	Al-6061T6
Spar #6	0.76	3	Al-6061T6
Spar #7	0.27	3	Al-6061T6
Trailing edge spar	1.42	3	Al-6061T6

8.2.5. Verification and Validation of the Simplified Model

The verification and validation procedures outlined in the baseline report [3] were used to verify and validate the simplified structural analysis. The verification of the simplified model analysis code was done by creating a simple wingbox shape and doing the full analysis of this simplified wingbox by hand. At each part of the simulation, the results of both analyses were compared. Finally, the final results of both analyses were the same, ensuring that the analysis code worked as intended.

This verification does however not guarantee that the simplified analysis gives a realistic result of the wing performance. Most of the assumptions that were made in the analysis of the wingbox structure were conservative. This was done intentionally for two reasons. First, making assumptions that are not conservative may lead to a design that fails before the ultimate load. Second, making conservative assumptions leads to early iterations being heavier rather than lighter. This means that the structural mass will go down instead of up, causing a snowball effect in the lighter direction instead of in the heavier direction.

To validate these expectations, a FEM analysis was done on the wingbox structure, a visualisation of which can be seen in figure 8.8. The loads in the analysis were including the design safety factor of 1.5. Hence, the factor of safety shown in figure 8.8b shows the structural margin on top of the already provided safety factor of 1.5.

Before discussing the results, limitations of the FEM analysis must be elaborated on. First, a FEM analysis is an approximation. In a FEM analysis, the model is meshed into small elements which are analysed. If the mesh size is too large, the analysis will be inaccurate. Second, the elements in the wingbox are defined as a 2D shell that is given a thickness. Because of the large surface of the elements compared to the thickness, a 3D mesh would simply be too large to analyse the structure accurately. As a result, no distinction is made between the different sides of the spars and the skin. This assumption can be considered valid if the structure is thin walled. The closer to the tip of the wing, the less accurate this assumption is. Third, perfect contact is made between the spars and the skin of the wing. This means that stress concentrations that are induced by rivets or screws are not considered in the analysis. Next, the lift is distributed as a pressure across the bottom side of the wing. Because no precise chordwise pressure distribution was available at this stage of the design, the analysis distributes the pressure evenly across the chord. Lastly, the wing skin and the spars are perfectly clamped at the end of the wingbox. As a result of this last assumption, there are stress concentrations at the end of the spars which do not accurately depict the real expected loads.

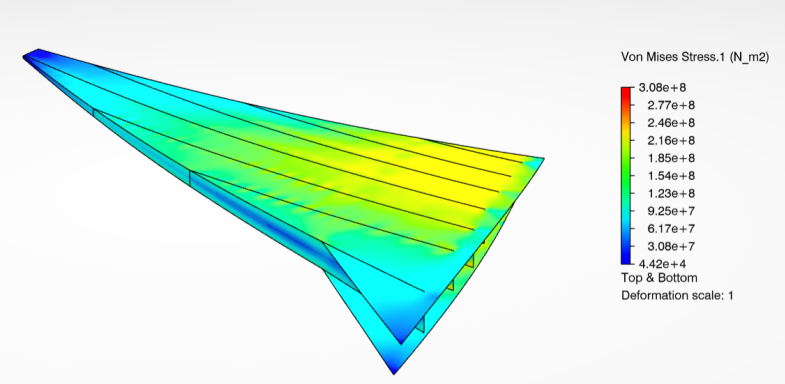

(a) *Von Mises stress*

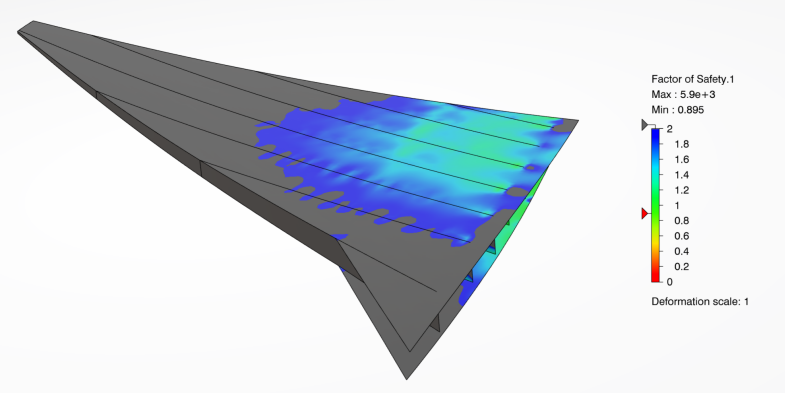

(b) *Safety factor of the result*

Figure 8.8: *FEM analysis of the wingbox*

The result of the FEM analysis confirms that the assumptions made were conservative. The simulated stresses around the kink of the wingbox are only 83% of the expected stresses in that region. The large discrepancy between the obtained stress using the FEM analysis and the simplified analysis likely arise from the simplified shape of the wingbox. The minimum safety factor of 0.895 that is shown, at which the structure supposedly yields, only occurs at the end of the spars in the region where the resulting stress is not valid as was previously discussed.

8.2.6. Dynamic Instabilities

In order to design a structure that can withstand the combination of mutual interactions within the inertial, elastic, and aerodynamic forces acting on structural members, the dynamic (in)stabilities like flutter, buffeting and the dynamic response of the system must be considered [52]. Aeroelastic problems play important roles in the flight envelope of aircraft structures, their design, and safety. If the aeroelastic divergence becomes theoretically infinite, the wing fails. Therefore, in the design, dynamic response of the wing must be considered.

To estimate dynamic response of the wing, FEM simulation in Catia is set up. The lowest natural (fundamental) frequency of the wing is 47 Hz, in a bending mode.

When considering flutter, design options like adjusting spars such, they do not coincide with quarter chord help to increase the damping ratio of the wing and therefore increase critical flutter speed. However,

8.2.7. Further Wing Structure Development

Due to the limited time that is available, only one iteration of the wingbox structure could be performed. As a result, the wingbox design is far from optimal. In this subsection, recommendations are given for future iterations of the wingbox structure.

With the layout of the wingbox known, the next step of the design is to make a more accurate analysis model. This model should consider the real shape of the airfoil and the position of the spars. With a more accurate model, the thickness of the spars and skin should be chosen more accurately. Furthermore, as the loads reduce closer to the wing tip the thickness of the spars and skin should be gradually reduced along the wing to save mass.
As the resolution of the design of the wingbox progresses, other weight saving measures like making holes in the sections of the spars that are not heavily loaded should be considered. Finally, as attachment and connection points of the wingbox elements are sized and spaced, special care should be taken that the stress concentrations caused by rivet or screw holes do not cause failure in the wingbox. Rib like elements should be considered at the root or across the wingbox to facilitate shear flow transfer between the spars and the skin of the wing.
Because of the leading edge, and trailing edge high lift devices, the leading edge and trailing edge are not considered to be load bearing. This does however not mean that the leading edge, and trailing edge will not be loaded. When designing the leading edge and trailing edge, they should be made to be less stiff than the rest of the wingbox. This lower stiffness will cause them to take lower loads and, hence, fail after the wingbox would fail.

The chosen type of aluminium could be reconsidered as well. As was mentioned before, aluminium 6061-T6 has a high fracture toughness and high corrosion resistance. These aspects reduce the operating cost, as this means the wingbox will require less maintenance. However, there are types of aluminium, like 7075 or 7068, that have a higher yield strength. As the wing is already relatively light weight, the drawbacks of using this higher performance material, like inter-granular corrosion and worse manufacturability, may outweigh the advantage of lower weight that can be achieved.
Lastly, due to operational requirements, namely RAD-TE-OTH-03, which states that the RAD, or its components, shall fit inside a standard ISO.1AA shipping container (SSC) with dimensions 40 ft × 8 ft × 8 ft 6 in, the wing has to be detachable. The attachment points connecting the wing and fuselage should be between the fuselage frames that go around the engine and transfer the lift force and the wing spars. This will create some stress concentrations near the attachments, which must be carefully investigated. Also, it will add complexity to the HLD design, as all the fly-by-wire systems must be able to be connected and disconnected very easily. Not only that but also such a connection will add weight to the structure, however in the weight estimation, it was accounted for it and therefore, no snowball effect because of this is expected.

8.3. Empennage Structure

A V-tail style empennage configuration is used in the red air drone. The tail partially shields the engine, lowering its IR signature, however from a structural point of view this introduces thermal stresses to the structure. Due to time constraints of the DSE, no structure was designed for the empennage. This section outlines the design loads that are expected on the empennage and will give considerations on the future development of the empennage structure.

8.3.1. Empennage Design Loads

The main function of the empennage is to provide stability and controllability. Therefore, the main function of the empennage structure is to provide a load path for the control forces. In addition to this, the empennage creates drag, therefore the structure also must withstand the drag forces. Finally, special attention should be paid to the thermal loads on the empennage.

8.3.2. Further Empennage Structure Development

Because the loads and shape of the empennage are very similar to those found in the wing, the structural design of the empennage is very similar to the structural design of the wing. The largest difference between the wing design and the empennage design is that the loads can be applied in both the up and down direction. The main result of this difference is that the top and bottom skin must have the same buckling stability. The very small thickness of the empennage will likely cause the stringers to be as large as the spars, causing the same situation as in the wingbox where the spar spacing is determined by the buckling conditions. Using the spars for buckling stability will have a positive effect on the aforementioned buckling conditions in the bottom skin. When choosing the material for the empennage, special consideration must be given to the thermal loading of the engine on the empennage. Having a higher temperature in the material may cause the material characteristics to change negatively. If the thermal loads turn out to be significant, materials like steel or titanium could be used, as these materials provide better performance at high temperatures.

8.4. Fuselage Structure

The fuselage is the last part of RAD considered in the structure design. Firstly, the design load must be analysed. Then, the structure is design to transfer the design load. However, due to time constrains not a whole fuselage structure is designed, therefore recommendations are given for further development.

8.4.1. Fuselage Design Loads

Being a lifting body, the fuselage creates a non-negligible amount of lift. Furthermore, the fuselage produces drag. Especially in the transonic regime, the fuselage contribution to the overall drag is major due to its wave drag. The fuselage also must transfer loads from one wing to another, with the engine in the way. Next, the engine buried in the fuselage also produces thrust that must be transferred. The empennage connected to the fuselage produces torsional loads that must be transferred to the entire structure. Finally, the loads on the landing gear during landing, and when moving on the ground, must be transferred throughout the entire aircraft.

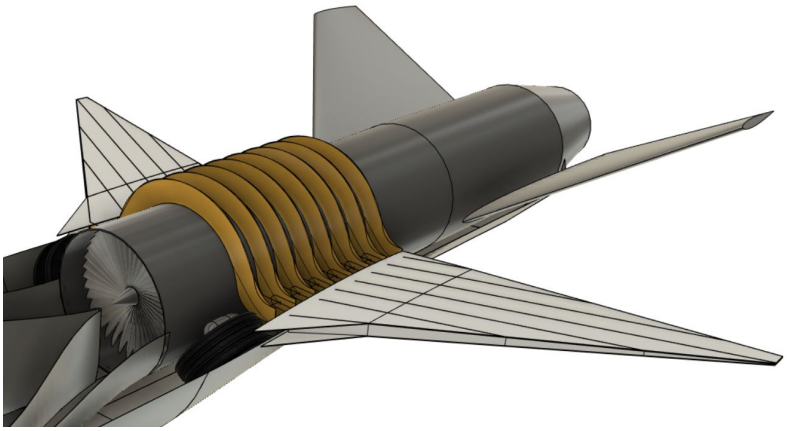

Figure 8.9: *Design of the fuselage frames, transferring the lift forces.*

8.4.2. Further Fuselage Structure Development

For future fuselage development, a more representative engine shape is needed. This would allow accurate sizing of the frames, that join the two wings, that go around the engine. Next, the connections between the empennage and the fuselage must be carefully designed, as they provide a load path mainly for torsional loads. Furthermore, the mounting points for the landing gear must be designed. The main landing gear attachment point is planned to be at fuselage frames that transfer lift loads, as they are already strong. For the nose landing gear this is not an option and therefore an attachment point has to be designed. The air inlet and the air duct are both supported by the fuselage; therefore, their loads must be analysed and designed for them. Lastly, the structure should be optimized for low observability, such that no energy that penetrates the skin is reflected.

9
Final Design Results

This chapter details the final design of the RAD. After the analysis of the different design aspects/subsystems of the drone some results become apparent. Firstly, section 9.1 outlines the finalized sizing of the RAD. Secondly, section 9.2 discusses the important low observability features found on the RAD for the chosen Genesis configuration. Thirdly, all systems interfaces are explained in section 9.3. Finally, section 9.4 looks at how the design performance changes if design parameters are changed by conducting a sensitivity analysis. The driving requirements can be seen in table 9.1

Table 9.1: *Requirements for the material selection and the structure of UAV to be considered.*

ID	Description
RAD-TE-LO-01	The red air platform shall be low observable in radar.
RAD-TE-LO-01-01	The geometry of the RAD shall be designed such that it has an RCS less than 0.1 m^2.
RAD-TE-LO-01-02	The RAD outer geometry shall use radar absorbing/deflecting materials/coatings to minimise the RCS such that it is lower than 0.01 m^2.

9.1. Final Sizing

The final design of the RAD results in the drawing depicted in figure 9.1. This design is established by combining all subsystems discussed in previous chapters. The figure shows the main dimensions of the RAD looking from different perspectives.

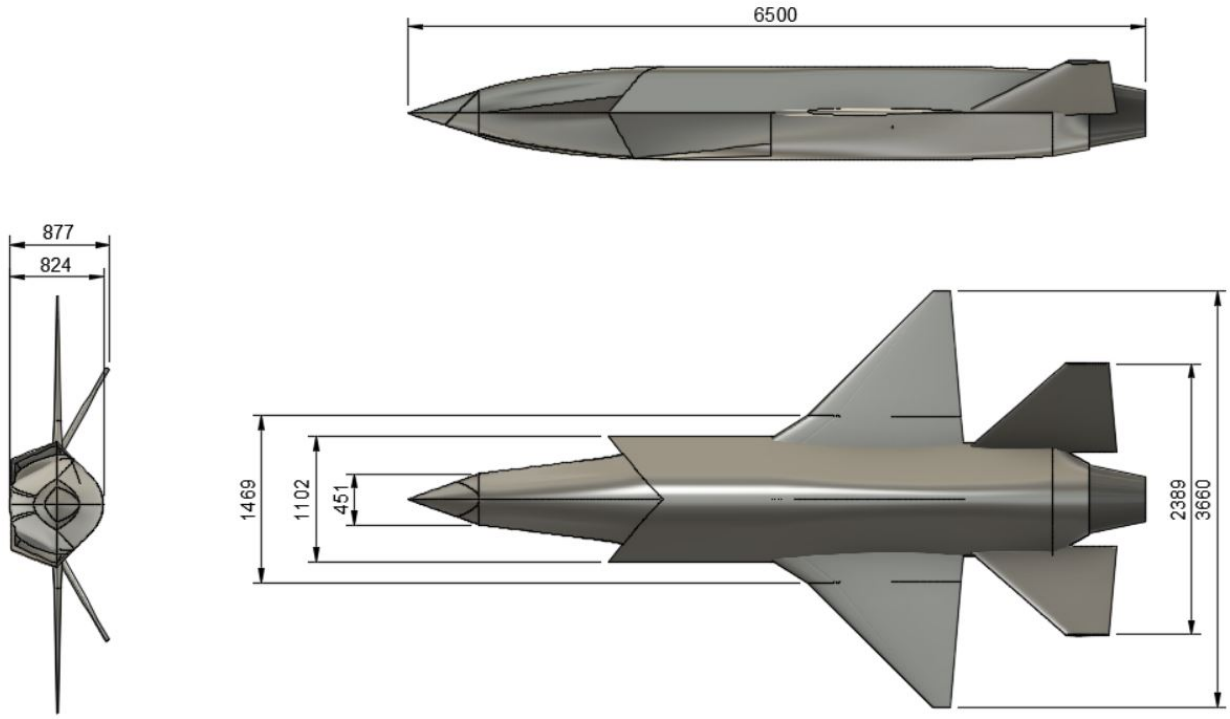

Figure 9.1: *Dimensions of the RAD body, the dimensions are in mm.*

It should be noted that the drawing in figure 9.1 does not include the payload, but is mere to give an overview on

the size and shape of the final design of the drone.

9.2. Low Observability

Since the early days of military aviation, engineers figured out that low observability is important to gain the advantage over the opponent. This was done in World War I already, for example, using cellulose acetate to create transparent canvases for aircraft such as the Fokker E.III to become less visible for other pilots to see the aircraft [53]. In modern aircraft camouflage is still used to blend in with the sky around the aircraft. However, in the present day beyond visual range combat is more common, instead of the human eye spotting an aircraft (although this can still happen when close), radar systems or infrared cameras on the aircraft take over this task.

Similarly, air-to-air missiles also use radar systems to guide themselves to their target. These can be integrated into the missile as seen in so called 'fire and forget' systems, for example in the AIM-120 AMRAAM or require assistance from the aircraft's radar as seen in missiles such as the AIM-7 Sparrow. Alternatively, infrared seekers are installed, and the missile guides itself to an infrared source it can see. Both can also be used in combination with each other [54].

For these reasons low observability against radar systems, infrared systems and the visual signature of the RAD are of vital importance in the design as without good low observability the design will lack capability to emulate current modern aircraft and future low observable aircraft. This is because the RCS of the RAD can always be increased using passive or active RCS augmentation, but it cannot be reduced. Hence the RAD is made low observable.

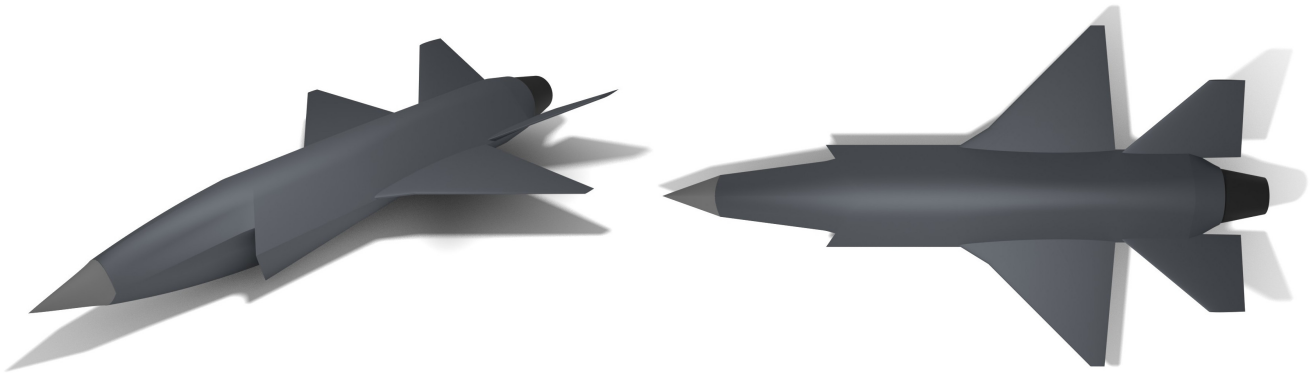

(a) *Isometric view of the RAD.* **(b)** *Top down view of the RAD.*

Figure 9.2: *The 3D views of the RAD.*

9.2.1. Stealth for Radar

To become low observable for a radar system, the reflected energy towards its receiver must be reduced as much as possible. There are multiple factors involved in figuring out the amount of energy that is returned to the receiver such as the transmit power, gain, polarization, signal losses, the amount of time the radar beam spends on the target (the dwell time), the radar cross-section, etc. All these factors are controlled by the radar operator except for the radar cross-section, which can be controlled by the designer. [1] For that reason, reducing the RCS of the RAD is important for minimizing the energy send back to the receiving antenna. To comply with the driving requirement RAD-TE-LO-01 it is assumed that a monostatic radar system is used and is operating at a frequency of 10 GHz. To comply with RAD-TE-LO-01-01, multiple design features are integrated into the design to reduce the radar cross-section and achieve the requirement.

When taking a look at figure 9.2a and figure 9.2b the first eye-catching feature is likely the sharp and grouped edges. The edges are paired in group and made parallel to each other as much as possible. Note the leading edge is aligned with the leading edge of the canted stabilizer but also the intake. The trailing edge of the wing is aligned with the trailing edge of the canted stabilizer.

[1] Source: https://www.radartutorial.eu (retrieved on 13 June 2022)

Another striking feature and a rather unconventional choice that catches the eye is that there is no horizontal stabilizer and a canted wing that combines both the vertical and horizontal stabilizers into a single canted tail. This wing is mounted under an angle of 30 degrees, which will reduce the RCS from a side perspective considerably. Another benefit is that the wing does not overlap the area of the canted stabilizer and therefore does not create a corner reflector, again reducing the RCS from the side perspective.

A point that is easy to forget but is very important is the structure behind the radome, as it is electromagnetically transparent to radar and is thus a source of energy that can reflect to the receiver. For this reason, the structure behind the radome is canted at an angle equal to that of the leading edge sweep of the wing, as seen in figure 9.3.

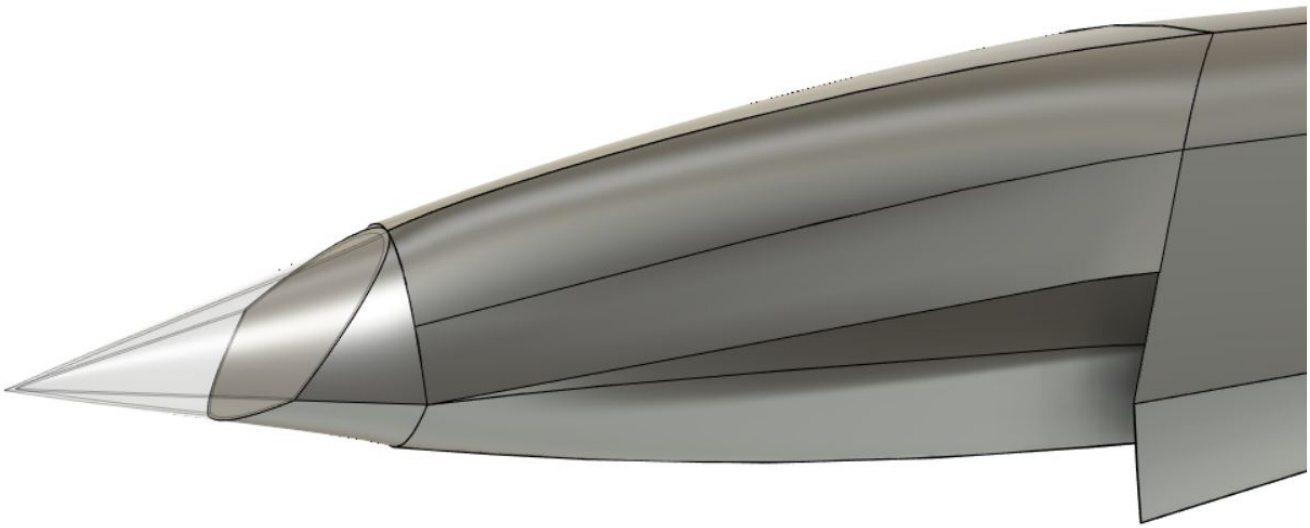

Figure 9.3: *Radome plate of the RAD.*

Moving onto the nose (see figure 9.5), curves can be noted as the aerodynamics benefit from this quite a lot. Faceted design was previously proposed but has not been chosen due to its poor aerodynamic performance and instead the nose section tries to create a constant varying radii curvature to reduce the head-on RCS. Think about your own reflection in a spoon, when rotating the spoon your own reflection disappears off the edge. Some parts are still visible however, since some of the energy will return to the receiver. Do this same thing with a sphere and your reflection can be seen all around. See figure 9.4 [2] as this same thing happens with the radar energy and therefore spreads out the radar energy more. However, this design option proved to be difficult to perfect with the tools available and requires further design steps such that it can be finalized.

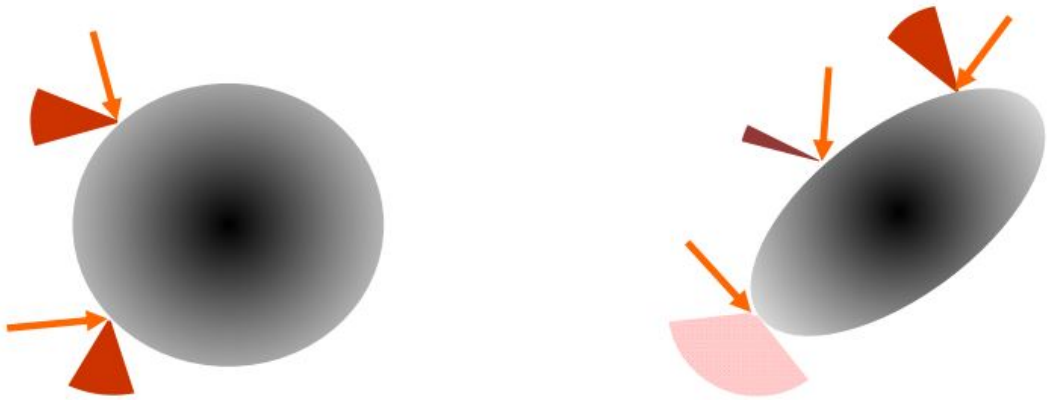

Figure 9.4: *Effect of non-constant radii curvature on radar reflection.*

[2]Source: https://understandingairplanes.com (retrieved on 13 June 2022)

Figure 9.5: *Side view of the RAD.*

A combination of this same technique and the faceted design has been used along the rest of the fuselage, as can be seen in the cross-section shown in figure 9.6.

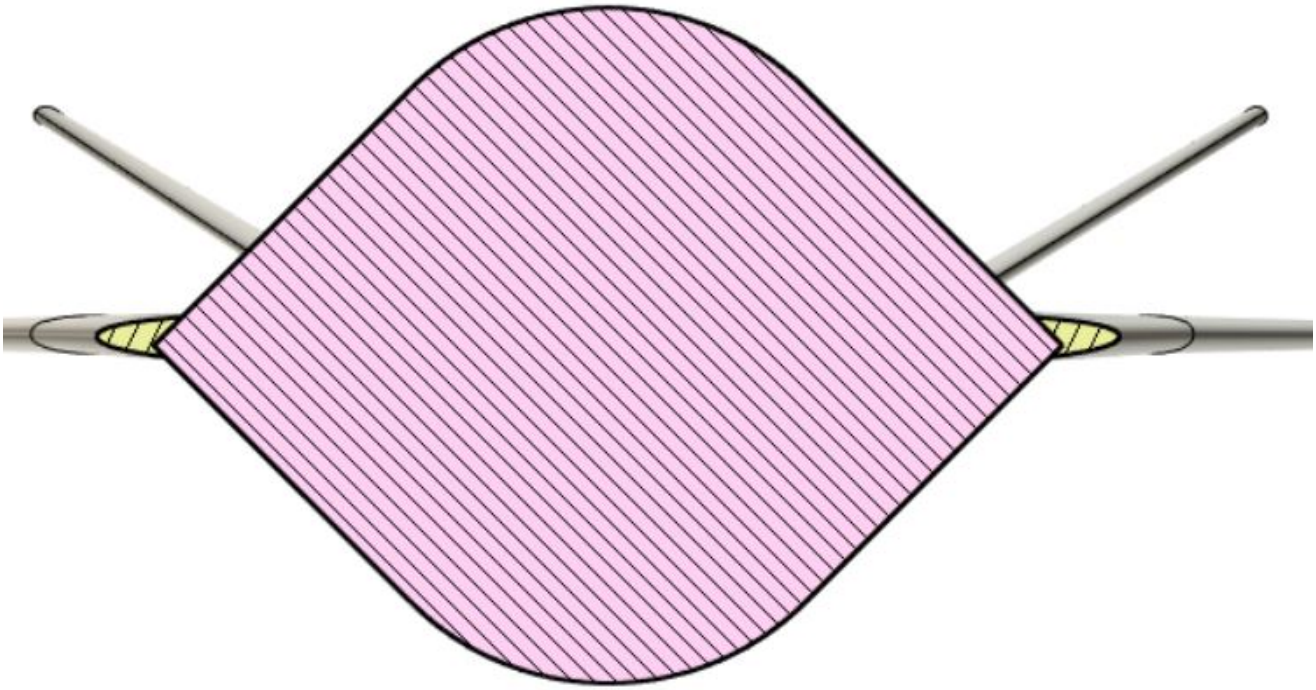

Figure 9.6: *Fuselage cross-section of the RAD.*

The outside of the RAD will be coated in RAM to absorb as much energy as possible. This coating will also be dull which, unlike a shiny metallic surface, spread the reflections out instead of shining them in a single direction. This also caused sunlight to be dispersed, making the aircraft less visible by the eye and prevents sun glare. These coatings are more effective at absorbing shorter wavelengths, as used by most fighters and air-to-air missiles [55], [56].

One of the critical parts in becoming stealthy is hiding the first stage of the engine compressor. Therefore, the intake is designed to have a serpentine y-duct design, see figure 9.7. This ensures that from the outside you cannot visually see the engine, the same applies to radar waves. Due to the curves, the radar waves bounce around inside the intake a lot and slowly lose more and more energy that can potentially be returned. To increase that effect, the insides of the inlet ducts will also be coated in RAM to absorb as much radar energy as possible. The reason the intake points forward has a little to do with low observability, it allows the intake to be shielded from side angles better. However, the main reason is to allow the y-duct to bend towards the outside than back inwards, making it harder to see the engine whilst using as little space as possible and creating more space in the nose of the aircraft. Unlike some other fighter aircraft there is no gap between the fuselage and the intake because a diverterless supersonic inlet was chosen meaning that the boundary layer is directed away from the intake. This helps low observability, as there are no cavities around the inlet where radar waves can easily reflect straight back.

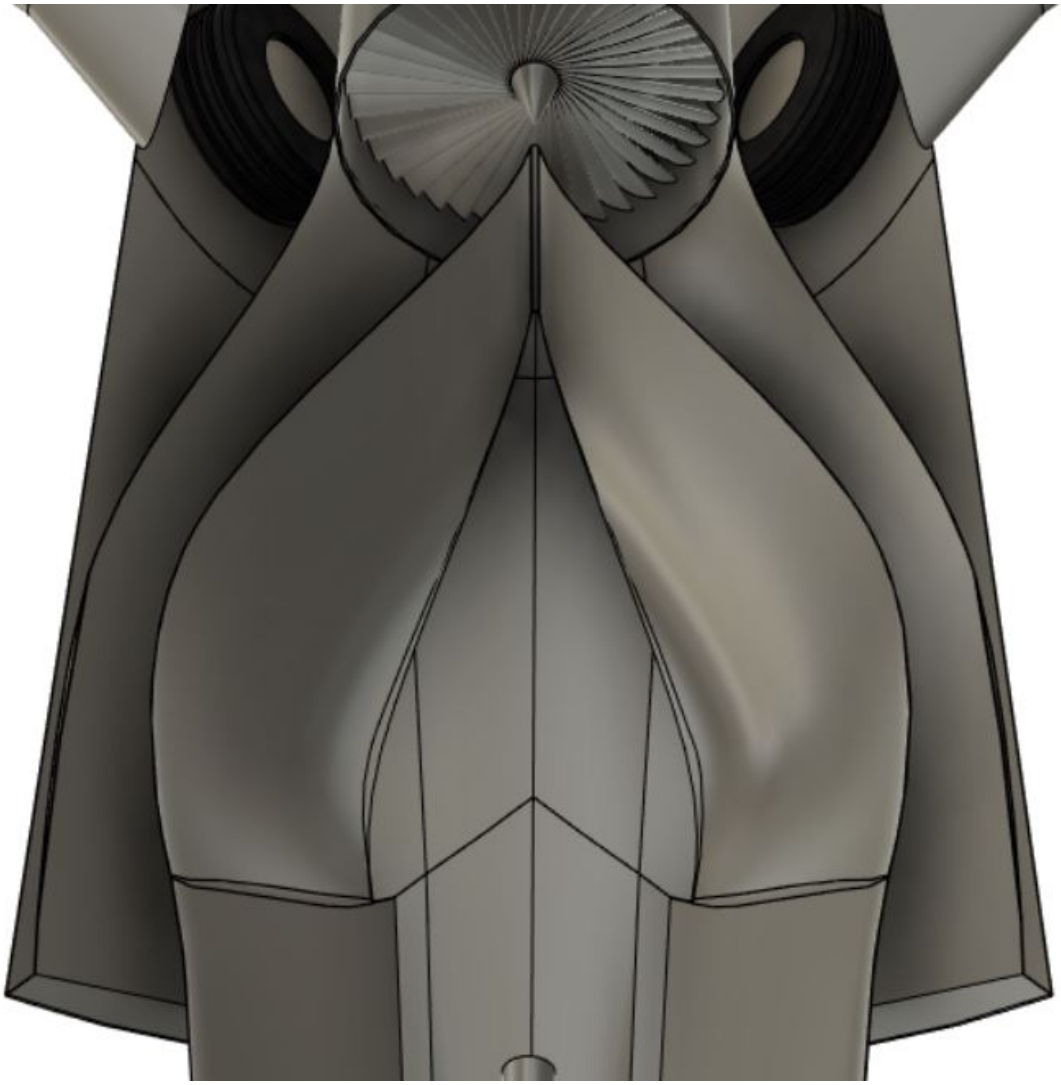

Figure 9.7: *Intake duct of the RAD as seen from a sliced plane.*

Lastly, the size of the RAD reduces the RCS a lot as well. It is after all a small UAV so compared to full sized red air fighter aircraft; the amount of energy returned to the receiver is due to the size a lot smaller already. This can be seen pretty clearly in figure 9.8.

9.2.2. Infrared Stealth

In the current day and age almost, everything uses radar but because these radar systems have become so advanced, and it is increasingly difficult to improve and counter the modern stealth aircraft's, a focus on infrared technology can be seen. It is therefore important to also be low observable in the infrared spectrum, especially for future proofing the design.

This is once again tricky to achieve and to predict as a bunch of factors affect it such as ambient conditions, therefore some simplifications are made. There are two main infrared sources for the aircraft, the engine exhaust and the RAD's skin during dashes. The body heat is difficult to predict, but the upper limit can be estimated using the stagnation temperature as seen in equation (9.1) [3] assuming that the ratio of specific heat γ is constant. From this, the temperature's in table 9.2 can be obtained.

For the engine exhaust, the engine exhaust gas temperature has been estimated using the propulsion model that has been built and described in section 6.4 and is shown in table 9.3. It is important to note that the mixing and cooling of the bypass flow has not been considered for these estimates and the temperatures are therefore overestimated. These temperatures are lower than the exhaust temperatures of the F404-400, which has an

[3]Source: https://www.grc.nasa.gov/www/BGH/stagtmp.html (retrieved on 13 June 2022)

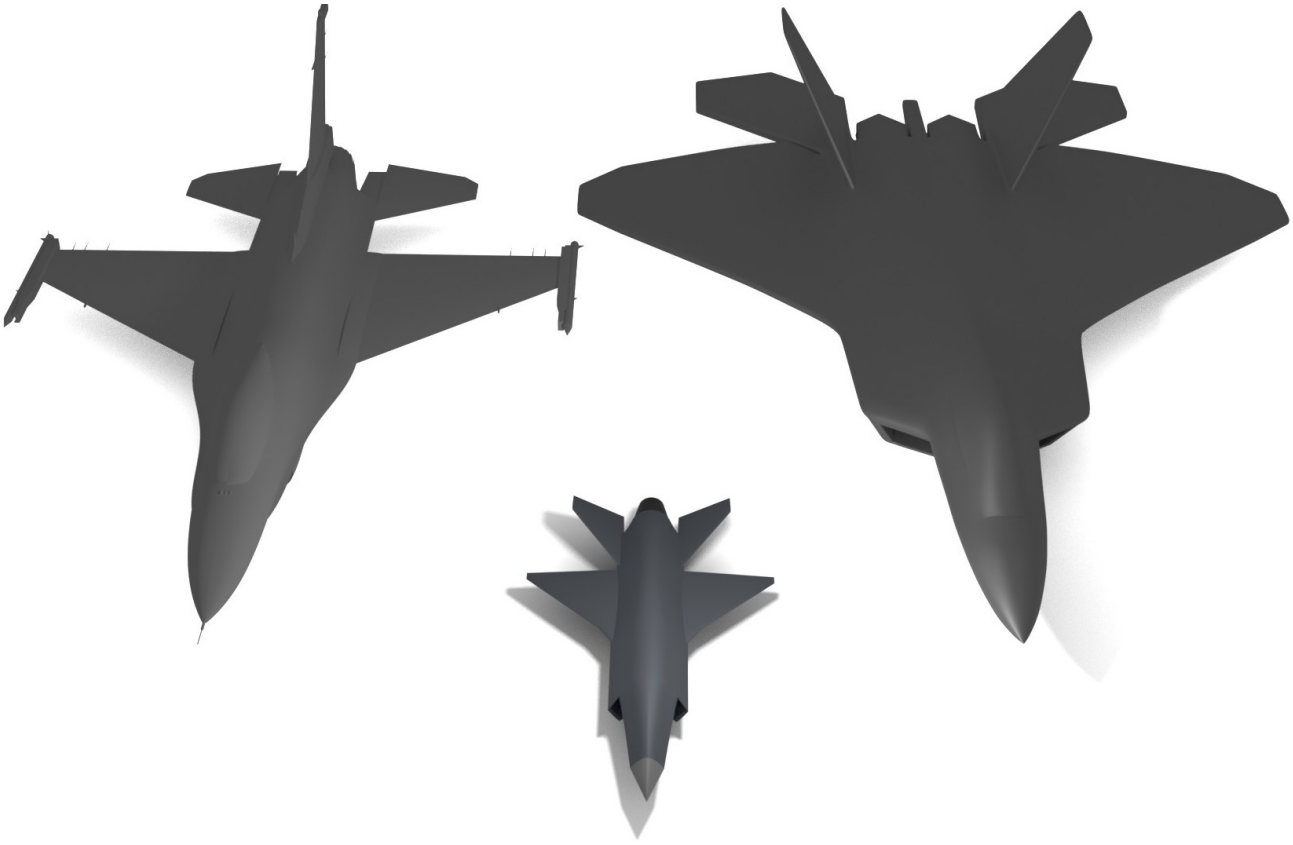

Figure 9.8: *The RAD with an F-16 on the left of it and an F-22 on the right of it at scale.*

exhaust temperature of 1,726 degree Celsius (2,000 K) [57] and is used in aircraft such as the F-117. To reduce the signature of the engine exhaust, the V-tail is partially detached from the fuselage and runs alongside the engine, hiding it from certain angles.

$$T_s = T[1 + \frac{M^2(\gamma - 1)}{2}] \tag{9.1}$$

Table 9.2: *Estimated body temperature at various flight conditions in the reference mission [4], using a +30 K ISA offset.*

Condition	Ambient temperature [K]	Body Temperature [K]
Cruise	292	313
Subsonic dash	246	291
Supersonic dash M = 1.6	246	372
Supersonic dash M = 2	246	443

Table 9.3: *Estimated exhaust gas temperature for various flight conditions.*

Condition	Exhaust Gas Temperature [K]
Cruise M = 0.9	942
Subsonic dash M = 0.95	872
Supersonic dash, full afterburner	1789

9.2.3. Augmentation

To replicate the low observability performance of several red air aircraft, the RCS or IR signature may want to be augmented to get a more realistic representation of the aircraft that is being emulated. In the case of the RCS, it is also important during transport or other operations where an air traffic controller wants to see the RAD on its radar system. For this reason, the RAD also carries with it a transponder.

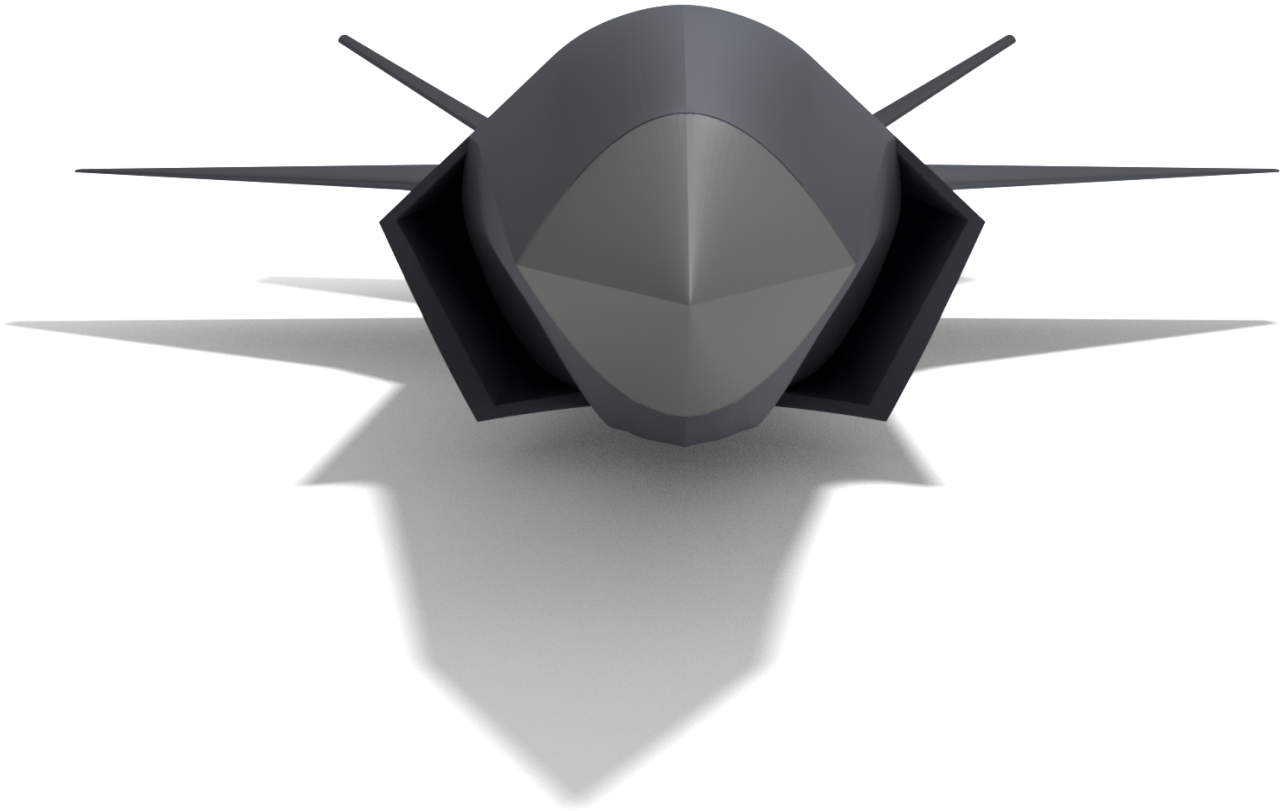

Figure 9.9: *Front view of the RAD.*

For this purpose, it is proposed to use Luneburg lenses. These lenses reflect radiation in the direction that it came from all angles and is therefore perfect for use during operations where stealth is not desired. For red air this may however not be desirable as you lose your stealth capabilities and instead one wants to emulate the peaks that form on the polar plot of the emulated red air aircraft. Corner reflectors may work for this purpose but are not ideal due to its wide range of angles on which it will increase the RAD's RCS. This can instead be achieved using dihedral corner reflectors or a simple small flat plate. The dihedral corner reflectors will increase the RCS at a small range of angles in one direction but a wide range of angles in the other. This wide range can be tuned by increasing or decreasing the angle between both plates whilst a single small flat plate will only show a peak in a single direction.

For the infrared augmentation a simple infrared lamp can be used to augment the signature at the exhaust. This lamp will have to be placed close to the engine, for instance integrated into the vertical tail.

9.2.4. Results and Recommendations

To simulate the radar cross section, electromagnetic simulation software's has been used. For the initial estimates WIPL-D software was used. This allowed for relatively fast predictions of the radar cross section. It proofed difficult to verify and validate the results however, so these results where only used to attain a trend in the result and therefore it was deemed not so important to verify the results. The more sophisticated software package Altair FEKO has been used in later stages of the development to get a more accurate prediction of the radar cross section. The results of these simulations are shown in figure 9.10. The frontal view shows a radar cross section of 1-2 m^2 which means RAD-TE-LO-01-01 has not been accomplished. The main reason of the increase in frontal radar cross section is however not the engine face but instead seems to be the intake itself it is therefore recommended to investigate this as it could potentially decrease the RCS even further. When applying radar absorbent materials inside of the engine ducts however, the simulation returns a radar cross section sufficiently small to reach the target of 0.01 m^2 therefore satisfying requirements RAD-TE-LO-01 and RAD-TE-LO-01-02.

The radar cross section from an azimuth between 50 and 310 degrees seems to be rather large compared the other angles and is unexpected. The reasons for this are difficult to narrow down. However, the air intake is thought to have caused these high peaks due to the random scattering that occurs. However, it may also be

caused by a small corner reflector that formed between the intake and the nose, as shown in figure 9.11. A solution to this could be to investigate the effect of changing the concave V-shape to a convex V-shape instead, this would reduce the internal space and require a partial rework of the intake duct design however, so a simpler solution may be to chamfer the (red) edge to create an outward facing edge instead.

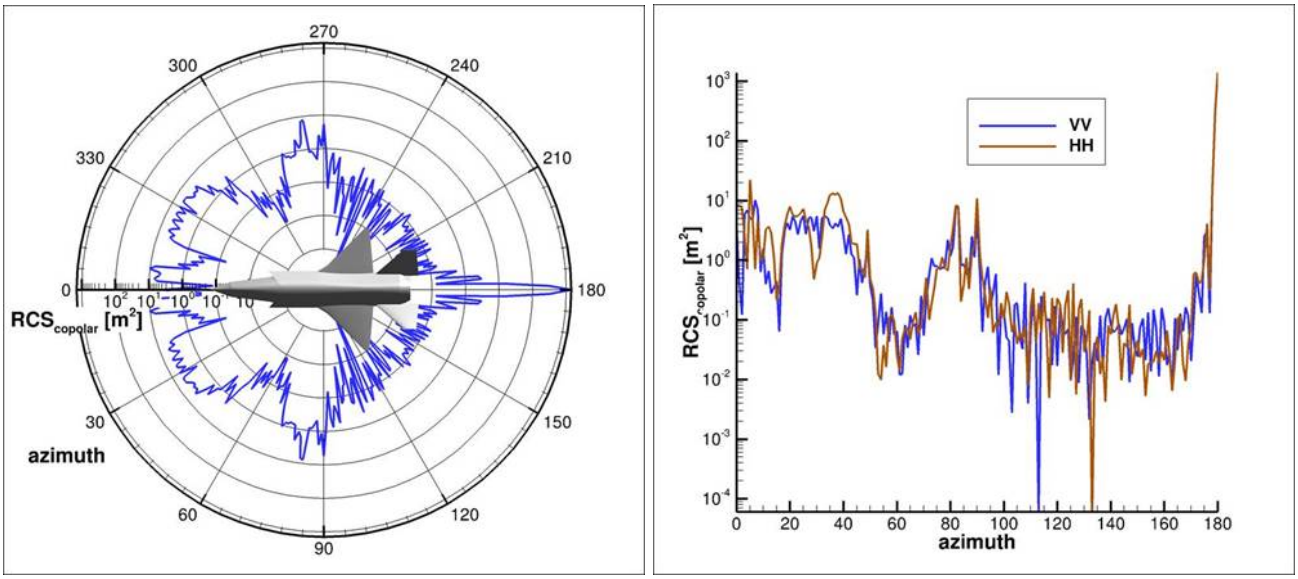

(a) *Polar plot of the radar cross-section of the red air drone*

(b) *Radar cross-section*

Figure 9.10: *The radar cross-section of the red air drone plotted for different angles of azimuth.*

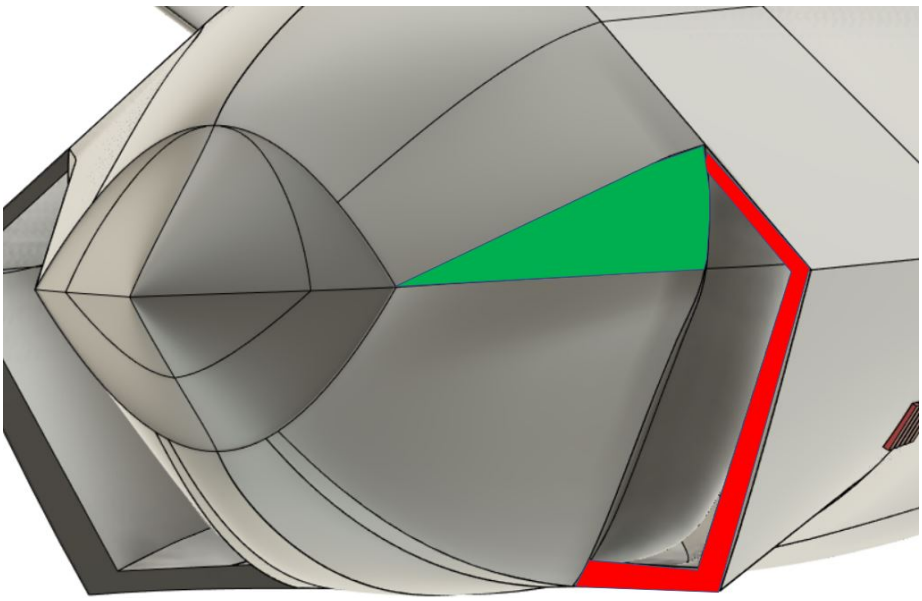

Figure 9.11: *Possible corner reflector between the red intake face and green face of the nose cone.*

Furthermore, it is recommended to increase the trailing edge sweep of the wing and canted tail to create a bigger azimuth from the nose to the RCS peak that is created by the trailing edge of the wing. The effect of the low amount of trailing edge sweep is clearly seen in the polar plot. The angle of the strake at the front of the wing should also be aligned with the angle created by the nose, as the nose angle is such that the drag due to a detached bow shock is reduced at the supersonic dash speeds.

Due to the time-consuming simulations and a limited licence that is available to the team, it is recommended to experiment using an anechoic panel on top of the flat canted plate behind the radome as seen in figure 9.3 to reduce the returned energy even more. These could also be used inside the aircraft structure, especially around

sharp edges.

It is also recommended to investigate the non-constant radii curvature of the nose and body and to add a bigger angle to the bottom side of the intake surfaces of the RAD to see further improvement on the RCS.

The infrared signature could also be further reduced by using anti-detonant injection into the engine. However, this must be a clean injection to avoid smoke plumes created at the exhaust, which could compromise the visual low observability of the RAD. It could also prove itself being worthwhile to bring the tail even more backwards and mount it directly next to the engine, as can be seen in other aircraft such as the F-15.

9.3. System Interfaces

This section discusses the hardware and software interfaces of the RAD in subsection 9.3.1. Furthermore, the data handling block diagram is shown in subsection 9.3.2. Finally, the communication flow diagram is presented in subsection 9.3.3.

9.3.1. Hardware and Software Block Diagrams

The hardware block diagram can be seen in figure 9.12. This diagram shows the hardware on the red air system and their interactions with each other. The red air system includes the ground control station, and the aircraft. Both systems have been specified, and their component relations have been established. Furthermore, the software block diagram can be seen in figure 9.13. This diagram compliments the hardware diagram, as operations and processes are controlled by the software.

9.3.2. Data Handling Block Diagram

The data handling block diagram can be found in figure 9.14. It shows the flow of data throughout the RAD's digital system. Every line represents state data, commands, or a combination of the two. Black lines are data streams coming into the main flight computer, while red dotted lines are streams coming out of the main flight computer. In the end, this diagram allows the sizing of the communications link connecting the ground station and the RAD. On top of that, the flight recording system (FRS) can be sized. Note that the choice was not made to store the video feed on the FRS, as this would dramatically increase the capacity (and mass) of the FRS.

This diagram was set up with the idea that sensors refresh 60 times per second. This is higher than necessary; 24 Hz is already enough. This cuts many data streams in half, which is especially favourable for external communication bandwidth requirements.

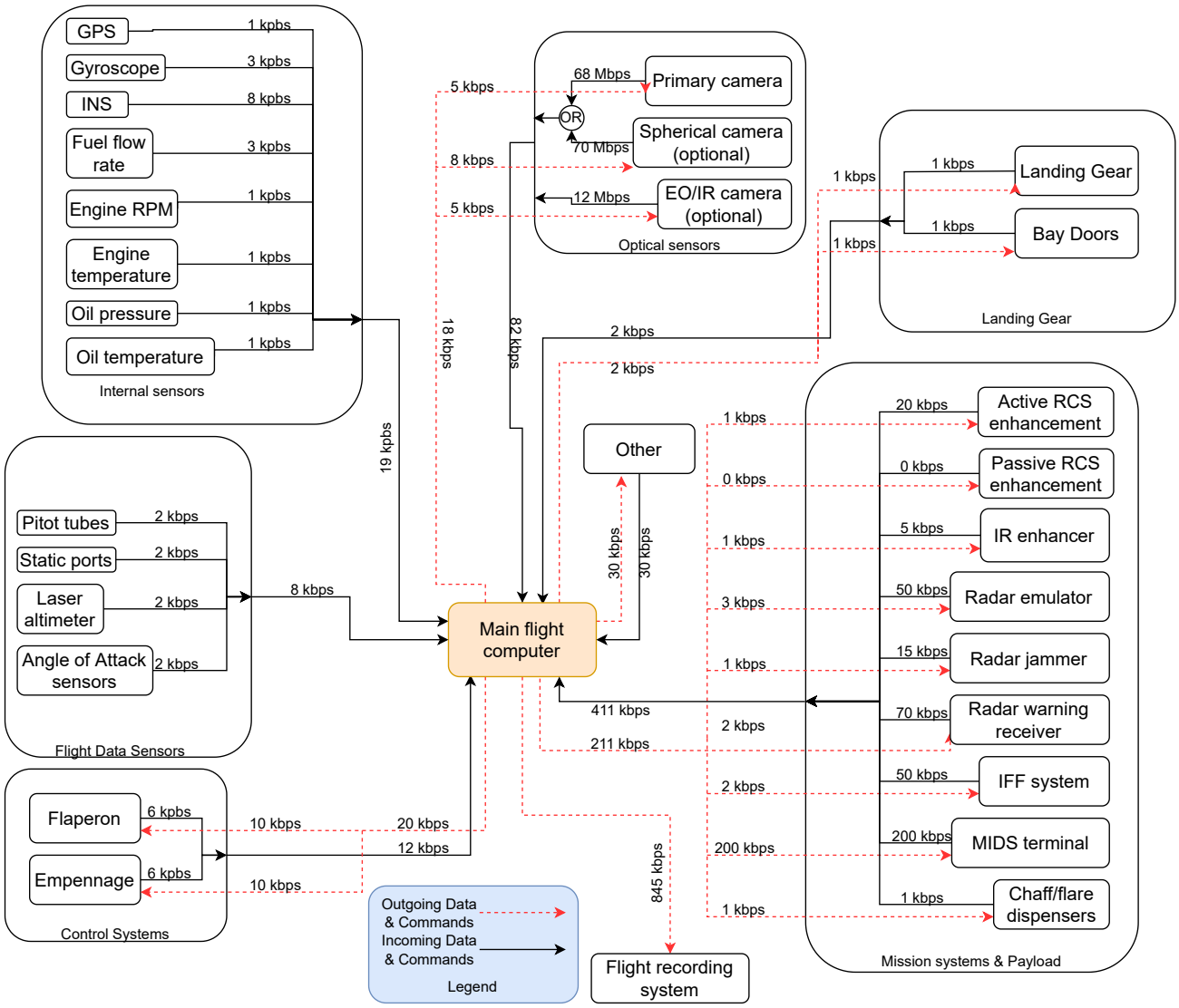

Figure 9.14: *Data handling block diagram for the red air drone. A legend explains the data streams.*

9.3.3. Communication Flow Diagram

The communication flow diagram, found in figure 9.15, is a more zoomed-out version of the data handling block diagram. It describes the parties between which communication flows are present. In this diagram, only sections that must be explicitly designed are considered in detail. Air traffic control and mission control are considered as finished designs, where the internal communication is not relevant to the RAD.

Looking back at figure 9.14, one can see that the SATCOM and SHF data stream must have a downlink speed of 22.482 Mbps is needed. However, this is purely the data rate. Additional factors for serializing data, encryption, and packeting should be included in this number to get a total data rate requirement. However, the additional factor for encryption depends heavily on the type of encryption used, so no accurate estimate can be made for now. However, for the data transmission it has been chosen to packet data in the following way:

1. Input data to transmit
2. Define what type of data is transmitted
3. Serialize the data
4. Apply security layers
   (a) Encrypt data with chosen encryption standard
   (b) Compute hash of the encrypted data for performing an integrity check (this prevents data tampering during transfer)
   (c) Create packet header (encrypted data + integrity check) and encrypt the header
5. Send final output data

The uplink data rate is much lower, as the downlink data stream is dominated by video. Uplinking commands only requires 281 kbps in data rate. This is easily achievable using SATCOM or SHF systems.

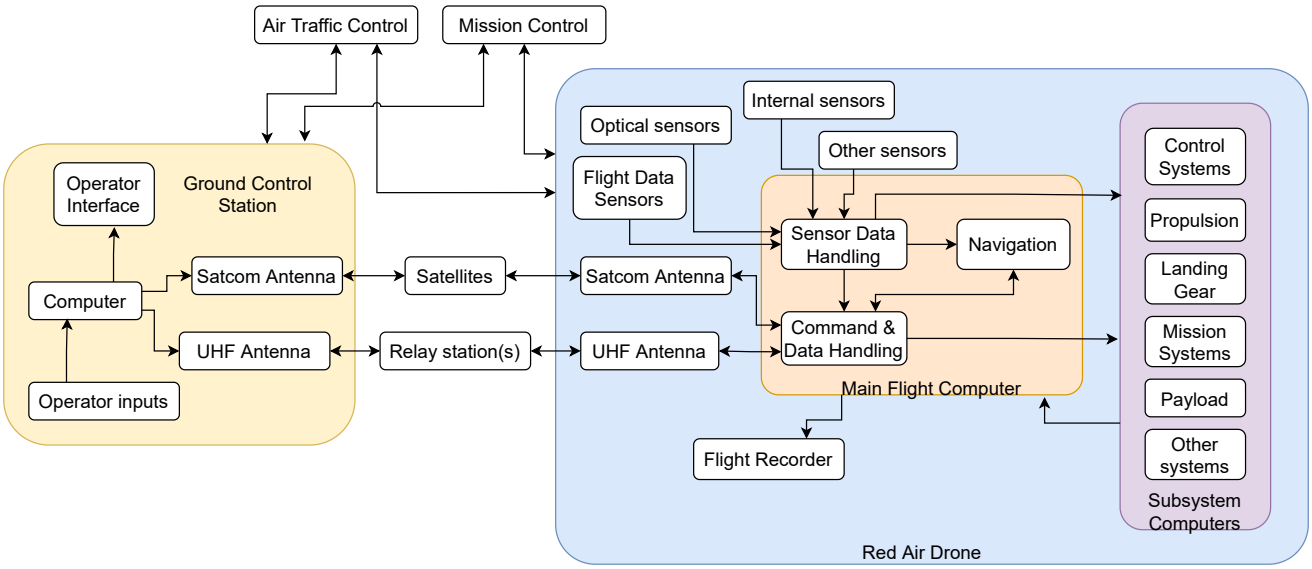

Figure 9.15: *Communication flow diagram for the RAD.*

9.4. Sensitivity Analysis

The sensitivity analysis is performed to ensure that the final design is investigated for possible changes in design or its requirements. It investigates the response of the design to changes and to what extent these drive the design. For instance, what happens to the design if the RAD must go 10% faster during the dash, use a 10% shorter runway, has a 10% increase in payload mass.

The design characteristics that are the most important for the RAD are the radar cross-section, maximum dash speed, endurance, costs, and size. Therefore, these will be used as the response variables in the sensitivity analysis. That being said, the radar cross-section takes a long time to predict per iteration and requires extensive modelling, hence it will be ignored for the analysis and is assumed to scale with size instead.

In figure 9.16 the results are shown. The larger the change in design parameter, the more sensitive the parameter is to that specific output. This means that if there is change driving parameters, such as maximum dash speed, shown by the percentage change on the x-axis of figure 9.16, the change in design parameter such as drag will be shown on the y-axis. The greater the change in design parameter, the greater the sensitivity. The two most sensitive parameters are the thrust required with an increase in Mach, as the most sensitive, followed by an increase in runway length and the effect it has on the size of the wing. These two most drastically influence the design of the RAD and it must be understood why and what can be done to decrease the sensitivity.

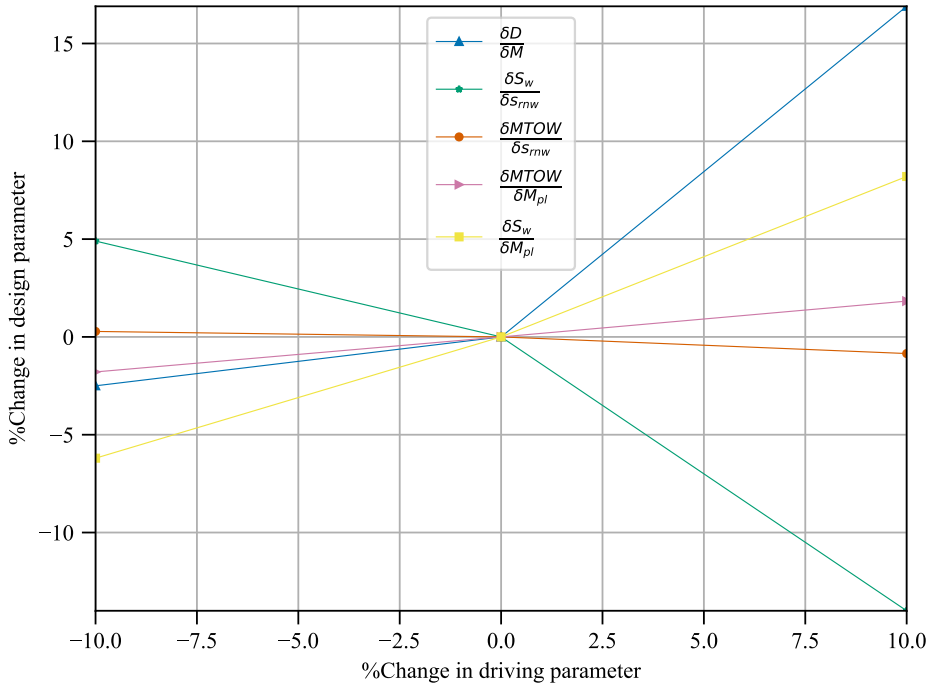

Figure 9.16: *Sensitivity analysis showing the slope of changing a parameter displayed in the legend, between -10% to 10%.*

The first main design driver is the supersonic Mach speed that the RAD must be able to reach. The supersonic drag is much greater than the subsonic drag and this can be seen in section 5.4 of chapter 5. Furthermore, the rate of increase in drag is also more drastic. This means that if the Mach number the RAD must reach increases by 10%, the change in thrust required will dramatically increase as well, namely by 16.9%. This is what makes the parameter so sensitive, it may even require a change in engine, altering the design even more. As seen in section 6.2 of chapter 6, a change in engine has huge implications on weight, size and price of the RAD. If a higher thrust is required, due to higher Mach number required, a larger engine must be chosen. Meaning the size of the RAD increase, weight increases, and drag increases. All these have a large effect on the size of the wing, and therefore the high sensitivity makes sense. Additionally, a smaller engine reduces weight and size and will snowball into a much smaller RAD design. Thus, if the thrust needed changes drastically due a change in Mach number required for the RAD, it affects the design greatly and will do even more so if a different engine must be considered to meet the requirement. The recommendation is to apply more area ruling to decrease drag to increase the maximum Mach number, as a change in engine would overhaul all design parameters and lead to a very different design. The change in Mach number sensitivity can also be reduced by using a more accurate model for the drag so that small variation in the design do not greatly change the drag. This makes optimising the drag performance a lot easier and changes in performance requirements can be better dealt with.

The second big design driver is the landing of the RAD. For this, the runway-length is critical, as it dictates landing performance the RAD must have. The shorter the runway, the less space for the RAD to brake and slow down and the slower it must land. This results in the RAD needing sufficient lift at slower speeds, which means the wing must be sized accordingly to allow for the required C_L. The knock-on effect is that the drag performance changes and the supersonic performance changes too if the wing must be optimised more for high lift and low speeds. Conversely, if the runway length is increased, the RAD can land faster, meaning less low speed lift required. The effect of either on the wing is great and influences the overall design greatly, as is seen in figure 9.16 as a result. The recommendation is to fully detail the brakes of the RAD and the performance they provide and possibly investigate additional braking mechanisms such as a drag chute. If the runway length is decreased, the RAD could still land at its desired landing speed if its deceleration is large enough. Knowing the braking performance decreases the uncertainty and will make the sensitivity of the parameter decrease. Furthermore, if a drastic decrease in runway length is required, then a drag chute option should be considered as this does have as big of an impact on the other design parameters as changing the wing sizing.

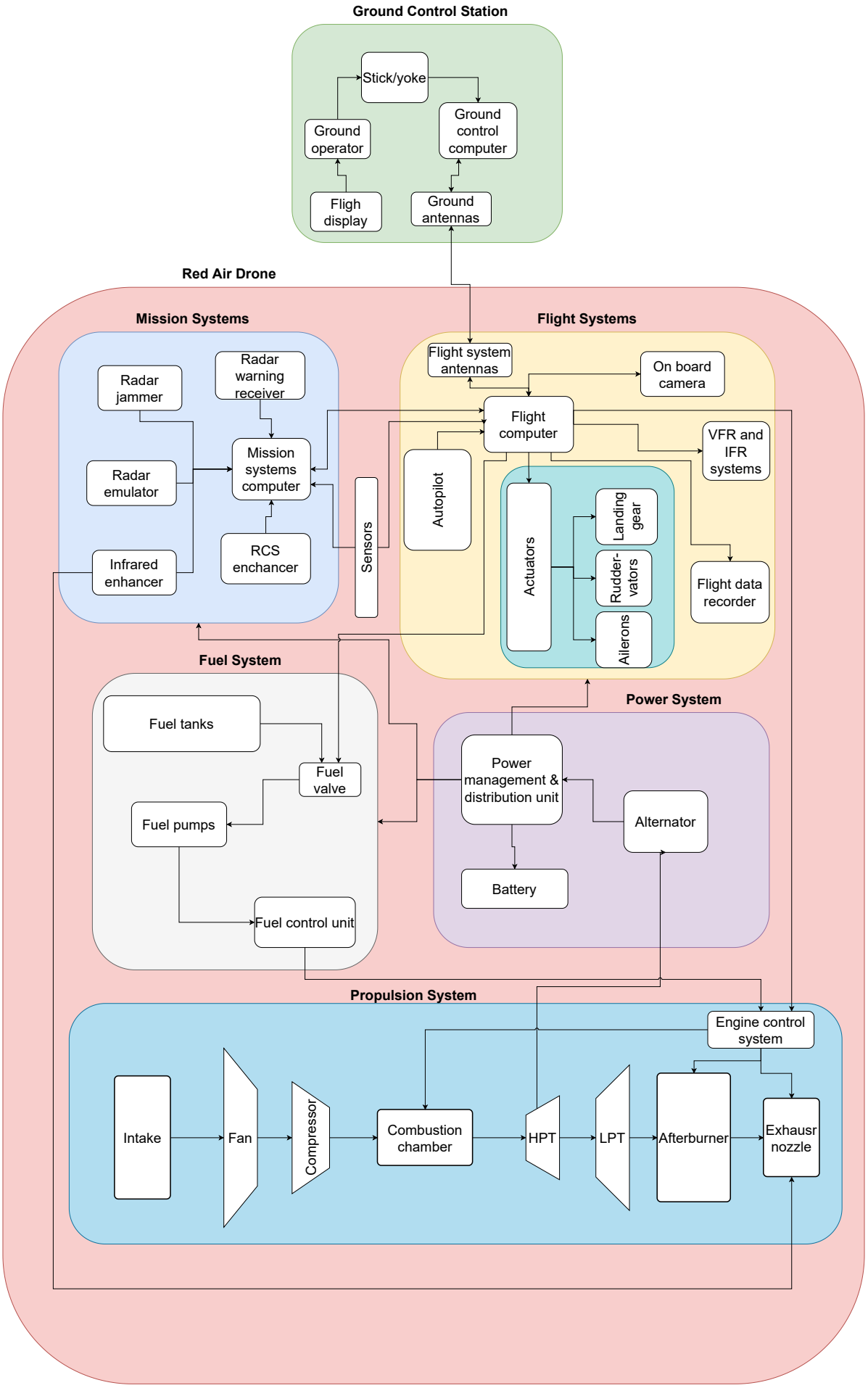

Figure 9.12: *Hardware diagram for the RAD system*

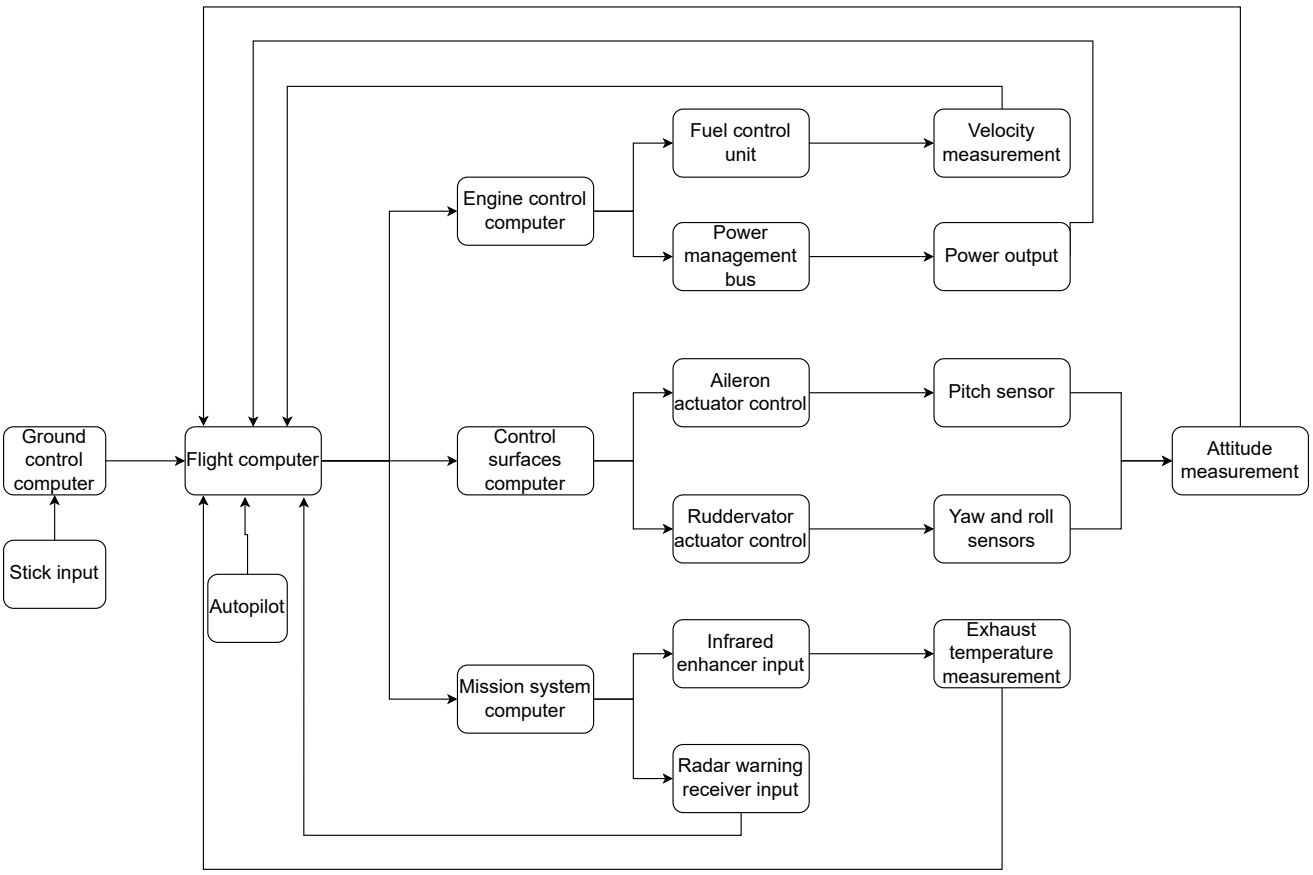

Figure 9.13: *Software diagram for the RAD system*

10 Drone Performance

As several parameters of the RAD design changed compared to the conceptual design, it must be investigated whether it still meets the imposed performance requirements. The requirements for performance being given in table 10.1.

Table 10.1: *Performance requirements for the RAD to satisfy.*

ID	Description
RAD-TE-PER-01	The RAD shall have a flight performance as required by the stakeholders.
RAD-TE-PER-01-01	The maximum speed of the RAD shall be at least Mach 1.60 above 30,000 feet.
RAD-TE-PER-01-02	The RAD shall have a typical cruise speed of Mach 0.90 from S/L to ceiling.
RAD-TE-PER-01-03	The RAD shall have a minimum endurance of 1.5 hours between T/O and LDG.
RAD-TE-PER-01-04	The RAD shall have a minimum flight ceiling of 45,000 feet.
RAD-TE-PER-01-05	The RAD shall be able to perform a dash move increasing its Mach number by at least 0.7 while staying in the nominal flight envelope.
RAD-TE-PER-02-01	The RAD shall have a payload capacity of at least 78 kilograms.
RAD-TE-PER-02-02	The RAD shall be operational for temperatures between ISA -30°C to ISA +30°C.
RAD-TE-PER-02-03	The RAD shall be able to take off from a paved runway with maximum length of 6,000 feet at altitudes from S/L to 4,000 feet MSL.
RAD-TE-PER-02-04	The RAD shall be able to operate in T/O and LDG for the set-out wind limits.
RAD-TE-PER-02-04-A	The RAD shall be able to operate in T/O and LDG for a 25 kt maximum crosswind component.
RAD-TE-PER-02-04-B	The RAD shall be able to operate in T/O and LDG for a continuous wind gusting of 35 kt.
RAD-TE-PER-02-04-C	The RAD shall be able to operate in T/O and LDG for a maximum wind gusting of 42 kt.
RAD-TE-PER-02-05	The RAD shall have a MTOW between 150 and 20,000 kg.
RAD-TE-PER-03	The RAD shall be able to sustain and perform manoeuvres as specified by the stakeholders.
RAD-TE-PER-03-01	The RAD shall be able to sustain loads higher than 4g for an altitude of 25,000 feet & at Mach number of 0.90.
RAD-TE-PER-03-02	The RAD shall be able to perform sustained turns.
RAD-TE-PER-03-02-A	The RAD shall have a sustained turn rate of 9 deg/sec.
RAD-TE-PER-03-02-B	The RAD shall have a sustained turn radius of 6000 ft.
RAD-TE-PER-03-03	The RAD shall be able to perform instantaneous turns.
RAD-TE-PER-03-03-A	The RAD shall have an instantaneous turn rate of 15 deg/sec.
RAD-TE-PER-03-03-B	The RAD shall have an instantaneous turn radius of 3500 ft.

10.1. General Considerations for Performance

The performance requirements which are applicable to this stage of the design are given above.In [2] a design point was chosen which would ensure that several key requirements are met as shown in figure 10.1. Using the new wing surface of 4.53 m^2 found in chapter 5, a weight of 2,126 kg in subsection 4.3.5 and thrust values found in chapter 6 two points for figure 10.1 can be found. For both points the W/S equals to 4604. For the dry engine (no afterburner) the T/W_{TO} is equal to 0.518 (4604,0.518). For the wet engine (with afterburner) the T/W_{TO} is equal to 0.996 (4604, 0.996). Looking at figure 10.1 it can be seen that for both configurations the point will be within the acceptable bounds as imposed by the requirements but for landing a C_L of 1.15 is needed. This is not a problem as using HLDs as described in section 7.5 a $C_{L_{\text{max}}}$ of 1.31 can be reached.

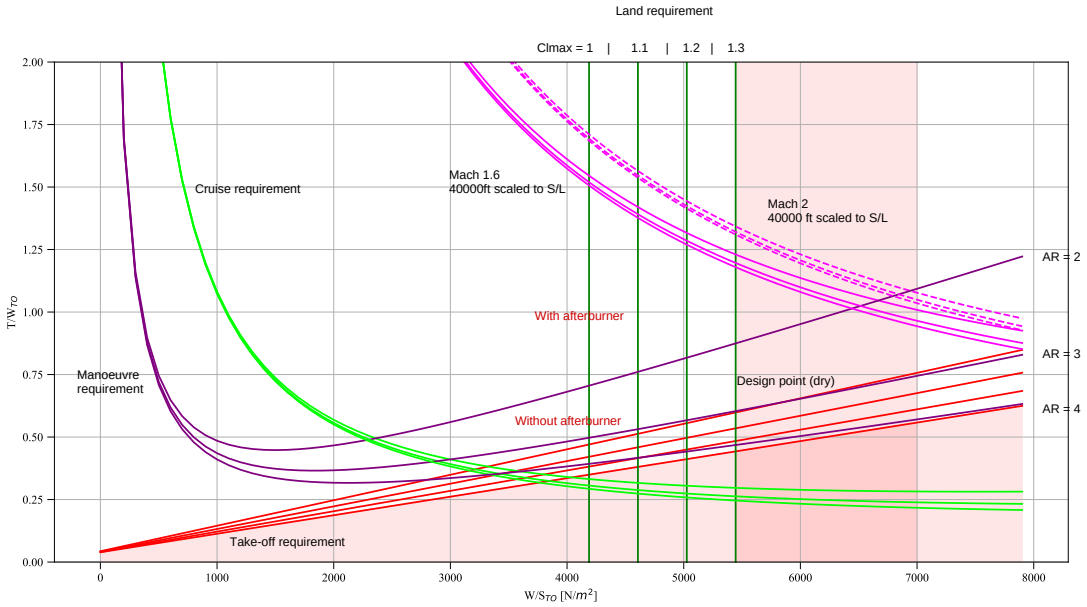

Figure 10.1: *The design space with the chosen design point in the conceptual design and the resulting preliminary design points.*

Having confirmed that the RAD still meets the TO, landing, cruise, supersonic dash and manoeuvre requirements it is still important to look at if the RAD can meet the mission profile wholly. This will be done in the rest of the chapter.

Lastly before looking at the performance analysis, a general method must be established to model the drag. Because the RAD flies at subsonic, transonic, and supersonic speeds, the drag varies substantially with the Mach number. Therefore, the simplified drag model (which is typically used for preliminary performance analysis) must be adjusted such that it is a function of the Mach number. Throughout chapter 10 the Mach number dependant simplified drag model given by equation (10.1) shall be used.

$$C_D = C_{D_0}(M) + k(M)C_L^2 \tag{10.1}$$

From the aerodynamic performance analysis, the C_D, C_{D_0} and C_L^2 are known for various Mach numbers. Rearranging equation 10.1 such that it is a function of k and using the known coefficients, it is possible to find the proportionality constant k for a particular Mach number. If the simplified drag model is applicable, it becomes possible to use the methods for performance analysis as described in [43].

10.2. Mission Profile

The drone needs sufficient fuel to perform the mission according to the mission profile. The reference mission from the reader [4] is depicted below in figure 10.2. This mission has a minimum endurance of 1.5 hours between take-off and landing.

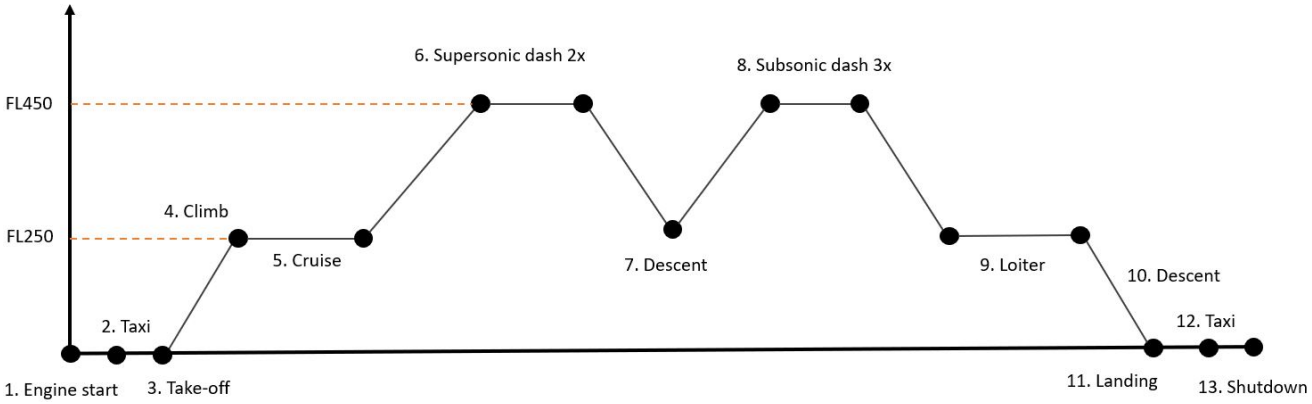

Figure 10.2: *Generic mission profile for the red air drone. Altitude on the y-axis and time on the x-axis.*

Where **1**: Start-up 5 min idle. **2**: Taxi for 5 min. **3**: Take-off. **4**: Climb to 25,000 ft at the max climb thrust and best climb speed. **5**: Accelerate to M = 0.9. **6**: Perform 2 dashes to 40,000 ft at M = 1.6 maintained for 1.5 min each dash. **7**: Return to 25,000 ft at M = 0.9 after each dash. **8**: Perform 3 dashes to 40,000 ft at M = 0.95 maintained for 2 minutes. **9**: Return to 25,000 ft at M = 0.9 and allow for 30 min loitering. **10**: Descend to S/L at idle thrust and best glide speed. **11**: Landing. **12**: Taxi for 5 min. **13**: Shutdown.

The table 10.2 shows the times required to reach each of the flight conditions in terms of seconds. It can be seen that excluding the added loiter time, the most time-consuming flight condition is the climb to cruise from sea level to 25000 ft. This is due to the low speeds at take-off and low thrusts at lower subsonic values because of the intake design. When the manoeuvres and runway operations are summed up, it is determined that the reference mission without the descent will take around 71.4 minutes. With descending, it is estimated that the reference mission will have an endurance greater than required 1.5 hours.

Table 10.2: *The fuel masses and times for the critical phases of the reference flight*

Condition	Fuel mass [kg]	Time [s]	Afterburner
Climb to cruise	47.15	199	No
Acceleration to Mach 0.9	10.02	55	No
Climb at Mach 0.9 to dash	26.67	138.8	Yes
Subsonic dash	4.11	14	No
Supersonic dash	57.30	79	Yes
Sustain subsonic	5.94	120	No
Sustain supersonic	51.21	90	Yes
Loiter	130.95	1800	No

10.3. Take-off

During take-off the RAD should comply with the ground run requirement RAD-TE-PER-02-03. A lift-off speed (V_{LOF}) is found of 75.6 m/s at sea level altitude and 80 m/s for a ground run at 4,000 feet, for a $C_{L_{max}}$ of 1.31 (full flaps deployed flying at a maximum angle of attack).

For these lift-off speeds it can be found (using equation (10.2) [43]) that at sea level a ground run of at least 1,459 ft is required. For a runway at 4,000 ft a ground run of at least 1,623 ft is required. These ground runs are excluding the airborne part of the take-off (rotation, transition distance and potential climb over obstacle distance). With more than 2,000 ft left, it will be assumed that the ground run is long enough.

$$S_G = \frac{V_{LOF}^2 W}{2g[T - D - \mu(W - L)]_{at(V_{LOF}/\sqrt{2})}} \tag{10.2}$$

10.4. Climb

The climb analysis was based on the reference mission profile, which states that the climb must be performed to 25,000 ft at the maximum climb thrust & best climb speed. Furthermore, a climb must be performed from cruise to dash altitude of 40,000 ft. This climb to dash altitude must be done for different speeds: for M = 0.95, but also for M = 1.6. For climbing, equation (10.3) is used to determine the various ROC's and the according climb angles.

$$ROC = \frac{P_a - P_r}{W} = \frac{TV - DV}{W} = V \sin\gamma \tag{10.3}$$

Using methods from [58] it is possible to find values for the power required at low altitude using the idea of minimizing C_L^3/C_D^2 to get the minimum power required(P_r). Then look at the power available(P_a) at different Mach numbers, find the maximum difference between P_a and P_r to find the best ROC. This must be done for both 0 ft and 40,000 ft altitude, then compute the average ROC of these two (as the maximum ROC changes with altitude). This will be an overestimation as the craft will spend more time climbing at high altitudes as the ROC is lower there, so the ROC will be overall lower than the average one. But in this phase of the design, this discrepancy will not be addressed in further detail.

For higher altitude climb to dash altitude, the thrust is evaluated at the interesting speeds for both the dry and wet engine configurations, using the known thrust and drag values for these speeds. All the described ROC's have been described in table 10.3 together with the according average climb angle and average climb times. As mentioned before, due to only evaluating average maximum ROC, the ROC values will be slightly overestimated, angle overestimated and time underestimated.

Table 10.3: *Average climb rates of the RAD with their according average climb angle and time required to get to the altitude.*

Average climb rates:	ROC[m/s]	Climb Angle[deg]	Time[s]
Climb to cruise altitude	125.6	25.4	199.0
Climb to dash 0.95(dry)	52.5	10.9	286.0
Climb to dash 0.95(wet)	108.1	28.8	138.8
Climb to dash 1.6(wet)	145.2	27.4	103.3
Climb to dash 2.0(wet)	105.8	22.3	141.8

10.5. Cruise and Dashes

A substantial part of the mission profile is taken up by the cruise and the supersonic dashes. Following RAD-TE-PER-01-02 the RAD should be able to cruise at $M = 0.9$ from cruise altitude to ceiling. Figure 10.4 shows for different altitudes if enough thrust is available to maintain the cruise speed as described in the requirement. For the dashes, figure 10.3 shows the relation between drag experienced to the thrust available for that particular Mach number and altitude.

It can be seen that the RAD can theoretically reach a Mach number of about 1.4 without using the afterburner, and 2.0 using an afterburner. However, it must be noted that reaching these speeds will be harder as the acceleration will be very low to the higher theoretically possible speeds due to a small excess thrust being left for acceleration.

Figure 10.4 depicts that for increasing altitude, cruising and even acceleration from cruise is possible as excess thrust is left after countering the drag. Even at 45,000 ft cruising at 0.9 is theoretically possible with the chosen configuration.

The maximum theoretical ceiling of the RAD is calculated using the thrust values at each altitude with a Mach number of 0.95. For each altitude, the drag was also calculated until 45,000 ft. The drag over this altitude was assumed to be equal to the drag at 45,000 ft as constant Mach number is assumed and hence, velocity as well as density are decreasing substantially. With this method, the maximum theoretical ceiling is calculated to be 55,000 ft. However, the service ceiling is determined to be 45,000 ft as after this altitude, the excess thrust becomes very low, leaving no safety margins for the flight.

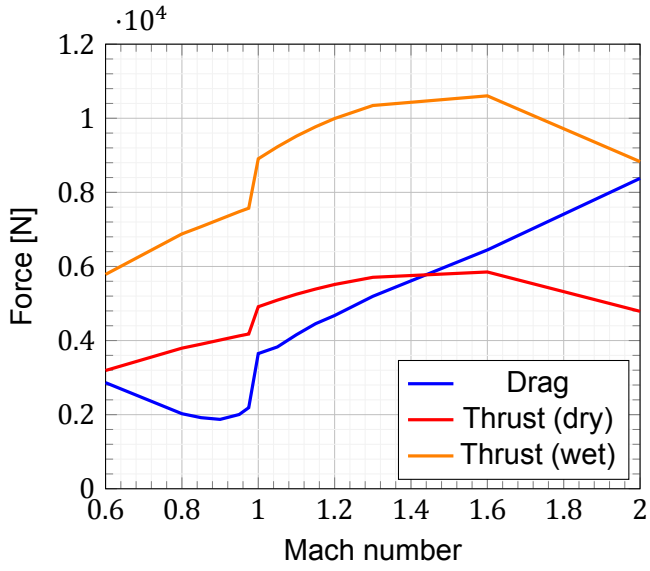

Figure 10.3: *Thrust and Drag versus Mach number at 40,000 ft*

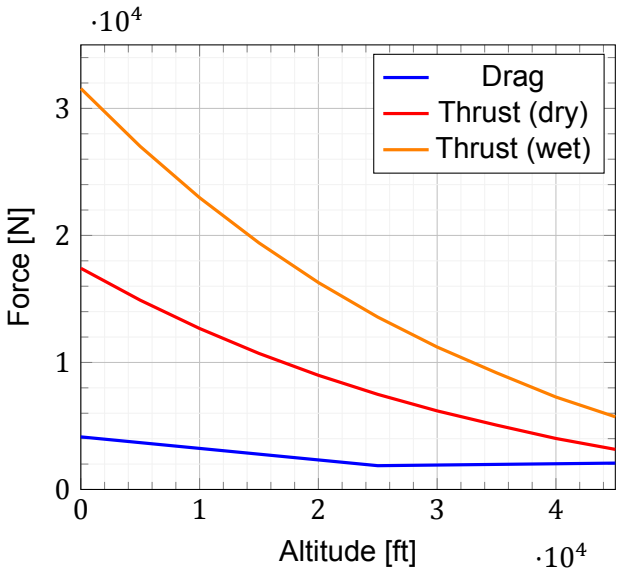

Figure 10.4: *Thrust and Drag versus altitude at Mach 0.9*

10.6. Descent

The rate of descent for a constant airspeed is determined by how fast the aircraft loses its energy. Increasing the rate of descent can be done in a multitude of ways. Increasing the airspeed, flying at a higher load factor, and deploying air brakes are all effective ways to expedite the descent of the aircraft. The more critical aspect of the descent is the optimal glide slope. Flying at the optimal glide speed ensures that the aircraft has the highest range when the power is cut. Furthermore, flying at the best glide speed provides the best fuel efficiency during the descent phase of the aircraft, as no energy is wasted. This optimal glide speed is the speed at which the aircraft reaches the highest L/D ratio. This speed changes with the total aircraft mass, and it is plotted in figure 10.5.

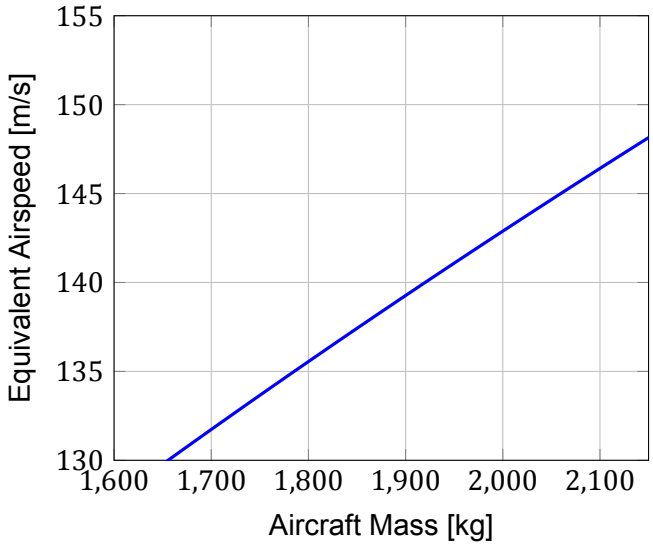

Figure 10.5: *Best glide speed as a function of aircraft mass*

10.7. Landing

The most important aspect of the landing performance is the landing distance. In this section, a calculation of the landing distance is made. In order to satisfy the requirement, this landing distance has to be smaller than 6,000 ft or 1,829 m. As shown in figure 10.6, the landing distance is defined as the distance from 50 ft above the ground to a full stop.

The landing distance is divided into three parts. The air distance, S_A, the freeroll distance, S_{FR}, and the braking

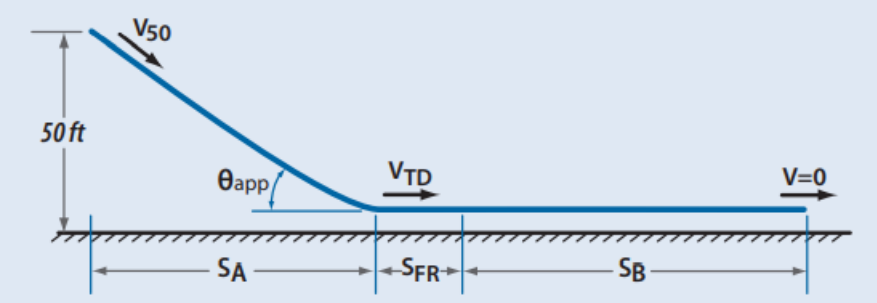

Figure 10.6: *Schematic for the landing analysis [39]*

distance, S_B

The approach distance is can be calculated using equation (10.4). In this equation, S_{50} is the approach speed at the 50 ft point, and V_{TD} is the touchdown speed, which is assumed to be $1.15V_{stall}$ [39]. Assuming the aircraft brakes with a constant acceleration, a_d, of 0.4 g [32] the distance to stop is given in equation (10.5).

$$S_A = \frac{L}{D}\left[\frac{V_{50}^2 - V_{TD}^2}{2g} + 15.24\right] \quad (10.4) \qquad S_B = \frac{1}{2}\frac{V^2}{a_d} \quad (10.5)$$

Assuming that using modern automatic braking systems, the free roll distance can be neglected, The total landing distance is the sum of the air distance and the break distance. The result of this calculation, at the maximum landing weight, which is assumed to be 1,726 kg or after 400 kg of the fuel is used at MTOW, results in a landing distance of 1,734 m. This landing distance is smaller than the available runway length, meaning the landing requirement is satisfied.

10.8. Endurance Analysis

As the requirement RAD-TE-PER-01-03 states, the RAD shall have a minimum endurance of 1.5 hours between T/O and landing. The drone carries 524 kg of fuel. Considering 30 kg will be absolute fuel reserve for landing, 494 kg of fuel can be used for the mission and loiter. Optimum L/D ratio for loiter is equal to C_D/C_L ratio. Optimum C_L is found using (10.6). Next, knowing zero lift drag coefficient, the overall drag coefficient is calculated using (10.7) [46].

$$C_L = \sqrt{\pi ARe C_{D_0}} \quad (10.6) \qquad C_D = 2C_{D_0} \quad (10.7)$$

This leads to an optimum L/D for loiter of 11.53. Knowing TSFC of the engine used, and the initial weight, MTOW and final weight, MTOW minus maximum available fuel, the endurance is calculated using (10.8). This leads to endurance of 11,562 s or 3.21 hours. Therefore, the requirement RAD-TE-PER-01-03 is fulfilled.

$$E = \left(\frac{1}{c \cdot g}\right) \cdot \frac{L}{D}_{loiter} \cdot ln\left(\frac{W_i}{W_f}\right) \quad (10.8)$$

When it comes to the reference mission, table 10.2 shows the fuel mass required in each critical stage of the reference mission. The decent manoeuvres were neglected in this analysis as the descent will be mostly gliding, however, the engine will not be fully shutdown and will have the minimum restart rpm. It should be noted that each of the flight stages were calculated independently, nevertheless this is not the case in application as the mass of the aircraft decreases also the fuel required for manoeuvres decrease. When this is considered, the total required fuel for the reference mission and the loiter is 518 kg. However, for this the loiter should be done in an altitude below 15,000 ft. The total reference mission will take 48 minutes excluding decent which will be gliding, and loiter for 30 minutes.

10.9. Conclusion and Recommendations

The performance analysis is an essential part of the whole aircraft system as it shows the capabilities of the RAD as well as demonstrates the compliance with significant amount of stakeholder requirements. The mission

profile was also demonstrated to see whether the RAD is capable of adhering to the reference mission. It was determined that the RAD can perform every manoeuvre inside the reference mission profile. For that the take-off speed was determined at 75.6 m/s at sea level and a speed of 80.0 m/s for a runway at 4,000 ft above sea level. For these take-off runs, the maximum amount of runway required is 1,632 ft at an altitude of 4,000 ft runway.

After the take-off, the climb performance was considered. The rate of climb was maximised for climb performance as this was included in the reference mission. The maximum rate of climb is 145.2 m/s occurring at climb to supersonic dash, where an afterburner is used.

Furthermore, the cruise and dash performance of the RAD was also analysed to check if the dash manoeuvres and cruise are comfortably in the achievable flight envelope. It was determined that the thrust available exceeded the thrust required at each desired altitude and Mach number. It was found that Mach 2 at 40,000 ft is achievable, however due to low acceleration, implementing a Mach 2 manoeuvre in the reference mission wouldn't be possible due to the required fuel mass. It was also determined that the theoretical maximum ceiling is at 55,000 ft. However, the service ceiling is determined to be at 45,000 ft. This is due to the low amount of excess thrust above 45,000 ft.

The descend phase of the RAD will be executed by turning off the engine to the lowest possible throttle setting, where the engine could be restarted. This means that a glide is assumed for descending phases of the mission. The best glide speed is dependent on the aircraft mass and changes in every phase of the flight.

The landing performance follows from the final gliding descend. Also, for the approach, the best gliding speed is used dependent on the landing weight. At maximum landing weight the required runway distance is 1,734 m. This is less than the available runway length and hence, the requirement is satisfied.

Performances of the RAD at different stages in the flight envelope of the mission was analysed as independent points. It is recommended in the next phase of the design to look at the flight more continuously and see the effects of different flight stages onto other stages. This way more accurate estimations can be made for the performance of the RAD, especially considering the added effect of mass loss due to the burnt fuel. Furthermore, it is recommended to further analyse the turning performance of the RAD.

11 Operations and Logistics Concept Description

This chapter outlines the operations and logistic description of the RAD. Firstly, it describes the support systems for its operation in section 11.1. Thereafter, it discusses the operation of the primary system in section 11.2. Furthermore, a graphical summary of this chapter is shown in figure 11.3. Note that a large portion of this chapter was copied and adapted from the baseline report [3]. This section was adapted from the previous version, found in the midterm report [2, Ch. 11].
Two key requirements are considered in the design of operations. They can be found in table 11.1. However, this cannot yet be fully verified at this stage of the design.

Table 11.1: *Key requirements related to operations.*

ID	Description
RAD-TE-OTH-01	The RAD shall be operational on ground as specified by the stakeholders.
RAD-TE-OTH-03	The RAD, or its components, shall fit inside a standard ISO.1AA shipping container (SSC) with dimensions 40 ft × 8 ft × 8 ft 6 in

11.1. Support System for Operations

The understanding of the support system is critical for the operation and design of the primary system. As specified in the ”Handbook of Unmanned Aerial Vehicles” [59], the operation can be divided into two parts: the primary system and the support system. A constant interchange of information should be flowing from the primary system design to the support system design. The support system can be divided into eight aspects which all need to be planned for to have a successful operation [59, p. 2568]. These eight aspects have been visualised in figure 11.1, and will be expanded upon further in this section. Additionally, personnel is required which is incorporated with these eight aspects.

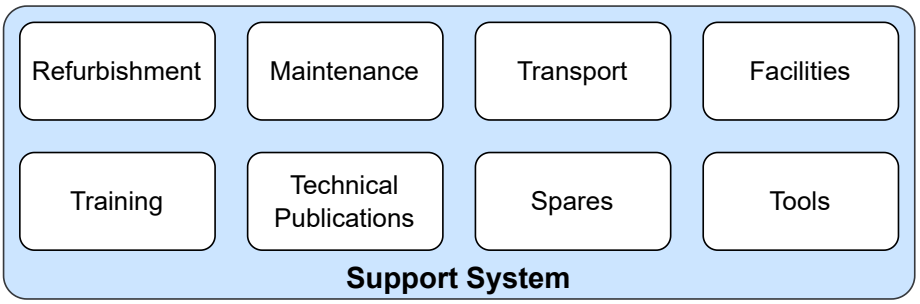

Figure 11.1: *The eight different aspects of the support system [59, Fig. 107.3].*

11.1.1. Refurbishment

Refurbishment is an overhaul to keep compliance with modern standards and upgrades to newer configurations that are developed after the product is released. Refurbishment often takes longer than regular maintenance, so it requires more planning and resources. It is likely that special facilities are needed to perform refurbishment, as they often involve lengthy disassembly. Refurbishment can be combined with depot-level maintenance, as they often require the same level of disassembly and available facilities. This is a necessary part of a vehicles' lifetime and cannot be avoided. These facilities are not present at every airport, so the RAD will likely need to

be transported to a special location to carry out refurbishments. However, as the RAD operates mostly out of bases located in friendly territories, it is expected that facilities are never far away and readily available, albeit with rigorous planning.

With the rapid progression in technology, especially the mission systems will likely need to be upgraded multiple times across the lifetime of the RAD. This can be combined with a refurbishment of the aircraft as a whole.

11.1.2. Maintenance

The scope of the operational maintenance required is an important consideration. Aircraft in general require twelve hours of maintenance (individual work) for every hour flown [60, p. 2620]. On top of that, not only does the drone need maintenance, but the ground control station does as well. There are multiple types and levels of maintenance, which all require different facilities and down-times. A result of this is that aircraft are not always operational, which means multiple units are needed at an airbase if continuous operation is required on the long term. Furthermore, maintenance crews are required to perform the maintenance of the drone. These in turn require technical publications, which is elaborated on in a subsection below.

Pre- and post-flight operations also fall under maintenance. These are typically quite general, and do not require intricate knowledge of the aircraft. However, it still needs allocated personnel. Considering the size of the RAD, at most two people are needed on the ground to perform these operations. Note that they are done in cooperation with the pilot in the ground control station, who has control over systems like control surfaces, propulsion, and hydraulics. An example of pre-flight operations can be found in the functional breakdown structure, as seen in the baseline report [3]. Summarised, the pre-flight operations consist of:

- Ensuring RAD operational safety
- Ensuring RAD operational reliability
- Ensuring RAD mission readiness
- Removing the vehicle from storage
- Performing digital system startups
- Performing physical system startups
- Checking proper execution of all previous steps

With the choice of an engine that has been in use for years, engine maintenance can be minimised, as maintenance plans have been optimised with technical publications and experience.

11.1.3. Transport

To transport the aircraft, the ground control station and spare parts or any other physical objects needed for the operation of the RAD, require elaborate planning and resources. For example, while the aircraft might need a dedicated cargo plane to move long distance, smaller components or crew can be placed on existing flights. As such, transport is a key part of operations.

To facilitate transport, one requirement was that the RAD must be able to be transported by containerised transport. The requirement was then set that one RAD must fit in a 40 ft container, as specified in RAD-TE-OTH-03. This requirement was met, as four RAD's fit in a 40 ft container at once, as illustrated in figure 11.2. This allows the RAD to be transported through air, sea, or land. However, this transport does require the RAD's to be partially disassembled. Particularly, both main wings and a vertical tail must be taken off for a unit to fit.

However, this disassembly is worth the lost time. This capability means that transportation costs can be minimised tremendously, as reported in the Midterm Report [2, pp. 50–51]. Up to 24 RAD's can be carried in a C-5 Galaxy at once, as six of these containers fit in its cargo hold. With an OEW of 1431 kg and a 40 ft container weight of 3750 kg[1], 24 RAD's and six containers would only be half of the C-5's cargo capacity[2].

Another challenge in transport is getting the required approval to get advanced military technology across borders. Often, this requires explicit approval by any country involved, perhaps even countries that the RAD crosses when being transported to its destination. The destination country will likely give permission quite easily, as its military

[1]Source: https://www.icontainers.com/help/40-foot-container/ (retrieved on 13 June 2022)
[2]Source: https://www.af.mil/About-Us/Fact-Sheets/Display/Article/104492/c-5m-super-galaxy/ (retrieved on 13 June 2022)

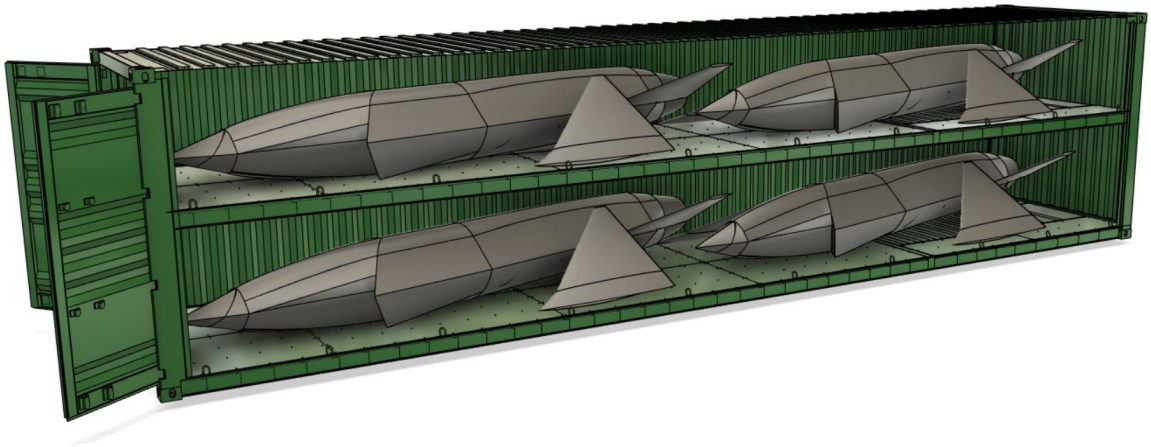

Figure 11.2: *Four RADs inside a single 40ft container using a divider floor.*

will likely be the party requesting the use of the RAD. Moreover, NATO countries already cooperate closely, and already cross each other's airspace with military flights, so they will not pose a big problem. As an example, the engine comes from Japan, a country that is not currently a member of NATO. However, its export regulations for military technology are quite lenient with many, but not all, NATO member states [61]. The countries where leniency is involved are for example the Netherlands, Germany, the UK, or the USA.

However, the mission systems are different. It is unknown from which countries they originate, so especially during assembly of the aircraft, problems with transport might arise. All mission systems most definitely fall under regulations regarding sensitive military equipment, so this needs to be taken into account. The easiest option here is to import these systems in large batches, so the hurdle only must be dealt with a minimum number of times.

A last challenge related to transport is the delivery of the RAD to a commercial company. If, like with many current solutions, red air is outsourced to a commercial company, this company will first have to acquire a RAD. However, since in this case it is not a government requesting it, getting permission is more difficult or impossible. If difficulties mostly lie with sensitive secrecy around the mission systems, the producer could opt to offer a version of the RAD with fewer or no mission systems. The company then must retrofit less advanced technology or provide training capabilities that do not need these special systems.

11.1.4. Facilities

The red air platform will need supporting infrastructure. Except for the additional staff capacity that will be needed on site for drone operators and maintenance staff, the drone will need to be stored in a hangar. This hangar should be large enough to allow for storage, and pre-flight operations such as installing mission systems. Furthermore, the drone needs additional equipment and facilities for maintenance. Maintenance could be done in a separate hangar or in the storage hangar depending on how the operator decides to operate the platform. On top of that, fuel, lubricants, and any other required fluids need to be supplied to the drone. This will likely be present at any friendly airbase the drone is operated out of.
Lastly, any airbase has the general infrastructure required to operate flights, else it would not be an airbase. Services like air traffic control, ground navigation assistance and paved runways of sufficient lengths are assumed to be present but are analysed to assure compatibility.

11.1.5. Training

The staff must be trained in operation of the RAD. The staff include the maintenance staff, fuelling staff and the operators controlling the RAD from the ground. The staff will be provided with technical publication, elaborated in the next subsection, which helps with their respective tasks. However, technical handbooks are often not sufficient to fully be able to operate the drone and therefore require training, especially the operators. This is a significant consideration as overly complicated maintenance and difficult flight operation may require a lot of training and therefore large operating hindrance and cost. Therefore, careful consideration must be given to the level of training required for the operation of the RAD in further design. The design will therefore aim to minimize training need for operation [60, pp. 2610–2611].

Considering the chosen engine, significant training will be needed to get personnel qualified to perform maintenance on the engine. Assuming personnel is already trained for general maintenance on aircraft engines, personnel will need about five hours per person to get familiar with this new engine. This training can be given by experienced personnel from Japan, where this engine is already being used.

11.1.6. Technical Publications

The RAD should be supplied with technical publications that help the maintenance and ground personnel for operation of the drone. These would include maintenance procedures, damage repair guides, parts overview and replacements and further documents to support operation. These handbooks are significant as the staff must be able to understand and maintain the drone as well as be able to prepare the necessary tools and resources for the RAD. This information will be provided by the technical publications provided with the RAD [60, p. 2610].

11.1.7. Spares and Tools

The availability of spare parts and the correct tools is especially important in operation. If a part of the drone needs to be replaced, the right spare part must be available. Furthermore, the correct tools are required to access the parts and to replace them. For this purpose, it is useful if the drone only requires tools that are already available to the maintenance crew. Thus, if the drone only requires the same tools as other military aircraft, this will greatly simplify operation and decrease cost. For the RAD it is therefore important that it only requires tools that are already readily available to the maintenance crew. Additionally, it must be considered that spares require storage and must be ordered from the factory and be transported. Thus, careful planning for ordering parts and reliability consideration for the design must be made with the RAD [60].

Acquiring spare parts will be more difficult for the engine, as this is produced in Japan. Therefore, it is important to have a acquire a large supply of spare parts ready for usage. These spare parts may once again be subject to regulations regarding exporting military technology. However, as discussed before, this depends heavily on the destination country, and most Western military powers are on a list where more leniency is given.

11.2. Primary System

The exact definition of the primary system is not given in the Handbook of Unmanned Aerial Vehicles [59]. Therefore, the primary is defined in this section. The primary system consists of the elements that are directly involved in the operation of the aircraft. First, operation of the airframe is discussed in subsection 11.2.1. Then, communications is discussed in subsection 11.2.2. Finally, the ground control system is discussed in subsection 11.2.3.

11.2.1. Aircraft

Operation of the aircraft relies on many aspects, including the support system. Since for drones, the pilot is not in the vehicle, humans are not a consideration here. However, what does need to be considered is how a human outside the aircraft can still fly it. From the ground control station, the operator must be able to see everything they would if they were inside the cockpit. This means there need to be cameras and sensors constantly feeding data to the operator.

11.2.2. Communication

Communications is a crucial part of the mission. As discussed before, the aircraft is a human-operated drone, so it needs a steady data link to conduct its mission. Luckily, the concept of a human-operated drone is nothing new. Furthermore, as the same control hardware will be used compared to existing drones, the communications equipment will show many similarities to current solutions. Current drones, like the *RQ-4 Global Hawk*, rely on satellite communication once they cross the horizon. The RQ-4 specifically uses a military X-band satellite data link for control. However, as the RAD solely flies in friendly airspace, a UHF or VHF link that is relayed over the horizon is can also be used, as specified in section 4.4.

However, as no communications link is perfect, a contingency plan needs to be in place for the case where the communications link becomes impaired to such an extent, prolonged or for a brief period, that the RAD cannot be controlled from the ground station anymore. For example, the aircraft could automatically start flying straight

and level or back on a course back to base.

11.2.3. Ground Control Station

As proposed by the user, the drone should be compatible with ground stations currently in use for existing drones. This means that the drone will be operated using existing equipment by a human operator. However, measures should be in place to allow the drone to become more autonomous in the future. If the drone is directly operated by a human, the communications link from the aircraft to the ground station needs to be stable. In case the RAD does not use satellite communication, the ground control station needs to be located close to the airfield of operation, as the communications link will then only have a limited range. Having the ground control close to the RAD improves the latency of the communication as well.

Furthermore, the ground control station is subjected to the same support necessities as the aircraft. Not as intensive or frequent as the aircraft, but it still needs to be accounted for. In case this does not happen, the ground control station could fail to fulfil its mission.

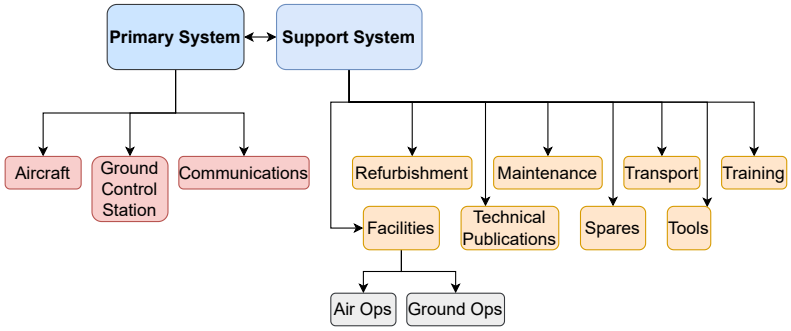

Figure 11.3: *Operations and logistics block diagram for the RAD system.*

11.3. Concept of Operations

To see where the operations of the RAD differ from current solutions, a clear picture needs to be built of what operation of such a mission entail.

11.3.1. Current Red Air

Typically, adversary air training consists of two teams: A red team and a blue team. The red team is the simulated enemy, and they often adopt tactics and doctrines of other nations that could be seen as a potential enemy, in order to provide a realistic training to pilots[3]. However, in the end, the aircraft that is flown is a friendly one, which is also confirmed by their detectable signatures. This red team currently often consists of fighter aircraft or jet trainers. Both teams approach each other, far Beyond Visual Range (BVR)[4]. They both try to shoot each other down using simulated missiles. If a blue aircraft is virtually hit, they are ordered to leave the training area. IF a red team aircraft is virtually hit, they are sent back to the airport, or a regeneration zone, after which they can re-join the fight. In the Red Flag exercise, held in the USA, many aircraft fly at once, which means extensive planning and monitoring is needed. From an external location, either in an aircraft or on the ground, a separate unit monitors all operations to ensure safety and proper execution of the training.

11.3.2. Future Red Air

The operations of the RAD largely differ from current methods in two aspects: Versatility and ease of operation. First, its versatility. The mission system on board enables the RAD to emulate a range of hostile fighter aircraft. Although numbers are not publicly known, the small size and RCS-optimised design of the RAD allows assumption that the RAD will have a smaller RCS than any military aircraft not designed for low RCS. This enables the RAD to use its mission systems to increase its RCS to anything above its base value. The RAD can then even change which aircraft it is emulating mid-flight. For example, after it is virtually shot down, it could start emulating a different signature to change the fight for the blue team.

[3]Source: https://en.wikipedia.org/wiki/Exercise_Red_Flag (retrieved on 18 June 2022)

The RAD is also easier to operate than current alternatives, and it only gets better in the future. Communication runs through satellites, which means the fleet of RADs can be controlled from anywhere in the world. Furthermore, the fact that it is controlled remotely means that automation can be built into the control system. Parts of the flight or the full flight can then be automated and controlled with commands. For example, one operator could then operate multiple drones by giving them commands or assignments. Moreover, the drones could be commanded directly by the training coordinators.

The use of the RAD in the adversary air training will introduce new operational procedures. These procedures include the ground segment and flight operations segment separately. With the addition of the ground control station of the RAD, the controllers of the training will need to establish communication between the ground control station and the blue air ground station. Also, the operators of the RAD will need training beforehand. Operators could then include experienced (ex-)military pilots who are not able to fly manned aircraft anymore.

For longer training missions, the RAD with the current maximum fuel capacity requires refuelling. In these situations, either the RAD can return to base for refuelling or another RAD can be used to replace the first.

11.4. RAMS Characteristics

To assess the Reliability, Availability, Maintainability and Safety (RAMS) characteristics of the RAD, one needs to assess the exotic design features that makes it depart from trends in the sector. To do this, every factor is explored separately.

11.4.1. Reliability

The first factor is reliability. The reliability of the RAD depends on how often systems fail in such a way that its mission performance or safety is impaired. A key factor in this is the engine. Engines are delicate machines with many components that could all fail. Over 30% of maintenance costs in commercial aviation are spent on propulsion systems[4]. The engine that is being used has already been in operation in military trainer aircraft since 1988. As such, technical publications and overall experience with the engine have made sure that common faults have been mitigated or can easily be predicted. Therefore, this is not expected to be a problem. However, the afterburner may fail more often, as it is newly developed. Due to the lower complexity of this part of the engine, it is not expected to present a significant impact on reliability. During redevelopment of the afterburner, reliability should be assessed separately from the aircraft to ensure that this is not a problem.

A second exotic component in the RAD is the mission systems. They are intricate technologies that are often state-of-the-art, which means they are expected to fail more often than the average system.

Lastly, the simplicity of the RAD is expected to improve total reliability. The aircraft has little moving surfaces. Only the landing gear doors, flaperons and V-tail control surfaces can move in flight. In contrast, many aircraft have spoilers, airbrakes or more empennage control surfaces, all of which can fail.

However, reliability does not only depend on the RAD. As it is a drone, the bigger picture needs to be considered. Communication systems could fail, or the GCS could stop working. However, since the RAD drone is compatible with existing infrastructure for controlling UAV's, this is not expected to pose a big problem in the reliability of the system. Furthermore, as an engineer is always on call to fix any problems with the GCS, failures in the GCS would not often result in mission failure.

11.4.2. Availability

As discussed in section 11.4.2, not all systems are perfectly reliable. As assumed in section 13.6.4, the aircraft needs 12 man-hours of maintenance for every flight. As such, it will not be available 24/7. However, especially low-level maintenance can be performed at night, or in between scheduled flights. This allows availability to be flexible and optimised. On the other hand, unexpected depot-level maintenance has a substantial impact on availability. However, this is extremely unlikely to happen.

[4]Source: https://aviationweek.com/air-transport/opinion-oems-focus-mature-aircraft-aftermarket-growth (retrieved on 14 June 2022)

A cause of unavailability that cannot be mitigated is the regular checks and operations needed between flights. For example, system checks, refuelling, flight recorder data extraction and safety checks need to be performed between every flight. In total, this can be done within half an hour, as the aircraft is rather small, and checks can be performed quickly. Furthermore, refuelling does not take long compared to existing aircraft, as the needed mass of fuel is much less.

Maintenance of the GCS also needs to be performed, but is less critical than maintenance on the RAD. If the entire GCS fails, another unit that is not in use at that time could be connected to the RAD as a backup. This redundancy and the presence of a maintainer means that the GCS will not cause any availability problems.

11.4.3. Maintainability

Due to its small size, the RAD is easily accessible for maintenance. The slender body means that systems are never buried far into the fuselage, except the engine. However, the engine integration and mounts can be designed in such a way that it can be easily taken out of the aircraft when it needs to be replaced or taken apart.

Furthermore, as many mission systems must be on or near the surface to perform their function, they are inherently accessible. This is especially important considering their questionable reliability.

As discussed in section 11.1.2, pre-flight and post-flight procedures also fall under maintenance. These operations require cooperation between the ground crew and the operator in the GCS. Protocols for this already exist and are in use for operational UAVs.

Lastly, a distinction must be made between several types of maintenance. Generally, there is scheduled and non-scheduled maintenance. Scheduled maintenance is performed when the recommended lifetime of a component or system has been reached. For example, tires, brakes, and engine components all have a defined service life, after which they should be refurbished or replaced. This type of maintenance can be planned for in a manual that is delivered with the aircraft when it is acquired and adapted as more technical publications are made.

Non-scheduled maintenance occurs when a component breaks unexpectedly and impairs the performance or safety of the RAD to such an extent that operating it becomes unfeasible. Faults like fluid leaks, mechanical components breaking, or software bugs do occur and all need to be fixed. The goal of maintenance is to minimise the occurrence of non-scheduled maintenance, as this often means that the recommend lifetime of a component was wrong, the component had a manufacturing fault or assembly was not performed correctly. As the service life of the RAD progresses, common unscheduled maintenance causes get identified and can be turned into scheduled maintenance activities using technical publications. Then, the fault can be fixed before it occurs. However, non-scheduled maintenance can never be fully avoided, as damage due to external factors can always occur. Therefore, the aircraft should be accompanied by commonly used spare parts when it travels to a mission area.

Especially the engine is expected to be the cause of a lot of unscheduled maintenance, as the afterburner is a relatively modern design and overall, the engine consist of many components. Therefore, spare parts for the engine especially need to be readily available at a mission area. Furthermore, an operator should acquire more engines than aircraft to have spares ready when one fails to such an extent that the entire unit must be replaced.

11.4.4. Safety

Safety is a critical aspect of the design. For the aircraft to safely operate, it must at all times have the following functions:

- Autopilot for loss of data link
- Functional control surfaces
- working flight and navigational sensors
- Working onboard computer
- Functioning TCAS

As such, these functions must have a fail-safe or redundant design. Even if the fail-safe fails the drone has a parachute recovery system, which can be used to slow down the drone and let it land on a safe location.

12
Future Development Logic

In this chapter, the manufacturing plan is detailed in section 12.1. Furthermore, the risk analysis is performed in section 12.2. Finally, the project design and development logic is discussed in section 12.3.

12.1. Manufacturing, Assembly and Integration Plan

The production flow is mainly dictated by the number of orders in order book and expected delivery times. This determines the number of sub-assembly and assembly lines needed to keep up with the demand. The sales forecast offers information on the expected volumes of the aircraft to be manufactured. This in turn determines capacity planning and batch sizes for the parts.
In the case of the red air drone, the raw materials (aluminium, steel, etc.), a number of crucial parts (engine, tires, etc.), and the systems (mission systems) are outsourced. This creates demand on the supply chain and expected delivery intervals of incoming parts. A warehouse also needs to be present to store delivered items.

In-house made parts, like the wing skin or the fuselage frames, are made in a batch production. A warehouse is needed to store this incoming batch of manufactured parts as well. Next, the manufacturing divisions must be made. Splitting up the aircraft into four sub-assemblies, namely the wing, fuselage, empennage, and landing gear sub-assembly allows for smaller station, such that the production benefits from the learning curve of the crew. The last step of line production is the main assembly, where all the sub-assemblies meet together with off-the-self parts like the engine to become the red air drone. Finally, the ground station must be built and when connected to the red air drone, the red air platform is finalized. Figure 12.1 visualises the process of manufacturing, assembly, and integration of the red air platform

12.2. Risk Analysis & Risk Map

This section goes over the risks that have been identified in the planning stages of the design [2], [3], [17] and reassesses them.. New identified risks have been added and are discussed in section 12.2.1. The resulting updated risk map is given in section 12.2.2.

12.2.1. New Identified Risks

During this stage of development, no new technical risks have been identified. However, one new organisational risk has been found and will be identified with *RISK-ORG-19*, see table 12.1. The mitigation strategy is to bring a speaker to presentations where one or more members cannot attend. A video will be shown in a corner to show the speaker talk about his part of the presentation.

Table 12.1: *Newly identified organisational risks.*

ID	Risk
RISK-DEV-10	Simulations require a long time to perform, stalling the development
RISK-TECH-OP-54	Transition to supersonic regime causes instabilities

12.2.2. Technical Risk Map

The technical risk map before any mitigation can be seen in table 12.2, the technical risk map after mitigation can be seen in table 12.3. These matrices put all identified risks, both operational and developmental, into the matrix, this way the most important risks can be easily identified [3].

Note that the risk maps have not been altered since the risks have been established as there are no new risks.

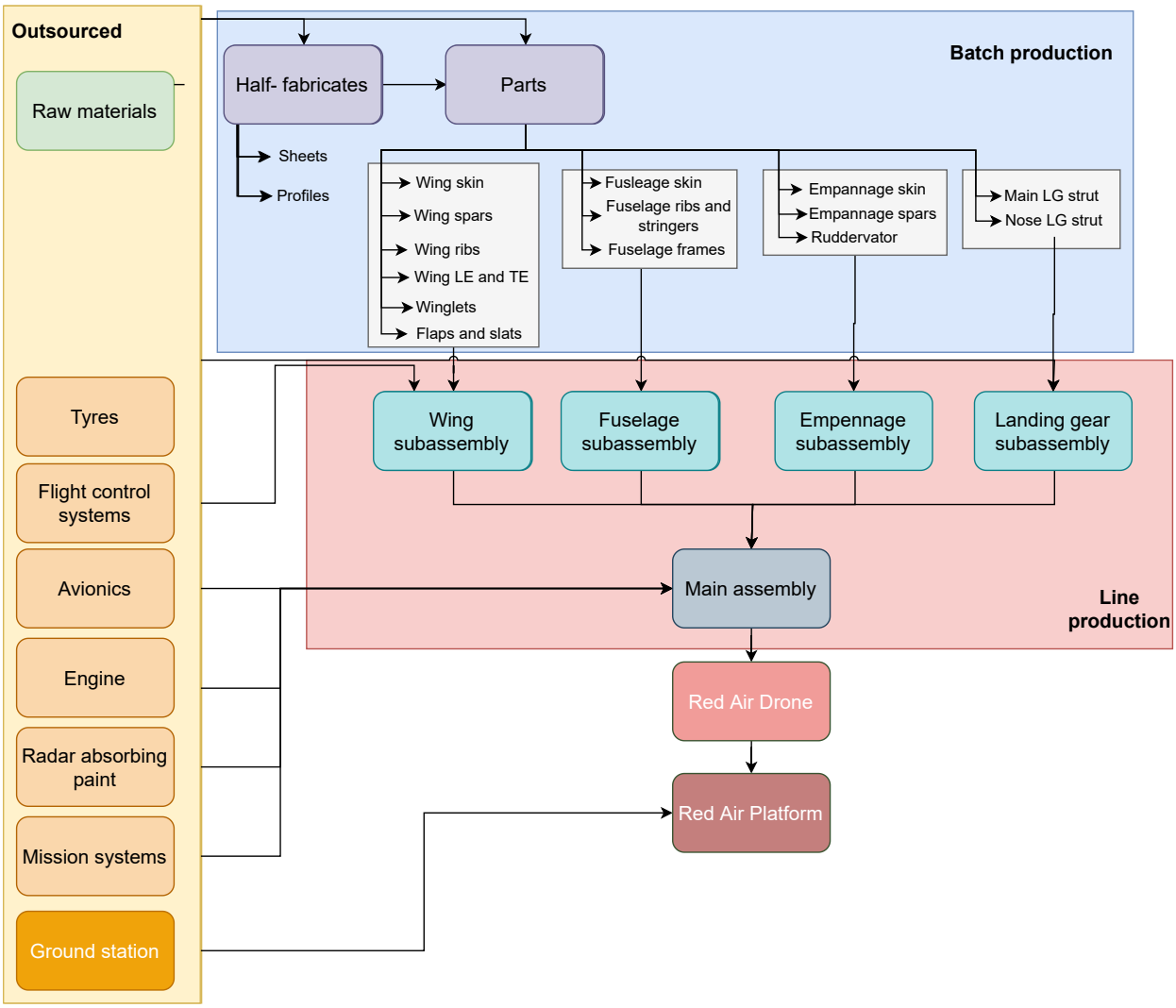

Figure 12.1: *Manufacturing, Assembly, Integration plan of the RAD system.*

Project specific risks are marked using bold text. It should also be pointed out that the risk mitigation strategies were also not changed and therefore are not discussed here but given in [3].
The scale used for the impact probability/severity in table 12.2 is the following: Negligible: Inconvenience or non-operational impact. Marginal: Degradation of secondary mission or small reduction in technical performance. Critical: Mission success is questionable or some reduction in technical performance. Catastrophic: Mission failure or significant non-achievement of performance. Fatal: Mission failure and loss of vehicle and/or loss of life.

For table 12.3 the scale used for the impact probability/severity is redefined in the following way: Negligible: Inconvenience. Marginal: Design not at significant risk, minor loss of time. Critical: A lot of work must be redone, no risk of entire project failing. Catastrophic: Development is at high risk of not being completed. Fatal: The design is ruined.

12.3. Project Design and Development Logic

After the project design phase is finished, a prototype of the product should be developed. This is the first step towards bringing the product to the market. Before a product can be operational, several steps must be performed before. These steps include verification, validation, and certification. The product needs to be produced as well. An end-of-life strategy is required as well to reduce the environmental impact of the product after operation; however, optionally the drone can be ceremonially put out of commission by using it for real target practice. A planning for these steps is made and displayed in this chapter by a Gantt chart and work breakdown structure. These steps are called different stages of the development logic. Stage 1 entails the verification and validation of the prototype design. Followed up by stage 2 that requires the design to be certified. After the certification,

Table 12.2: *Risk map before mitigation of risks.*

Risk / Impact	Negligible	Marginal	Critical	Catastrophic	Fatal
Very high		RISK-TECH-OP-21	RISK-TECH-OP-14		**RISK-TECH-OP-42**
High	**RISK-TECH-OP-53**	RISK-TECH-OP-12 **RISK-TECH-OP-19** RISK-TECH-OP-27 RISK-TECH-OP-31 RISK-TECH-OP-49	**RISK-TECH-OP-15** **RISK-TECH-OP-39** RISK-TECH-OP-43	**RISK-TECH-OP-51** **RISK-TECH-DEV-01**	**RISK-TECH-OP-36** RISK-TECH-OP-37
Moderate	RISK-TECH-OP-29	RISK-TECH-DEV-06	**RISK-TECH-OP-07** RISK-TECH-DEV-03 RISK-TECH-OP-44 RISK-TECH-OP-46 RISK-TECH-OP-47	RISK-TECH-OP-26 RISK-TECH-OP-52 **RISK-TECH-DEV-07**	RISK-TECH-DEV-02
Low	RISK-TECH-OP-20 RISK-TECH-OP-28	RISK-TECH-OP-10 RISK-TECH-OP-22	RISK-TECH-OP-02 RISK-TECH-OP-13 RISK-TECH-OP-23 RISK-TECH-OP-24 RISK-TECH-OP-25 RISK-TECH-OP-45 RISK-TECH-OP-48 **RISK-TECH-DEV-05**	RISK-TECH-OP-03 RISK-TECH-DEV-08	RISK-TECH-OP-01 RISK-TECH-OP-04 RISK-TECH-OP-09 **RISK-TECH-OP-18** RISK-TECH-OP-30 RISK-TECH-OP-38 **RISK-TECH-OP-50** RISK-TECH-DEV-04 **RISK-TECH-DEV-09**
Very low	RISK-TECH-OP-40	**RISK-TECH-OP-08** RISK-TECH-OP-11 RISK-TECH-OP-17 RISK-TECH-OP-32	**RISK-TECH-OP-16** RISK-TECH-OP-35		RISK-TECH-OP-05 **RISK-TECH-OP-06** **RISK-TECH-OP-33** RISK-TECH-OP-34 RISK-TECH-OP-41

Table 12.3: *Risk map after mitigation of risks.*

Risk / Impact	Negligible	Marginal	Critical	Catastrophic	Fatal
Very high					
High					
Moderate	**RISK-TECH-OP-53**	RISK-TECH-OP-12 **RISK-TECH-OP-39** RISK-TECH-OP-49 **RISK-DEV-10**	RISK-TECH-OP-14 RISK-TECH-DEV-03	**RISK-TECH-DEV-01** RISK-TECH-DEV-02	
Low	RISK-TECH-OP-28	RISK-TECH-OP-26 RISK-TECH-DEV-06	**RISK-TECH-OP-15** RISK-TECH-OP-46 RISK-TECH-OP-47	RISK-TECH-OP-09 **RISK-TECH-OP-51** **RISK-TECH-DEV-07** RISK-TECH-DEV-08 **RISK-TECH-OP-54**	RISK-TECH-DEV-04
Very low	**RISK-TECH-OP-08** RISK-TECH-OP-11 RISK-TECH-OP-20 RISK-TECH-OP-29 RISK-TECH-OP-40	**RISK-TECH-OP-07** RISK-TECH-OP-10 RISK-TECH-OP-13 **RISK-TECH-OP-16** RISK-TECH-OP-17 **RISK-TECH-OP-19** RISK-TECH-OP-21 RISK-TECH-OP-22 RISK-TECH-OP-27 RISK-TECH-OP-31 RISK-TECH-OP-32 RISK-TECH-OP-35	RISK-TECH-OP-02 RISK-TECH-OP-23 RISK-TECH-OP-24 RISK-TECH-OP-25 RISK-TECH-OP-43 RISK-TECH-OP-44 RISK-TECH-OP-45 RISK-TECH-OP-48 **RISK-TECH-DEV-05**	RISK-TECH-OP-03 RISK-TECH-OP-04 RISK-TECH-OP-05 RISK-TECH-OP-34 RISK-TECH-OP-37 RISK-TECH-OP-52	RISK-TECH-OP-01 **RISK-TECH-OP-06** **RISK-TECH-OP-18** RISK-TECH-OP-30 **RISK-TECH-OP-33** **RISK-TECH-OP-36** RISK-TECH-OP-38 RISK-TECH-OP-41 **RISK-TECH-OP-42** **RISK-TECH-OP-50** **RISK-TECH-DEV-09**

stage 3 can begin which considers the production process. Stage 4 is when the product is in use and performing its red air mission. Finally, stage 5 details the end-of-life strategy. The WBS can be found in subsection 12.3.1 which lays out the logical next steps to be performed after the initial design has been finished. Subsection 12.3.2 shows the Gantt chart.

12.3.1. Post-Design Work Breakdown Structure

A work breakdown structure describes the steps that must be made after the initial design has been developed. This work breakdown structure is shown in figure 12.2. The structure consists of five stages. These include stage 1, the verification and validation of the design; stage 2, certification of the final design; stage 3, production of the final design; stage 4, operation; and stage 5, end-of-life.

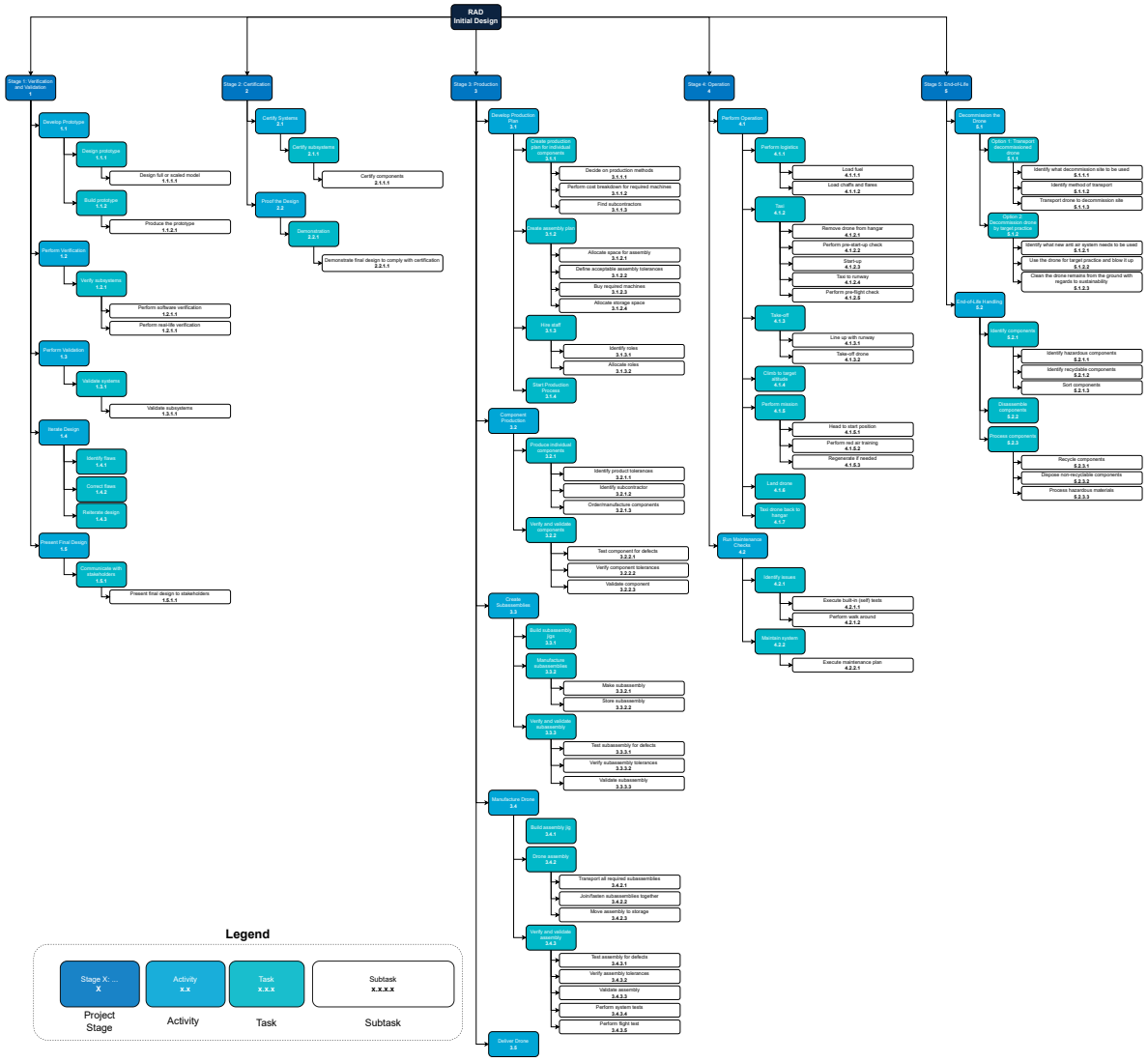

Figure 12.2: *Work breakdown structure, outlining tasks to be performed after completion of the initial design.*

12.3.2. Post-Design Gantt Chart

A Gantt chart can be seen in figure 12.3. This Gantt chart describes all the tasks that should be performed after the design process, as well as give a timeline indication of the task flow.

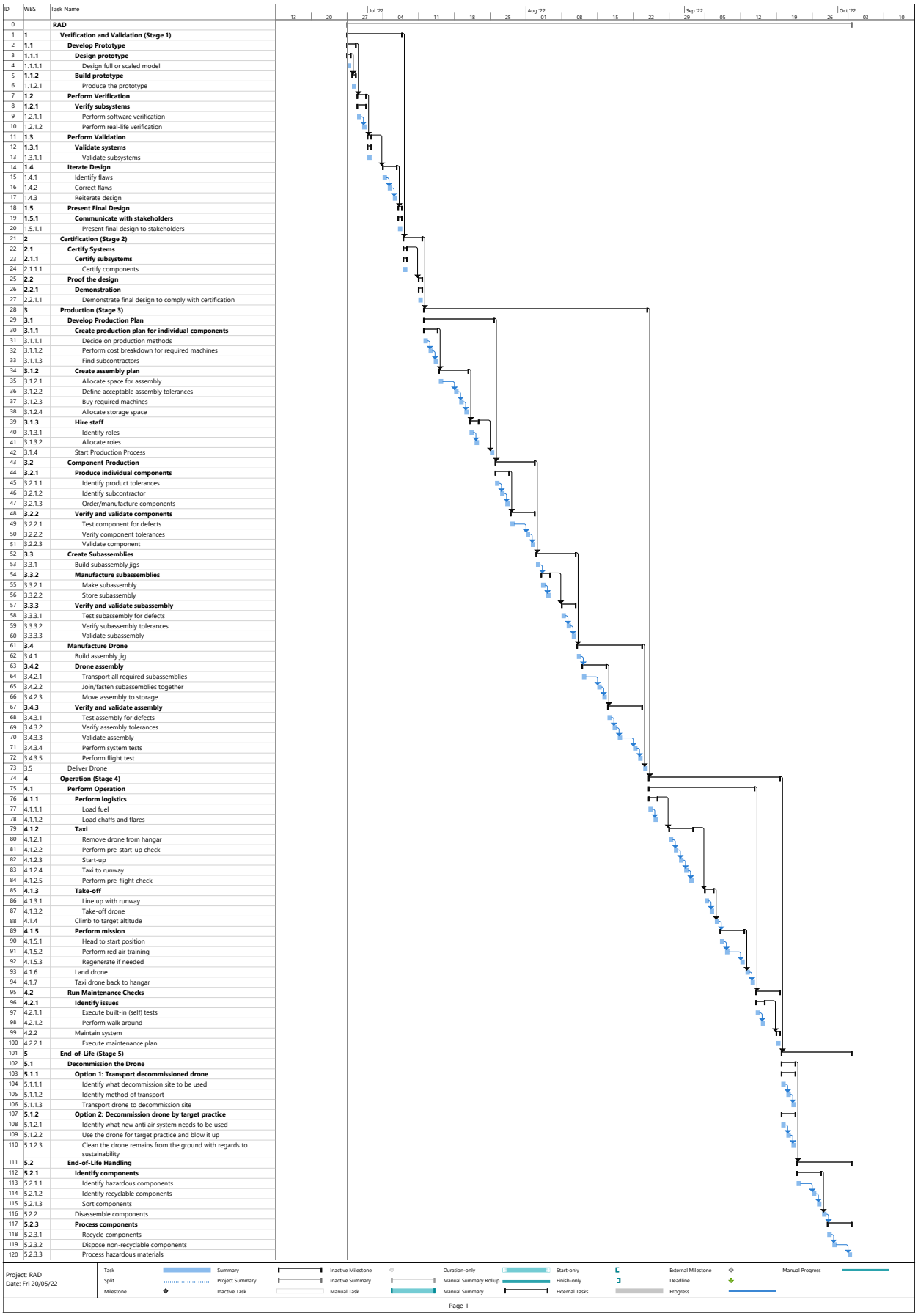

Figure 12.3: *Gantt chart displaying the tasks to be performed after completion of the initial design.*

13
Economic Analysis

This chapter describes how the RAD is situated in the market. Firstly, the demand for the platform is discussed. Then, the various cost categories of the RAD are analysed. In the last section, the cost of the RAD is compared to similar platforms.

The financial performance of the RAD is not tied to specific requirements. However, two requirements are currently TBD, both of which can be changed to numbers at the end of this chapter. On the other hand, the project objective of delivering a more cost-effective solution can already be verified using the results of this chapter.

Table 13.1: *Key requirements related to economics.*

ID	Description
RAD-CO-RES-02-01-A	The Life Cycle Costs of the system shall be lower than 'TBD' USD
RAD-CO-RES-02-02	The RAD design and manufacturing costs shall be less than 'TBD' USD

13.1. Market Analysis

The red air mission is a crucial part in developing and maintaining pilot skills. It was shown that the US Air Force pay exorbitant sums of money for commercial services to make their pilots ready for combat. These services are used to avoid placing combat-capable pilots in aggressor squadrons, where their only purpose is to provide training to other pilots. Sometimes, this still happens, which means both the pilot and airframe are not used for their intended purpose. When a stealth red air aircraft is needed, the F-35 is used.[1] This is a big waste, as operating this aircraft costs more than 13,000 USD per flight hour in direct operating costs alone [62]. This excludes personnel, acquisition and support infrastructure. With a price tag of 100 Million USD and an expected lifetime of as low as 2,100 hours[2], just factoring in the depreciation cost adds 47,000 USD to the hourly rate. There is clearly a need for an alternative.

13.2. Demand Analysis

An important aspect of market analysis is analysing the demand that exists for the product that is being developed. The purpose of this section is to provide a brief overview of recent and future demand for products that fulfil a similar Mission Need Statement.

Back in the Vietnam War, air-to-air kill ratios for American pilots were deemed too low, and a study was done to assess why this was happening and how to improve this. The result of this is the red air mission, which aims to train pilots in engaging dissimilar combat aircraft[3]. So, adversary combat training is nothing new. However, in recent years the way it is done has been shifting due to new technological developments and changes in budget. Still, armed forces want to train their assets in the most effective way possible. In the US military, the number of contracted adversary flight hours has been increasing substantially [63].

In February 2019 the USAF kick-started a new initiative in the field of adversary training which would cover 21 bases across the US and encompass 50,000 hours of flight time. This adversary training to be provided by the

[1]Source: https://www.nellis.af.mil/News/Article/3058572/65th-aggressor-squadron-reactivates-at-nellis-with-aggressor-force-of-f-35s/ (retrieved on 19 June 2022)
[2]Source: https://militarywatchmagazine.com/article/disposable-fighter-pentagon-report-reveals-f-35-s-extremely-short-lifespan (retrieved on 31 May 2022)
[3]Source: https://www.airforcemag.com/article/1100flag/ (retrieved on 31 May 2022)

private sector, this initiative called: private adversary air (ADAIR). The Air Force has set aside 6 billion dollars over a course of ten years to provide this adversary training by the private sector, 600 Million USD per year. To operate a fleet of F-16 for adversary training for a year with the new initiative in mind for adversary training it would cost a minimum 419 Million USD per year (excluding the acquiring, infrastructure, maintenance, pilots, engineers, support and airworthiness costs). This means that the cost per hour of the ADAIR programme should be below 12,118 USD, a very strict requirement.

On top of that, there is an issue of availability of pilots to provide red air for blue air training. Both the leadership and pilots themselves do not want to fly red air. Due to the fact that red air does not provide a pilot with any useful training for combat: flying like the enemy does not help you in beating the enemy in actual combat. Furthermore, it requires lots of studying the enemy and training to fly like the enemy. If the red air mission will continue to grow, it is required that more pilots are available for this.

Furthermore, dedicating a combat-capable aircraft to a training squadron that does not use it for its intended purpose is a waste of its potential. Fighter aircraft are over designed for the task, and as such they use more resources than needed. High-tech aircraft are worn out doing tasks that could be performed by cheaper and simpler alternatives. Furthermore, a current fighter cannot mask itself as a foreign type, for example a MiG. It still emits signatures that are known and recognised as friendly. Payload exists to change emissions into something that mimics an enemy aircraft, but aircraft that can carry this payload cannot mimic the performance of these aircraft. Nothing exists that can mimic both signature and performance.

Therefore, designing an unmanned platform that is easier to operate, easier to deploy, and can provide better training in a more cost-effective and sustainable way will be attractive. It will solve the pilot issue, shall be easier to deploy, and can mimic the adversaries better than current manned alternatives. For the future, with the continuing development of applicable technologies, UAV platforms will become more and more important to the military around the world.

13.3. Competitor Analysis

There are several competitors that fulfil a similar Mission Need Statement as the red air Drone. In this section, general red air services are discussed first. Finally, specific UAV platforms are discussed that come close to the Project Objective Statement.

13.3.1. General Red Air Services

Currently, adversary air is provided either by the military itself or by private contractors such as Draken International or ATAC LLC. These contractors generally operate decommissioned military aircraft and light combat aircraft. In current contracts, the costs per flight hour for aircraft with similar performance, like the F-5, are set at 16,800 USD for the USAF [63].

In the past decades the USAF has been mostly operating F-16's as adversaries for red air, which have a Direct Operating Cost between 8,374 USD to 14,833 USD per hour (excluding the acquiring, infrastructure, maintenance, pilots, engineers, support and airworthiness costs).
With ADAIR, launched in February 2019 by the Air Force, the Direct Operating Cost for red air should be below 12,118 USD.

13.3.2. UAV Red Air Platforms

Table 13.2 displays the general characteristics of similar UAV platforms compared to the red air Drone. It should be noted that there are platforms which carry similar payloads, however, none of them are able to operate at supersonic speeds. This is therefore a distinctive feature of the red air Drone, as it will provide a better adversary. Most systems are used as targets for air-to-air or surface-to-air missiles whereas the red air Drone can be used for more general beyond-visual-range combat training.

On top of the reference aircraft considered in section 4.5.1, the Blue Force Fury has been added to table 13.2. This is a conceptual design of a UAV similar to the RAD, although subsonic. It can do dashes up to M 1.0[4]. It

[4]Source: https://www.forbes.com/sites/erictegler/2022/03/30/a-drone-with-a-small-bizjet-eng

promises to have a unit cost between 3 and 5 Million USD, although it does not specify what is included in this cost. The designer did not specify the mission systems on board, so these could be excluded in this cost.

Table 13.2: *Competitive Position of the red air drone compared to existing UAVs.*

Type	**ŞIMŞEK** [5]	**Do-DT55**[6]	**BQM-177A** [7]	**BQM-167A** [8]	**QF-16** [9]	**Banshee Jet 80+** [10]	**Fury**	**Red Air Drone (RAD)**
Company	TUSAŞ	Airbus	Kratos	Kratos	Boeing	Qinetiq	Blue Force	Red Team
Max Launch Weight [kg]	75	22	635	930	10800	N/A	2268	2126
Max Payload [kg]	10	8	45 + 77	N/A	5443	N/A	N/A	150
Service Ceiling [ft]	20000	25000	40000	50000	50000	30000	N/A	45000
Max Velocity	206 m/s	234 m/s	M .95	316 m/s	M 2.0 @ 40,000 ft	200 m/s	< M 1.0	M 1.6-2.0 @ 30,000 ft
g limits [-]	6	N/A	-2 / 9	-2 / 9	9	N/A	9	-1 / 6
Range [km]	90	55	N/A	740	3889	100	277.8	**<TBD>**
Radius of Operation [km]	90	N/A	277	N/A	N/A	N/A	N/A	**<TBD>**
Endurance [s]	2700	N/A	3600	10800	N/A	2700	14800	11556
Power plant [-]	1 Turbojet	1 Turbojet	1 Turbojet	1 Turbojet	1 Turbofan	2 Turbojets	! Turfofan	1 Turbofan
Countermeasures	Yes	Yes	Yes	Yes	Yes	Yes	N/A	Yes
RCS Augmenter	Yes	Yes	Yes	Yes	No	No	N/A	Yes
IR Signature Augmenter	Yes	Yes	Yes	Yes	No	Yes	N/A	Yes

Note that the US Air Force currently has a contract running for a Next-Generation Aerial Target (NGAT), which has capabilities almost identical to the RAD. The biggest exceptions here are the top speed and service life. The requirement for the NGAT is only Mach 0.95, while the RAD must reach Mach 1.6. Furthermore, the NGAT will only have an average lifetime of flight 30 hours, after which it will be destroyed. However, the mission systems on the NGAT carry similar requirements to those present in the RAD. The NGAT must be able to emulate the same range of signatures as the RAD. Although no exact RCS target is mentioned, it is required to emulate the RCS of foreign fighter jets with low-observable designs. Note that these are all minimum capabilities, as described by the initial desired capabilities[11]. However, it is mentioned in the Freedom of Information document that these desired capabilities can be changed if that is needed to meet the cost target.

13.3.3. SWOT Analysis

Figure 13.1 shows a SWOT analysis of the market. It provides an overview of the current market together with future opportunities and hazards.

ine-might-simulate-5th-generation-fighters-for-cheap/?sh=24a6cdf37f82 (retrieved on 19 June 2022)

[11] Source: https://imlive.s3.amazonaws.com/Federal%20Government/ID629538839000663258696052186 07318175315/Next_Gen_Aerial_Target_RFI.pdf (retrieved on 7 June 2022)

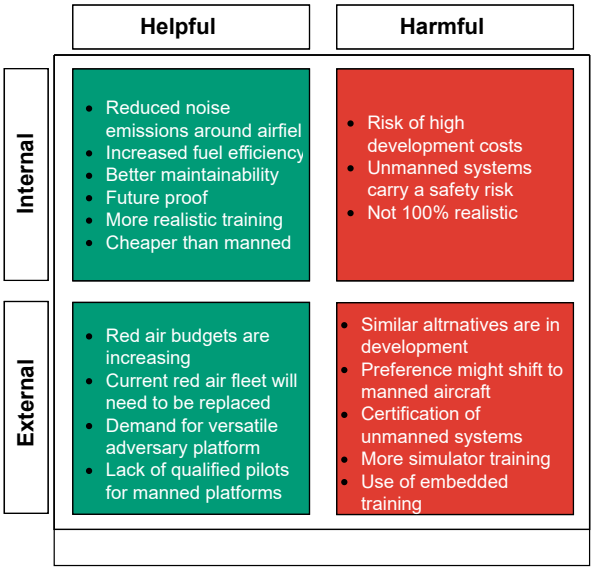

Figure 13.1: *SWOT Analysis of the red air market.*

13.4. Cost Breakdown Structure

As discussed in the Midterm Report [2], the costs of buying and operating the RAD can be divided in many categories. This is summarised in the cost breakdown structure, which can be seen in figure 13.2.

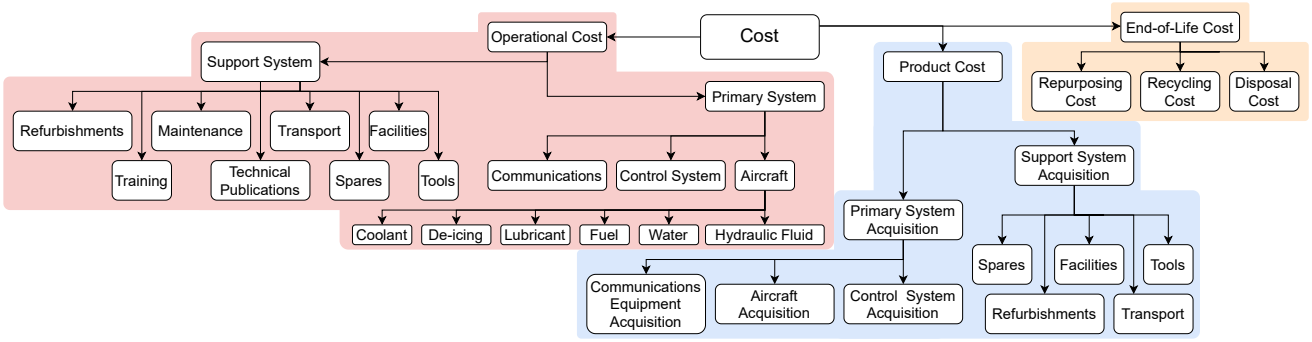

Figure 13.2: *Cost breakdown structure for the RAD.*

13.5. Prices of Alternatives

In order to build a picture of the cost savings the RAD can bring, the cost of current solutions first must be analysed. This is done for various cost components.

13.5.1. Next-Generational Aerial Target

As described in section 13.2, the Air Force is currently seeking a Next-Generational Aerial Target. As also described in their formal request, the production cost should be less than 10 Million USD and development cost should be limited to 300 Million USD.[12]. As capabilities in flight hours and top speed for the RAD far exceed that of the NGAT, a good cost target is that of the NGAT. Staying below this is even better, as this would also make the RAD a competitive option for the NGAT contract.

13.5.2. US Air Force

Taking the US Air Force (USAF) as one of the alternatives, the costs of using several of their fighter aircraft is investigated, with the intent of finding cost categories where the RAD needs improvement to compete. These numbers have been summarised in table 13.3 for three aircraft types. First of all, their Cost per Flying Hour (CPFH) when they are lent out to a different party within the US Department of Defense (DoD). This number is

published every year by the DoD [62]. Then, their Maintenance Man Hours per Flying Hour (MMH/FH)[12] [13] [64, Part 2, p. 226]. This is a number that varies per aircraft, most notably for the F-35. Its MMH/FH is far lower than the F-16 and F-15, which could stem from fact that these numbers come from different sources, and no source states whether Depot-Level Maintenance is included in this number. Furthermore, acquisition cost[14][15][16] and expected service life are shown[17] [18] [19]. Lastly, pilot hourly costs are added. These were also published by the DoD [62]. Unfortunately, insufficient data for the T-38 jet trainer is available to add it to this comparison.

Furthermore, the isolated maintenance costs can be estimated. As $CPFH_{DoD}$ generally only considers fuel use and maintenance [65, p. 14], subtracting fuel use from the numbers in table 13.3 can provide an estimate of hourly maintenance costs. Taking the fuel capacities of the F-16[20], F-15[21] and F-35[22], and an estimated fuel price of 1,335 USD per metric ton[23], an estimated hourly maintenance cost can be produced. This is subsequently divided by the respective MMH/FH values in order to find a maintenance cost per man-hour.

Table 13.3: *Costs for existing fighter jets in USAF inventory.*

Type	**$CPFH_{DoD}$**	**MMH/FH**	**Acquisition cost** [2022 USD]	**Service life** [hrs]	**Pilot costs** [2022 USD/hr]	**Maintenance per man-hour** [USD]
F-16	10,866	33	33,710,000	8000	105	265
F-15	18,799	28	55,770,000	8000	105	360
F-35	13,185	4.79	78,000,000	8000	105	1599

13.5.3. Commercial Companies

Another alternative to contract commercial companies to provide red air. The US Department of Defense awards these contracts to private companies that can provide this training. Table 13.4 gives an overview of the value of these contracts over the past years. The table includes both USAF and USN/USMC contracts.

Table 13.4: *Contract prices for commercial red air forces as awarded by the US Department of Defense [63, p. 11].*

Year	**Original contract price [USD]**	**Inflation** [%]	**Price** [FY 2022 USD]	**Hours**	**Price per hour** [FY 2022 USD]
2015	83,000,000	23	102,355,600	10208	10,027
2018	280,000,000	12	314,552,000	16800	18,723
2015	295,000,000	23	363,794,000	19600	18,561
2018	109,000,000	12	122,450,600	11700	10,466
2021	442,000,000	8	477,360,000	42750	11,166

[12] Source: https://www.dvidshub.net/news/252906/114th-maintenance-group-instrumental-achieving-4000-flying-hours (retrieved on 18 June 2022)
[13] Source: https://www.defensedaily.com/u-s-f-35-maintenance-man-hours-per-flight-hour-rate-improves-since-2018-but-mission-capable-rates-lag/air-force/ (retrieved on 18 June 2022)
[14] Source: https://www.af.mil/About-Us/Fact-Sheets/Display/Article/104499/f-15e-strike-eagle/ (retrieved on 18 June 2022)
[15] Source: https://www.af.mil/About-Us/Fact-Sheets/Display/Article/104505/f-16-fighting-falcon/ (retrieved on 18 June 2022)
[16] Source: https://www.defensenews.com/air/2019/10/29/in-newly-inked-deal-f-35-prices-fall-to-78-Million-a-copy/ (retrieved on 18 June 2022)
[17] Source: https://www.globalsecurity.org/military/systems/aircraft/f-15-life.htm (retrieved on 18 June 2022)
[18] Source: https://militaryembedded.com/avionics/safety-certification/u-s-air-force-extends-f-16-service-life (retrieved on 18 June 2022)
[19] Source: https://militarywatchmagazine.com/article/disposable-fighter-pentagon-report-reveals-f-35-s-extremely-short-lifespan (retrieved on 18 June 2022)
[20] Source: https://customer-janes-com.tudelft.idm.oclc.org/Janes/Display/JAU_1617-JAU_#Specifications (retrieved on 18 June 2022)
[21] Source: https://customer-janes-com.tudelft.idm.oclc.org/Janes/Display/JAWA1183-JAWA#Specifications (retrieved on 18 June 2022)
[22] Source: https://customer-janes-com.tudelft.idm.oclc.org/Janes/Display/JAWA1347-JAWA#Specifications (retrieved on 18 June 2022)
[23] Source: https://jet-a1-fuel.com/price/netherlands-the (retrieved on 10 June 2022)

Costs per flying hour are also available for aircraft platforms that are often used by red air contractors. These are shown in table 13.5.

Table 13.5: *Contractor costs per flying hour by service and contractor aircraft platform [63, p. 32].*

Service	**Aircraft platform**	**Contract CPFH** [FY 2020 USD]	**CPFH** [FY 2022 USD]
USAF	F-5	16,800	18,974
	F-1	12,400	14,004
	L-159	9,100	10,277
USN/USMC	F-5	11,500	12,988
	F-1	15,000	16,941
	Hawker Hunter	11,000	12,423

13.6. Costs of the Red Air Drone

Now that a picture is built of the price of competitors, the costs of the RAD can be analysed. This is done for three components: Development cost, production cost, acquisition cost and operational cost.

13.6.1. Development Costs

Development cost estimation is a difficult endeavour. Not many budgets and development costs are public and finding the variables that influence this number the most requires a long study. Elaborate methods are known, require more data than is known at this stage of the design process. Therefore, software from DARCorporation was used. It is called ”Advanced Aircraft Analysis” and can be used for many more engineering tasks than just cost estimation. It requires many inputs and then breaks down development cost into different categories, often using empirical estimations. The inputs that were used can be found in appendix A.

In the end, three components of development costs were found. First of all, design cost was found to be 28.2 Million USD, following that, the development, support and testing cost is 9.27 Million USD. On top of that, flight test operations are estimated to cost 5.54 Million USD. Lastly, the cost of all flight test airplanes is 123.1 Million USD. As these numbers are all based on empirical data and a highly sensitive model, a margin of 40% is applied to capture all uncertainty in these cost factors.

The sensitivity of the model mostly depends on ambiguous factors that lack explanation and must be found in a subjective manner. Examples of these factors are the ”Difficulty factor”, ”CAD Judgement factor” and ”Low observability factor”. All these factors are 1.0 by default and increase a cost component in direct proportion when they are changed. Obviously, these factors have little mathematical origin are merely obtained by making an educated guess. To correct for this ambiguity, a big uncertainty margin is used.

Finally, the total research, development, test and evaluation cost is estimated to be 233 Million USD. This is much lower than the maximum development cost proposed in the NGAT program[24]. This leaves budget to, for example, develop mission systems further.

13.6.2. Production Costs

Production costs are difficult to predict. Literature for military aircraft exists, but dates back to 1976 [66]. However, this is currently the best estimate that can be given. First, two key parameters must be identified. Most equations are based on airframe unit weight W_t and the maximum speed. Airframe unit weight has a lengthy definition, which is explained in detail in the first step of the cost estimations [66, p. 19]. This Airframe unit weight was determined to be 1575.5 lbs. Although this number changes with every iteration, the changes in cost are minimal, and the general inaccuracy of this method means that these small differences are not reliable in the first place.
The second factor is the maximum speed of the aircraft. This is simple to calculate, as it is a requirement. Mach 1.6 at 40,000 ft means the aircraft is flying at most 979 kts, which occurs with an ISA temperature offset of 30 K.

[24] Source: https://www-janes-com.tudelft.idm.oclc.org/defence-news/news-detail/usaf-moves-ngat-programme-ahead-with-new-rfi (retrieved 9 June 2022)

Using these methods, various components of total production cost are generated. First of all, the engineering hours, or E_X. These are the number of man-hours of engineering work needed to produce an X number of units. The same counts for tooling hours, or T_X. This is the number of man-hours needed to design and produce tooling and jigs required for production and assembly of the aircraft. Next up is non-recurring manufacturing hours, or ML_{NR}. This consists of the man-hours needed to produce mock-ups and test items to develop the production method. This does not depend on the volume of aircraft created. Following that are recurring manufacturing hours, or ML_X. These are the man-hours needed to produce X units. One more cost component is the material cost. First of all, this consists of nonrecurring material cost, MM_{NR}. This is the cost related to materials used for mock-ups and test items that are needed to develop the production process. Logically, the next cost component is the recurring material cost, MM_X. This is the cost for the material that is actually needed for the production of X units. Lastly, quality control is considered. This is calculated in hours, as a percentage of nonrecurring and recurring manufacturing hours. This percentage varies for many different aircraft, but 12% is a good estimate for a non-cargo aircraft [66, p. 38]. However, as the RAD does not need to be combat-capable and does not carry humans, safety tolerances can be more lenient, so this number is lowered to 10% for the RAD.

As the regression constants in the variable equations differ as more units get produced, the equations change too. Constants are available for volumes of 25, 50, 100 and 200 aircraft. To interpolate between these, new constants must be calculated. The process of doing this is thoroughly described in the Rand report [66, p. 55]. This starts by calculating the local slope, which is done using equation (13.1).

$$S = \frac{Y_{X_2}}{Y_{X_1}} \tag{13.1}$$

$$b = \frac{\log S}{\log 2} \tag{13.2}$$

Where Y is E, T, ML, or MM, and $X_2 > X_1$. For example, $S = \frac{E_{50}}{E_{25}}$ gives the slope valid for volumes between 25 and 50 units. This is then converted to a logarithmic slope using equation (13.2). Following that, the end result is found using equation (13.3).

$$Y_X = Y_{X_1} \cdot \left(\frac{X}{X_1}\right)^b \tag{13.3}$$

Here, X is the quantity for which the production cost category needs to be calculated and X_1 is the highest volume equation for that cost category where $X_1 < X$. For example, X can be engineering hours at 150 units, or E_{150}. X_1 is then E_{100} and X_2 is E_{200}. For volumes above 200, X_1 is changed to 200 only in equation (13.3). In the end, costs per unit can be found in figure 13.3. However, it takes some processing to arrive at these numbers. First of all, man-hours need to be converted to money. For this, salary costs were assumed in two levels. First, engineering salary costs were assumed to be 150 USD per hour. This consists of salary costs and costs for supporting the engineering process. Secondly, the manufacturing salary costs were assumed to be 100 USD per hour. Engineering, tooling and quality control was assumed to require an engineer's salary, while nonrecurring and recurring manufacturing hours were assumed to require a production salary.

Secondly, as this report stems from 1973, material costs are not accurate anymore. The aircraft from which empirical data was taken were not developed in 1973, but the report did adjust the material cost to FY 1973 USD. To adjust these to FY 2022 USD, the inflation of the index "Aerospace Product and Parts Manufacturing" was taken. However, as this only goes back to 1985[25], the inflation was extrapolated to 1973. The index increased to 254.7% of its original value compared to 1985, which means the average yearly inflation rate is 2.56%. Taking this rate from 1973, the index value reaches 344.9% of its original value, in 2022. Therefore, all material costs are multiplied by 3.449 to reach a cost value that is representative of today's material and manufacturing costs.

By adding up all of these components and subsequently dividing by X, an average cost is found. This was done for volumes between 25 and 500, the results of which can be found in figure 13.3. As an example, if 200 units are produced, the production of one-unit costs 3.69 Million USD.

Note that this is purely assembly of the aircraft, initially expressed in hours of labour and material costs. Therefore, systems from third parties are not included in this cost. For example, propulsion system cost and mission

[25]Source: https://fred.stlouisfed.org/series/PCU3364133641#0 (retrieved on 7 June 2022)

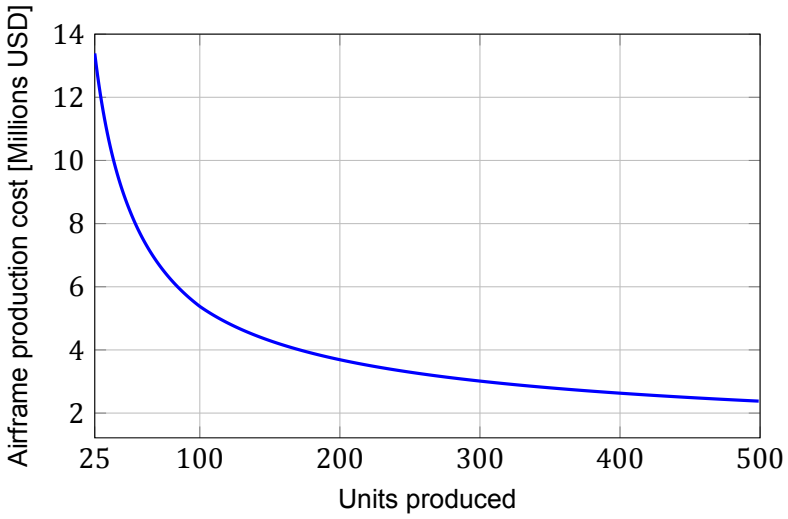

Figure 13.3: *Unit production costs as a function of total production volume.*

system cost still must be added, as these are likely produced by contractors. Furthermore, system costs unique to UAVs must be added to this number, as this empirical method is based on manned aircraft.

Estimating propulsion system cost is difficult, as no data is available on actual price. Therefore, a Cost Estimating Relation (CER) for military jet engines is used. From literature, an equation is available for estimating the cost of the 375th engine in production. Costs scale down with volume, so a higher volume will have a lower average cost. Although 550 units of the IHI F3 were already produced, the production line is not active anymore, so engine cost should be estimated using a lower volume number. The cost of redeveloping the afterburner is already incorporated in the CER. The equation that is used to estimate the production cost C_{prod} can be seen in equation (13.4), which was taken from a report made by the Rand Corporation [67, p. 82]. Similarly, the equation used to estimate engine derivative development cost C_{dev} was taken the same report [67, p. 82]. It can be found in equation (13.5).

$$\ln\left(C_{prod}\right) = -10.40 + 1.162\ln\left(T_{turbine}\right) + 0.482 \cdot ab + 0.262\ln\left(W_{dry}\right) \tag{13.4}$$

$$\ln\left(C_{dev}\right) = -39.422 + 5.066\ln\left(T_{turbine}\right) - 1.299\ln\left(SFC\right) + 0.582\left(T_{test}\right) \tag{13.5}$$

With a turbine inlet temperature $T_{turbine}$ of 1036 °F, an ab of 1 (as it has an afterburner) and a dry weight of 1104.52 lbs, production cost is estimated to be 986,000 USD (FY 2001). Next up is the costs related to developing a derivative of an existing engine. As the F3 engine already exists, and tests were already conducted with the afterburner, these are not expected to be significant. Therefore, the amount of full-scale test hours was assumed to be 1000. Then, using an SFC of 0.7 $\frac{\text{lb}}{\text{lb.h}}$, the development costs are estimated to be 1.27 Million USD (FY 2001).

Combining these two costs, an estimate for the acquisition price of the engine can be found. First of all, it is assumed that 250 units of the engine are to be produced. This is to be consistent with the assumption of 200 aircraft being produced. Therefore, to include development and spare engines, it was assumed that 250 engines must be produced. Furthermore, inflation must be considered. For this, the index ”Aircraft Engine and Engine Parts Manufacturing” is taken from January 2001 to April 2022. This gives an inflation value of 76%. This means the costs taken from equation (13.4) and (13.5) must be multiplied with a factor of 1.76 in order to get a price in 2022 USD. Following this, an additional margin of 15% is used to include additional costs and a profit margin. In the end, this results in an engine cost of 2.00 Million USD (2022). This cost seems high, but no factor could be found that is causing this high number. Therefore, this number is taken as the estimated price, although it is expected to be lower in reality.

Another additional cost factor is the RAM coating. Not much data is available on this, so assumptions must be made. It is assumed that 150 EUR per square foot. With a wetted area of 26.855 m^2, the cost of applying the RAM to the skin of the aircraft is 47,000 USD.

Table 13.6: *Mission system cost.*

System type	Cost [USD]
Daylight camera	≤ 1 M
EO/IR camera	1 - 20 M
Radar Confusion	1 - 20 M

Assembly then also brings the mission systems into play. These are quite expensive, as described by [5, Fig. 4]. Some systems relevant to the RAD are shown in table 13.6. Although the RAD will not the most advanced cameras, even just a selection of the mission systems that will be used already impose a significant burden on the cost of the RAD. Furthermore, this table does not capture every mission system present in the RAD. Therefore, unit cost for just the airframe will have to be minimised.

With the current cost of the engine and production of the airframe combined, 4.26 Million USD is left over if the production cost target 10 Million USD is considered. Assuming that 15% of this leftover budget is used for unforeseen production expenses, 3.62 Million USD can be used for production or acquisition of the mission systems. However, due to their classified nature, it is difficult to get an estimate on the exact costs of incorporating all mission systems. Now that development and production cost estimates have been found, the TBD in RAD-CO-RES-02-02 can be replaced by their sum.

13.6.3. Acquisition Cost

When acquiring the entire system, more factors than just production cost come into play.

First of all, using satellite communications costs a significant sum of money. The USAF only applies this as a one time cost[26]. In this procurement sheet, it is described that four units of Primary Satellite Links (PSL) are acquired, along with ten Ground Control Stations (GCS) and 29 MQ-9 Reaper drones. In total, this PSL costs 2.965 Million USD (FY 2016), which means per unit it costs 741,000 USD (FY 2016) per unit. Adjusted for inflation, this is 862,000 USD per unit. It is remarkable that there are seven drones per PSL and three per ground control station in this procurement sheet. On the contrary, for the RAD it is assumed that every aircraft has a corresponding GCS and PSL, such that every aircraft can operate at the same time.

Then, assuming the customer does not yet own one, the GCS needs to be acquired as well. Looking at the procurement sheet again[15], this costs 3.17 Million USD (FY 2016). Once again adjusting for inflation, it costs 3.69 Million USD (FY 2022).

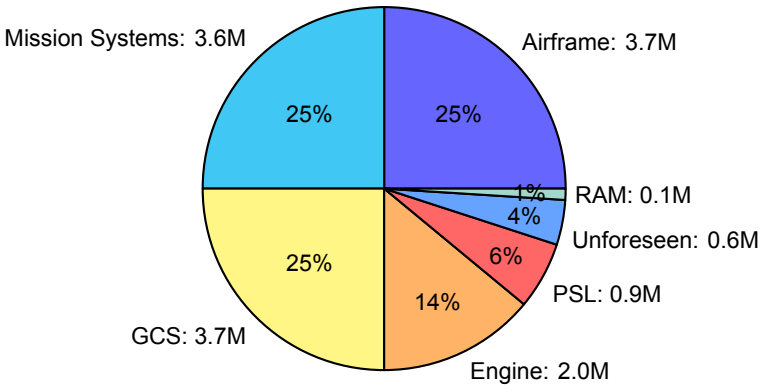

Figure 13.4: *Composition of full system costs.*

Adding production cost to these newly introduced factors, the total cost is 14.55 Million USD, before adding any

[26]Source: https://dronecenter.bard.edu/files/2015/10/MQ-9-Procurement-Web-Sheet1-1.pdf (retrieved on 10 June 2022)

profit margins. With a 5% profit margin, this becomes 15.3 Million USD. However, this number relies on the assumption that all mission systems can be included for 3.7 Million USD. If this ends up being cheaper, the total price goes down. Furthermore, this takes into account the higher than expected engine price. Lastly, this is assuming that every aircraft has an assigned PSL and GCS. An operator could choose to make two aircraft share one of both of these, which already lowers the price by 2.27 Million USD. If the same GCS and PSL distribution would be taken as the USAF takes with their MQ-9 Reapers[15], the price would drop by 3.16 Million USD from the initial estimate. The cost categories of the overall system have been illustrated in figure 13.4, which shows conveniently which categories should be optimised to benefit the total cost the most.

13.6.4. Operational Cost

Operational cost can be expressed in many terms, which all include or exclude specific factors, such as depreciation or salary costs. To allow a fair comparison to current alternatives, one must know which factors are taken into account in their operational costs. The US military is the most transparent in this. As described in a study done by the RAND Corporation [65, p. 14], the $CPFH_{DoD}$ found in table 13.3 is found using equation (13.6).

$$CPFH_{DoD} = \frac{\text{Fuel} + \text{Consumables} + \text{DLRs} + \text{Depot Maintenance} + \text{Variable CLS}}{\text{Flying Hours}} \tag{13.6}$$

Here, Fuel is the cost of fuel per flight hour, Consumables is the average cost of consumables per flight hour, DLR and Depot Maintenance represent Depot-level repairs and upgrades respectively. Lastly, CLS represents Contractor Logistics Support.

These costs must be analysed to compare operational costs with existing alternatives. In the end, this is one of the most important factors in assessing the competitiveness of the RAD in a financial sense. First of all, fuel use must be assessed. This is quite straightforward, as a fuel weight was found during sizing of the aircraft. This fuel represents mission fuel and reserve fuel for half an hour of flight. With a mission length of approx. 1.5 hours, all fuel is burnt in 2 hours. Taking the price of Jet A-1 per metric Ton as 1,335 USD per metric ton[24], using 524 kg of fuel over 2 hours means that 350 USD per flight hour is spent on fuel.

Following this, it is assumed that Consumables, DLR and Depot Maintenance can be addressed in one cost factor. First of all, it is assumed that the RAD needs twelve hours of maintenance per flight hour [60, p. 2620]. That is also within the range found in table 13.3. This number is assumed to include all levels of maintenance and repair, including depot-level. Secondly, it is assumed that every man-hour of maintenance costs 250 USD, excluding personnel costs. This number cannot be accurately determined yet, as it needs a detailed analysis of mean time to failure and the cost of components. However, one can argue that these costs will not be higher than for bigger, heavier and higher-performing aircraft. The maintenance cost per man-hour for three of these can be seen in table 13.3. This confirms that 250 USD per flight hour is a reasonable estimate for this stage of the design.

Using this and applying a factor of 1.15 to capture unforeseen costs such as transport, a result is found for cost per flight hour: 3,852 USD per flight hour. However, this is only the figure that allows comparison to operational costs within the US Air Force.

A quick look at the RAND paper on hourly rates [65, pp. 14–15] shows that the cost per flying hour if it were to be rented out to the public, or a different air force for example, can be found using equation (13.7).

$$CPFH_{public} = CPFH_{DoD} + \frac{\text{Crew Salary Costs} + \text{Depreciation} + \text{Unfunded Retirement Costs}}{\text{Flying Hours}} \tag{13.7}$$

Where depreciation covers the declining value of the aircraft caused by flying it, and unfunded retirement costs apply a 7.2% increase to the salary of civilian contractors [68, p. 3].

The first step is to include the crew salary in the hourly rate. Looking at number from the US Air Force, who break down hourly rate in Operation & Maintenance costs (the same as the $CPFH_{DoD}$), and an additional factor for salary. For drone operators operating for example the MQ-9 Reaper, they charge 155 USD per flight hour [62, p. 5]. However, for this drone, two operators are needed. One pilot and one sensor operator. For the RAD, only a pilot is needed. Therefore, this hourly rate can be halved. The standard rate per hour is therefore 77.5 USD per flight hour, which remarkably is lower than the hourly rate for manned strike aircraft, as seen in table 13.3.

However, when providing the service to external entities, other crew costs also must be taken into account. First of all, a maintenance expert for the ground control station must be on watch during flight to fix any faults in the ground control station. Assuming one expert can be on watch for two ground control stations at a time, and assuming everyone charges the same hourly rate, this expert costs 39 USD per hour. Furthermore, it was assumed that 12 man-hours of maintenance must be performed for each flight hour. On top of that, it is assumed that ground operations and administration both add two man-hours of salary per flight hour. This means that in total, 17.5 man-hours of work is performed per flight-hour. It is assumed that these people all earn the same salary.

Following that, unfunded retirement costs can be considered. Note that this only applies to work performed by civilian contractors. Assuming that two man-hours of work is performed by civilians per flight hour, 11 USD per flight hour is added by applying the 7.2% factor to the standard hourly rate.

Lastly, depreciation of the airframe is considered. This can be calculated in many ways, so the method of the US Air Force will once again be copied. Looking at the hourly depreciation rates in the US Air Force, found in the ”Asset Utl” column in the Reimbursement Rates [62], one can see that usually, the depreciation fee is equal to about 4.12% of the $CPFH_{DoD}$. The distribution of this percentage across the entire USAF fleet, except three outliers, can be found in figure 13.5. Outliers are the MQ-1B, T-41D and T-53A. Their $CPFH_{DoD}$ values are inexplicably low, which gives reason to omit them from this analysis. So, in the end, depreciation is added as 4.12% of the $CPFH_{DoD}$.

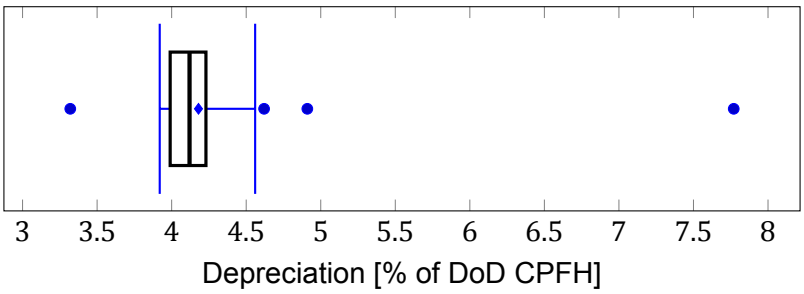

Figure 13.5: *Box plot of depreciation fees as a percentage of Reimbursement Rates for USAF aircraft.*

In total, this gives a $CPFH_{public}$ of 5,378 USD per hour. Now, these factors cover everything that is described by the official methods supplied by RAND [65]. For example, this rate could be used for services provided to foreign air forces. However, a commercial company would apply more factors to this. First of all, facilitary fees. It is assumed that these cost 50 USD per hour. This number is quite low, as the party requesting the service will likely own the facilities that are needed.

Following that, a commercial company needs to earn back the costs incurred in acquiring the necessary systems to operate the RAD. This is the idea behind incorporating a depreciation charge, but this does not suffice when the sole purpose of the aircraft is to be rented out. Over 8000 hours, the depreciation charge currently only captures about 10% of the value of the RAD. Therefore, a surcharge is required for a commercial company providing the service. It is assumed that the company will use this charge to break even within 8000 flight hours, which means this charge is simply the acquisition cost of the system divided by 8000. This brings the cost per flying hour for the company to 7,179 USD. Applying a 10% profit margin, an external party would pay 7,897 USD per flight hour to use the red air service. This fee is also known as the Cost per Flying Hour with a Commercial Charge ($CPFH_{CC}$). Note that depreciation is a significant portion of this, so reducing the acquisition price of the entire system by 1 Million USD reduces the external fee by 138 USD per flight hour. To summarise, the three types of CPFH can be found in table 13.7.

To give an indication of the composition of these CPFH values, these three types of CPFH have been broken down in figure 13.6. Here, a user can see which cost categories should be optimised the most if decreases in operational cost are needed.

$CPFH_{DoD}$ [USD/h]	$CPFH_{Public}$ [USD/h]	$CPFH_{CC}$ [USD/h]
3,852	5,378	7,897

Table 13.7: *Cost per flying hour for the RAD per type.*

Looking back at the Cost Breakdown Structure in figure 13.2, one can see that all cost categories have now been accounted for. That means that a total picture of operational costs has now been built, and the comparison to alternatives can start.

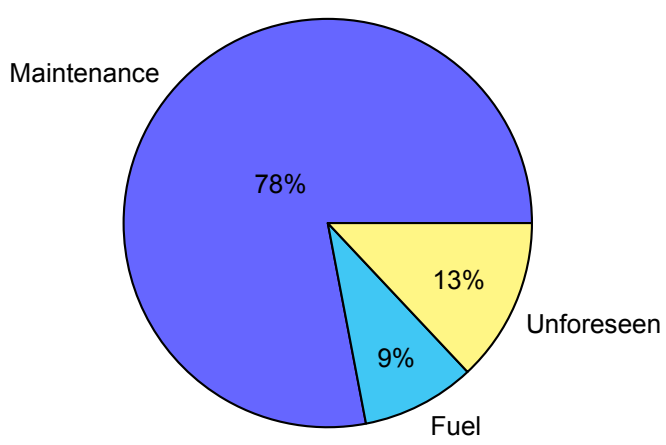

(a) *Composition of reimbursible rate type CPFH.*

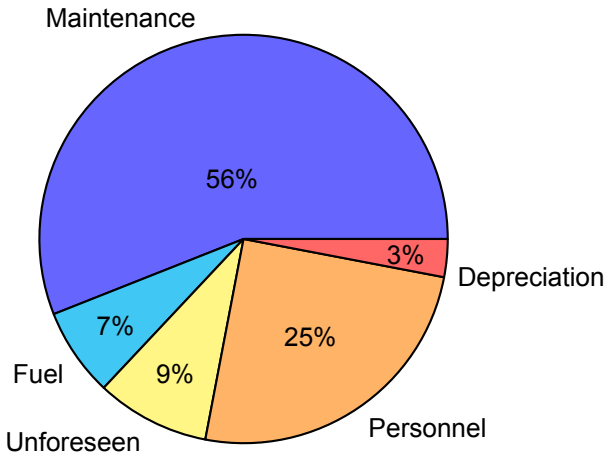

(b) *Composition of public type CPFH.*

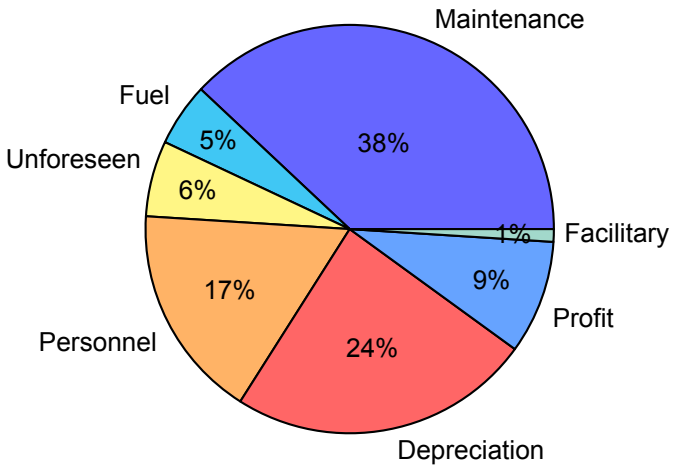

(c) *Composition of commercial charge type CPFH.*

Figure 13.6: *Composition of various types of cost per flying hour.*

13.7. Operational Profit

Now that models have been built showing the cost composition of alternatives and the RAD, the operational profit can be analysed. In the end, this is the metric that says the most about the cost-effectivity of the RAD.

13.7.1. Air Force Owned

The RAD should be able to replace aircraft in current aggressor squadrons. The USAF operates F-16s, used to operate F-15s and have now started operating F-35s in their aggressor squadrons. Therefore, the relevant CPFH values have been plotted in figure 13.7. This shows how much cheaper the RAD is to current USAF alternatives. What becomes apparent from this figure is the difference in public and DoD component rates. Whereas the USAF only takes the pilot cost to calculate salary charges, the RAD takes into account all relevant salary costs. Only considering the pilot cost would drop the public type CPFH for the RAD by 1,279 USD, which brings the difference in the two CPFH types more in line with the USAF ones.

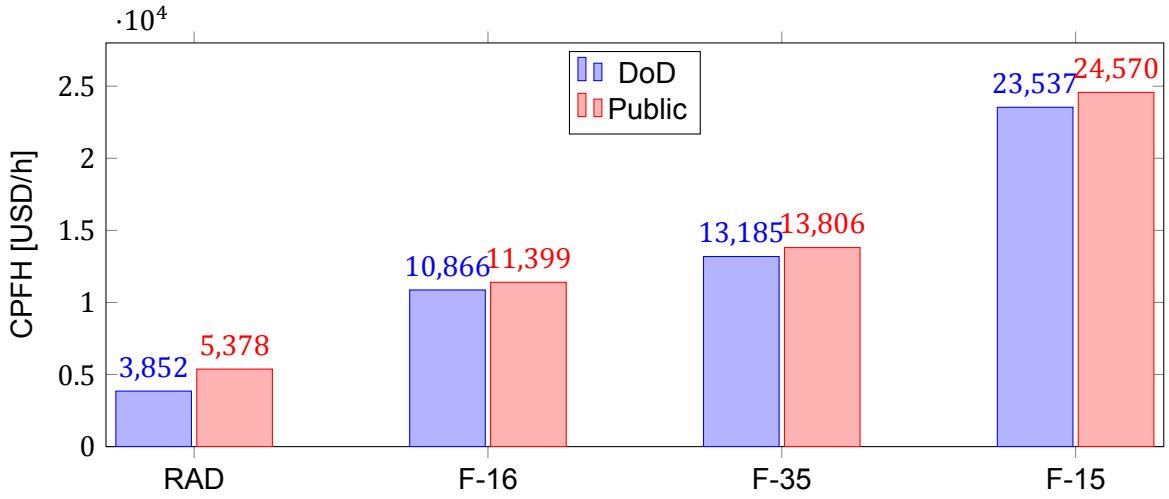

Figure 13.7: *Comparison with Air Force CPFH.*

The conclusion that can be drawn from figure 13.7 and this section is that the RAD offers an extraordinary improvement in costs related to RAT as offered by aggressor squadrons. Operational cost reductions go as far as 83%, which means up to five RADs could be used to replace one current aggressor.

Note that this improvement only counts for Beyond Visual Range RAT. When training for Air Combat Maneuvering (ACM), better known as Dogfighting, the RAD does not have adequate performance to replace current alternatives. Therefore, manned fighter jets will still have to be used. This was never the goal of the RAD, so this was expected.

With an initial investment of 233 Million USD to offset the development cost, the investment is returned after $\frac{233*10^6}{10866-3852} = 33,219$ hours of flying the RAD as a replacement for the F-16. If the lifetime of the RAD is 8000 flight hours, only five units already offset the development cost over their lifetime. The life cycle cost, taken as the sum of development cost, acquisition cost and lifetime Operations&Maintenance costs ($CPFH_{DoD}$) for 200 units, is then 9.46 Billion USD. That means the TBD in RAD-CO-RES-02-01-A can be changed to a value of 46.1 Million USD.

With this exceptional performance, the assumption of selling 200 units becomes realistic. This confirms that the costs in this section are accurate, if not overestimated.

13.7.2. Commercial Service

As discussed in section 13.6.4, if a commercial company owns the RAD, more charges are involved for its use. Therefore, it is important to compare this charge with prices of current commercial red air Services, as described in section 13.5.3. The cheapest CPFH for commercial companies that was found is 10,227 USD. This is higher than the commercial CPFH of the RAD, which is 7,897 USD per hour. This is also visualised in figure 13.8, where commercial prices of three USAF aircraft have been added. These were estimated using the same method, using data from table 13.3. This shows that RAD is also a cheaper alternative for commercial companies. That means these companies will likely adopt the RAD as the platform for their BVR training services. Note that the RAD is cheaper but has more capabilities than an L-159, both in top speed, stealth performance and mission systems.

This cheaper cost means a government will be interested in investing in the development of the RAD. This investment is already offset after $\frac{233 \cdot 10^6}{10,227-7,897} = 100,000$ hours of red air using the cheapest contract. For the most expensive one, it would be worth it after 21,035 hours. Taking the weighted average price from table 13.5, breakeven is reached after 40,423 hours. Again assuming 8,000 hours per RAD in its lifetime, this is worth it after nine RADs. Or, assuming every pilot needs ten red air missions, all lasting two hours, the investment is worth it when 2021 pilots must be trained. Considering that the USAF alone had a pilot shortage of 1,650 pilots in just 2022[27],

[27]Source: https://www.flyingmag.com/u-s-air-force-is-short-1650-pilots-report-says/ (retrieved

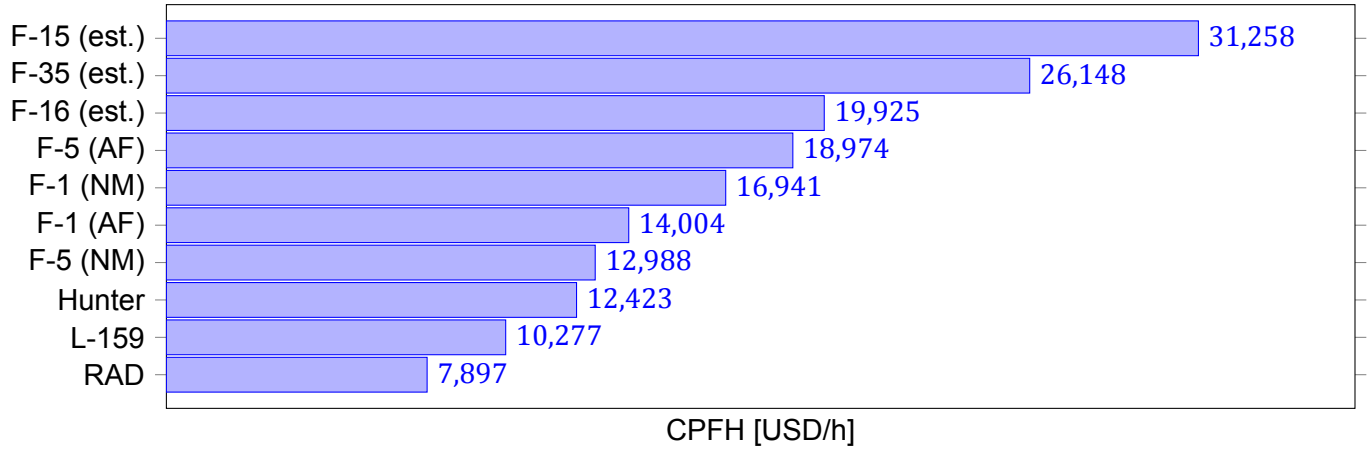

Figure 13.8: *Comparison with commercial CPFH.*

many more need to be trained across the world in the coming years.

As such, one can reasonably assume that the RAD will also take a significant share of the commercial red air market. That once again validates the assumption that 200 units can be sold. Else, the cost would be higher.

13.7.3. Market Breakthrough

Considering that the RAD can be a big success, both in Air Force ownership and commercial ownership, this drone is worth the investment. The development costs can be funded by a multitude of NATO countries, all of whom need red air for blue air training. Furthermore, the RAD meets the project objective of delivering a more cost-effective solution.

The USAF has currently contracts running for at least 100,000 hours of commercial red air [63, p. 11]. This means the USAF could save 580 Million USD on these contracts alone by just by replacing the jets by red air Drones. These contracts all last at most five years, and the USAF uses more red air for blue air training and services than just these contracts.

Considering that this is just a part of the total market, one can conclude that cost savings across the entire market is in the order of Billions of USD, within ten years. Furthermore, these cost savings mean that the red air Drone has reached one more of its project objectives. A goal was to be cheaper than current alternatives. This was achieved, both in operational costs and in acquisition costs.

It is likely more expensive than target drones, although no data is available on their exact cost breakdown. However, due to their generally smaller size, it can be assumed that they are cheaper to acquire and operate. However, the RADs capabilities far exceed those of existing target drones, especially in flexibility caused by a low RCS. The only target drone that comes close to the capabilities of the RAD is the BQM-167A. However, this is unable to simulate modern stealth fighters and cannot fly at supersonic speeds. Therefore, looking into the future, demand for this type of drone will fade away, while demand for the RAD will grow, as the RAD can simulate stealth adversary aircraft.

13.7.4. Sensitivity

Finally, as many numbers in this section are based on assumptions, it is important to analyse the sensitivity of operational costs to these assumptions. Mainly, the assumption of maintenance cost per man-hour. This was assumed to be 250 USD (excluding salary) but could end up being much higher or lower. Figure 13.9 shows how much maintenance can cost per hour (excluding salary) in order to stay competitive with the cheapest USAF alternative. The hourly cost at which the two intersect is 756 USD per hour. However, due to the much smaller size, one can reasonably assume that the RAD will have lower maintenance costs than the F-16.

on 13 June 2022)

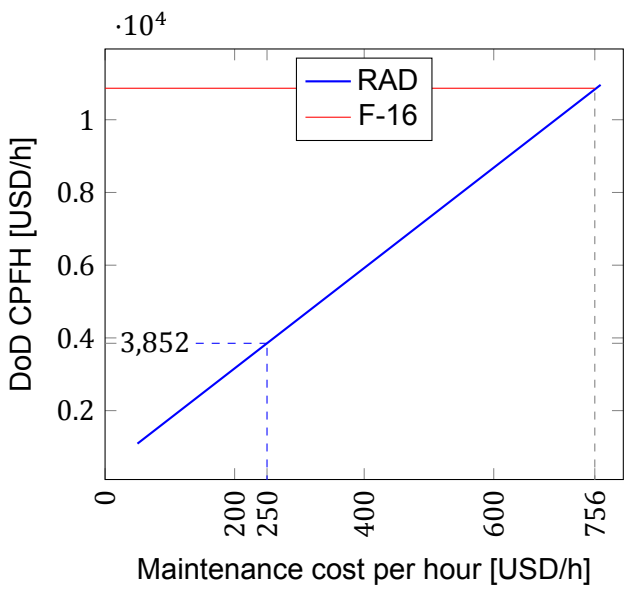

Figure 13.9: *Allowable hourly maintenance costs for the RAD compared to Air Force-owned solutions.*

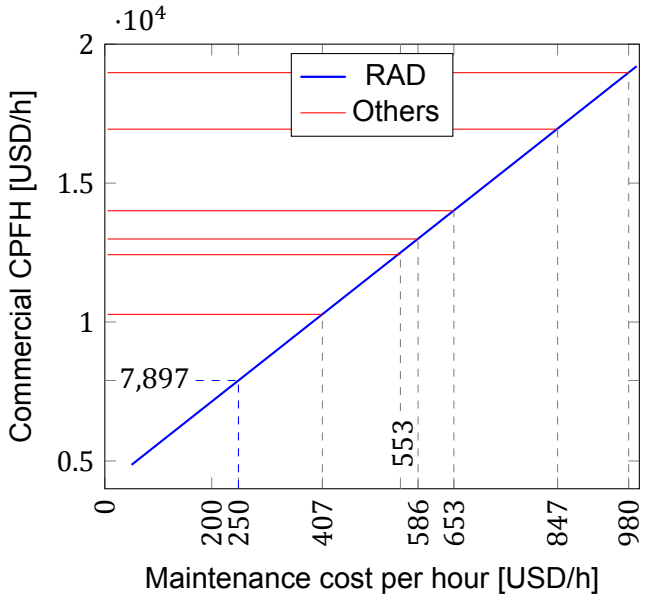

Figure 13.10: *Allowable hourly maintenance costs for the RAD compared to commercial solutions.*

Furthermore, in ownership of commercial companies, hourly maintenance costs would have to rise to 400 USD/h in order for the RAD to become more expensive than the L-159. However, considering that the RAD still has more capabilities, the competitiveness would not be lost. One more factor that was assumed is the number of man-hours of work needed per flight hour. However, this factor has much less impact on operational cost compared to maintenance cost, so no graphic analysis is done. If this number would be double of the current estimate in reality, the RAD would still be cheaper than any alternative in any category. On top of that, the price of RAM coatings was also assumed. No public data is available on this, so an estimate based on an educated guess was the only method to estimate the price. However, considering that this is currently only a fraction of the price of the RAD, inaccuracies in this assumption will not have a large impact on the total price.

One last set of assumptions with a big impact on this section is the choice of estimation methods. Especially, the estimation of production costs. This report stems from 1976, so only aircraft from before this year were considered. However, this is the best publicly available method of estimating *military* aircraft costs, as it is transparent in its methods it was easy to see where costs could be different in 2022. For example, changes in wage and material do not carry the same factor and could be adjusted separately. However, with changes in safety regulations and tolerance allowances, the accuracy of this estimate can be put to question. The method to estimate engine costs is more modern, so it is expected to produce reasonably accurate results. Furthermore, this method is purely focused on military jet engines, which improves the accuracy for this use case. However, this method did not distinguish between different production volumes, so the learning curve of production was not considered in this estimate. Lastly, the estimation of development costs. This number is found using an old software that is not transparent in its calculation methods. Furthermore, several ambiguous factors are present in this software, all of which have a big influence on total costs. However, it is not explained how these factors can be determined. The cost components that this software produced look somewhat reasonable, but due to its general ambiguity, a factor of 40% was applied to the estimate produced by this software. A recommendation for the future is to look more into estimating the development costs, as a more accurate estimate could result in a lower estimate.

For future development stages, it is recommended to use more detailed cost estimation methods to build a picture of expected costs. For example, RAND corporation has an extensive study on maintenance and life cycle costs [69]. This can be used to generate a more accurate estimate for maintenance costs, for example. Furthermore, a more extensive market survey would benefit the sales of the RAD. It would help to know the total number of sorties or flight hours of red air per year in western countries. This would enable the distributor of the RAD to accurately determine the market position and the total yearly savings the RAD can bring. This number could be found by surveying western air forces about their exact red air needs.

14 Compliance Matrix

This chapter contains the compliance matrix for the RAD. The requirements that have been met are shaded green in the matrices. The requirements that have not been met are shaded in red. The requirements shaded orange can not be confirmed at this stage of the design, as the level of detail for the RAD design is not sufficient. This does not mean that the requirement will not be met in later design stages.

Table 14.1: *Compliance matrix for the performance requirements.*

Identifier	Requirement	Identifier	Requirement
RAD-TE-PER-01	The RAD shall have a flight performance as required by the stakeholders.	RAD-TE-PER-01-01	The maximum speed of the RAD shall be at least Mach 1.60 above 30,000 feet.
RAD-TE-PER-01-02	The RAD shall have a typical cruise speed of Mach 0.90 from S/L to ceiling.	RAD-TE-PER-01-03	The RAD shall have a minimum endurance of 1.5 hours between T/O and LDG.
RAD-TE-PER-01-04	The RAD shall have a minimum flight ceiling of 45,000 feet.	RAD-TE-PER-01-05	The RAD shall be able to perform a dash move increasing its Mach number by at least 0.7 while staying in the nominal flight envelope.
RAD-TE-PER-02	The RAD shall operate under conditions as defined by the stakeholders.	RAD-TE-PER-02-01	The RAD shall have a payload capacity of at least 78 kilograms.
RAD-TE-PER-02-02	The RAD shall be operational for temperatures between ISA -30°C to ISA +30°C.	RAD-TE-PER-02-03	The RAD shall be able to take off from a paved runway with maximum length of 6,000 feet at altitudes from S/L to 4,000 feet MSL.
RAD-TE-PER-02-04	The RAD shall be able to operate in T/O and LDG for the set-out wind limits.	RAD-TE-PER-02-04-A	The RAD shall be able to operate in T/O and LDG for a 25 kt maximum crosswind component.
RAD-TE-PER-02-04-B	The RAD shall be able to operate in T/O and LDG for a continuous wind gusting of 35 kt.	RAD-TE-PER-02-04-C	The RAD shall be able to operate in T/O and LDG for a maximum wind gusting of 42 kt.
RAD-TE-PER-02-05	The RAD shall have a MTOW between 150 and 20,000 kg.	RAD-TE-PER-03	The RAD shall be able to sustain and perform manoeuvres as specified by the stakeholders.
RAD-TE-PER-03-01	The RAD shall be able to sustain loads higher than 4g at an altitude of 25,000 feet & at Mach number of 0.90.	RAD-TE-PER-03-02	The RAD shall be able to perform sustained turns.

Identifier	Requirement	Identifier	Requirement
RAD-TE-PER-03-02-A	The RAD shall have a sustained turn rate of 9 deg/sec.	RAD-TE-PER-03-02-B	The RAD shall have a sustained turn radius of 6000 ft.
RAD-TE-PER-03-03	The RAD shall be able to perform instantaneous turns.	RAD-TE-PER-03-03-A	The RAD shall have an instantaneous turn rate of 15 deg/sec.
RAD-TE-PER-03-03-B	The RAD shall have an instantaneous turn radius of 3500 ft.	RAD-TE-PER-04	The RAD shall withstand loads/accelerations as specified by the stakeholders.
RAD-TE-PER-04-01	The RAD structure shall be able to withstand load factors during operation.	RAD-TE-PER-04-01-A	The RAD structure shall withstand load factors lower than -1.
RAD-TE-PER-04-01-B	The RAD structure shall withstand load factors higher than 6.		

Table 14.2: *Compliance matrix for the observability requirements.*

Identifier	Requirement	Identifier	Requirement
RAD-TE-LO-01	The red air platform shall be low observable in radar.	RAD-TE-LO-01-01	The geometry of the RAD shall be designed such that it has an RCS less than 0.1 m2.
RAD-TE-LO-01-02	The RAD outer geometry shall use radar absorbing/deflecting materials/coatings to minimise the RCS such that it is lower than 0.01 m2.	RAD-TE-LO-01-03	The RAD shall carry RCS enhancing systems onboard.
RAD-TE-LO-02	The RAD shall have IR detection confusion features and IR signature enhancing systems.	RAD-TE-LO-02-01	The RAD shall carry chaff/flare dispensers onboard.
RAD-TE-LO-02-02	The RAD shall carry IR emitters onboard.		

Table 14.3: *Compliance matrix for the system requirements.*

Identifier	Requirement	Identifier	Requirement
RAD-TE-SYS-01	The RAD shall have an internal volume of at least 14 liters available for the payload and onboard systems.	RAD-TE-SYS-01-01	The RAD shall have available volume of 1.1 liters in the forward part 1.
RAD-TE-SYS-01-02	The RAD shall have available volume of 5.6 liters in the rear part.	RAD-TE-SYS-01-03	The RAD shall incorporate a volume of 3 liters on its outer geometry.
RAD-TE-SYS-01-04	The RAD shall incorporate a payload volume of 125 liters.	RAD-TE-SYS-02	The RAD shall be able to provide power to all necessary equipment onboard for safe operation.
RAD-TE-SYS-02-01	The RAD shall provide a minimum continuous electrical power of 5 kW.	RAD-TE-SYS-02-02	The RAD shall be able to provide a minimum peak electrical power of 10 kW.

Identifier	Requirement	Identifier	Requirement
RAD-TE-SYS-02-03	The RAD shall have at least 2 sources of electrical energy for onboard electronics.	RAD-TE-SYS-03	The RAD shall have the necessary systems to complete its mission.
RAD-TE-SYS-03-01	The RAD shall carry the necessary equipment for manipulating observability.	RAD-TE-SYS-03-01-A	The RAD shall carry radar cross-section enhancement systems.
RAD-TE-SYS-03-01-A1	The RAD shall have two forward facing and two rear facing antennae for the active radar cross section transmitter.	RAD-TE-SYS-03-01-A2	The RAD shall have two forward and two rearward antennae for passive radar cross-section reflector.
RAD-TE-SYS-03-01-B	The RAD shall have an infrared signature enhancer at the rear of the aircraft.	RAD-TE-SYS-03-01-C	The RAD shall carry a radar emulator and a radar jammer.
RAD-TE-SYS-03-01-D	The RAD shall have two antennae in the front and two antennae in the rear for both the radar jammer and radar emulator.	RAD-TE-SYS-03-01-E	The RAD shall carry a radar warning receiver.
RAD-TE-SYS-03-02	The RAD shall have equipment for conducting military communications.	RAD-TE-SYS-03-02-A	The RAD shall carry an IFF system.
RAD-TE-SYS-03-02-B	The RAD shall be able to carry out Link 16 communications.	RAD-TE-SYS-03-03	The RAD shall have the necessary equipment for VFR operations.
RAD-TE-SYS-03-03-A	The RAD shall have sensors to produce airspeed indications.	RAD-TE-SYS-03-03-B	The RAD shall have sensors to produce altitude indications.
RAD-TE-SYS-03-03-C	The RAD shall have sensors to produce flight heading indication.	RAD-TE-SYS-03-03-D	The RAD shall have the equipment to measure engine(s) working speed.
RAD-TE-SYS-03-03-E	The RAD shall have the equipment to measure the temperature of the engine(s).	RAD-TE-SYS-03-03-F	The RAD shall have the equipment to measure the pressure of the engine(s).
RAD-TE-SYS-03-03-G	The RAD shall have the equipment to measure the quantity of fuel during operation.	RAD-TE-SYS-03-03-H	The RAD shall have the equipment to interpret the landing gear position.
RAD-TE-SYS-03-03-I	The RAD shall have approved position lights for night operations.	RAD-TE-SYS-03-03-J	The RAD shall have anti-collision lights.
RAD-TE-SYS-03-03-K	The RAD shall have necessary systems to avoid collisions during flight.	RAD-TE-SYS-03-04	The RAD shall have necessary equipment for IFR operations.
RAD-TE-SYS-03-04-A	The RAD shall carry the necessary equipment for two-way radio communication and navigation within the 30-1000 MHz frequency range.	RAD-TE-SYS-03-04-B	The RAD shall have sensors to measure the rate-of-turn.
RAD-TE-SYS-03-04-C	The RAD shall have sensors to produce slip and skid measurements.	RAD-TE-SYS-03-04-D	The RAD shall have equipment to transform mechanical or chemical energy to electrical energy.

Identifier	Requirement	Identifier	Requirement
RAD-TE-SYS-03-04-E	The RAD shall have sensors to measure the pitch motion.	RAD-TE-SYS-03-04-F	The RAD shall have sensors to measure the yaw motion.
RAD-TE-SYS-03-04-G	The RAD shall have sensors to measure the roll motion.	RAD-TE-SYS-03-04-H	The RAD shall have sensors to measure the bank angle.
RAD-TE-SYS-03-05	The RAD shall have necessary equipment for an instrumented approach and landing.	RAD-TE-SYS-03-05-A	The RAD shall have equipment to measure distance using the UHF range.
RAD-TE-SYS-03-05-B	The RAD shall have equipment to measure distance using the VHF range.	RAD-TE-SYS-03-05-C	The RAD shall have equipment to interpret the horizontal position with respect to the approach path.
RAD-TE-SYS-03-05-D	The RAD shall have equipment to interpret the vertical position with respect to the approach path.	RAD-TE-SYS-03-06	The RAD shall have supplementary equipment to complete operation during flight.
RAD-TE-SYS-03-06-A	The RAD shall have necessary equipment to operate in icing conditions.	RAD-TE-SYS-03-06-B	The RAD shall have an autopilot.
RAD-TE-SYS-03-06-C	The RAD shall have equipment for a camera system on board.	RAD-TE-SYS-03-06-D	The RAD shall have a flight recording system.
RAGP-TE-SYS-04	The ground control station shall have necessary equipment on ground to operate the RAD during flight.	RAGP-TE-SYS-04-01	The ground control station shall have necessary equipment on ground for VFR operations.
RAGP-TE-SYS-04-01-A	The ground control shall have equipment for displaying airspeed.	RAGP-TE-SYS-04-01-B	The ground control shall have equipment to display the altitude.
RAGP-TE-SYS-04-01-C	The ground control shall have equipment to display the flight heading.	RAGP-TE-SYS-04-01-D	The ground control shall have equipment to display the working speed of engine(s).
RAGP-TE-SYS-04-01-E	The ground control shall have equipment to display the quantity of fuel onboard of the RAD.	RAGP-TE-SYS-04-01-F	The ground control shall have equipment to display the position of the landing gear.
RAGP-TE-SYS-04-01-G	The ground control shall have a warning system for possible mid-air collisions.	RAGP-TE-SYS-04-01-H	The ground control shall have equipment to visualise the position of the RAD in a scalable map.
RAGP-TE-SYS-04-01-I	The ground control shall have equipment to display the airspeed limitations.	RAGP-TE-SYS-04-01-J	The ground control shall have equipment to display the sideslip angle.
RAGP-TE-SYS-04-01-J	The ground control shall have equipment to display the angle of attack.	RAGP-TE-SYS-04-01-K	The ground control shall have equipment to display the free air temperature
RAGP-TE-SYS-04-01-L	The ground control shall have equipment to display the attitude in terms of roll and pitch angles.	RAGP-TE-SYS-04-01-M	The ground control shall have equipment to display the vertical speed.
RAGP-TE-SYS-04-01-N	The ground control shall have equipment to display the time.	RAGP-TE-SYS-04-01-O	The ground control shall have equipment to display the navigation system status.

Identifier	Requirement	Identifier	Requirement
RAGP-TE-SYS-04-01-P	The ground control shall have equipment to display the wind direction and speed.	RAGP-TE-SYS-04-01-Q	The ground control shall have equipment to display the oil pressure for the engine(s).
RAGP-TE-SYS-04-01-R	The ground control shall have equipment to display the oil temperature for the engine(s).	RAGP-TE-SYS-04-01-S	The ground control shall have equipment to display the oil quantity for the oil tank(s).
RAGP-TE-SYS-04-02	The RAD shall have necessary equipment on the ground station for IFR operations.	RAGP-TE-SYS-04-02-A	The ground control shall have equipment to display the rate of turn.
RAGP-TE-SYS-04-02-B	The ground control shall have equipment to display the pitch and bank.	RAGP-TE-SYS-04-03	The ground control shall have necessary equipment to control the RAD.
RAGP-TE-SYS-04-03-A	The ground control shall have equipment to visualise the output of the camera on board		

Table 14.4: *Compliance matrix for the sustainability requirements.*

Identifier	Requirement	Identifier	Requirement?
RAD-CO-SUS-01	The RAD shall comply with the environmental sustainability requirements.	RAD-CO-SUS-01-01	The noise emissions of the RAD shall be lower than 109dB felt at 1000 ft.
RAD-CO-SUS-01-02	The RAD shall use less fuel than the F-16	RAD-CO-SUS-01-03	The RAD shall be at least 80% recyclable.
RAD-CO-SUS-02	The RAD and its associated ground systems shall be maintained a with sustainability philosophy.	RAD-CO-SUS-02-01	The periodic maintenance time of RAD shall not exceed the periodic maintenance time of the F-16.
RAD-CO-SUS-02-02	The periodic maintenance of RAD shall be performed with already available tools.	RAD-CO-SUS-02-03	The maintenance of the ground control station shall be completed within ”TBD” hours.

Table 14.5: *Compliance matrix for the other/miscellaneous requirements.*

Identifier	Requirement	Identifier	Requirement
RAD-TE-OTH-01	The RAD shall be operational on ground as specified by the stakeholders.	RAD-TE-OTH-01-01	The RAD shall be able to taxi on a paved taxiway.
RAD-TE-OTH-01-02	No arresting equipment shall be needed to operate the RAD.	RAD-TE-OTH-01-03	The RAD shall be stored in a covered basing.
RAD-TE-OTH-01-04	The RAD shall make use of current military airbase infrastructure.	RAGP-TE-OTH-02	The operator of the ground control station shall have control authority over the RAD throughout the entire flight envelope.

Identifier	Requirement	Identifier	Requirement
RAGP-TE-OTH-02-01	The RAD shall be controlled from a suitable manned, ground-based control station.	RAGP-TE-OTH-02-02	The ground control station shall be able to provide attitude control inputs to the RAD.
RAGP-TE-OTH-02-02A	The ground control station shall be able to provide pitch control inputs to the RAD.	RAGP-TE-OTH-02-02B	The ground control station shall be able to provide roll control inputs to the RAD.
RAGP-TE-OTH-02-02C	The ground control station shall be able to provide yaw control inputs to the RAD.	RAGP-TE-OTH-02-03	The ground control station shall be able to provide thrust control inputs to the RAD.
RAGP-TE-OTH-02-04	The command & control data link shall have a bandwidth of at least 'TBD' to allow linking of all control inputs.		

15
Conclusion & Recommendations

In this chapter a conclusion of the report is given in section 15.1. Recommendations on all aspects of the future development of the RAD are given in section 15.2.

15.1. Conclusion

The aim of this report was to design a UAV that can fill the role of red air in aerial combat training, and that satisfies the requirements set by the NLR. The UAV must have a maximum speed of at least Mach 1.6, a radar cross-section smaller than 0.01 m^2, and must withstand a normal load factor of 6 g. Furthermore, the UAV must be more sustainable and economical than the current alternatives. The resulting configuration can be seen in figure 15.1.

The design features a compound delta planform, a V-tail, and a single engine with two air intakes. The aircraft groups the angles for the intakes, the wings, the empennage, and the nose to reduce the radar cross-section of the aircraft. The maximum take-off mass of the aircraft is 2,126 kg. This is lower than the current alternatives. As a result of lower mass, the UAV uses less fuel and produces less noise than the alternatives. This makes the UAV inherently more sustainable than its alternatives. It promises a reduction in CO_2 emissions of up to 94%. Furthermore, the cost of operating the drone is up to 83% lower than the cost of operating a manned aircraft. Furthermore, UAVs can be partially or fully automated, allowing for one single pilot to control several UAVs.

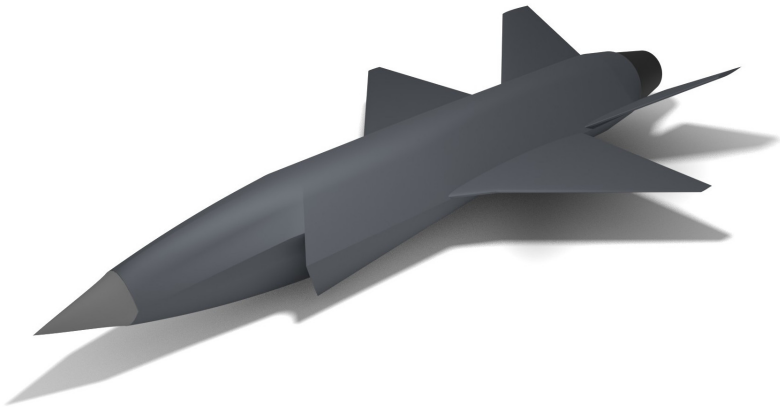

Figure 15.1: *Overview of the red air drone.*

The requirements that drive the design the most are low observability requirement and the maximum speed requirement. Due to the low payload mass of the UAV, the driving factor of the size was finding an engine that was as small as possible while still being able to propel the aircraft to the required speed of Mach 1.6. The engine that was eventually chosen for the aircraft is the IHI F-3. This engine features a custom afterburner and can provide a thrust force of 29.5 kN. As such, it provides a thrust to weight ratio that is high enough to propel the aircraft to Mach 1.8. Driving the shape of the aircraft was not only the aerodynamics, but also the low observability requirement. Optimising for low observability involves having no frontal facing surfaces and grouping the angles of the lines that make up the shape of the aircraft like the leading edge and trailing edge of the wing, the angle of the nose, and the leading and trailing edge of the empennage. These limitations in term have a negative influence on how well the aerodynamic shape of the aircraft could be optimised. In the end, a compromise had to be made that both satisfied the low observability requirement while keeping the drag as low as possible.

15.2. Recommendations

The recommendations provide methods of improvement for the design of the RAD.

15.2.1. Aerodynamics

The wave drag is very high due to lack of stringent area ruling. If the area ruling is more stringently applied, the wave drag could drastically decrease and allow for much better L/D performance and greater supersonic speed.

The RAD could reach Mach 2 comfortably and with a good acceleration if the drag is decreased through area ruling. Furthermore, if the wave drag is decreased sufficiently, it is recommended to increase the airfoil thickness, possibly to 5 or 6 % t/c. This will allow more space for fuel in the wings, better integration of high lift devices and an overall more efficient wing structure. The next step for the design, is to create a better model to more accurately investigate the lift and drag performance.

15.2.2. Low Observability

For low observability, it is recommended to increase the trailing edge sweep of the wing and canted tail. It is also recommended to investigate the non-constant radii curvature of the fuselage and nose and the possible corner reflector created by the nose and fuselage as seen in figure 9.11 to further optimize for stealth and aerodynamics. Moving the V-tail further back to cover the engine exhaust as much as possible is also recommended for the infrared visibility from the side aspect.

15.2.3. Structures

First, recommendations for the wingbox include making the wings detachable, and reducing the thickness of the spars and skin close to the tip. Furthermore, the material chosen can be reconsidered, as a higher yield stress might be achievable with a different type of aluminium. The loads in the fuselage are recommended to be transferred by continuous elements between both wings that go around the engine. From these structural elements, the loads can be transferred via stringers and the skin to the rest of the elements in the fuselage. The structures in the empennage can be very similar to the structures in the wing.

15.2.4. Empennage

The control surfaces on the tail have not been properly sized in this design. Therefore, the ruddervators must be properly sized to realise a finished design. If controllability becomes a bigger requirement or is considered to be a niche feature, then the canted fins could be designed as an all-moving tail.

15.2.5. Landing Gear Design

For the next stages of design, it is recommended to take into the tire choice. For example, the rim dimensions, dynamic loading, deformations, and tire profile. For this preliminary sizing, only the aircraft weight and landing speed were considered.

15.2.6. Operational Profit

As many numbers in the cost analysis of the RAD were based on assumptions, the validity of the cost model can be questioned. Therefore, it is recommended to continuously improve this model throughout the next design phases. This can be done by incorporating a more detailed design and by using an updated statistical analysis. Although no data is publicly available, on can reproduce a cost model using the same methodology as the Rand Corporation did [66]. Furthermore, operational costs could be refined by using a different study performed by the RAND Corporation [69]. Lastly, a better image of total cost savings could be built if a more extensive market survey is done.

15.3. Final Remarks

The UAV that was designed during the DSE has remarkable economic, environmental, and operational benefits. Not, to mention, the enormous benefit it would have on the combat readiness of pilots, and all the other personnel and units that have a role in aerial combat. The need for proper red air training is greater than ever. It is therefore recommended that the project should be taken into the further stages of development as soon as possible.

Bibliography

[1] B. D. Laslie, *The Air Force Way of War: U.S. Tactics and Training after Vietnam*. Lexington, Kentucky: University Press of Kentucky, 2015.

[2] DSE Group #25, *Red Air Drone - Midterm Report*. Delft, NL: Faculty of Aerospace Engineering, May 2022, Unpublished.

[3] ——, *Red Air Drone - Baseline Report*. Delft, NL: Faculty of Aerospace Engineering, May 2022, Unpublished.

[4] A. in 't Veld, *Project Guide Design Synthesis Exercise - Red Air Drone*. Delft, NL: Faculty of Aerospace Engineering, Apr. 2022.

[5] P. Malone, H. Apgar, S. Stukes, and S. Sterk, "Unmanned Aerial Vehicles unique cost estimating requirements," Mar. 2013, pp. 1–8. doi: 10.1109/AERO.2013.6496852.

[6] F. De Florio, "Chapter 1 - Flight Safety," in *Airworthiness*, F. De Florio, Ed., 3rd ed., Oxford, UK: Butterworth-Heinemann, 2016, pp. 1–3. doi: 10.1016/B978-0-08-100888-1.00001-X.

[7] ——, "Chapter 11 - Airworthiness of Unmanned Aircraft Systems (UAS)," in *Airworthiness*, F. De Florio, Ed., 3rd ed., Oxford, UK: Butterworth-Heinemann, 2016, pp. 471–493. doi: 10.1016/B978-0-08-100888-1.00011-2.

[8] A. van Heerden, D. Judt, S. Jafari, C. Lawson, T. Nikolaidis, and D. Bosak, "Aircraft thermal management: Practices, technology, system architectures, future challenges, and opportunities," *Progress in Aerospace Sciences*, vol. 128, p. 100 767, 2022. doi: 10.1016/j.paerosci.2021.100767.

[9] L. Pepermans, E. Menting, M. Rozemeijer, *et al.*, "Comparison of various parachute deployment systems for full rocket recovery of sounding rockets," in *Proceedings of the 8th European Conference for Aeronautics and Space Sciences*, Madrid, Spain: EUCASS, Jul. 2019, pp. 1–4. doi: 10.13009/EUCASS2019-411.

[10] N. Larsen, "Electronically Steerable Antennas for Satellite Communications," Ph.D. dissertation, Dept. of Electrical Eng., Technical University of Denmark, Oct. 2007.

[11] E. Bertran and A. Sànchez-Cerdà, "On the Tradeoff Between Electrical Power Consumption and Flight Performance in Fixed-Wing UAV Autopilots," *IEEE Transactions on Vehicular Technology*, vol. 65, no. 11, pp. 8832–8840, Nov. 2016. doi: 10.1109/TVT.2016.2601927.

[12] H. Chao, Y. Cao, and Y. Chen, "Autopilots for small unmanned aerial vehicles: A survey," *International Journal of Control, Automation and Systems*, vol. 8, no. 1, pp. 36–44, Feb. 2010. doi: 10.1007/s12555-010-0105-z.

[13] Q. Su, S. Chang, Y. Zhao, H. Zheng, and C. Dang, "A review of loop heat pipes for aircraft anti-icing applications," *Applied Thermal Engineering*, vol. 130, pp. 528–540, 2018. doi: 10.1016/j.applthermaleng.2017.11.030.

[14] Y. Cao, W. Tan, and Z. Wu, "Aircraft icing: An ongoing threat to aviation safety," *Aerospace Science and Technology*, vol. 75, pp. 353–385, 2018. doi: 10.1016/j.ast.2017.12.028.

[15] P. Burris, D. Carter, S. Brandt, and W. Anemaat, "Fifth-Generation Target Drone Phase I Design," in *11th AIAA Aviation Technology, Integration, and Operations (ATIO) Conference*. Jun. 2012. doi: 10.2514/6.2011-7012.

[16] M. D. Guenov, X. Chen, A. Molina-Cristóbal, A. Riaz, A. S. J. van Heerden, and M. Padulo, "Margin Allocation and Tradeoff in Complex Systems Design and Optimization," *AIAA Journal*, vol. 56, no. 7, pp. 2887–2902, Jul. 2018. doi: 10.2514/1.J056357.

[17] DSE Group #25, *Red Air Drone - Project Planning*. Delft, NL: Faculty of Aerospace Engineering, Apr. 2022, Unpublished.

[18] J. D. Anderson, *Fundamentals of Aerodynamics*, 6th ed. New York City, USA: McGraw-Hill Education, 2017.

[19] R. Whitford, *Design for air combat*. Coulsdon, UK: Janes Information Group, 1987.

[20] R. Vos. "AE-4245: Advanced Aircraft Design II." (2020), [Online]. Available: https://brightspace.tudelft.nl/d2l/le/content/278242/viewContent/1803150/View.

[21] T. G. Ayers, "A wind-tunnel investigation of the application of the NASA supercritical airfoil to a variable-wing-sweepfighterairplane," Langley Research Center, NASA Technical Paper NASA TM X-2759, 1973.

[22] D. P. Raymer, *Aircraft Design: A Conceptual Approach*, 6th ed. Reston, VA, USA: American Institute of Aeronautics and Astronautics, Inc., Sep. 2018.

[23] Techwinder, *XFLR5*.

[24] D. E. Hoak, *USAF Stability and Control DATCOM, Pt. 1-11*. Ohio, US: Air Force Flight Dynamics Laboratory, Flight Control Division, 1960.

[25] NASA, *OpenVSP*.

[26] S. F. Hoerner, *Fluid-Dynamic Drag*. California, US: published by author, 1965.

[27] M. J. Waddington, "Development of an interactive wave drag capability for the OpenVSP parametric geometry tool," M.S. thesis, Dept. of Aerospace Eng., California Polytechnic State University, Jul. 2015. doi: 10.15368/theses.2015.126.

[28] E. Roux, *Turbofan and Turbojet Engines Database Handbook*. Blagnac, France: Éditions Élodie Roux, 2007.

[29] J. D. Anderson, *Aircraft Performance and Design*. New York City, USA: The McGraw-Hill Companies, 2007.

[30] L. Cwojdziński and M. Adamski, "Power units and power supply systems in UAV," *Aviation*, vol. 18, pp. 1–8, Apr. 2014. doi: 10.3846/16487788.2014.865938.

[31] A. Cervone, *Power & Propulsion - part 2 - Electric Power Systems*, Delft University of Technology, 2022.

[32] J. Roskam, *Airplane Design: Layout Design of Landing Gear and Systems*, ser. Airplane Design. St. Lawrence, KS: DARcorporation, 1989.

[33] F. Oliviero, *AE3211-I: Systems Engineering and Aerospace Design - lecture 7 - Design for AC Longitudinal Stability*, Delft University of Technology, 2019.

[34] L. M. Nicolai, *Fundamentals of Aircraft Design*. Xenia, OH: METS, Jan. 1975.

[35] R. D. Schaufele, *The elements of aircraft preliminary design*. Santa Ana, CA: Aries Publications, 2007.

[36] D. Raymer, *Aircraft Design: A Conceptual Approach*, ser. AIAA Textbook Series. Reston, VA: American Institute of Aeronautics and Astronautics, 1989.

[37] J. Roskam, *Airplane Design: Preliminary Configuration Design and Integration of the Propulsion System*, ser. Airplane Design. St. Lawrence, KS: DARcorporation, 1989.

[38] A. Sanchez-Carmona and C. Cuerno-Rejado, "Vee-tail conceptual design criteria for commercial transport aeroplanes," *Chinese Journal of Aeronautics*, vol. 32, no. 3, pp. 595–610, 2019. doi: 10.1016/j.cja.2018.06.012.

[39] L. M. Nicolai and G. E. Carichner, *Fundamentals of Aircraft and Airship Design*, ser. Aircraft Design. 1801 Alexander Bell Drive, Reston, VA 20191-4344: AIAA, 2010.

[40] R. Slingerland, "Prediction of a tail downwash, ground effect and minimum unstick speed of jet transport aircraft," Jan. 2005.

[41] E. Torenbeek, "Synthesis of subsonic airplane design," 1982, Publisher: Delft University Press. (visited on 04/25/2022).

[42] F. Oliviero, *AE2111-II: Aircraft aerodynamic analysis: Mobile surfaces of the wing*, Delft University of Technology, 2020.

[43] S. Gudmundsson, *General Aviation Aircraft Design*. Boston, MA, USA: Butterworth-Heinemann, 2014.

[44] O. Al-shamma, R. Ali, and H. Hasan, "An educational rudder sizing algorithm for utilization in aircraft design software," *International Journal of Applied Engineering Research*, vol. 13, pp. 7889–7894, Oct. 2018.

[45] ——, "An instructive algorithm for aircraft elevator sizing to be used in preliminary aircraft design software," *Journal of Applied Engineering Science*, vol. 15, pp. 489–494, Jan. 2017. doi: 10.5937/jaes15-14829.

[46] R. Vos and J. Melkert, *Aerospace Design and Systems Engineering Elements I- lecture 7 - Wing Postioning. Landing Gear and Empennage Design*, Delft University of Technology, 2019. [Online]. Available: https://brightspace.tudelft.nl/d2l/le/content/213451/viewContent/1472043/View.

[47] Akhilesh Jha, "Landing Gear Layout Design for Unmanned Aerial Vehicle," NIT, Durgapur, India, Dec. 2009.

[48] N. S. Currey, *Aircraft landing gear design: principles and practices*, 4. print, ser. AIAA education series. Washington, DC: American Institute of Aeronautics and Astronautics, 1988.

[49] S. van der Zwaag, *Materials Science Lecture 4: Material selection and plastic deformation*, 2019. [Online]. Available: https://brightspace.tudelft.nl/d2l/le/content/213438/viewContent/1577789/View.

[50] ——, *Materials Science Lecture 7: Fracture and toughness*, 2019. [Online]. Available: https://brightspace.tudelft.nl/d2l/le/content/213438/viewContent/1581598/View.

[51] M. Ashby, H. Shercliff, and D. Cebon, *Materials: Engineering, Science, Processing and Design*, 4th ed. Cambridge, UK: Butterworth-Heinemann, Nov. 2018.

[52] T. Megson, *Aircraft Structures for Engineering Students*, 6th ed. Cambridge, UK: Butterworth-Heinemann.

[53] G. Haddow and P. M. Grosz, *The German Giants – The German R-Planes 1914-1918*, 3rd ed. Putnam.

[54] D. Miller, *Illustrated Directory of Modern American Weapons*. Duluth, MN, USA: Zenith, 2002.

[55] D. Richardson, *Stealth Warplanes*. St Paul, MN, USA: MBI Publishing Company, 2001.

[56] J. Jones and M. Thurber, *Stealth Technology: The art of black magic*. New York City, USA: TAB Books inc, 1989.

[57] J. T. Walton and F. W. Burcham Jr., "Exhaust-gas pressure and temperature survey of f404-ge-400 turbofan engine," NASA Technical Memorandum 88273, Dec. 1986.

[58] G. Ruijgrok, *Elements of Airplane Performance*. Delft, The Netherlands: Delft University Press, 1990.

[59] S. Chiesa and M. Fioriti, "Uav logistic support definition," in *Handbook of Unmanned Aerial Vehicles*, K. P. Valavanis and G. J. Vachtsevanos, Eds. Dordrecht: Springer Netherlands, 2015, pp. 2565–2600. doi: 10.1007/978-90-481-9707-1_79.

[60] C. Karaağaç, A. G. Pakfiliz, F. Quagliotti, and N. Alemdaroglu, "Uav logistics for life-cycle management," in *Handbook of Unmanned Aerial Vehicles*, K. P. Valavanis and G. J. Vachtsevanos, Eds. Dordrecht: Springer Netherlands, 2015, pp. 2601–2635. doi: 10.1007/978-90-481-9707-1_89.

[61] Center for Information on Security Trade Control, *Overview of japan's export controls*, Jun. 2015.

[62] "Fiscal Year (FY) 2022 Department of Defense (DoD) Fixed Wing and Helicopter Reimbursement Rates," Memorandum, 2022.

[63] United States Government Accountability Office, "Military Air Support, Dod has increased its use of contracts to meet training requirements," Report to the Committee on Armed Services GAO-22-104475, Dec. 2021.

[64] *Hearings on military posture and H.R. 11500 [H.R. 12438] Department of Defense authorization for appropriations for fiscal year 1977 before the Committee on Armed Services House of Representatives Ninety-fourth Congress second session*. Washington, DC, USA: US Government Printing Office, 1976.

[65] M. Boito, E. G. Keating, J. Wallace, B. DeBlois, and I. Blum, *Metrics to Compare Aircraft Operating and Support Costs in the Department of Defense*. Santa Monica, CA: RAND Corporation, 2015. doi: 10.7249/RR1178.

[66] J. P. Large, H. G. Campbell, and D. Cates, "Parametric equations for estimating aircraft airframe costs," The Rand Corp., Santa Monica, CA, USA, Report R-1693-1-PA&E, Feb. 1976.

[67] O. Younossi, M. V. Arena, R. M. Moore, M. Lorell, J. Mason, and J. C. Graser, *Military Jet Engine Acquisition, Technology Basics and Cost-Estimating Methodology*. Santa Monica, CA, USA: RAND, 2003.

[68] "Fiscal Year (FY) 2022 Department of Defense (DoD) Civilian Personnel Fringe Benefits Rates," Department of Defense Comptroller, Memorandum, 2022.

[69] R. A. Pyles, *Aging Aircraft, USAF Workload and Material Consumption Life Cycle Patterns*. Santa Monica, CA, USA: RAND, 2003.

A

Advanced Aircraft Analysis Inputs

Table A.1: *Weight component inputs used to calculate the AMPR weight (all weights in Newton)*

W_E	W_{ess}	W_{els}	W_{api}	W_{wheels}	$W_{cooling}$	W_{iae}	W_{apu}	W_{eng}	$W_{FuelCell}$	W_{arm}	W_{tfo}
14038	264.9	427.7	0.0	1196.8	0.0	466.0	0.0	4915	0.0	0.0	0.0

Table A.2: *Inputs and outputs of the first step of development cost estimation*

N_{rdte}	F_{cad}	$R_{e_{rdte_{1989}}}$	$V_{h_{eas}}$	$F_{difficulty}$	Year
5	1.5	30.00 $/h	843.27 km/h	1.5	2022

$MHR_{aed_{rdte}}$	$R_{e_{rdte}}$	CEF	$C_{aed_{rdte}}$
448283.4 h	62.95 $/h	6.71	$ 28.218·10^6

Table A.3: *Inputs and outputs of the second step of development cost estimation*

W_{AMPR}	$V_{H_{eas}}$	N_{rdte}	$F_{difficulty}$	Year
6767.6 N	843.27 km/h	5	1.5	2022

CEF	$C_{dst_{rdte}}$
6.71	9.27

Table A.4: *Inputs and outputs of the third step of development cost estimation*

W_{AMPR}	N_{static}	$C_{eng_{rdte}}$	Year	R_{rdte}
6767.6 N	2	$ 2.5·10^6	2022	0.5
$V_{H_{eas}}$	$F_{difficulty}$	$K_{av_{rdte}}$	$R_{man_{rdte_{1989}}}$	
843.27	1.5	1.25	20.00 $/h	
N_{flight}	F_{mat}	$P_{ap_{market}}$	$R_{t_{rdte_{1989}}}$	
3	2.5	$ 10·10^6	30.00 $/h	

N_{rdte}	$C_{mat_{rdte}}$	$C_{t_{rdte}}$	$R_{t_{rdte}}$	$C_{fta_{rdte}}$
5	$ 16.028·10^6	$ 31.924·10^6	62.95 $/h	123.069
$C_{man_{rdte}}$	$C_{av/ap_{rdte}}$	$MHR_{t_{rdte}}$	$C_{qc_{rdte}}$	
$ 26.652·10^6	$ 12.5·10^6	507164.87 h	$ 3.465·10^6	
$MHR_{man_{rdte}}$	CEF	$R_{man_{rdte}}$	$C_{EngAv_{rdte}}$	
635103.49 h	6.71	41.96 $/h	$ 45·10^6	

Table A.5: *Inputs and outputs of the fourth step of development cost estimation*

W_{AMPR}	N_{rdte}	Year	F_{obs}
6767.6 N	5	2022	5.0
$V_{H_{eas}}$	$F_{difficulty}$	N_{static}	
843.27 km/h	1.5	2	

CEF	$C_{fto_{rdte}}$
6.71	$ 5.540·10^6